The Sr isotopic stratigraphy of the LCZ-UCZ transition in the Western Limb of the Bushveld Complex.

Mafete Malatji

Dissertation submitted in fulfilment of the requirements for the degree:
Master of Science in Geology
2021

Faculty of Natural and Agricultural Sciences
University of the Free State
Bloemfontein

UNIVERSITY OF THE
FREE STATE
UNIVERSITEIT VAN DIE
VRYSTAAT
YUNIVESITHI YA
FREISTATA

UFS
UV

Declaration

I, Mafete Malatji declare that this dissertation is my own unassisted work, apart from referenced or acknowledged work by others. It is submitted for the qualification of Master of Science in Geology at the University of the Free State. No prior submission at other institutions for any qualification or examination was made. Additionally, I relinquish copyright in favour of the University of the Free State.

Signature: 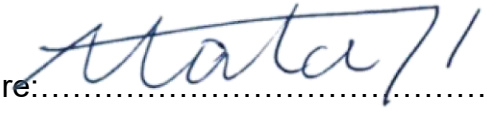 …… Date: 22/02/2022

Dedication

- To my late grandmother, Mokhadi'a Motzaneni ngwana wa motjiwa hole khauswi ghe tšhaba ditshele.

- To my loving parents Mashile le Moghwabhe for the unconditional love and support.

- To my siblings Mokhale, Sello, Maite, Tshepo, Mafeto le Modjadji, for always motivating and pushing me.

Acknowledgements

The support of the DST-NRF Centre of Excellence for Integrated Mineral and Energy Resource Analysis (DST-NRF CIMERA) towards this research is hereby acknowledged. Opinions expressed and conclusions arrived at are those of the author and are not necessarily to be attributed to the COE.

Impala platinum LTD is also acknowledged for donating the BH7929 core to the University of the Free State, which this dissertation is solely based on, particularly Mr Bennie Cilliers and Mr Philip Fouche.

A debt of gratitude is owed to my co-supervisors, Prof Frederick Roelofse and Mrs Justine Magson. Thank you for conceiving and assigning the project to me, as well as providing your guidance, support and expertise throughout the most trying times in our country, as a result of the novel corona virus pandemic. I appreciate every suggestion, correction and critique you afforded me, which was beneficial during the duration of the dissertation. Kudos to you both.

I would like to thank the following geology department laboratory staff members at the University of the Free State. Mr Daniel Radikgomo for preparing all the thin sections and polished blocks used in this study, Mr Pelele Lehloenya for preparing pressed pellets and fusion discs, lastly Mrs Megan Welman-Purchase for calibrating the XRF and SEM instruments. Mrs Rina Immelman, Mrs Charlene Van Der Vyver and Mr Andries Felix are also thanked for making all the proper arrangements necessary during the duration of the study.

From the Spectrum analytical facility of the University of Johannesburg, Dr Christian Reinke is acknowledged for assisting with Electron Micro Probe Analyzer. Ms Henriette Ueckermann and Prof Marlina Elburg are both acknowledged for assisting with Laser Ablation Multi-Collector Inductively Coupled Plasma Mass Spectrometry.
Mr Marlin Patchappa from the School of Geosciences' Earth Lab of the University of the Witwatersrand is also acknowledged for assisting with Inductively Coupled Plasma Mass Spectrometry.

Abstract

Data on the modal mineralogy, whole-rock geochemistry, plagioclase mineral chemistry and Sr isotopic compositions in lithologies covering an interval of ~100 m across the Upper Critical Zone (UCZ) and Lower Critical Zone (LCZ) transition in the Western Limb of the Bushveld Complex are presented in this study. The aims of this study were to (1) investigate the presence or absence of isotopic disequilibrium in plagioclase (2) to investigate differences between the LCZ and UCZ from a geochemical, petrological and Sr isotopic perspective and (3) to refine chromitite formation models using the data obtained over the course of the study. Samples were obtained from the BH7929 drill core donated by Impala platinum to the University of the Free State. Samples were analysed using transmitted light microscopy, X-Ray Fluorescence Spectrometry (XRF), Inductively Coupled Plasma Mass Spectrometry (ICPMS), Electron Probe Micro-Analyzer (EPMA) and Laser Ablation Multi-Collector Inductively Coupled Plasma Mass Spectrometry (LA MC-ICP-MS) to produce whole-rock major and trace element geochemistry and plagioclase elemental and isotopic compositional profiles across the UCZ-LCZ transition.

Results reveal that the LCZ is composed of orthopyroxene-dominated lithologies that display cryptic layering, hosting two chromitite layers (MG1-2), with plagioclase predominantly existing as an intercumulus phase. Plagioclase is predominantly cumulus in the UCZ, dominating the UCZ lithologies that display modal layering. Two chromitite layers were investigated in the UCZ (MG3-4). Compositional breaks in whole-rock major and trace elements are detected at the UCZ-LCZ transition and at the level of the chromitite layers, reflecting variations in the dominant mineral phases. Fractionation indices including whole-rock Mg# and Cr/V ratio reveal little variation throughout the study interval in silicate-dominated lithologies, with variations mostly detected at the level of chromitite layers. Plagioclase An% averages 82.10 ± 1.90% in the UCZ, whereas it averages 73.58 ± 2.60% in the LCZ. Chromitite layers in the LCZ reveal lower An% values in comparison with adjacent silicate lithologies, whereas the UCZ reveals very little to no variations between chromitites and silicate lithologies. Sri values in the UCZ average 0.7059 ± 0.0003, whereas Sri in the LCZ averages 0.7054 ± 0.0004. Decreases in the Sri value of plagioclase are observed at the level of the

chromitite layers in the LCZ, whereas the UCZ reveals a constant Sri up the stratigraphy.

The data provide credence to the importance of magma mixing (i.e. Irvine, 1977) as a process operational in the formation of chromitite layers within the LCZ and UCZ and argue against models suggesting variations in intensive parameters or in-situ crystallization as dominant processes in the formation of chromitite layers. It is proposed that the UCZ-LCZ transition displays credible evidence for the repeated intrusion of batches of isotopically distinct magmas, with chromitite layers in the LCZ forming in response to the mixing of newly introduced and resident magma in a manner analogous to that envisaged by Irvine. The MG3 layer in the UCZ also appears to have formed as a direct consequence of mixing between newly intruded UCZ magma and the residual LCZ magma. The MG4 layer does not preserve Sr-isotopic evidence for magma mixing as it has similar Sri as that of adjacent silicate lithologies. In order to account for the mass balance of Cr, it is argued that at the level of chromitite layers, intruded magma pulses were chromite-laden, with additional chromite formation occurring in response to magma mixing. The MG1 chromitite layer provides potential evidence in support of such an argument in the form of multiple isotopically distinct populations of plagioclase that may have been intruded along with suspended chromite crystals.

Table of Contents

List of figures

List of tables

1. Introduction

Previous workers have demonstrated that there are indeed Sr isotopic variations in the rocks of the Rustenburg Layered Suite (hereafter RLS), even at the level of individual crystals within some rocks. However, there is insufficient attention regarding such a topic especially in the noneconomical parts of the Critical Zone (CZ), with too much attention having been given to the more economically significant units such as the Merensky and UG2 units. This study utilises plagioclase chemistry (Sr isotope and mineral compositions), chromite mineral chemistry and whole-rock geochemistry to infer the probable processes operational during magma emplacement at the LCZ-UCZ transition as well as the origin of associated chromitite layers.

Sr isotopic studies have proved to be significant (recent studies include Roelofse *et al*. 2015; Mangwegape *et al*. 2015; Karykowski *et al*. 2018; Maghdour-Mashhour *et al*. 2020 and Beukes *et al*. 2021), particularly in providing a glimpse into magmatic and post magmatic processes during emplacement of igneous rocks (Davidson *et al*. 2007). The mineralogy of igneous rocks (e.g. Bushveld Complex or any other magmatic intrusion), particularly those that display isotopic variations between coexisting minerals or within a single mineral (inter and intra disequilibrium) hold critical information regarding their crystallization history. Magmatic evolution can be traced using mineral-scale isotopic data, which sheds light on various processes that might have affected the magma (Davidson *et al*. 2007) These processes include crustal contamination, partial assimilation, and magma recharge, which can be detected from isotopic variations, either from a single mineral (rim to core) or between co-existing minerals (Davidson *et al*. 2007). Therefore, isotopic variation can be utilized to infer the parental magma from which they formed as well as magmatic and post-magmatic processes, thereby constraining petrogenetic processes.

Some of the earliest ground-breaking isotope studies in the BC were conducted by Hamilton (1977), Kruger and Sharpe (1982), Sharpe (1985), Lee and Butcher (1990) and Kruger (1994), who solely focused on Sr isotopes throughout the entire stratigraphy of the Rustenburg Layered Suite (RLS) in different limbs using whole-rock data. However, the use of whole-rock data for isotopic studies can obscure significant petrogenetic aspects. Eales *et al*. (1990a; 1990b) provided the earliest Sr isotope work in the RLS focusing on mineral separates. Recently, focus has shifted to investigating

isotopic variations (i.e. Sr, Pb, Nd and Sm) between and within constituent minerals within the same rock in the BC (e.g. Prevec *et al*. 2005; Seabrook *et al*. 2005; Roelofse and Ashwal 2012; Chutas *et al*. 2012; Yang *et al*. 2013; Roelofse *et al*. 2015; Mangwegape *et al*. 2015; Lehloenya, 2017; Karykowski *et al*. 2018; Maghdour-Mashhour *et al*. 2020 and Beukes *et al*. 2021).

Early workers have demonstrated that the stratigraphy of the RLS reveals breaks and reversals in strontium isotopic data (i.e.$^{87}Sr/^{86}Sr$), which occurs at various zones and subzones of the stratigraphy along with changes in mineral assemblages (Hamilton, 1977; Kruger and Sharpe, 1982 and Kruger, 1994). For example, the transition between the Lower Critical Zone (LCZ) and Upper Critical Zone (UCZ) reveals an increase in initial $^{87}Sr/^{86}Sr$, where this ratio is higher in the UCZ than in the LCZ. This transition also reveals changes in mineral phases, where plagioclase, which is not a cumulus phase in the LCZ, becomes a cumulus phase in the UCZ.

Strontium isotopic variations are also detected within and between coexisting mineral populations within the same rock as reported by previous workers (i.e. Prevec *et al*, 2005; Seabrook *et al*, 2005; Roelofse and Ashwal, 2012). These findings indicate that magmatic processes that lead to the emplacement of the BC rocks are complex. Therefore, strontium isotopic variations can be used to infer magmatic to post magmatic processes occurring in the overall Bushveld chamber as well as pinpointing the provenance or origin of the multiple magma influxes, thus constraining Bushveld petrogenetic models.

The present study focused on the determination of variations in mineral chemistry and strontium isotopic compositions of plagioclase, as well as whole-rock major and trace element abundances using closely spaced samples through 3 sections, one from the LCZ, another across the LCZ-UCZ transition (i.e. MG2-MG3) and another from the UCZ. The following aspects were evaluated in particular:

1. Is there any evidence for the existence of multiple, isotopically distinct populations of plagioclase that could point to the mixing of minerals as opposed to magmas in the genesis of the CZ (cf. Seabrook *et al*. 2005)?

2. How does the nature of cyclic units differ between the LCZ and UCZ from a geochemical, petrological and Sr-isotopic perspective?

3. How can the data obtained during this study be used to comment on or refine models that have been proposed to explain the formation of (PGE-enriched) chromitite layers in the CZ?.

1.1. Bushveld Complex background

Dated at 2055.91 Ma (Zeh *et al*. 2015), the RLS (Fig 1) of the Bushveld Complex (BC), is the largest recognized layered igneous intrusion on Earth, covering an area of over 60000 km^2, with a 9 km vertical extension (Wilson *et al*, 2017; Cawthorn, 2015). Substantial and exceptional economic mineralization of PGEs, chromium and vanadium are also hosted by the RLS rocks (Willemse, 1969; Lee, 1996; Schouwstra *et al*. 2000). The intrusion lies within the Kaapvaal Craton in the north-eastern part of South Africa, cropping out in four main limbs (Fig 1), namely the Far-western, Western, Eastern and Northern limbs (Du Plessis and Walraven, 1990). A fifth limb, termed the Southern/Bethal limb, exists under sedimentary cover (Eales and Cawthorn, 1996). Using geophysical data, Webb *et al.* (2004) and Cawthorn and Webb (2001) proved connectivity of the BC limbs at depth. A downwarp of the Moho is seen underneath the BC, which is interpreted as a result of airy isostatic balance in order to compensate for the weight of the BC. VanTongeren (2018) envisages a 150 km N-S and 450 km E-W extension of the BC, assuming connectivity at depth.

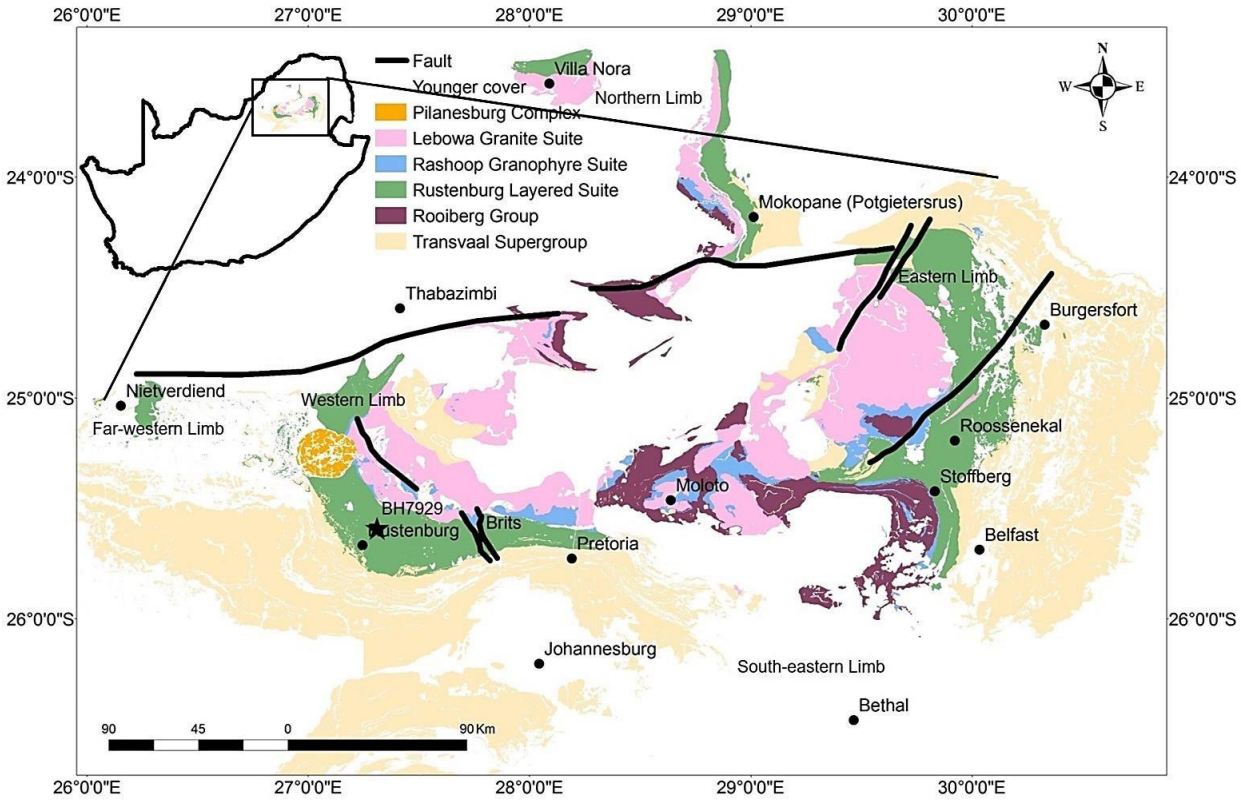

Figure 1: Geology of the Bushveld Complex and location in South Africa (prepared in ArcGIS using geospatial data provided by the Council for Geoscience).

The Western limb, which is the focus of this study, is poorly exposed. It is a 200 km long (Cawthorn *et al.* 2006; Cawthorn, 2015), eastern dipping crescent-shaped body extending from Thabazimbi (north) to Pretoria (south). The majority of mining activities have historically been conducted on the Western limb, specifically exploiting the uppermost parts of the Critical Zone. The Far-western limb is largely eroded. However, two zones that are underlain by a substantial thickness of BC rocks were identified by Biesheuvel (1970), one located west of Pilanesberg and the other ~60 km further to the west. Outcrops of the Far-western limb extend from the west of Pilanesberg to the border of Botswana (Cawthorn *et al.* 2006, Cawthorn *et al*. 2015). The Eastern limb mirrors the Western limb in the east, with virtually identical lithology and layering (Faure, 2001). It crops out as a western dipping crescent-shaped body extending from Chuniespoort (north) to Stoffberg (south), covering a 200 km long area (Cawthorn *et al*. 2006). The Northern limb is partly covered by sediments. Only the eastern edge of the limb and the Villa Nora fragment are exposed (Cawthorn *et al*. 2006). It crops out as a north-south sinuous outcrop (Kinniard, 2005). The Southern or Bethal limb occurs under sedimentary cover and its existence is known only from borehole and geophysical data (Eales and Cawthorn, 1996).

Emplacement of the RLS is thought to have occurred through numerous magma batches that intruded the supracrustal rocks of the Transvaal Supergroup, with each pulse closely spaced and having variable compositions (Eales and Cawthorn, 1996; Cawthorn and Walraven, 1998). Recently, the idea that the RLS was emplaced via a series of sills rather than as a large magma chamber has gained traction (Scoates *et al.* 2021). Contrasting models and theories are suggested regarding the provenance and emplacement of the magmas that formed the RLS. In broad terms, the RLS is thought to be a product of a massive rising asthenopheric plume in contact with the base of the lithosphere, which then assimilated and integrated the subcontinental lithospheric mantle and great quantities of the continental crust (VanTongeren, 2018).

According to the South African Committee for Stratigraphy (SACS, 1980), the BC is multifaceted comprising of diverse components of magmatic rocks that are synchronous (Table 1), with emplacement inferred to have occurred from a single magmatic event over a short period of time. These components include:

1) A basal suite of mafic sills that are intrusive into the Transvaal Supergroup.

2) The ultramafic to mafic RLS

3) Felsic rocks of the Rashoop Granophyre Suite and Lebowa Granite Suite.

4) Similar age intrusive satellite bodies; e.g. Molopo farms and Nkomati-Uitkomst.

Table 1: Ages for components of the BC (from Kinnaird, 2005).

Lithostratigraphic unit	Subdivision	Age (Ma ± 95%)
Lebowa Granite Suite	Makhutso Granite	2053.4 ± 3.9[1]
	Nebo Granite	2054.2 ± 2.8[1]
	Steelpoort Park Granite	2057.5 ± 4.2[1]
Rashoop Granophyre Suite	Rooikoppies Porphyry	2057.3 ± 5.5[1]
Rustenberg Layered Suite	Critical Zone (SHRIMP)	2054.4 ± 2.8[1]
	Critical Zone (IDTIMS)	2054.5 ± 1.5[1]
Satellite Intrusions	Molopo Farms	2044 ± 24[2]
	Mashaneng Complex	2054 ± 2[3]
	Uitkomst Complex	2044 ± 8[4]
		(2055 +45/-17)[4]

Ages obtained from [1]Harmer and Armstrong (2000); [2]Kruger (1989); [3]Mapeo *et al*. (2004) and [4]de Waal *et al*. (2001).

1.1.1. The Rustenburg Layered Suite (RLS)

The RLS is the main focus of this study. It is characterized by spectacular laterally extensive layering from cm- to m-scale, extending to about 8 km vertically (Hall, 1932; Cawthorn *et al*. 2006). It is typically divided into 5 distinguishable zones. Specific marker horizons, mineralogy, geochemistry and isotopic data can be used to delineate boundaries depending on different workers (e.g. Eales, 2002). These zones (Fig 2) include the Marginal Zone (MRZ), Lower Zone (LZ), Critical Zone (CZ), Main Zone (MZ) and Upper Zone (UZ) (Hall, 1932). This study will solely focus on rocks of the Critical Zone. Eales (2002) postulated that each zone within the stratigraphy of the RLS starting from the CZ to UZ represents a new intruding magma batch.

1.1.2. Lithostratigraphic subdivisions of the Rustenburg Layered Suite

The MRZ varies in thickness from 0-800 m and is located at the base of the RLS, with infrequent and attenuated appearance in both the Eastern and Western limbs (Kinnaird, 2005). It is primarily composed of unlayered and quenched norite and pyroxenite (plagioclase and pyroxene cumulates), with an abundance of xenoliths of metasedimentary country rocks (Eales *et al*. 1993; Cawthorn and Walraven, 1998; Maier *et al*. 2012). Furthermore, the MRZ rocks contain variable quantities of accessory minerals like clinopyroxene, quartz, biotite and hornblende, which point towards varying degrees of contamination by the underlying sediments (Kinnaird, 2005).

The LZ is compartmentalised and is best developed in the northern extremities of the Eastern and Western limbs as well as the southernmost parts of the Northern limb (Kinnaird, 2005). It is about 1300 m thick and consists of 3 subzones that display varying mineralogical compositions. It is divided into a lower pyroxenite subzone, a middle harzburgite subzone and an upper pyroxenite subzone (Teigler and Eales 1996). The Lower Zone in the Eastern and Western limbs is characterised by a lack of chromitite (Roelofse, 2010).

The CZ is up to 1500 m thick and it is characterised by its layering as well as the presence of economically important PGE-bearing layers (the Merensky reef, UG2-reef and Platreef) and abundant chromite mineralization hosted within the Lower (LG),

Middle (MG) and Upper (UG) group chromitite layers (Fig 2) (Cawthorn *et al*. 2006). It is divided into two compositionally different subzones 1) the LCZ) and 2) the UCZ (Eales *et al*. 1993; Eales and Cawthorn, 1996). The LCZ is composed of thick successions of orthopyroxenites and subordinate harzburgite, with up to 7 layers of chromitite (LG1-7) (Cawthorn *et al*. 2006; Maier *et al*. 2012). Four chromitite layers (MG1-4) constitute the middle group chromitites, with MG1-2 found in the LCZ and MG3-4 found in the UCZ (Cameron, 1980; Kinnaird *et al.* 2002). The formation of the chromitite layers is still debated, with numerous theories suggested (e.g. immiscible separation of Cr-rich liquids (Van Zyl, 1970), magma mixing (Irvine, 1975; 1977), physico-chemical alteration (pressure, bulk composition and oxygen fugacity) in the magma chamber (Cameron, 1980), intrusion of Cr-rich crystal slurries (Eales, 2002) and cooling of superheated magmas that may have become saturated in chromite during ascent and emplacement (Latypov *et al*. 2018)). The appearance of cumulus plagioclase delineates the base of the UCZ. This transition occurs between the MG2 and MG3 chromitite layers (Eales *et al*. 1993; Cawthorn *et al*. 2006). Eight cyclic units are documented in the UCZ, comprising of a base of ultramafic cumulates (chromitite, harzburgite, pyroxenite) with feldspathic tops (norite and anorthosite) (Cawthorn *et al*. 2006; Maier *et al*. 2012). The UG1-2 chromitite layers are located towards the top of the UCZ, and the appearance of the Merensky reef marks the transition into the MZ (Eales *et al*. 1993; Cawthorn *et al*. 2006). The main focus of this study is the transition between the LCZ and UCZ, as indicated by red bar in Figure 2.

The MZ is the most voluminous zone of the RLS and attains a maximum thickness of 3000 m (Cawthorn *et al.* 2006). Fine-scale layering is scarce in this zone and it lacks lithological diversity compared to the CZ. Based on mineralogical variations and field relations, Nex *et al*. (1998) subdivided the MZ into five subzones A-E (Fig 2), bounded by lithological marker units. This subdivision was largely based on the previous work by Molyneux (1970), von Gruenewaldt (1971) and SACS (1980) where the MZ was divided into subzones A, B and C. According to Nex *et al*. (1998) subzone A, which is located at the base of the MZ is noritic with subordinate anorthosite, Subzone B is composed of gabbronorite with cumulus augite, Subzone C is also gabbronoritic characterised by the appearance of inverted pigeonite at its base. The disappearance of inverted pigeonite marks the base of Subzone D, which is comprised of porphyritic

gabbronorite whereas the re-emergence of inverted pigeonite marks the base of subzone E, which is composed of gabbronorite, with interstitial magnetite.

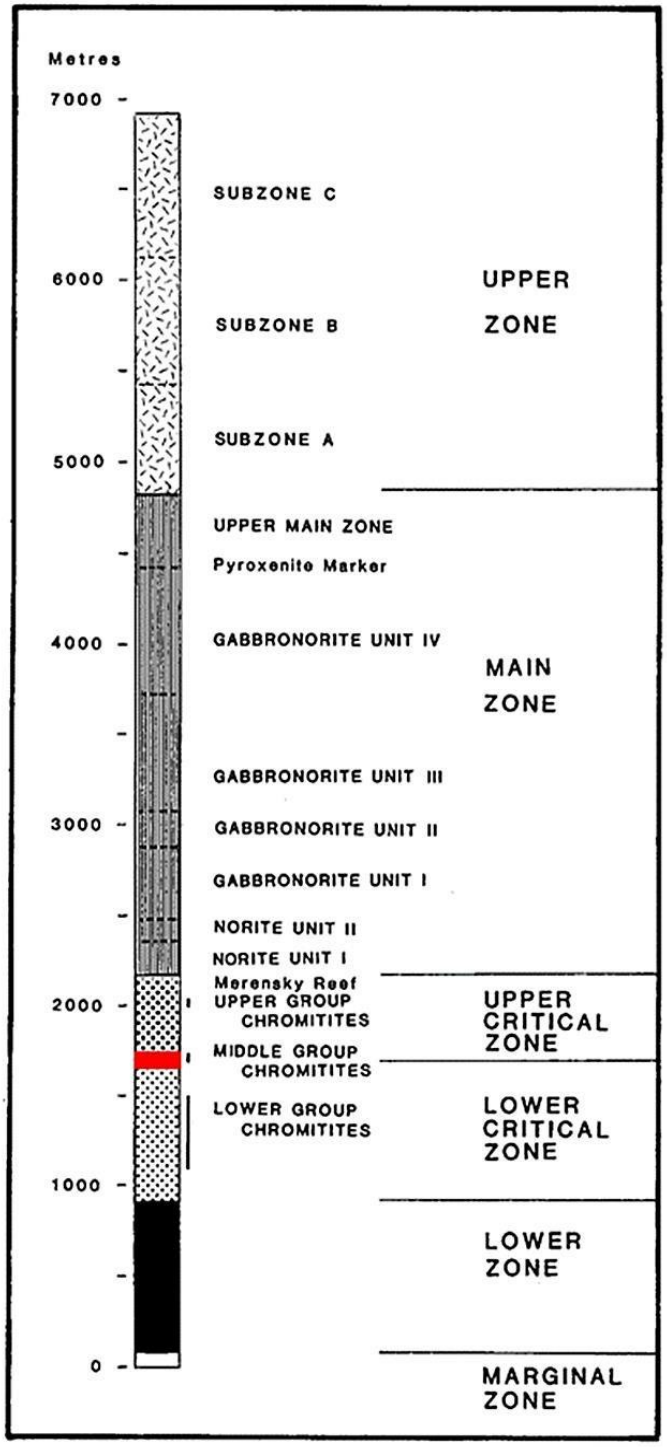

Figure 2: Zones and subzones of the RLS (from Eales et al. 1993). Red box indicates the study interval.

The appearance of cumulus magnetite delineates the base of the UZ, which is the most horizontally widespread zone within the RLS (Cawthorn *et al*. 2006). It reaches a thickness of about 2000 m with intermittent layering. The presence of 24 magnetitite layers distinguishes the UZ from the rest of the RLS zones (Molyneux, 1970). Based on cumulus mineralogy, the UZ is divided into 3 subzones (A-C) (Cawthorn *et al*. 2006): Magnetite attains cumulus status in Subzone A, which is composed of magnetite gabbronorite, anorthosite and 7 magnetitite layers. Subzone B is composed of olivine-magnetitite, gabbronorite, anorthosite, troctolite and 7 magnetitite layers. Subzone C is composed of a sequence of olivine-apatite diorite, anorthosite and 7 magnetitite layers, with apatite attaining cumulus status.

1.1.3. Preceding work

Hamilton (1977) performed pioneering strontium isotopic studies using a few samples through the stratigraphy of the RLS (Table 2). This groundbreaking work discovered an ascending step-like increase in the initial Sr isotope ratio, with each abrupt increase correlative to certain horizons and sudden irregularity in cryptic variation in the stratigraphy. In conclusion, Hamilton (1977) suggested that the fluctuations in initial Sr-isotope ratios through the stratigraphy of the RLS are indicative of emplacement as continuous magma influxes that were isotopically heterogenous.

Kruger and Sharpe (1982) conducted a similar study in the Western limb (Table 2), limiting their study on the Merensky unit and its adjacent footwall, whereas Sharpe (1985) performed Sr-isotope work of the Merensky unit in the Eastern limb (Table 2). The data revealed variations in the initial Sr-isotope ratio through the Merensky unit, increasing from 0.7060 at the base to 0.7080 at the top. Both studies agree with the preceding work conducted by Hamilton (1977), with abrupt increases of Sr isotope ratios correlative to certain horizons.

Subsequently, Kruger (1994: Table 2) and Kruger (2005) hypothesized emplacement of the BC as a two-stage process, (Fig 3) a lower open system integration stage characterised by injection of multiple isotopically heterogenous magmas, which formed the LZ, CZ and Lower Main Zone (LMZ) and an upper closed system differentiation stage, with minor magma addition that were isotopically homogenous forming the Upper Main Zone (UMZ) and UZ.

Table 2: Whole rock $^{87}Sr/^{86}Sr$ comparisons in the CZ.

Researcher (year)	Limb	Interval	$^{87}Sr/^{86}Sr$
Hamilton (1977)	Eastern	CZ interval	0.70646-0.71134
Kruger & Sharpe (1982)	Western	Merensky unit	0.70641-0,70740
Sharpe (1985)	Eastern	Merensky unit	0.7060-0.7080
Kruger (1994)	Western	CZ interval	0.70541-0.7064

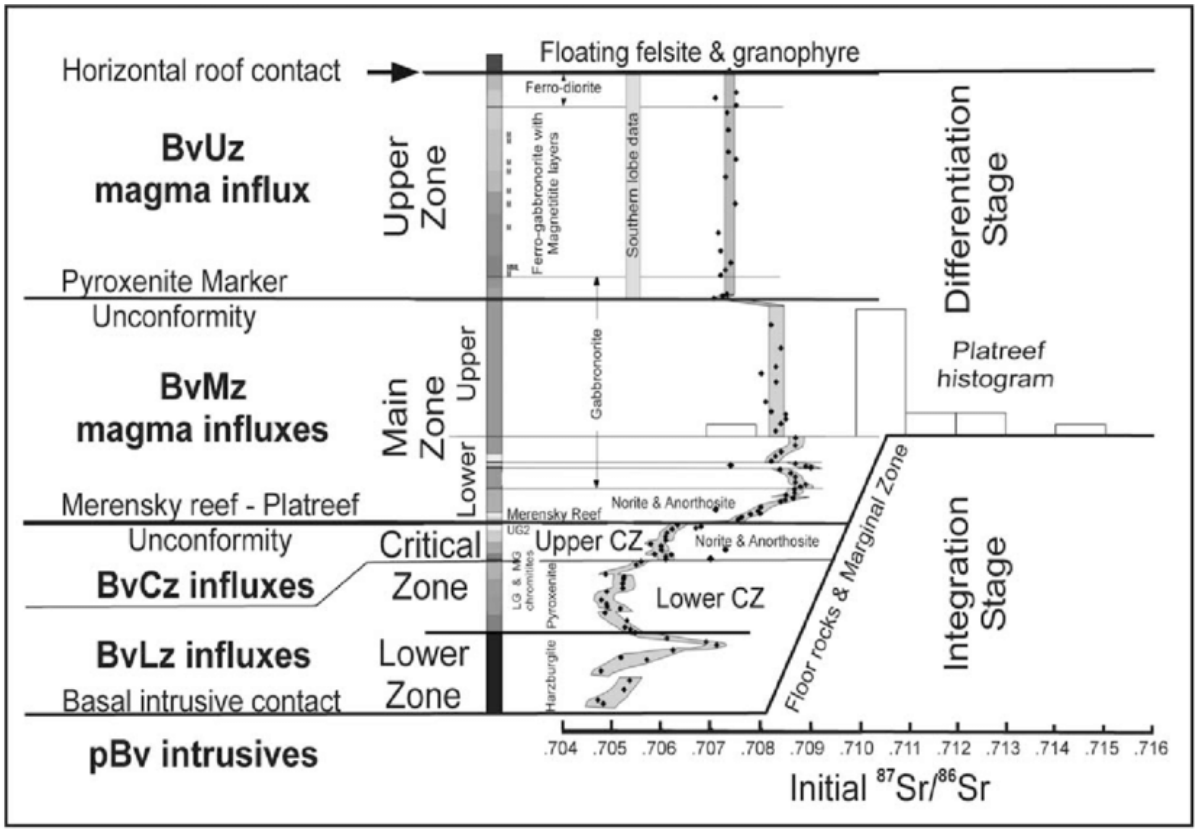

Figure 3: Composite diagram indicating variations in the initial Sr-isotope data through the RLS as well as relations to the integration and differentiation stage (from Kruger, 2005).

Prevec *et al*. (2005) proposed that caution must be taken when interpreting isotopic compositions of whole-rock samples or mineral separates in cumulus rocks, following the discovery of isotopic disequilibrium between coexisting plagioclase and orthopyroxene in the Merensky reef of the Western limb. Isotopic disequilibrium between plagioclase and orthopyroxene was revealed by Sm-Nd isotopic data, with ϵ_{Nd} values of -7.46 to -8.46 for orthopyroxene and ϵ_{Nd} values of -1.13 to -3.37 for plagioclase at 2.06 Ga. Isotopic disequilibrium between the two minerals was interpreted as being the result of mixing of two contrasting melts, with orthopyroxene derived from a melt affected by crustal contamination, which then settled into a crystal mush dominated by earlier formed plagioclase derived from an uncontaminated melt.

Sr isotope variations are reported by Seabrook *et al*. (2005) in plagioclase, along with variations in Cr/MgO values in orthopyroxene of the CZ and MZ in the Eastern limb. Plagioclase and orthopyroxene of the basal pyroxenite of the Merensky unit display isotopic signatures typical of the CZ, with Sr_i ranging between 0.7060 to 0.7068. However, in the overlying part of the Merensky unit, plagioclase displays a MZ signature, with Sr_i values greater than 0.7075. Likewise, the Bastard unit pyroxenite

exhibits Sr_i values greater than 0.7075, whereas the overlying pyroxenite decreases to a value 0f 0.7068. This indicates that the coexisting minerals crystallized from two contrasting but coexisting magmas. Seabrook *et al*. (2005) hypothesized upward displacement of the CZ magma due to MZ magma influxes at the base of the Merensky unit, with mixing not occurring between the two magmas. Orthopyroxene crystallized from the displaced CZ magma and then sank through the MZ magma due to density contrasts, accumulation occurred in the crystal pile to form the Merensky pyroxenite. Plagioclase was crystallized from the MZ magma as an interstitial mineral in the CZ orthopyroxene crystal pile, with both retaining Sr isotope ratios typical of their respective parental magmas. Furthermore, the Merensky unit and Bastard unit were classified as transitional zones at the boundary between the CZ and MZ due to mixing of minerals from both the MZ and CZ magmas.

Roelofse and Ashwal (2012) found Sr isotope mineral disequilibrium between coexisting orthopyroxene and plagioclase in the LMZ rocks of the Northern limb. Very limited differentiation in the LMZ was detected over a vertical interval of 1.3 km, as indicated by An% in plagioclase, Mg# in pyroxene and modified differentiation index. This was interpreted to be the result of repeated magma intrusions during the early stages of development of the Northern limb magma chamber. The authors interpreted that the intrusions were composed of crystal-charged mushes from a deep-seated staging chamber, rather than multiple influxes of aphyric liquids. Lack of layering in the LMZ is inferred to have resulted from the intrusion of the crystal-charged mushes. Moreover, the crystal-charged mushes suitably explain the non-cotectic relationship between plagioclase and pyroxene which are in Sr isotopic disequilibrium.

Chutas *et al*. (2012) cautioned regarding the use of whole-rock isotopic data for inference of primary magmatic processes, after discovering isotopic disequilibrium (Sr and Pb) between coexisting orthopyroxene and plagioclase in the LZ and CZ of the Eastern limb. They argued that isotopic signatures can be altered by post cumulus processes, specifically by contaminants such assimilated lithologies within the crystal mush, given the lengthy cooling and crystallization time of the BC. Moreover, they suggest that geochemical signatures can be different in coexisting minerals due to active recrystallization driven by radioactive decay, compaction, mineral inversion and infiltration of reactive fluids.

Sr isotopic disequilibrium data for plagioclase crystals in the CZ (Merensky interval) from the Union Section of the Western limb are reported by Yang *et al*. (2013). The authors discovered Sr isotope disequilibrium between rims and cores in plagioclase as well as between cores in different plagioclase crystals. A co-accumulation model was proposed, where crystallization of cumulus plagioclase from a intruding melt is followed by late-stage overgrowth of crystals from a residual liquid from a dissimilar level of the compacting cumulate pile. This is attributed to slumping of partly consolidated crystal slurries during subsidence of the centre of the intrusion.

Inter and intra-crystalline isotopic disequilibrium in plagioclase of the MZ and UZ of the Northern limb was discovered by Roelofse *et al*. (2015). Sr isotope heterogeneity was revealed within a population of coexisting plagioclase crystals present in the same rocks. The authors cautioned against the interpretation of isotopic data obtained by means of progressive leaching experiments and that such methods must be conducted with the utmost thoughtfulness. Micro-drilling or LA-ICPMS was suggested as the best technique by the authors for isotopic studies. Findings from this study supported the model proposed by Roelofse and Ashwal (2012), as discussed previously.

Using LA-MC-ICPMS, Mangwegape *et al*. (2015) obtained plagioclase Sr-isotope data across the complete stratigraphy of the UZ and MZ in the Northern limb. Fractionation is inferred to have been the prevailing petrogenetic process within the UZ and UMZ, as indicated by the persistent Sr isotopic composition of plagioclase along with extensive normal differentiation trends in plagioclase. Their findings also dismiss a CZ parentage for the troctolite horizon of the Northern Limb and its direct equivalence to the Pyroxenite Marker. According to Kennedy *et al*. (2018), the troctolite horizon is comprised of PGE-rich olivine-norite cumulates that are >200 m thick, found towards the top of the MZ within the Northern BC.

Lehloenya (2017) found Sr-isotopic variations in cumulate plagioclase across the boundary between the UZ and MZ in the Western limb. The LMZ contains higher initial Sr-isotope ratios when compared to UMZ and UZ, displaying an increase in the $^{87}Sr/^{86}Sr$ ratio up the stratigraphy. These results are in accord with Kruger (1994), indicating that both the UMZ and UZ were constructed from a single magma, which was homogeneous in terms of its Sr-isotopic composition. Moreover, the Pyroxenite

Marker is interpreted as a zone of continuous magma mixing as exemplified by the reversals in mineral compositions, variations in Sr-isotope ratios and the disappearance of inverted pigeonite.

Karykowski *et al*. (2018) provided Sr-isotope compositions along with corresponding plagioclase mineral chemistry covering >6 km of the BC stratigraphy. Samples were collected from various drill cores from the western and northern limb. High-resolution plagioclase elemental mapping along with in situ data reveal complex zonation and patterns in relation to mineral chemistry and Sr isotope composition. The authors suggest that interstitial plagioclase in the BC crystalized from multiple isotopically dissimilar melts that infiltrated through the previously existing cumulate framework, thus displacing the resident melt.

Maghdour-Mashhour *et al*. (2021) provide plagioclase chemistry (Sr-isotope, molar An% and LREE compositions) for the MG3F anorthosite layer which is overlain by the MG3 chromitite layer immediately above the UCZ-LCZ contact. They divided the MG3F layer into 2 halves that display variability in plagioclase chemistry. This is attributed to the injection of two sequential sill-like magmas into an occupant viscoplastic pyroxene crystal mush. They report that plagioclase in the lower half of the MG3F layer displays an upward increase in LREE concentration and an upward decrease in molar An%, with fairly consistent Sr-isotope compositions (0.7056-0.7057). The upper half of the MG3F layer displays an upward decrease in LREE concentration and upward increase in molar An%, with strong variation in inter and intra-crystalline Sr-isotope data (0.7053-0.7064).

Beukes *et al*. (2021) propose that the Flatreef intersected in drill-core UMT-393 on the farm Macalacaskop in the Northern limb correlates to the Merensky and Bastard units of the Western and Eastern limb. Plagioclase compositions (Sr_i and An%) of the Flatreef overlap with those of MZ and UCZ transition indicating similar origin. Furthermore, they also suggest that sulfides of the Flatreef were entrained then deposited during ascent of magma from deeper staging chambers.

2. Methodology

2.1. Sampling

BH7929 was drilled by Impala Platinum on the farm Elandsheuvel 282JQ (25°35'24.933''S 27°18'44.351''E), located near Rustenburg, North West province, South Africa. BH7929 is situated in the Western limb (Fig 4) of the BC and reached a depth of 1876.10 m. It covers a large part of the MZ down to the level of the LG4 chromitite layer of the LCZ. The interval of interest for this study is 100 m long, encompassing the depth interval between 1700 m and 1800 m of BH7929 (Fig 5). The LCZ interval (1755 m – 1800 m) is represented by 45 m of the core and it is entirely composed of mafic lithologies (>70% orthopyroxene), hosting 2 chromitite layers (MG1-2). The UCZ interval (1700 m – 1755 m) is 55 m long and is dominated by plagioclase-rich (>50% plagioclase) lithologies including 2 chromitite layers (MG3-4). The transition between the LCZ and UCZ occurs between the MG2 and MG3 chromitite layers, where plagioclase becomes a cumulus phase. The LCZ-UCZ boundary occurs at a depth of 1755.5 m within the drill core.

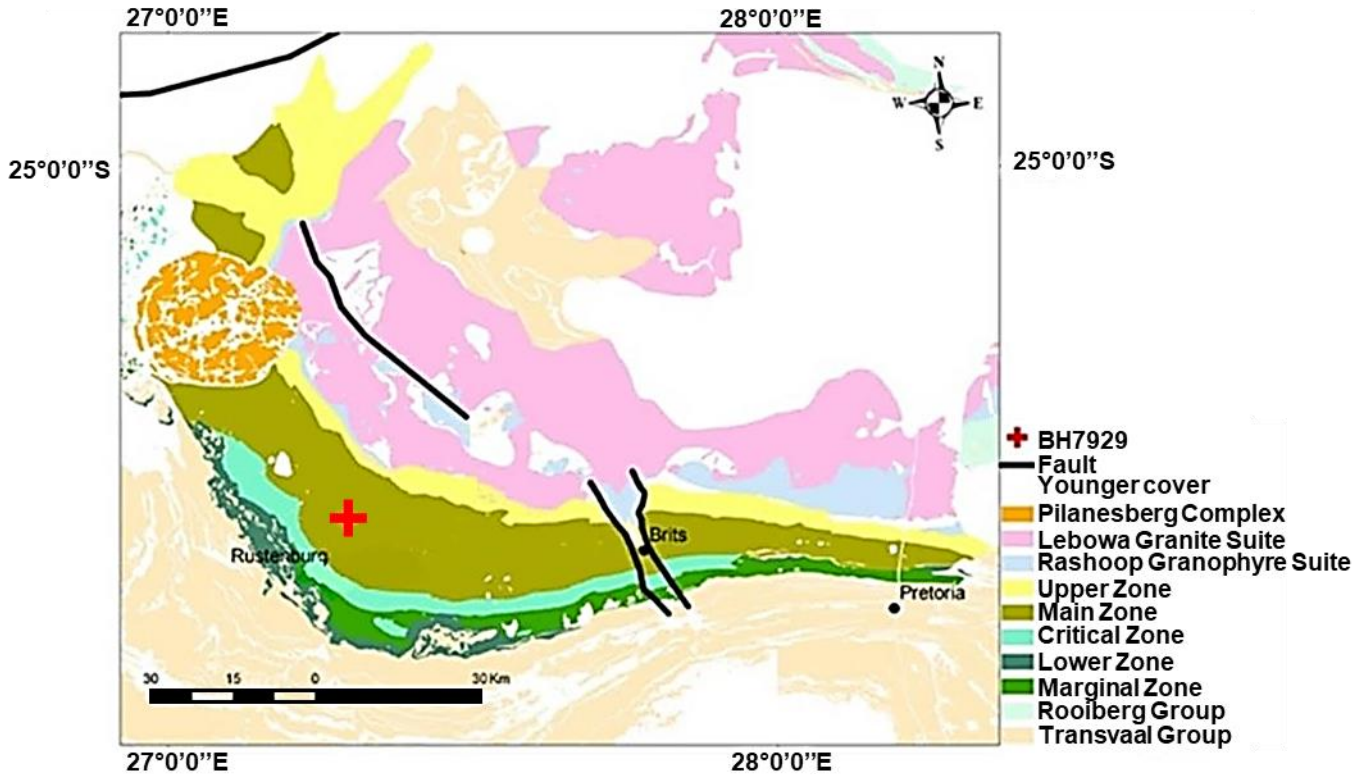

Figure 4: Location of the BH7929 drill hole in the Western limb (prepared in ArcGIS using geospatial data provided by the Council for Geoscience).

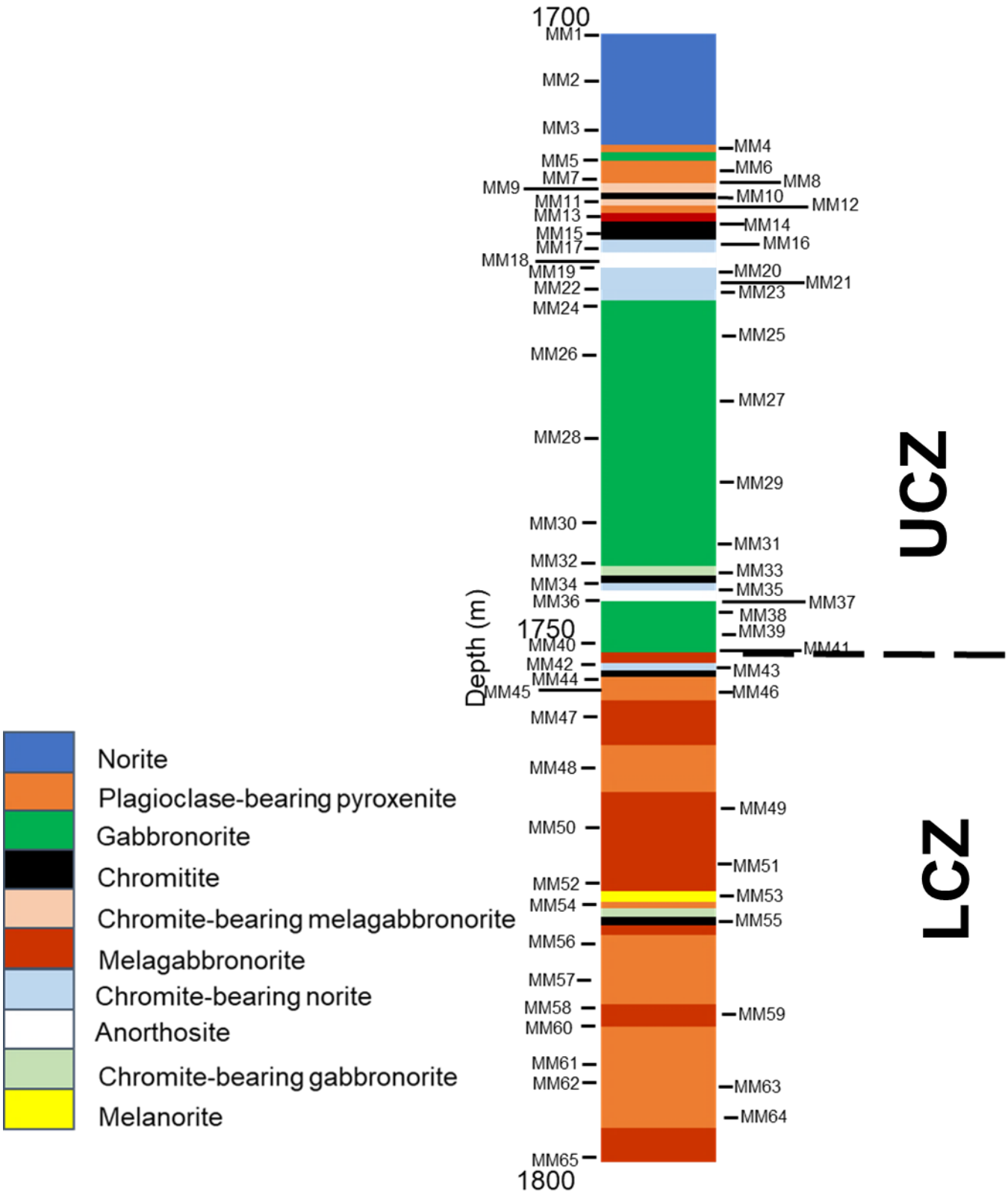

Figure 5: Graphic log of the study interval in the BH7929 drill core along with positions of sampling points (MM1 to MM65).

As part of this study, BH7929 was logged at the core storage facility of the University of the Free State. Upon completion of the logging, core sampling yielded a total of 65 samples (41 from the UCZ and 24 from the LCZ). Sampling was largely guided by the lithological variations within the core. Samples were taken on the basal and upper contacts of every lithology encountered, which were less than 10 cm long. However, the thickness of the lithology guided sampling spacing, which varied per lithology. The first sample was taken at a depth of 1701 m and the last sample was taken at 1797 m. The entire sample set was labelled MM1-MM65 (refer to Fig 5), from top to bottom.

2.2. Petrography

An Olympus BX51 transmitted light microscope was used to study polished thin sections (Fig 6) that were prepared of all 65 samples collected, with the aim of describing the relationships between constituent minerals. The microscope was furnished with an Olympus SC 30 camera and Analysis Imager software, which was used to take photomicrographs. Rocks were classified using the IUGS system according to Le Maitre *et al*. (1989).

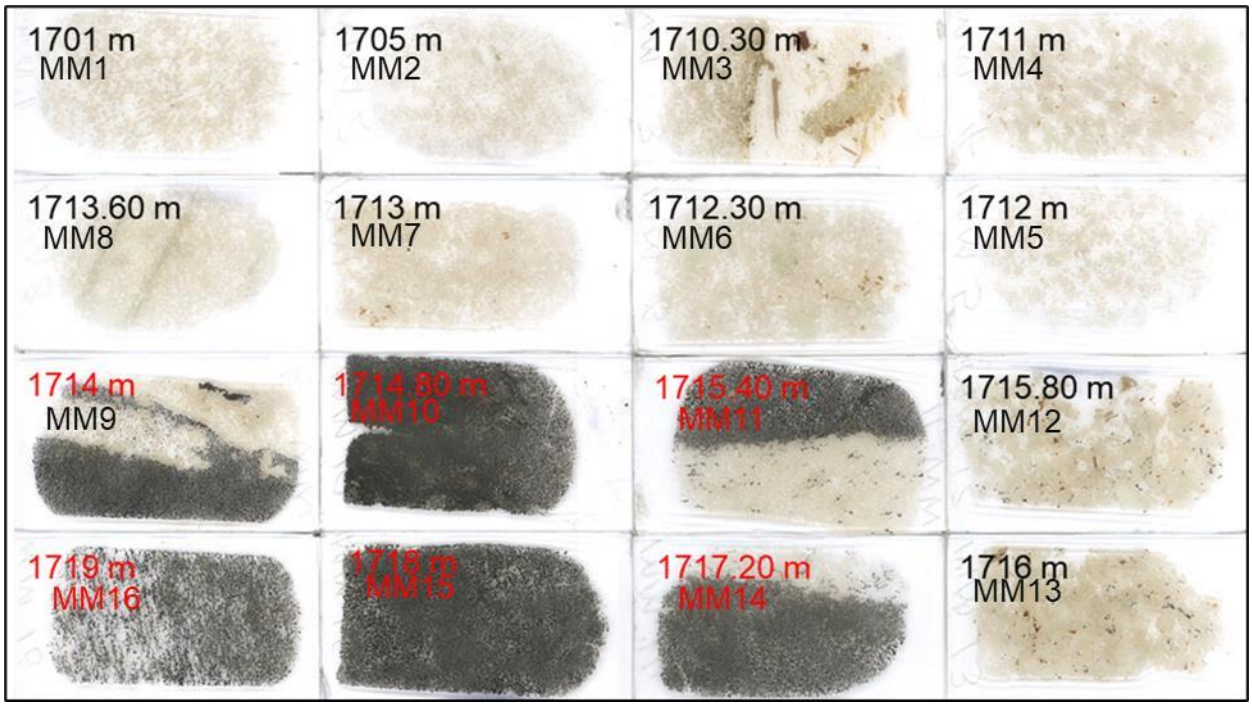

Figure 6: Thin sections prepared from BH7929 core samples (red labels were used for visual aid especially on chromitite samples).

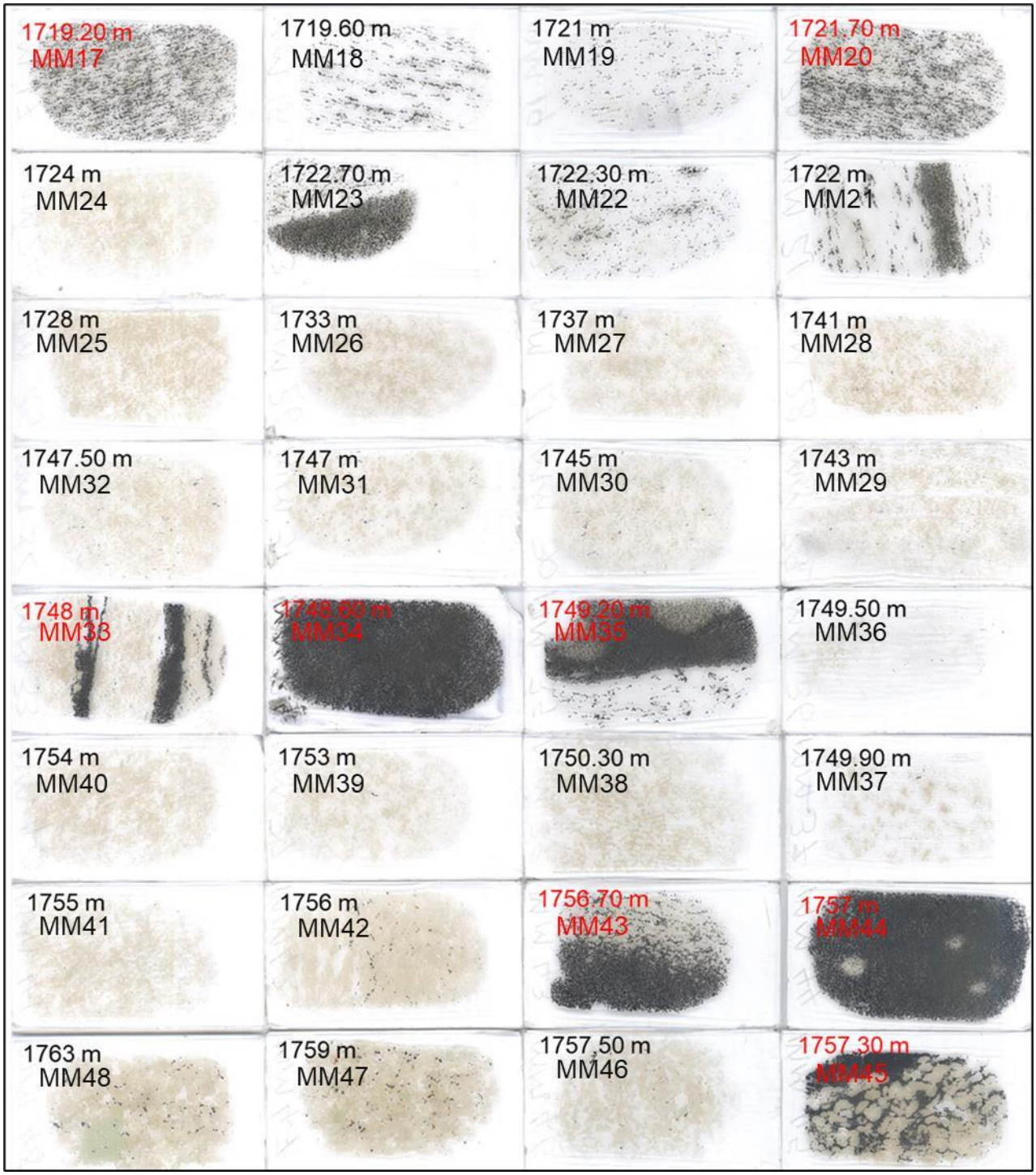

Figure 6: Continued

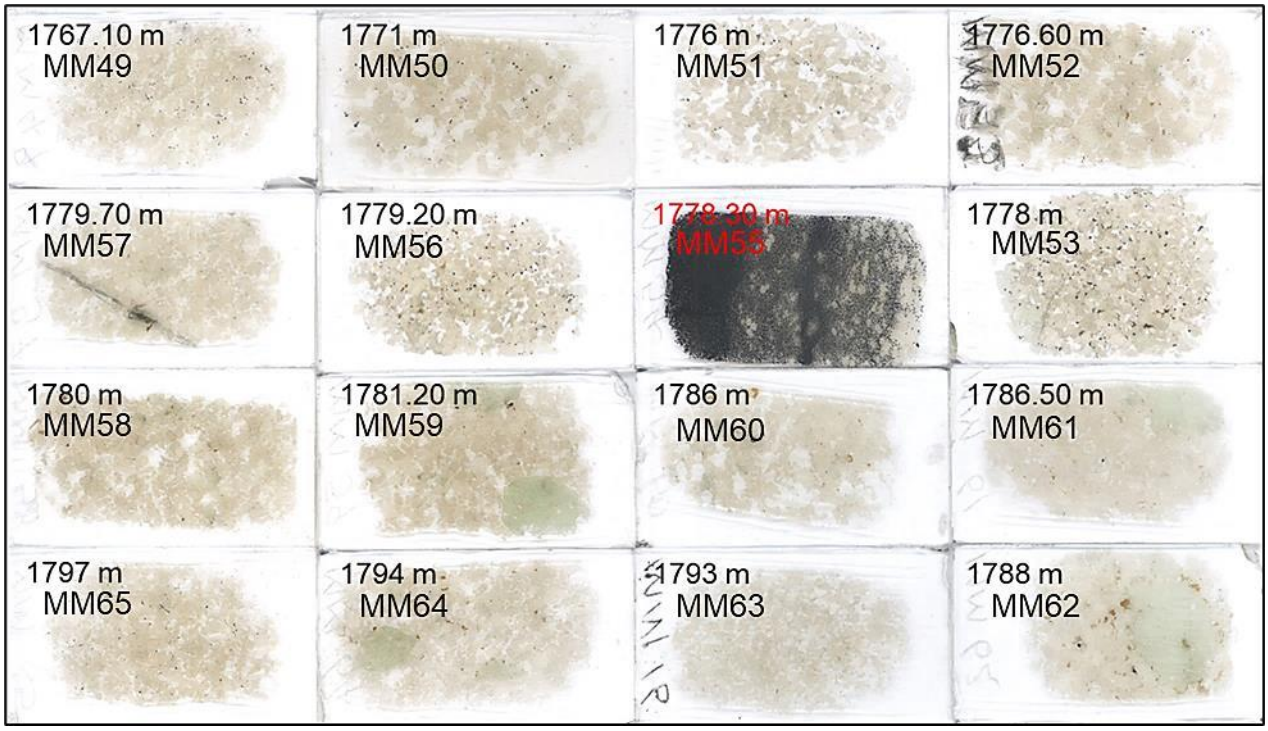

Figure 6: Continued

2.3. Whole-rock major and trace element geochemistry

Portions of the 65 samples collected were crushed and milled using a jaw crusher and swing mill, respectively.

For major element analysis, 10 g of sample powder was dried overnight at 110°C and then subjected to 1000°C for 4 hours, to gravimetrically determine the loss on ignition (LOI). 0.28 g of the sample powder was mixed with 1.5 g Alfa Aesor spectroflux (La_2O_3 (47%), $Li_2B_4O_7$ (37%), Li_2CO_3 (16%)) and 0.02 g $NaNO_3$. This mixture was then fluxed at 1000°C for roughly 5 minutes inside a Pt crucible. The melt was then moulded and pressed to produce fusion discs.

For trace element analysis and the determination of Na_2O, 8 g of the milled sample was mixed with 3 g of Hoechst wax ($C_6H_8O_3N_2$) (binder). This mixture was then homogenously blended using a Turbula shaker mixer for roughly 15-20 minutes. The mixture was then poured into an aluminium cup and pressed at 3000 lb/in^2 to produce pressed pellets. The prepared fusion discs and pressed pellets were then analyzed for major and trace elements by X-ray Fluorescence (XRF) spectrometry using a Rigaku Primus IV WD XRF Spectrometer equipped with a 4 kW Rh-tube, housed at the University of the Free State.

For chromite-rich samples, Cr was analysed by running traces on pressed pellets using reference materials suitably rich in Cr. The resulting Cr concentrations were used to calculate Cr_2O_3 and then added to the analytical totals of the major element determinations.

Measured values were compared to NIM-N (norite) and NIM-P (pyroxenite) certified reference materials (SARM, 2015) in Table 3 and 4.

Table 3: UFS measured values vs SARM certified standard reference values for major elements in wt.%.

	NIM-P		**NIM-N**	
Oxides	UFS	SARM	UFS	SARM
SiO_2	51.70	51.10	52.68	52.64
TiO_2	0.19	0.20	0.18	0.20
Al_2O_3	3.88	4.18	16.28	16.50
Fe_2O_3	12.68	12.70	9.07	8.97
MgO	24.92	25.33	7.41	7.50
MnO	0.23	0.22	0.19	0.18
CaO	2.64	2.66	11.70	11.50
Na_2O	0.13	0.37	0.34	2.46
K_2O	0.03	0.09	0.19	0.25
P_2O_5	0.02	0.02	0.02	0.03
NiO	0.07	0.07	0.02	0.02

Table 4: UFS measured values vs SARM certified standard reference values for trace elements in ppm.

	NIM-P		**NIM-N**	
Traces	UFS	SARM	UFS	SARM
Sc	40	29	40	38
V	300	230	180	220
Cr	22960	24000	30	30
Co	90	110	50	58
Ni	580	555	100	120
Cu	40	18	10	14
Zn	100	100	60	68
Rb	6	5	7	6
Sr	30	32	250	260
Y	10	5	10	7
Zr	10	30	10	23
Ba	60	46	70	100
Pb	bdl	6	bdl	bdl

2.4. Whole-rock REE geochemistry

A total of 49 samples were analysed at the Earth Lab of the University of the Witwatersrand by Inductively Coupled Plasma Mass Spectrometry (ICP-MS) on a Thermo Scientific iCAP RQ. Fifty mg of sample was weighed and digested in either a microwave digester (MARS from CEM) or using the open beaker/hotplate method depending on the sample type and digestibility. Easier to digest samples were digested using the open beaker/hotplate method. Samples that could not be digested using this method were digested using the microwave digester. The latter entailed adding 50 mg of sample to a Teflon vessel with 6 ml of ultra-high purity 2:1 HF:HNO_3. The mixture was then digested in the microwave for 40 minutes at 180˚C and 400 kPa. The sample was then transferred to a 15 ml Savillex beaker and the Teflon vessel was rinsed out thoroughly with deionised water. The Savillex beaker was capped and placed on a hotplate for 24 hours at 70˚C. The liquid portion of the sample was then evaporated off at 70˚C. 2 ml of HNO_3 was added to the sample and capped and placed on the hotplate for 24 hours. The acid was then heated at 70˚C and a further 2 ml of HNO_3 was added and allowed to evaporate. The samples were then removed from the hotplate and 300 µl HNO_3 was added. The samples were stored in this state until they were ready to be analysed.

The open beaker/hotplate method also began with 50 mg sample that was placed directly into a 15 ml Savillex beaker along with 3 ml of ultra-high purity 2:1 HF:HNO_3. The beaker was placed on a hotplate at 70˚C and allowed to evaporate. Once dry, 3 ml of HF:HNO_3 was added and the beaker was capped and placed on the hotplate at 70˚C for 72 hours. The sample was then dried down at 70˚C and 3 ml HNO_3 was added and evaporated. A further 3 ml HNO_3 was added and the beaker was capped and placed on the hotplate at 70˚C for 24 hours. The acid was then evaporated and 300 µl of HNO_3 was added again and allowed to evaporate. Samples were stored in this state until they were ready to be analysed.

The prepared samples were diluted to 50 ml (dilution factor 1:1000) with 5% HNO_3 containing 100 ppb Re and Rh as well as 50 ppb In and Bi. These elements were used as internal standards and were monitored throughout the analyses. Fluoride was minimised by allowing minimal contact between the sample and HF while still accomplishing total digestion. Samples were visually inspected for fluoride which

occur as a precipitate once diluted. Calibration standards were made at 5 different concentrations (10, 30, 50, 75 and 100 ppb) with analysed elements compared to certified reference materials.

All measurements were done in triplicate by the instrument and averaged. Replicate deviations greater than 2% were flagged. Certified reference materials (CRM, in Table 5), usually BCR-2, BHVO-2 (Raczek *et al*. 2001) and BIR-1 (Flanagan, 1984) were digested and analysed with the samples. A total of 2 duplicates of MM26 and MM56, labelled MM26C and MM56C were added to the analysed batch, respectively (Table 5). This was done to test if the lab can reproduce the same results within the same sample.

Table 5: REE reference material and duplicates in ppm.

	BCR-2 (R)	**BCR-2 (M)**	**BIR-1 (R)**	**BIR-1 (M)**	**BHVO-2 (R)**	**BHVO-2 (M)**	**MM26**	**MM26C**	**MM56**	**MM56C**
La	24.5	25.03	0.67	0.62	15.272	15.6	1.664	1.558	11.445	11.717
Ce	50.5	51.23	1.806	1.95	36.478	37	2.571	2.558	24.739	25.726
Pr	6.3	6.367	0.34	0.38	4.949	5	0.282	0.285	3.077	3.153
Nd	27	27.66	2.558	2.5	23.439	24	1.107	1.103	12.846	13.095
Sm	6.3	6.313	1.04	1.1	5.788	5.8	0.206	0.214	2.343	1.317
Eu	1.91	1.933	0.502	0.54	1.976	2	0.252	0.255	0.374	0.379
Gd	6.5	6.51	1.665	1.85	5.891	5.9	0.220	0.216	2.092	2.097
Tb	0.95	0.962	0.315	0.36	0.849	0.86	0.033	0.033	0.268	0.268
Dy	6	6.003	2.318	2.5	4.898	4.9	0.226	0.230	1.523	1.526
Ho	1.2	1.215	0.515	0.57	0.899	0.91	0.049	0.050	0.299	0.305
Er	3.3	3.348	1.485	1.7	2.267	2.3	0.154	0.154	0.830	0.839
Tm	0.46	0.47	0.219	0.26	0.293	0.3	0.026	0.025	0.115	0.117
Yb	3.2	3.327	1.589	1.65	1.946	2.02	0.179	0.182	0.770	0.785
Lu	0.47	0.471	0.224	0.26	0.26	0.26	0.028	0.028	0.118	0.117

2.5. Plagioclase mineral chemistry

Polished blocks (Fig 7) that are about 25 mm in diameter were prepared from the same material as the thin sections. A reflected light microscope was used to locate subhedral to euhedral plagioclase crystals (lath-like or tabular) that were visibly unaltered. A tungsten carbide scribe was used to circle positions of targeted plagioclase crystals on the blocks. The aim of this was to locate plagioclase crystals easily and quickly during analysis.

Figure 7: Polished blocks prepared from BH7929.

For the determination of in situ plagioclase major element compositions, carbon coated polished blocks were analysed using a CAMECA SX 100 Electron Probe MicroAnalyzer (EPMA) housed at the Spectrum analytical facility of the University of Johannesburg. The probe is equipped with 4 wavelength-dispersive spectrometers (WDS), fitted with gas flow detectors. Analytical conditions for quantitative analysis were as follows: accelerating voltage = 20 kV, beam current = 20 nA, spot beam size >1 μm. Table 6 presents the calibration standards used for quantifying the results, along with the crystals used during analysis as well as various counting times for each element.

About 2 to 4 subhedral to euhedral plagioclase crystals were selected for samples in which plagioclase was the cumulus phase, whereas subhedral to anhedral plagioclase were selected in samples in which plagioclase was an intercumulus phase. About 5 to 10 spots were analysed per crystal depending on the sizes of the crystals. Fractured and altered plagioclase crystals were avoided. Back-scattered electron (BSE) images were collected to visually record the location of spots analysed (Fig 8).

Table 6: Calibration standards for electron microprobe analysis and elemental counting times.

Element	Calibration standard	Concentration (wt.%)	Crystal	Counting time (s)
Si	DiopsidePH1	25.88	TAP	21
Ti	Rutile_PH1	59.95	PET	13
Al	AlmandinePH1	11.12	TAP	27
Cr	CrO_PH1	68.42	PET	18
Fe	HematitePH1	69.94	LIFF	14
Mn	RhodonitePH1	32.93	LIFF	16
Mg	OlivinePH1	31.76	TAP	16
Ca	Wollastonite_PH1	34.17	PET	16
Na	JadeitePH1	11.28	TAP	32
K	Orthoclase_PH1	12.20	PAT	19

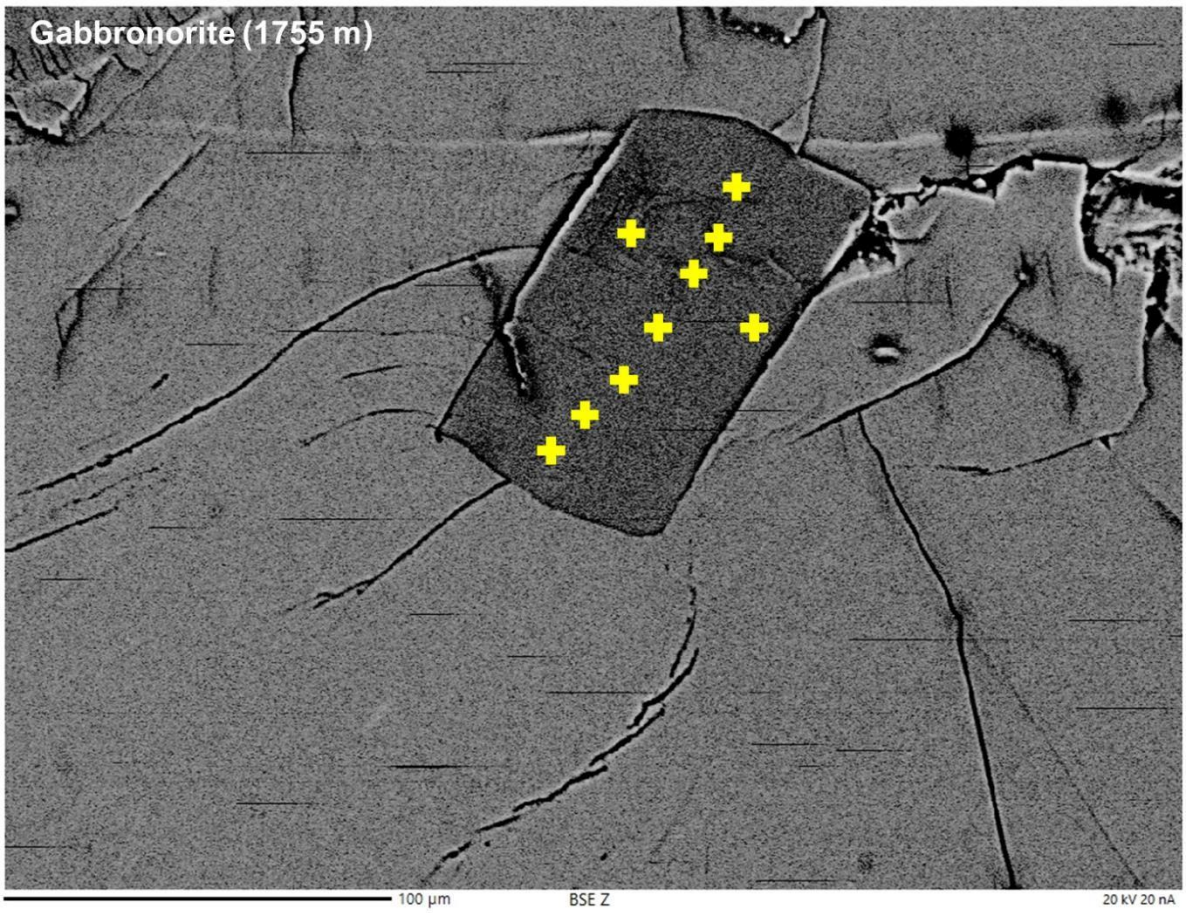

Figure 8: Back-scattered electron image indicating selected spots (yellow crosses) for EPMA (MM41).

2.6. Strontium isotopic determinations

For in-situ strontium isotope ratio determinations, the same plagioclase crystals selected for EPMA were analysed by Laser Ablation Multi-Collector Inductively Coupled Plasma Mass Spectrometry (LA-MC-ICP-MS) at the Spectrum facility of the University of Johannesburg.

A minimum of 2 to 3 plagioclase crystals was analysed per sample, with a maximum of 3 analysis spots selected depending on the size of the crystal (Fig 9). Ablation was performed on cores and rims to determine inter- and intracrystalline Sr-isotopic variability in plagioclase. Analysis was performed using a 193 nm ArFRESOlution SE Excimer laser connected to a Nu Plasma II MC-ICP-MS fitted with 16 Faraday detectors and 5 ion detectors. Samples were held within a Laurin Technic dual volume cell and helium gas was used to ablate the samples at 0.31 L/min gas flow. General conditions are listed in Table 7.

Table 7: General conditions for LA-MC-ICP-MS analysis.

Condition	Value
Plasma RF power	1300 W
Coolant gas flow	13 L/min
Auxiliary gas flow	0.88 L/min
Nebuliser gas flow	0.85 L/Min

Prior to ablation, blanks were measured for 20 s on peak positions, and subtracted from ablation signal to obtain blank-corrected intensities. An integration of 2 s was utilized. Depending on the available surface area of selected crystals, spot size diameter was set to between 60 and 100 µm, with ablation time set at 70 s for spot measurements. A repetition rate of 10 Hz was set for all the measurements, with the laser beam having a nominal energy of 6 mJ at 50% attenuation, supplying a laser density of 3.6 J/cm^2.

For mass bias correction, an $^{86}Sr/^{88}Sr$ ratio of 0.1194 (Steiger and Jäger, 1977) was used to calculate and correct Sr mass. The Sr correction factor was regularly adjusted through analysis of 2 standards (*viz.*an in-house plagioclase glass reference, as well as the BHVO-2G reference glass (Elburg *et al*, 2005)) after every 3 to 5 samples to correct Rb mass. The ^{87}Rb was calculated from ^{85}Rb after mass bias correction and subtracted from the total signal at mass 87 to obtain ^{87}Sr.

Krypton interference correction was conducted by subtracting ^{84}Kr from ^{84}Sr during blank correction. Background signal was collected on mass prior to ablation and subtracted from the signal for background correction.

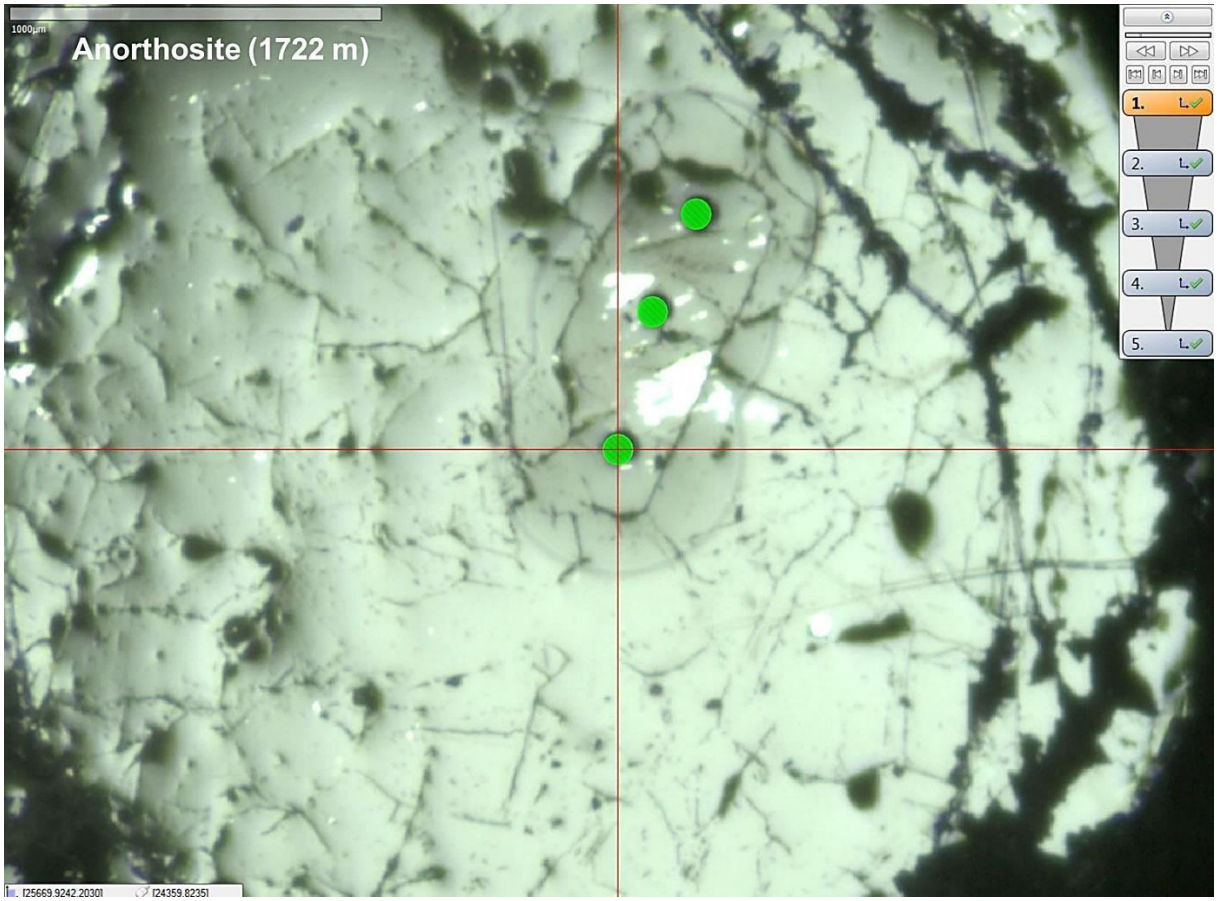

Figure 9: Reflected light image of ablated spots indicted by green dots (MM21).

2.7. Chromite mineral chemistry

A total of 14 chromite-rich polished blocks were selected for analysis by Scanning Electron Microscopy (SEM) at the Department of Geology of the University of the Free State. The polished blocks were carbon coated using a Quoram/Q150T Carbon Coater and then analysed using a JEOL JSM-6610 SEM, equipped with a Thermofisher Ultradry EDX detector. Two to three chromite crystals were selected per sample, with 7 to 14 analyses per crystal, depending on the size of the crystal. Analyses were performed at an acceleration voltage of 20 kV.

3. Results

3.1. Petrography

Modal mineralogical variations for the entire study interval are plotted against depth in Figure 10, along with the stratigraphic column.

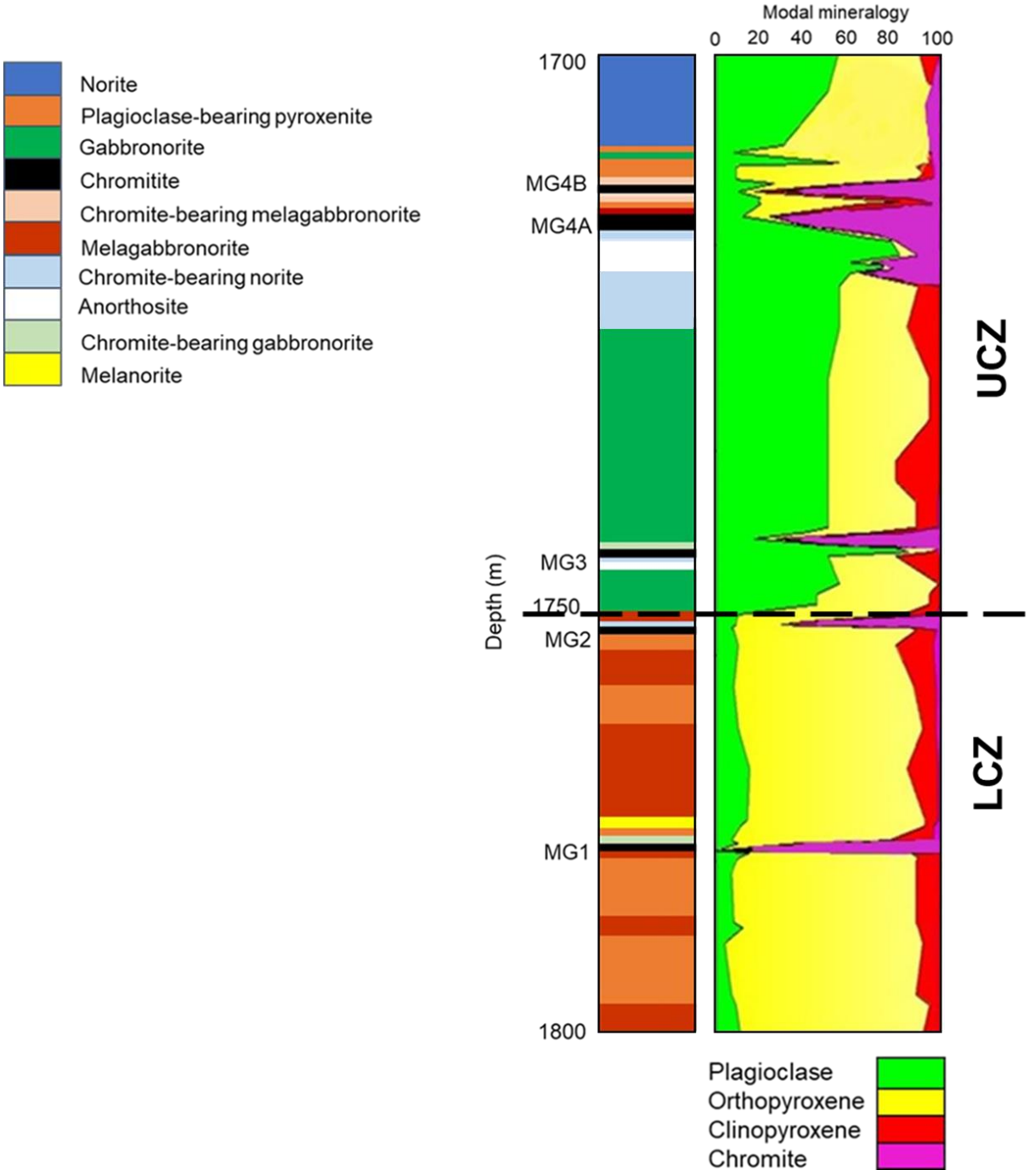

Figure 10: Modal mineralogy vs depth in the UCZ-LCZ interval, along with stratigraphic column.

3.1.1. Lower Critical Zone (LCZ)

Lithological diversity in the LCZ interval is minimal in comparison to the UCZ. Plagioclase-bearing pyroxenite and melagabbronorite are the major lithologies encountered, constituting 41.6% and 37.5%, respectively. Subordinate lithologies include chromitite (8.3%), melanorite (4.1%), chromite-bearing gabbronorite (4.1%) and chromite-bearing norite (4.1%). Chromitite is restricted to 2 main stringers, with close association to the chromite-bearing lithologies. Poikilitic texture is pervasive in the LCZ study interval,

Orthopyroxene and clinopyroxene are the main chadacrysts in plagioclase-bearing pyroxenite and melagabbronorite, which are predominantly enclosed by plagioclase. However, clinopyroxene can be found enclosing orthopyroxene and the reverse is also present throughout the LCZ interval.

Orthopyroxene is the prevalent mineral phase in the LCZ study interval, modally constituting between 6% and 86%. It is typically found as subhedral to euhedral chadacrysts that are enclosed by plagioclase (Fig 11A) and often it is also found enclosing clinopyroxene and other orthopyroxene crystals (Fig 11B). Characteristically, orthopyroxene displays 90˚ cleavage traces and elongation is observed in some crystals. Elongated crystals are arranged in a preferential orientation, suggesting igneous lamination. Exsolution lamellae (Fig 11C) of clinopyroxene in orthopyroxene are commonly present which can be bent (Fig 11D), signifying post emplacement deformation.

Clinopyroxene is subordinate to orthopyroxene throughout the LCZ study interval, constituting between 0% and 20%. It occurs as either subhedral or euhedral chadacrysts enclosed by plagioclase (Fig 11E) or as oikocrysts enclosing orthopyroxene and other clinopyroxene crystals (Fig 11F). Elongated crystals are also found which are oriented parallel to one another, signifying igneous lamination (Fig 11G). Orthopyroxene exsolution lamellae (Fig 11H) can also be found in clinopyroxene throughout the study interval and bending is common, indicating post emplacement deformation.

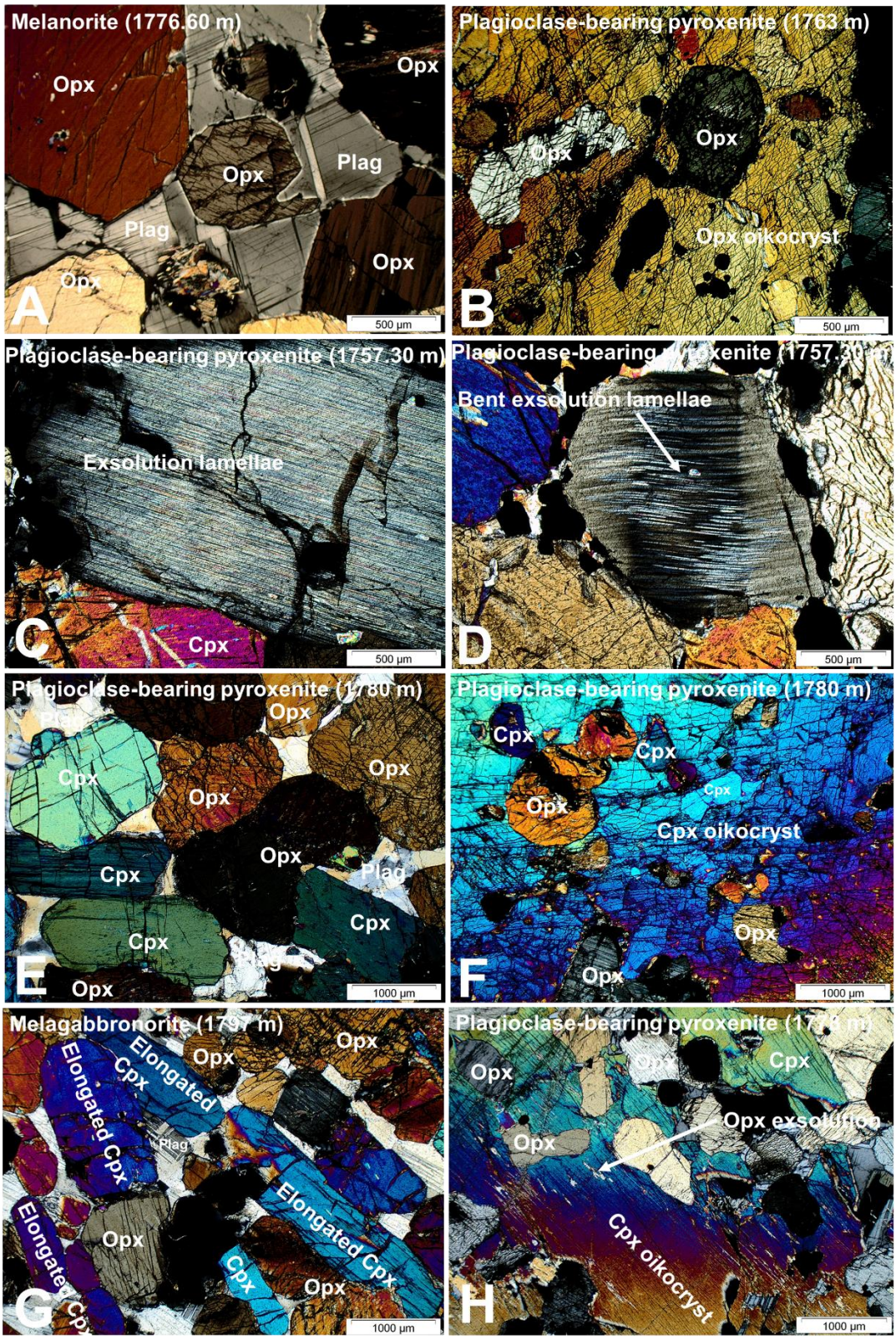

Figure 11: XPL photomicrographs of (A) orthopyroxene enclosed by plagioclase oikocrysts. (B) Orthopyroxene enclosed by orthopyroxene oikocrysts. (C) Exsolution lamellae in orthopyroxene. (D) Bent exsolution lamellae in orthopyroxene. E) Clinopyroxene and orthopyroxene enclosed by plagioclase oikocrysts. (F) Clinopyroxene enclosing orthopyroxene and clinopyroxene chadacrysts. (G) Elongated clinopyroxene chadacrysts. (H) Orthopyroxene exsolution in clinopyroxene

Chromite modally constitutes between 0% and 78% of the sampled LCZ lithologies, which mostly occurs as subhedral to euhedral chadacrysts enclosed by either plagioclase or pyroxene (Fig 12A-B) throughout the study interval. It is predominantly restricted to the chromitite layers where it is concentrated, whereas it is typically disseminated in chromite-poor lithologies (Fig 12C). Close association is observed between chromite and phlogopite, which is characterised by high birefringence and strong pleochroism (beige to brown), with phlogopite occurring in the vicinity of chromite crystals (Fig 12D).

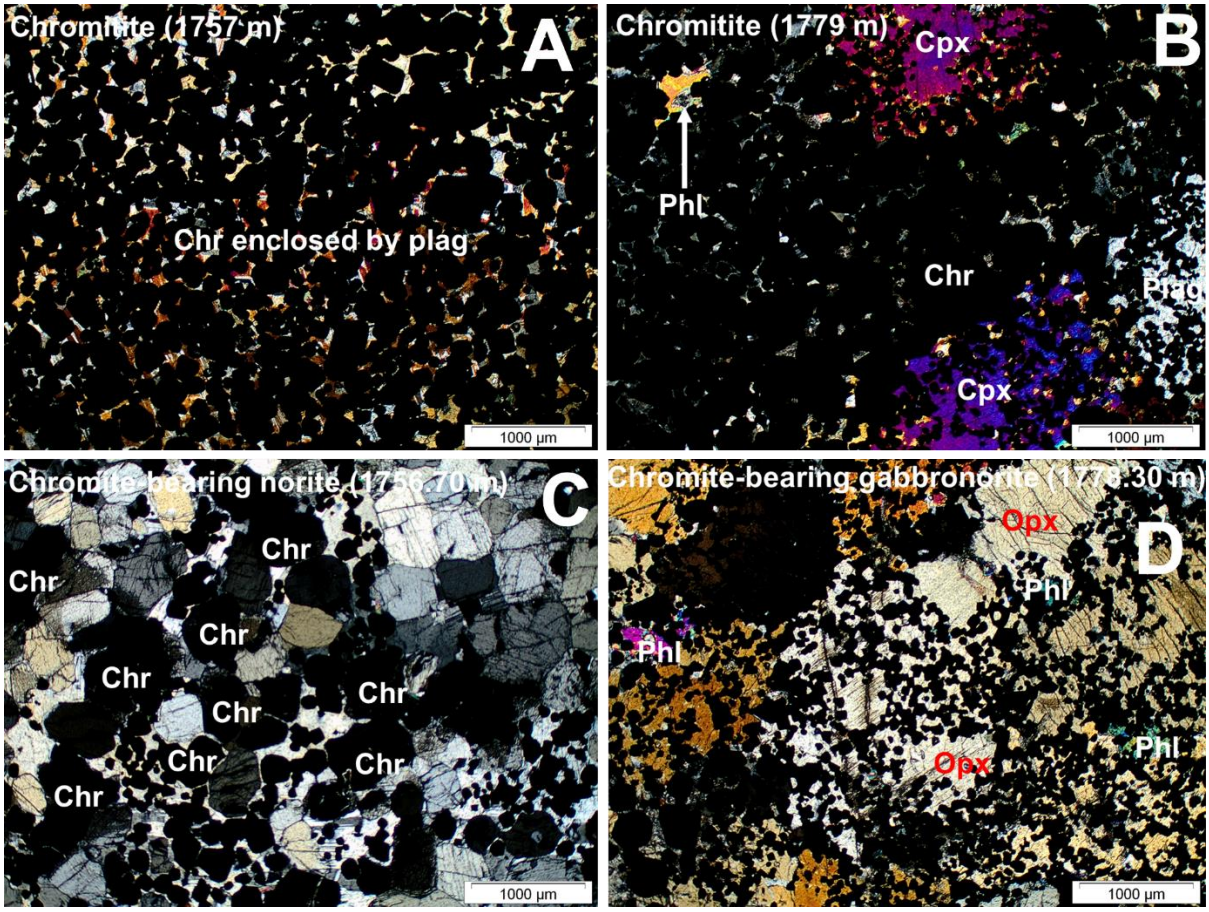

Figure 12: XPL photomicrographs of (A and B) concentrated chromite chadacrysts enclosed by plagioclase and pyroxene oikocrysts in chromitites. (C and D) Disseminated chromite chadacrysts in chromite-bearing gabbronorites.

Plagioclase is an intercumulus phase in the LCZ. It constitutes between 4% and 15% in the LCZ lithologies and it is principally found as anhedral to subhedral oikocrysts enclosing pyroxenes and chromite (Fig 13A-D). It is characterised by polysynthetic twinning and to a lesser extent simple twinning. The twinning can be wedge-shaped and bent (Fig 13A-B), indicative of post emplacement deformation.

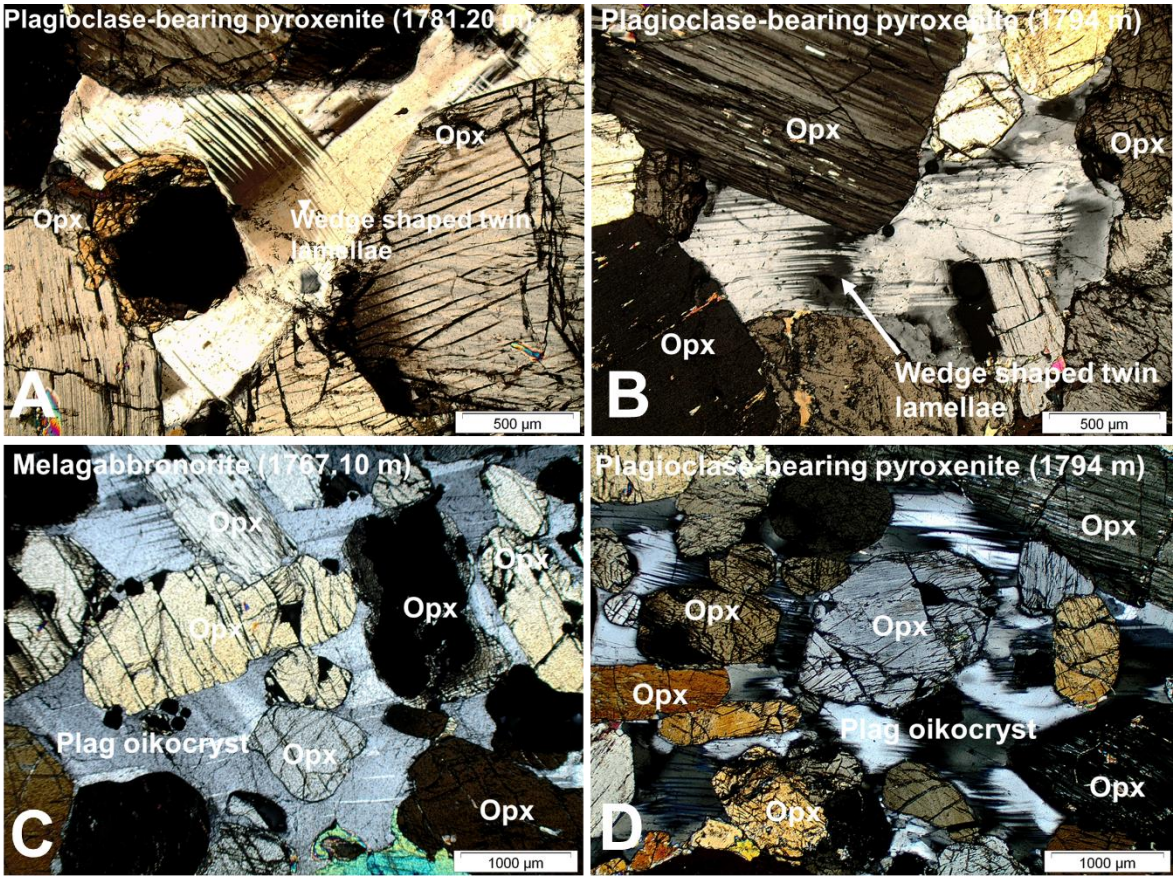

Figure 13: XPL photomicrographs of (A and B) wedge-shaped and bent twin lamellae in plagioclase (C and D) Plagioclase enclosing pyroxene.

Carbonate and sericite veins (Fig 14A-B) occur at various depths in the LCZ interval. Both vein-types are characterised by high birefringence, cutting across any mineral encountered. The veins are immediately surrounded by prominent blackish material (Fig 14A-B). Localised alteration of both ortho- and clinopyroxene are also found, with probably chlorite and serpentine alteration by-products (Fig 14CD).

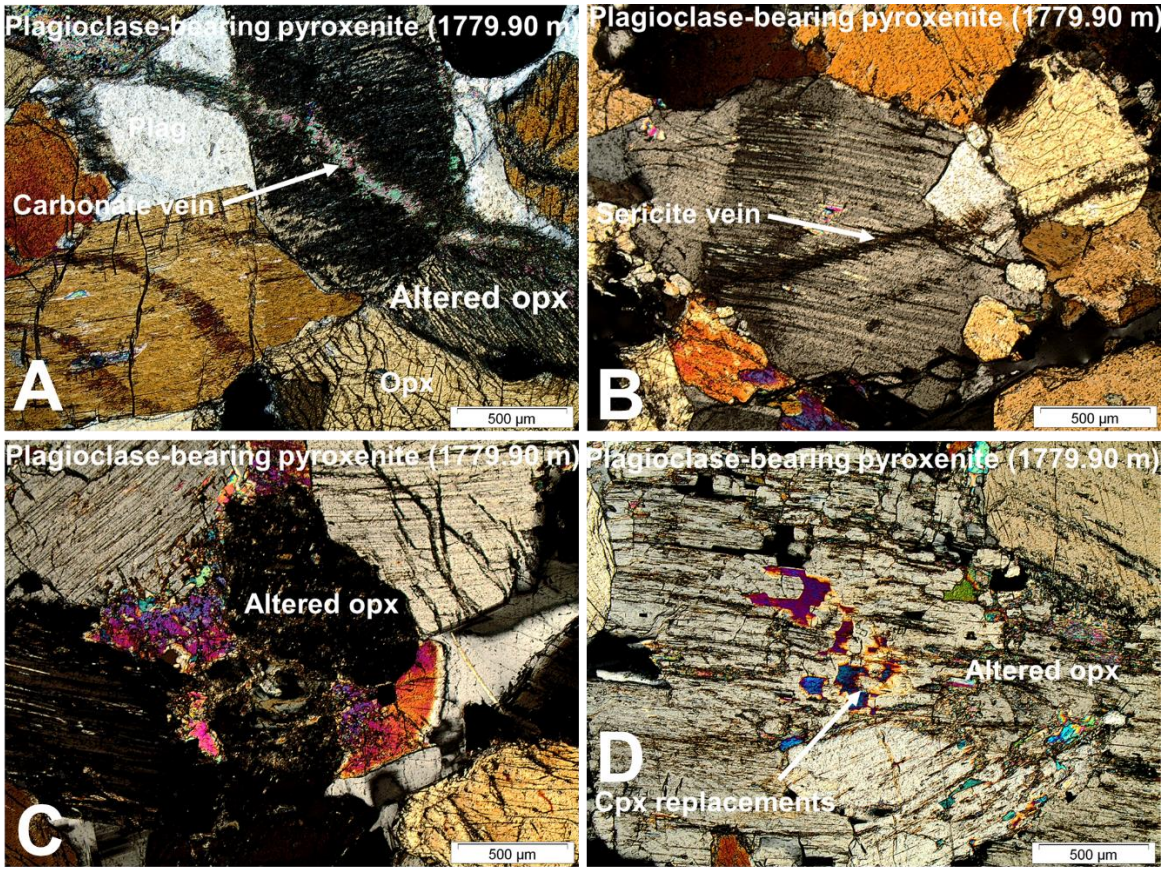

Figure 14: XPL photomicrographs of (A and B) carbonate and sericite veining. (C and D) Alterations in ortho and clinopyroxene.

3.1.2. Upper Critical Zone (UCZ)

The UCZ displays diverse lithologies in the BH7929 study interval, ranging from polymineralic lithologies (e.g. gabbronorite, norite, melagabbronorite, plagioclase-bearing pyroxenite and a quartzo-feldspathic patch) to nearly monomineralic lithologies (chromitite and anorthosite) as well as chromite (>15%) bearing lithologies (chromite-bearing melagabbronorite, chromite-bearing norite and chromite-bearing gabbronorite). Moreover, there is a lack of predictable layering in the studied interval as compared to the classical mafic bases (chromitites and pyroxenites) and felsic tops (anorthosites) (e.g. Cawthorn *et al*. 2006). Microscopic observations reveal that gabbronorite accounts for 35.1% of the studied samples, whereas anorthosite and chromite-bearing lithologies account for 18.1% each. Plagioclase-bearing pyroxenite and chromitite account for 13.2% and 10.8%, respectively, whereas norite accounts for 4.7%.

Two main textures are found in the UCZ study interval, namely intergranular and poikilitic texture. Intergranular texture is the most prevalent accounting for 71%, which is present in most of the studied samples. To a lesser extent, poikilitic texture is found as a subordinate texture, particularly in orthopyroxene-dominated lithologies. Plagioclase is the main cumulus phase in gabbronorite and anorthosite, enclosed by ortho- and clinopyroxene crystals. Poikilitic texture accounts for 21% of the rocks in the UCZ study interval. It is present in plagioclase-bearing pyroxenite, chromitite and the chromite-bearing lithologies. Chromite is the main chadacryst in chromitite and the chromite-bearing lithologies, enclosed by oikocrysts of plagioclase and pyroxenes. In plagioclase-bearing pyroxenite, orthopyroxene is the main chadacryst enclosed by plagioclase oikocrysts.

Plagioclase is a pervasive phase in the UCZ, modally constituting between 8% and 82% in the UCZ samples. It occurs between larger orthopyroxene crystals in gabbronorite and norite, and it is scarcely found as fine inclusions within pyroxene (Fig 15A). Moreover, clinopyroxene can also be found surrounding orthopyroxene crystals (Fig 15B). Plagioclase is cumulus in anorthosite, occurring as euhedral to subhedral crystals, with orthopyroxene occurring interstitially (Fig 15C). However, intercumulus status is observed in plagioclase-bearing pyroxenite, melagabbronorite and chromitites (chromite-bearing lithologies included), occurring as oikocrysts enclosing other minerals (Fig 15D). Plagioclase crystals are subhedral to anhedral laths which can be tabular and elongated, characteristically displaying polysynthetic twinning as well as simple twinning. Wedge-shaped and bent twin lamellae (Fig 15E and F) are observed at various depths which suggests post emplacement deformation as reported by Von Gruenewaldt (1971). Plagioclase laths are arranged parallel to the overall layering, with preferred orientation, specifically in chromite-bearing anorthosite and anorthosite (Fig 15G). This is interpreted as igneous lamination suggesting compaction during solidification. Moreover, visible zoning is rare in plagioclase crystals, with only a single occurrence observed in plagioclase-bearing pyroxenite at depth 1715.8 m (Fig 15H).

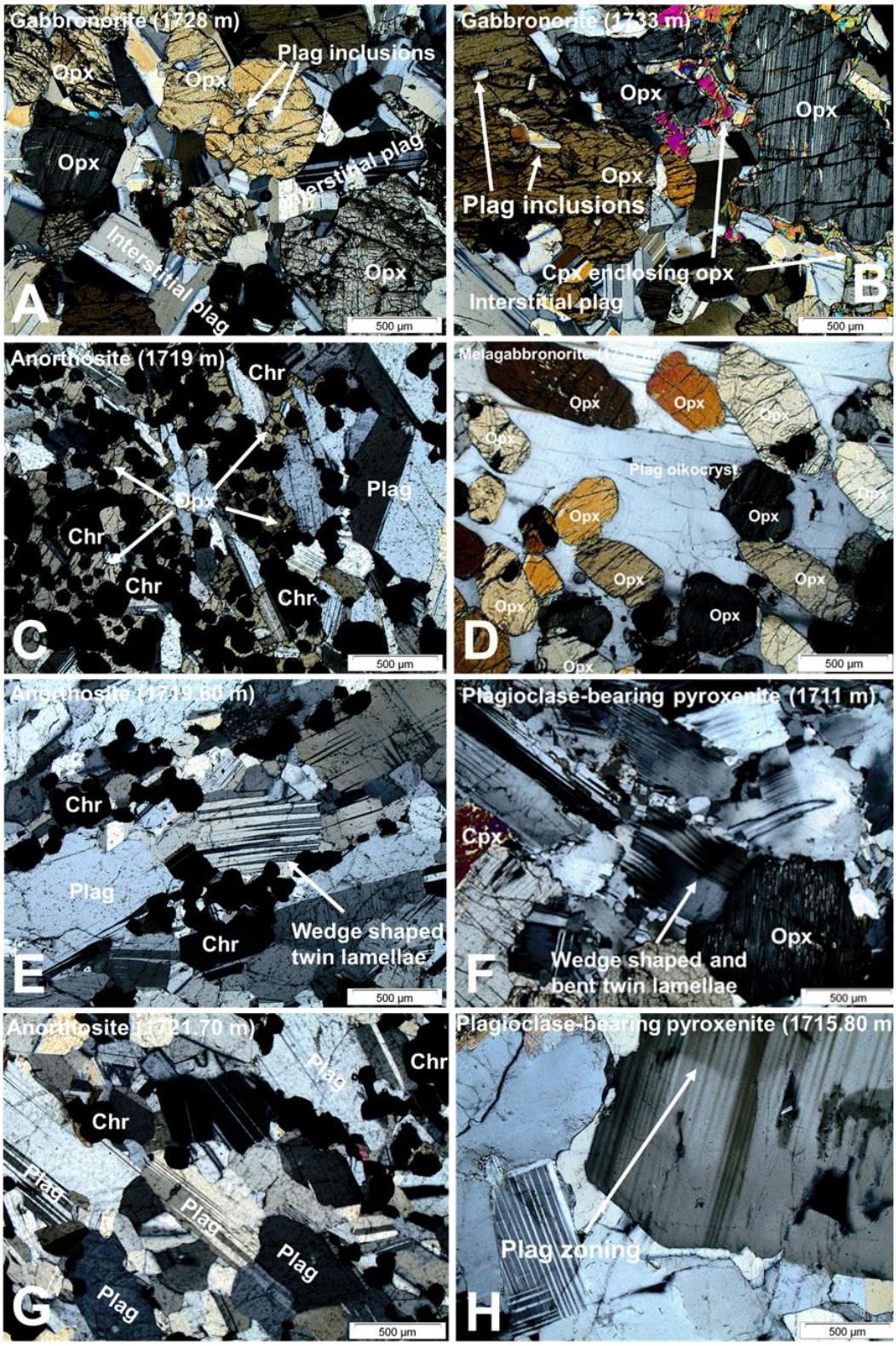

Figure 15: XPL photomicrographs of (A) interstitial plagioclase surrounding orthopyroxene crystals. (B) Plagioclase inclusions in orthopyroxene. Note clinopyroxene surrounding orthopyroxene on the right. (C) Interstitial orthopyroxene surrounding plagioclase. (D) Plagioclase oikocryst enclosing orthopyroxene. (E) Wedge-shaped twin lamellae in plagioclase. (F) Wedge-shaped and bent twin lamellae in plagioclase. (G) Preferential alignment of plagioclase crystals in chromite-bearing anorthosite. (H) Plagioclase crystal displaying zoning in pyroxenite.

Orthopyroxene is subordinate to plagioclase, modally constituting between 1% and 80% in the studied samples. It is a major constituent in plagioclase-bearing pyroxenite and melagabbronorite, occurring as subhedral to euhedral chadacrysts enclosed by plagioclase (Fig 16A). However, it can also be found as oikocrysts enclosing various chadacrysts including other orthopyroxenes (Fig 16B). In anorthosite, chromite-bearing norite and chromite-bearing gabbronorite, orthopyroxene crystals exist as highly fractured crystals that enclose larger plagioclase crystals which often contain smaller sized inclusions of plagioclase (Fig 16C). Clinopyroxene exsolution lamellae is abundant throughout the study interval, which appears as parallel and tightly spaced lamellae exsolving from orthopyroxene, characterised by high birefringence and bending of the lamellae as observed in some samples (Fig 16D).

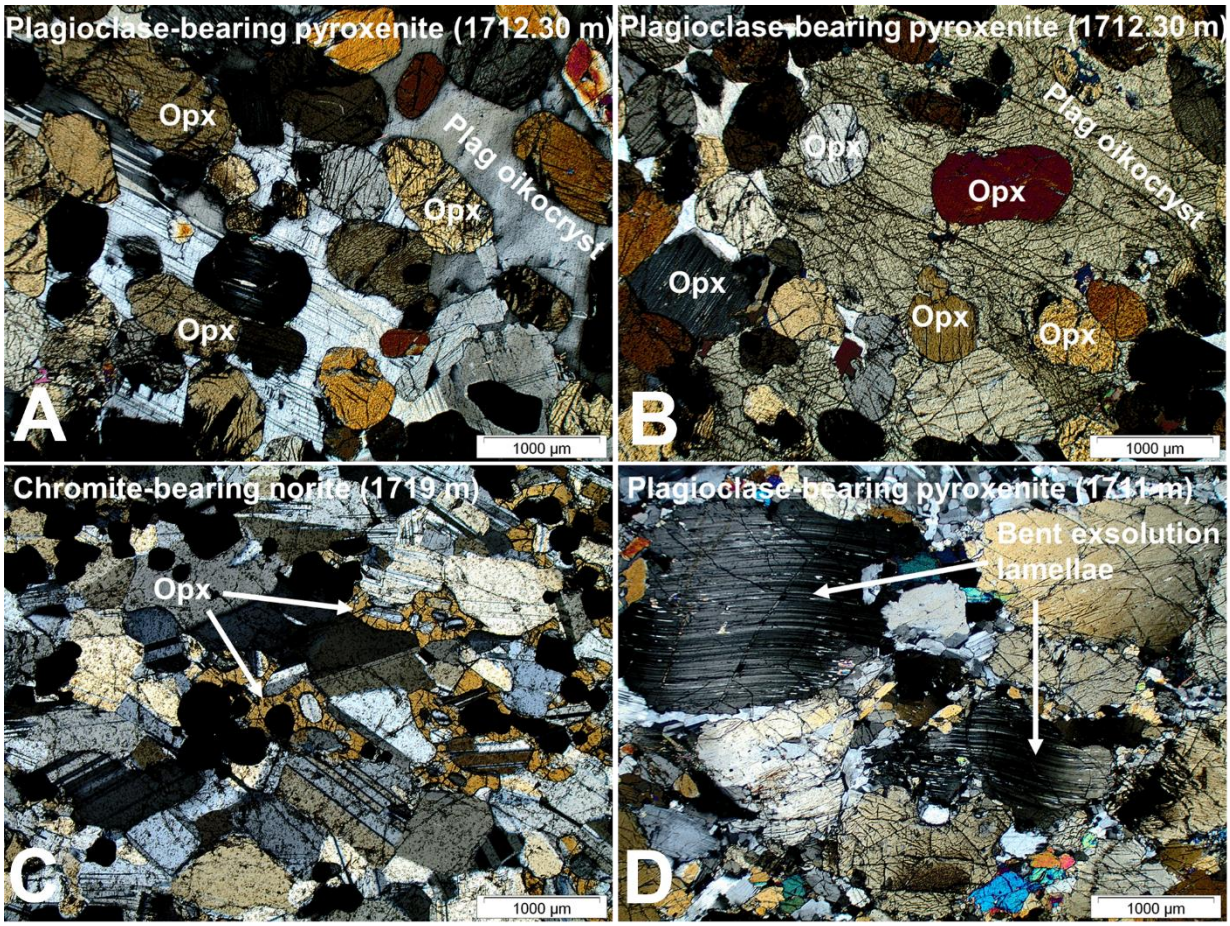

Figure 16: XPL photomicrographs of (A) orthopyroxene chadacrysts enclosed by plagioclase oikocryst. (B) Orthopyroxene oikocrysts enclosing clinopyroxene chadacrysts. (C) Orthopyroxene enclosing plagioclase laths. (D) Bent exsolution lamellae in orthopyroxene.

Clinopyroxene modally constitutes between 0% and 32% in the studied samples. It is abundantly found enclosing plagioclase and orthopyroxene in plagioclase-bearing pyroxenite and melagabbronorite (Fig 17A), to a lesser extent it can also be found as chadacrysts enclosed by plagioclase (Fig 17B). It is either absent or rare in anorthosite and chromitite (including the chromite-bearing lithologies). Exsolution lamellae of clinopyroxene is abundant in the study interval, wherein clinopyroxene is found exsolving from orthopyroxene.

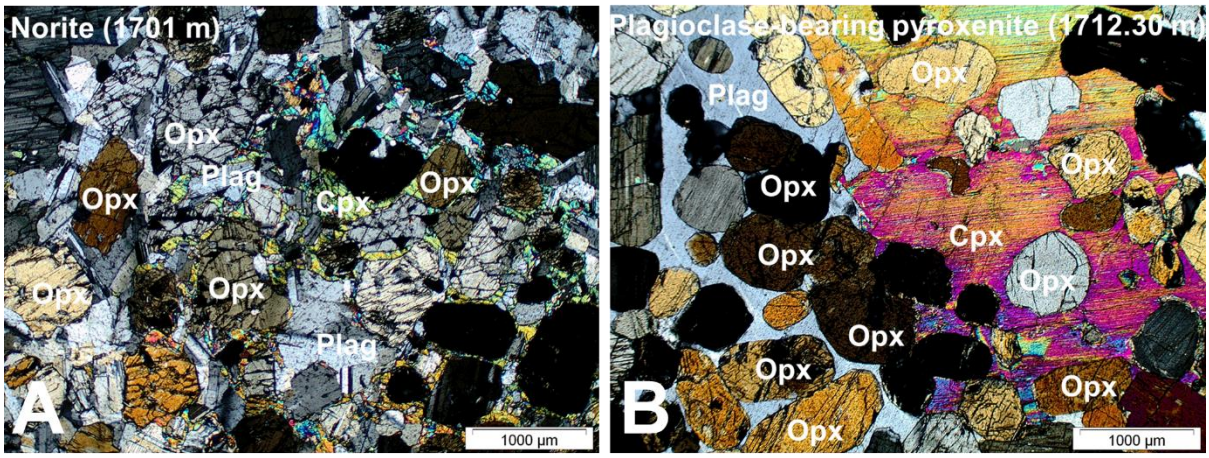

Figure 17: XPL photomicrographs of (A) clinopyroxene occupying the spaces between orthopyroxenes. (B) Clinopyroxene oikocryst enclosing orthopyroxene chadacryts.

Chromite constitutes between 0% and 80% in the studied samples. It is principally found as subhedral to euhedral crystals in chromitites and the chromite-bearing lithologies (Fig 18A). Chromite crystals are mainly restricted to stringers and crystal sizes tend to decrease away from the center of the stringer (Fig 18A). Its occurrence is disseminated in other lithologies, whereas it is concentrated in chromitite. Close association is observed between chromite and phlogopite, which is characterised by high birefringence and strong pleochroism (beige to brown), with phlogopite occurring in the vicinity of chromite crystals (Fig 18B).

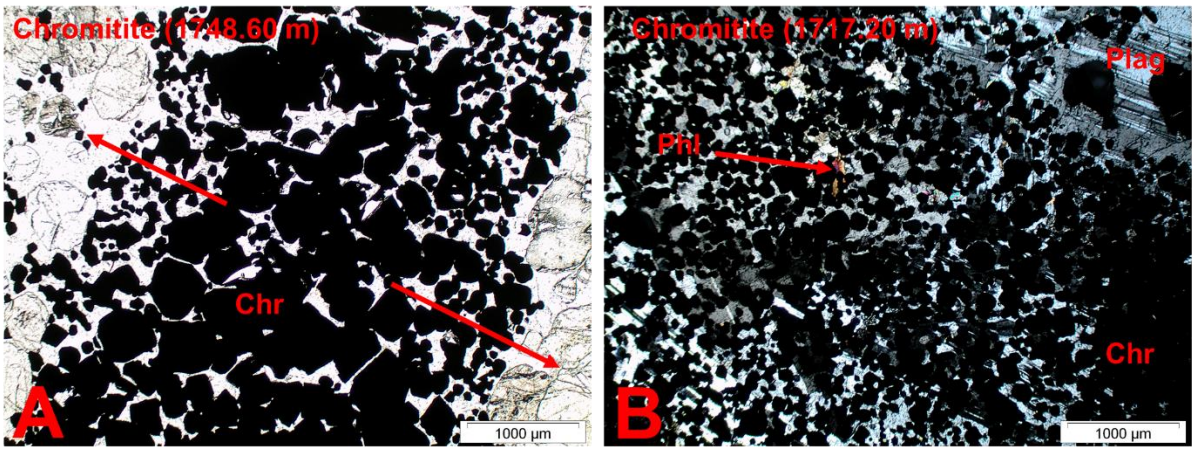

Figure 18: Photomicrographs of (A) chromitite stringer under PPL (note grain size reduction on the margins as indicated by arrows). (B) Phlogopite crystal in concentrated chromite crystals under XPL.

Alteration in the form of sericitization (Fig 19A) and epidotization (Fig 19B) is observed in the quartzo-feldspathic patch (at depth 1710.30 m). Plagioclase crystals are completely and partially replaced by both sericite and epidote. Sericite appears as fine material that has a brown to yellowish colour, whereas epidote has slightly larger crystals that displays high birefringence (2nd order colours) and green colour under plane polarised light.

Carbonate alteration is also present in the study interval which can be hard to differentiate from sericite (Fig 19C-D). Both occur as optically similar veinlets characterised by high birefringence. However, at the highest magnification, sericite has a fibrous texture whereas carbonate has a massive texture. Furthermore, an HCl test was taken to differentiate between the two. Both veins cut across and alter every mineral they encounter, leaving a trail of high birefringence fine material, which is immediately surrounded by blackish material. The veins are possibly attributed to post emplacement fluid infiltration.

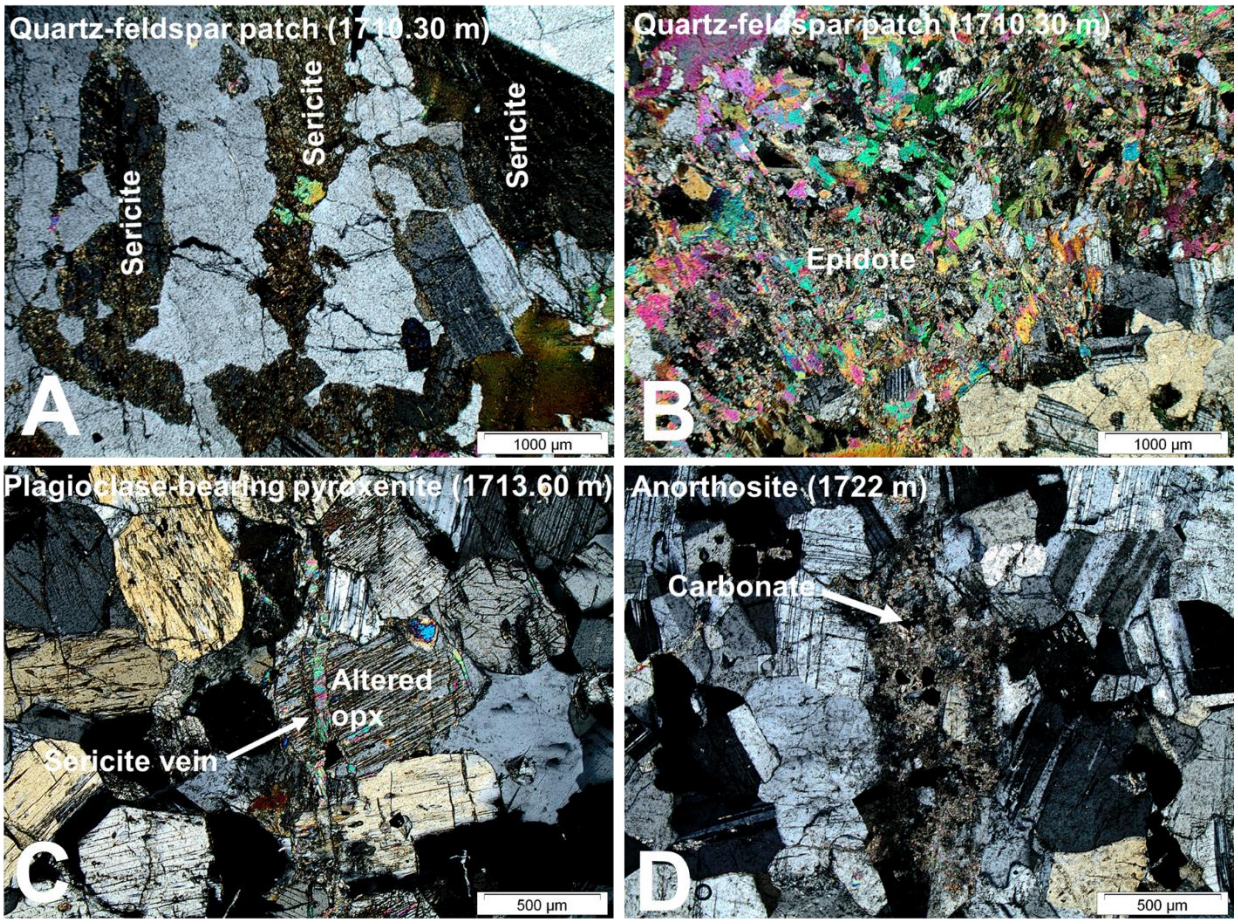

Figure 19: XPL photomicrographs of (A & B) sericitization and epidotization in the quartzo-feldspathic patch. (C) Sericite veining in pyroxenite. (D) Carbonate vein in chromite-bearing anorthosite

3.2. Whole-rock major element geochemistry

Binary variation diagrams for MgO vs oxides are presented in Figure 20 and whole-rock major elements vs depth is presented in Figure 21. Whole-rock major element measurements for all the analysed samples are presented in Appendix A. Whole-rock major element variations are largely attributed to variations in the dominant mineral phases, with the highest MgO value of 26.75 wt.% found in plagioclase-bearing pyroxenite (1788 m) and the lowest value of 0.76% wt.% found in anorthosite (1721 m). The Pearson correlation coefficient (r-value) matrix was used to comment on correlations between MgO and the other oxides (highlighted in red in Table 8). A strong correlation is equal to 1, whereas a weak correlation is less than 0.5. Negative correlations are just as useful as positive correlations.

Table 8: Correlation matrix for oxides in the study interval.

	SiO_2	TiO_2	Al_2O_3	Fe_2O_3	MnO	MgO	CaO	Na_2O	K_2O	P_2O_5	Cr_2O_3
SiO_2	1										
TiO_2	-0,876	1									
Al_2O_3	-0,327	-0,066	1								
Fe_2O_3	-0,722	0,9109	-0,361	1							
MnO	-0,224	0,5785	-0,833	0,792	1						
MgO	0,5044	-0,154	-0,961	0,1435	0,6857	1					
CaO	0,2959	-0,634	0,7938	-0,824	-0,978	-0,627	1				
Na_2O	0,3172	-0,595	0,6639	-0,732	-0,853	-0,515	0,88	1			
K_2O	0,2468	-0,052	-0,237	-0,055	0,1381	0,1469	-0,173	-0,102	1		
P_2O_5	0,1991	0,0231	-0,396	0,091	0,2901	0,3865	-0,272	-0,167	0,1891	1	
Cr_2O_3	-0,98	0,9186	0,1809	0,7896	0,3613	-0,382	-0,44	-0,459	-0,151	-0,152	1
	strong correlation = 1										

SiO_2 varies considerably throughout the study interval (Fig 20A), especially in the UCZ largely due to its lithological variability. SiO_2 averages 43.01 wt.% in the UCZ whereas it averages 45.96 wt.% in the LCZ. In Figure 20A two trends are recognised for SiO_2 that entail: 1) low values in chromite-rich lithologies and high values in chromite-free lithologies (also confirmed by Fig 21A); and 2) high values in MgO-poor lithologies and low values in MgO-rich lithologies. Melagabbronorite at depth 1797 m reveals the highest value of 54.82 wt.% whereas the lowest value is found at depth 1714 m, which is the MG4B chromitite layer having a value of 9.31 wt.%. Overall, SiO_2 displays moderate correlation with MgO (r = 0.5044).

Al_2O_3 (Fig 20B) displays a strong negative correlation with MgO (r = -0.961), varying between 2.96 wt.% at 1797 m (melagabbronorite) and 31.47 wt.% at depth 1721 m

(anorthosite). CaO (Fig 20C) varies between 0.93 wt.% at 1778.30 m (plagioclase-bearing pyroxenite) and 15.39 wt.% at 1749.90 m (anorthosite), displaying a moderate negative correlation with MgO (r = -0.627). Na_2O (Fig 20D) displays a moderate negative correlation with MgO, with measured values below 2 wt.%. K_2O (Fig 20E) has a weak positive correlation with MgO (r = 0.1489) and measured values never surpass 1 wt.%. Overall, K_2O averages 0.19 wt.% in the UCZ and 0.13 wt.% in the LCZ.

Fe_2O_3 (Fig 20F) displays a weak positive correlation with MgO (r = 0.1435), averaging 11.19 wt.%, varying between 1.44 wt.% at 1749.50 m (anorthosite) and 24.60 wt.% at 1748.60 m (chromitite). MnO (Fig 20G) displays a strong positive correlation with MgO (r = 0.6857), averaging 0.16 wt.%, varying between 0.021 wt. % at 1749.50 m (anorthosite) and 0.23 wt.% at 1714.80 m (chromitite).

Cr_2O_3 reveals two separate, albeit poorly constrained trends (Fig 20H): 1) a positive correlation with MgO in chromite-rich lithologies; and 2) a negative correlation with MgO in chromite-poor lithologies. In chromite-rich lithologies Cr_2O_3 averages 35.73 wt.% (chromitites), 21.95 wt.% in chromite-bearing melagabbronorite and 10.03 wt.% in chromite-bearing norite. In chromite-poor lithologies Cr_2O_3 averages 0.55 wt.% in norite, 0.73 wt.% in anorthosite and 0.99 wt.% in plagioclase-bearing pyroxenite, respectively.

Whole-rock TiO_2 (Fig 20I) is typically low in chromite-free lithologies averaging below 0.3 wt.%, whereas it increases in chromite-rich lithologies, averaging a value of 0.75 wt.% in the chromitite layers. Overall, it varies between 0.03 wt.% and 0.95 wt.%, displaying a weak negative correlation with MgO (r = -0.154).

P_2O_5 (Fig 20J) content averages 0.03 wt.% throughout the study interval, suggestive of incompatibility with major rock forming minerals in the study interval.

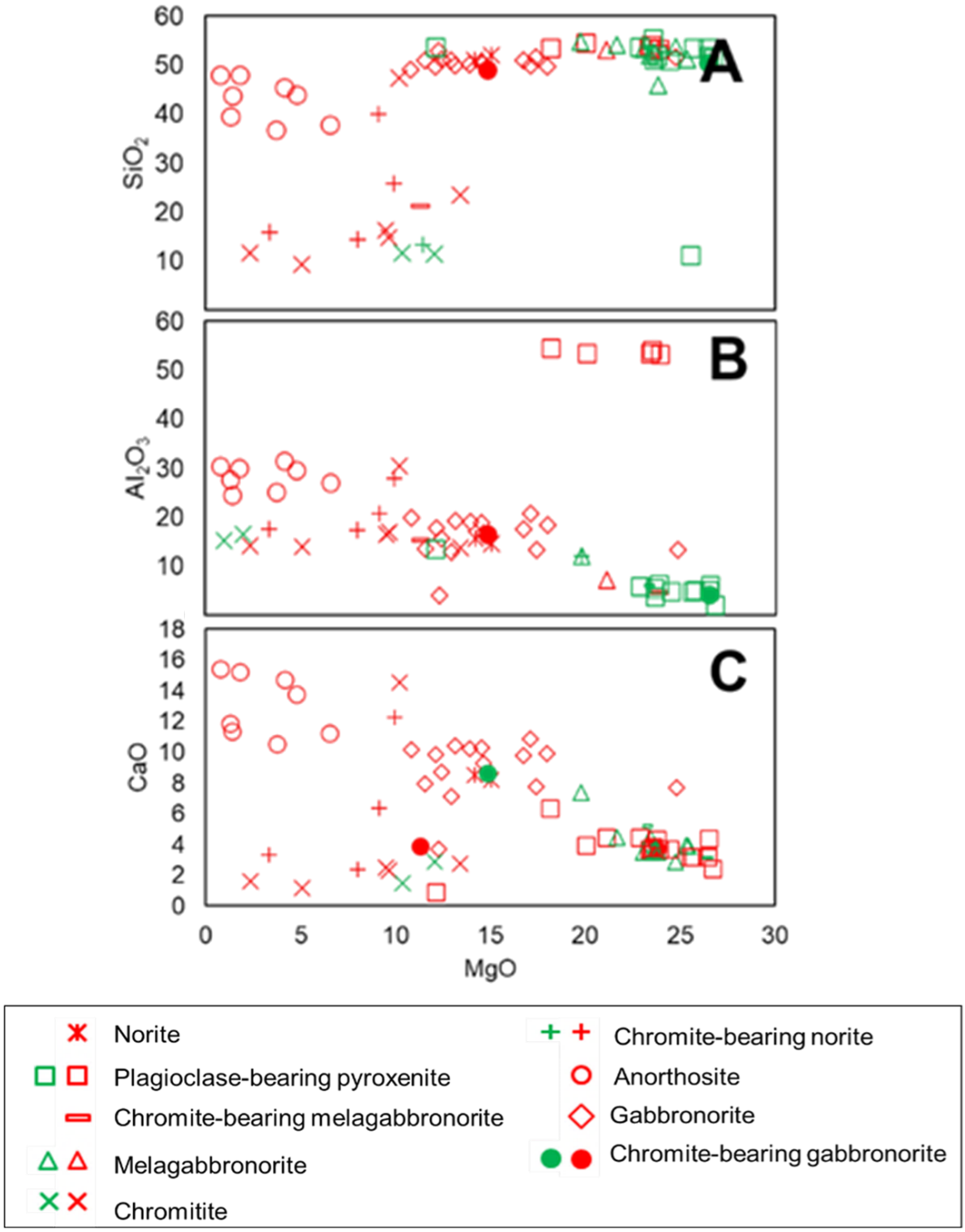

Figure 20: Binary variation diagrams for whole-rock major elements vs MgO in the study interval (Red = UCZ, Green = LCZ).

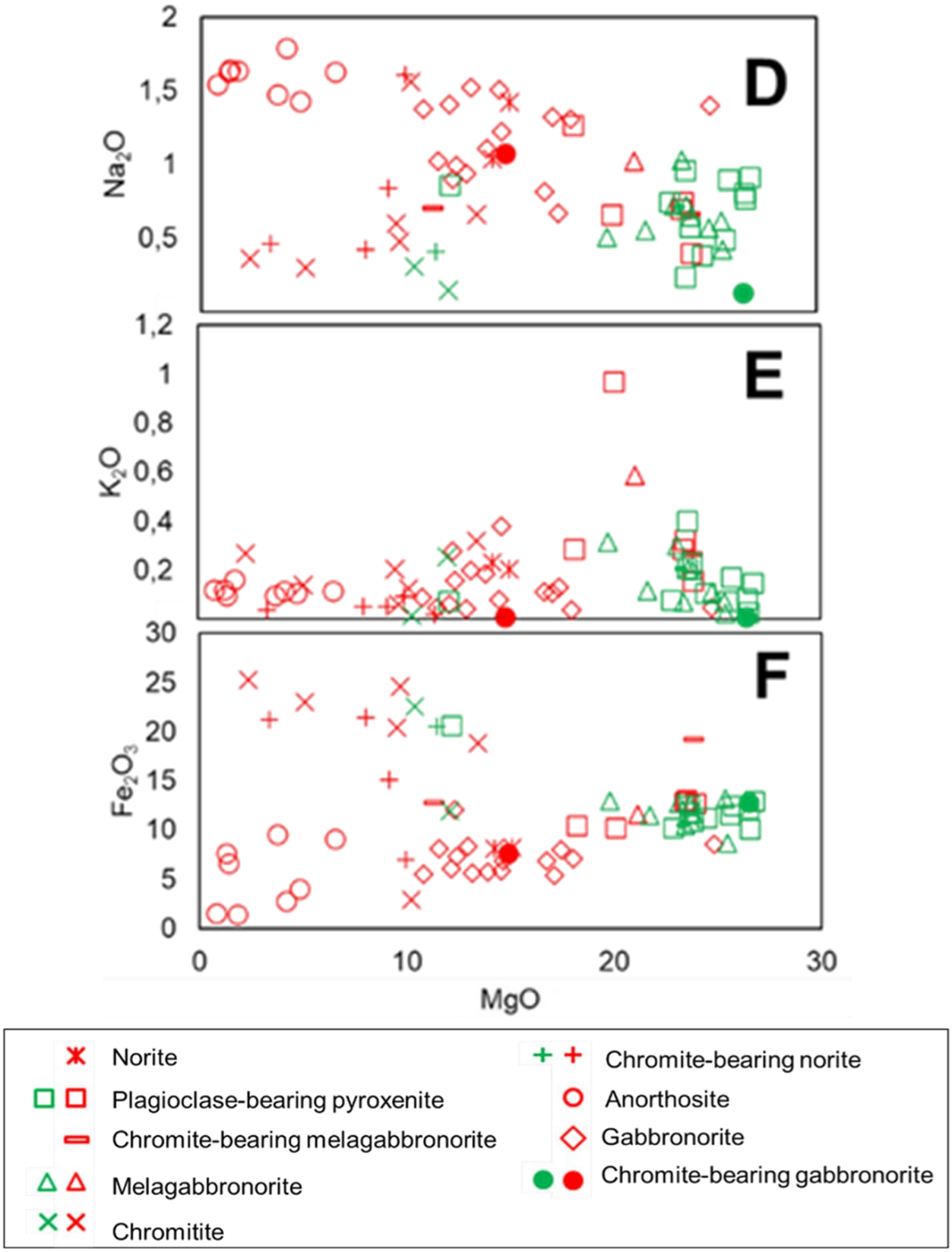

Figure 20: Continued

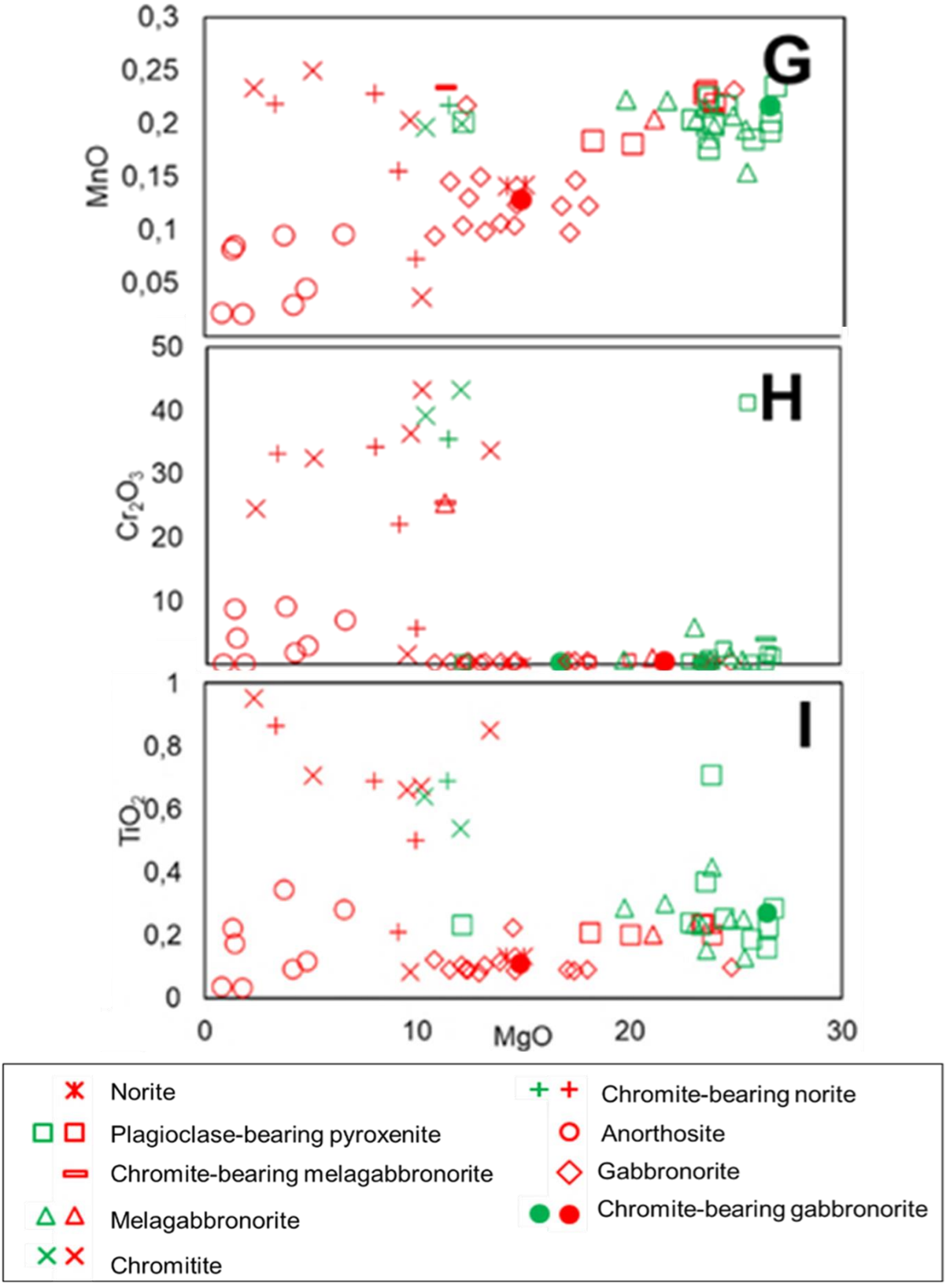

Figure 20: Continued

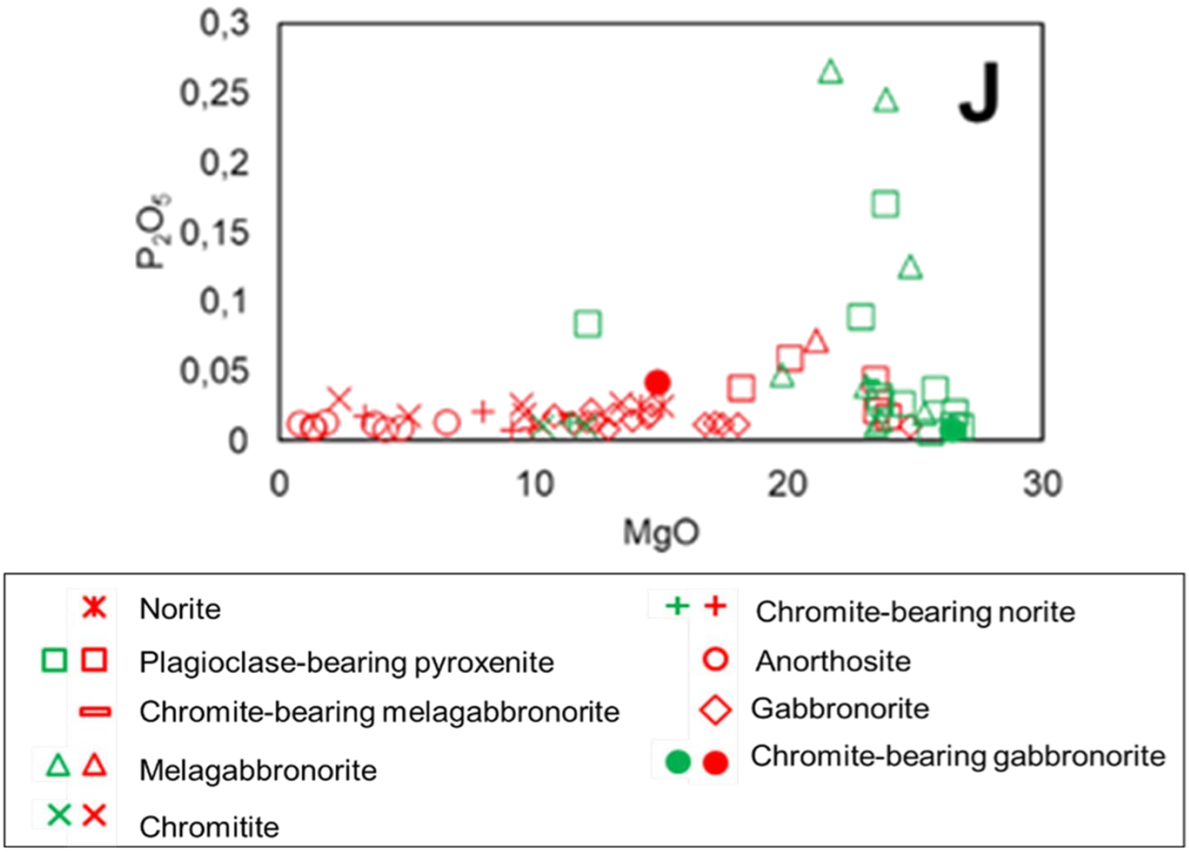

Figure 20: Continued

Major element chemistry is also reflective of dominant mineral phases when plotted against depth in the UCZ-LCZ interval as seen in Figure 21, with plagioclase dominant in the UCZ and pyroxene dominating in the LCZ.

SiO_2 displays an undeviating trend in chromite-free lithologies when plotted against depth in the UCZ-LCZ interval (Fig 21A). However, a decrease is seen in SiO_2 content at the chromitite layers. This reflects low silicates in chromite-rich lithologies in comparison to chromite-free lithologies.

Al_2O_3, Na_2O and K_2O (Fig 21 B, D and E respectively) display the same trend against depth. All have high values in the UCZ and low values in the LCZ. All are essential components of plagioclase and minor components in pyroxene. High values of these elements reflect high plagioclase content in the UCZ. Each reveal either an increase or decrease at the chromitite layers at various depths, therefore there is no consistent trend that can best describe their relationship with chromitites. CaO (Fig 21C) has the same trend as the previously mentioned major elements reflecting preference for

plagioclase. However, it must be noted that it is also a major component in clinopyroxene.

Fe_2O_3, and MgO (Fig 21F-I) all display a contrasting trend in comparison to the previously mentioned elements. All have high values in the LCZ and low values in the UCZ. All are major components in pyroxenes and minor components in plagioclase. This is reflective of low plagioclase content and high pyroxene content in the LCZ. There is no consistency in terms of distribution relative to the chromitite layers when all are plotted against depth, with each either increasing or decreasing at various chromitite depths.

Cr_2O_3 (Fig 21J) displays an undeviating trend through the bulk of the study interval. However, an increase is seen at the chromitite layers. Figure 21J also displays a reduced scale for Cr_2O_3 against depth, illustrating a slightly uniform distribution in chromite-free lithologies. However, there are some slight inflections below MG2 and MG4A. This is attributed to high chromite content below these layers.

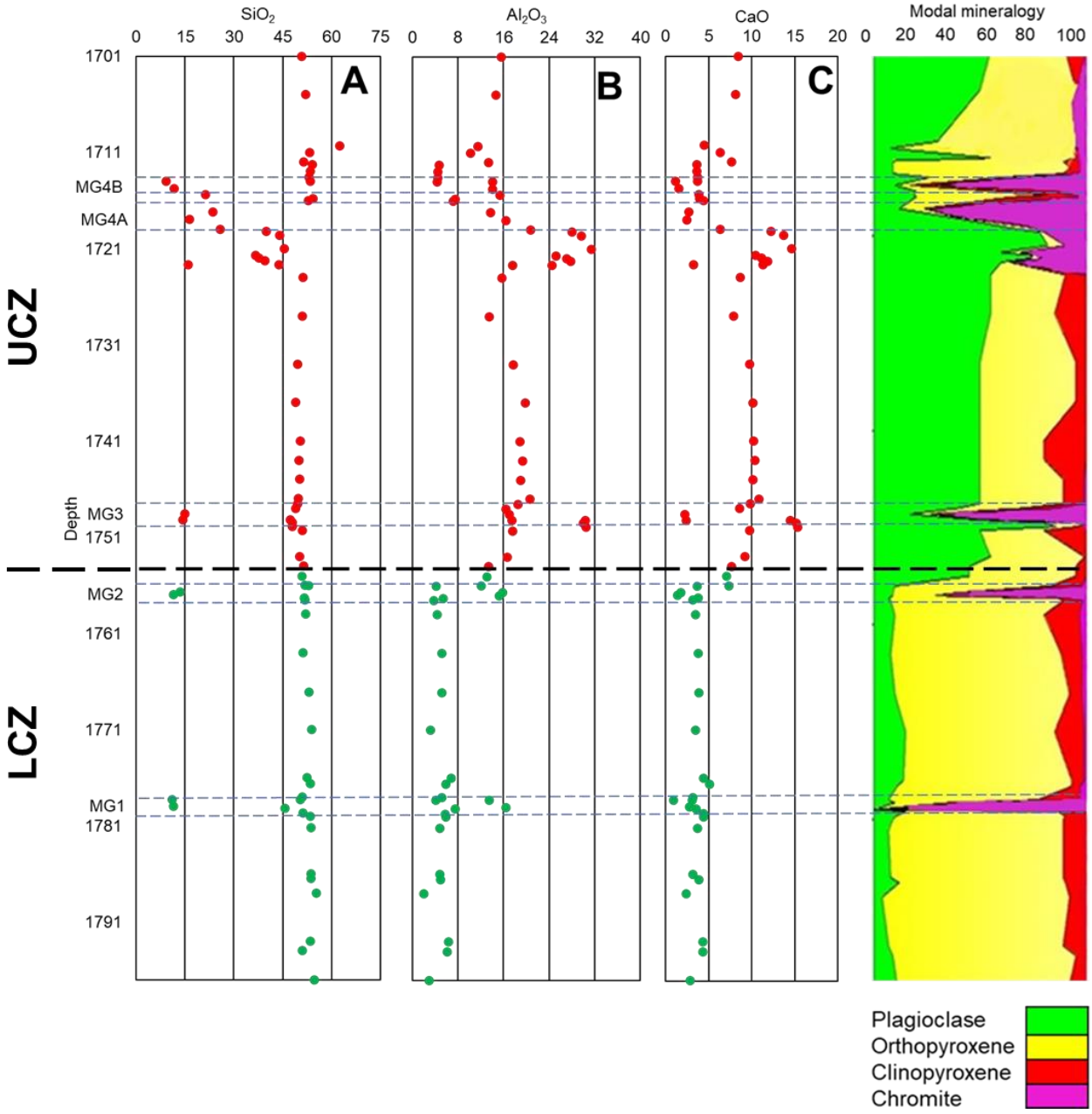

Figure 21: Whole-rock major elements vs depth along with modal mineralogy for the study interval (Red = UCZ, Green = LCZ). Dashed blue lines indicate extent of chromitite layers.

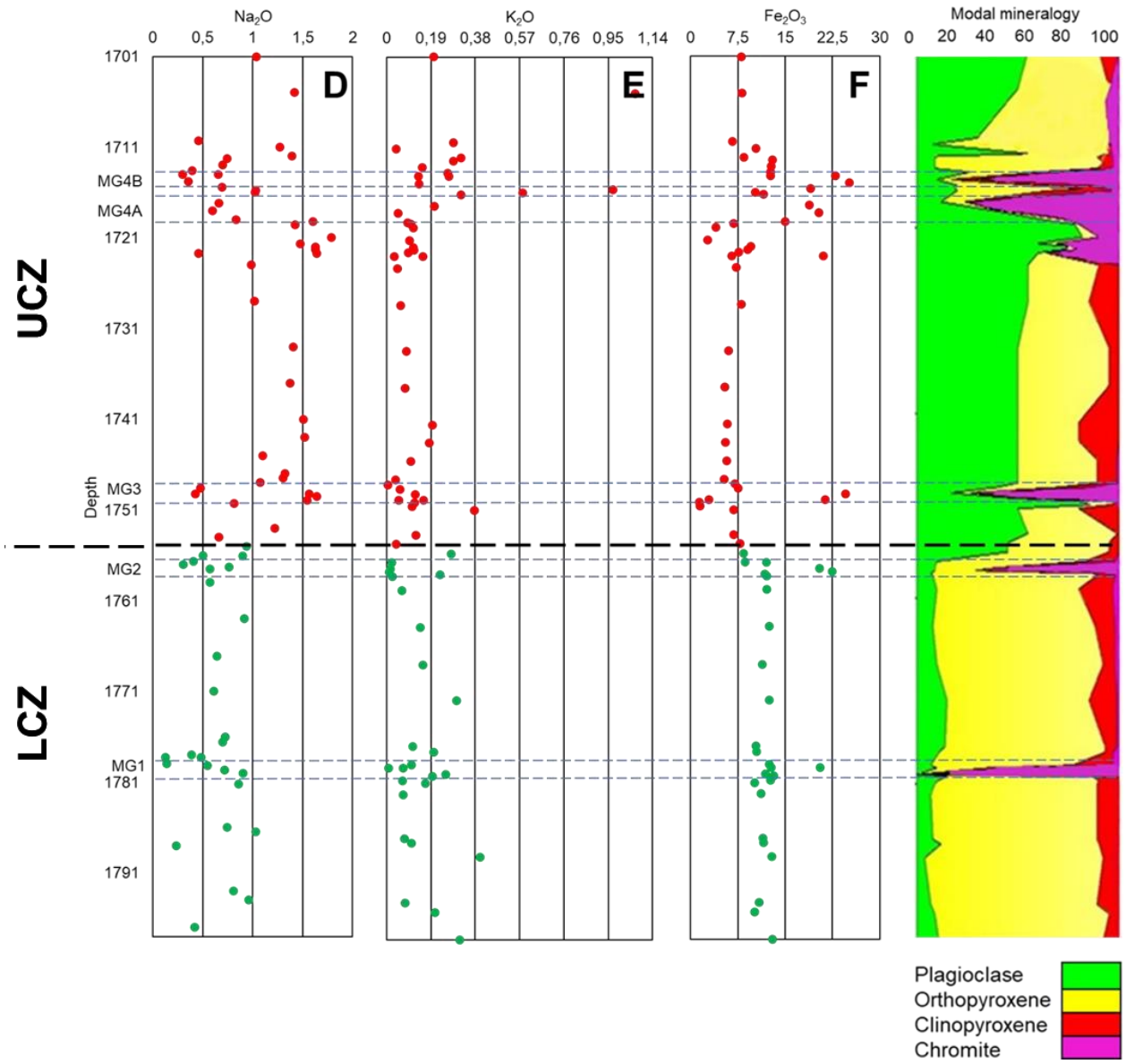

Figure 21: Continued

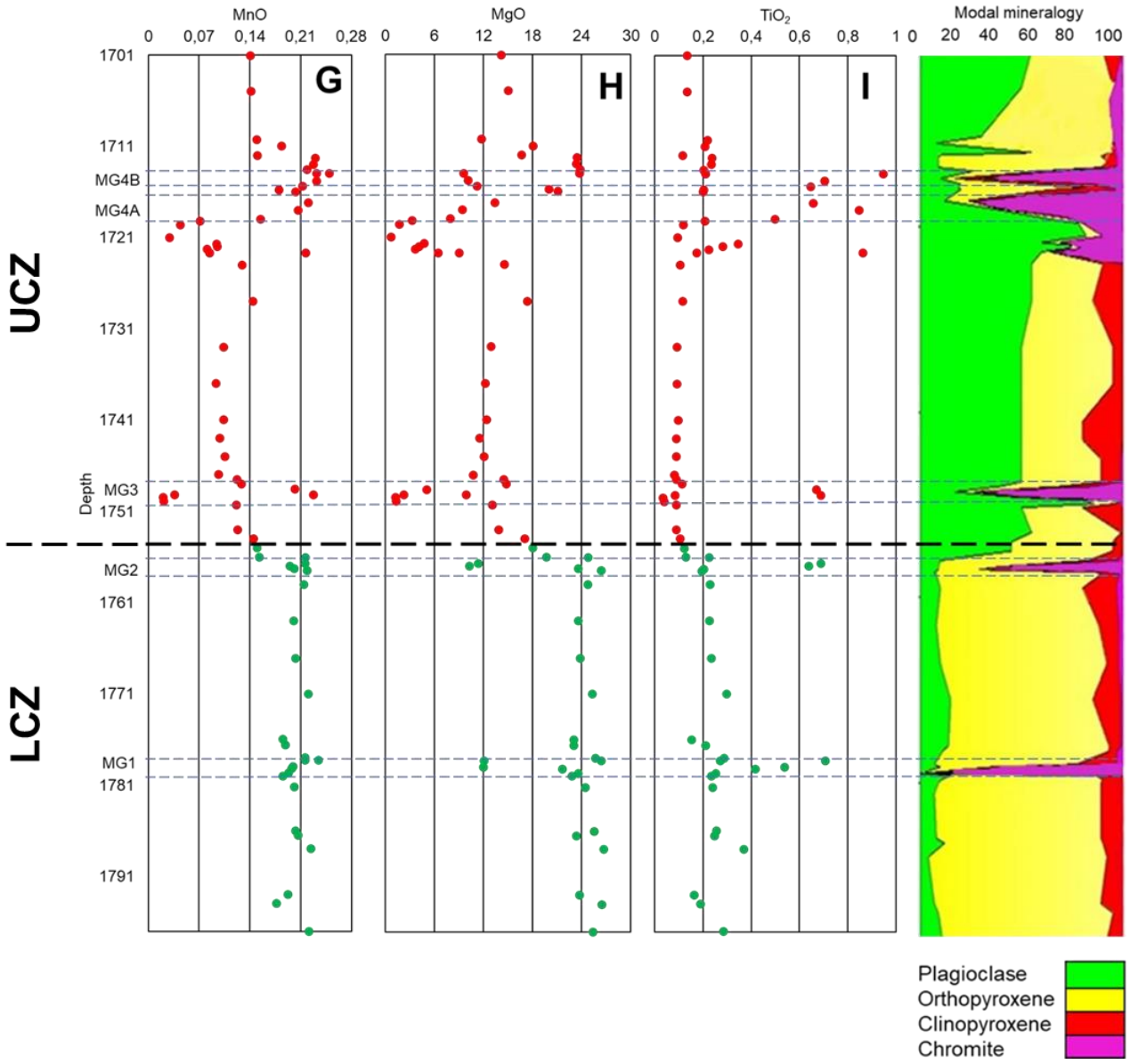

Figure 21: Continued

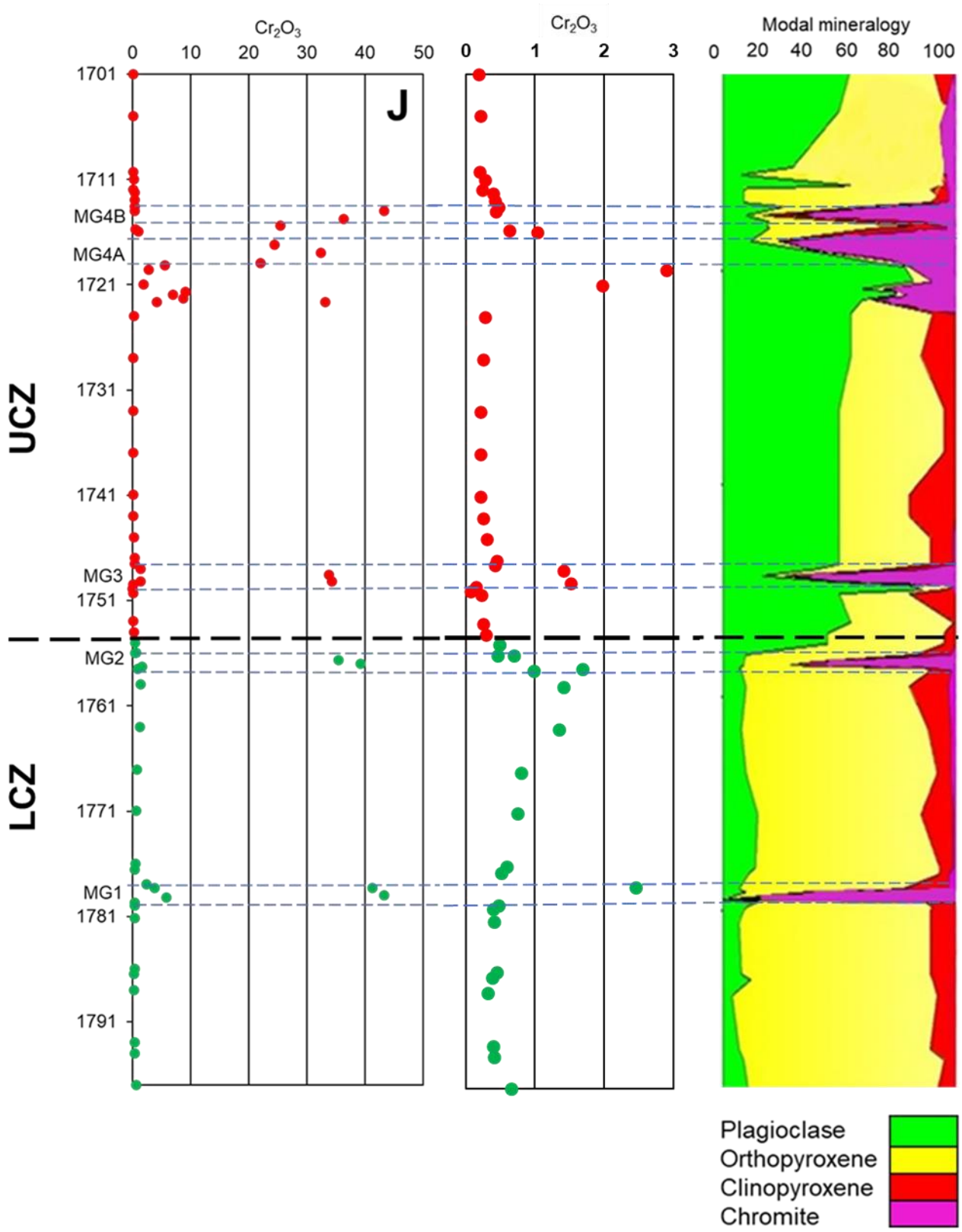

Figure 21: Continued

3.3. Whole-rock trace element geochemistry

Whole-rock trace element data are presented in Appendix B. Binary variation diagrams of selected trace elements versus MgO are presented in Figure 22. Variations of traces against depth are plotted in Figure 24. Detection limits for whole-rock trace elements are listed in Table 9, as analysed by XRF. The Pearson correlation coefficient (r-value) matrix was used to comment on correlations between MgO and traces (highlighted in red in Table 10).

Table 9: Detection limits for whole-rock trace elements in parts per million.

Element	Detection limit
Ba	17
Co	1
Cr	3
Cu	2
Nb	1
Ni	4
Pb	2
Rb	2
Sc	1
Sr	3
Th	3
U	1
V	4
Y	2
Zn	1
Zr	2

Table 10: Correlation matrix for major oxides in the study interval.

	Ba	Co	Cu	Ni	Sc	Sr	V	Zn	MgO
Ba	1								
Co	0,5306	1							
Cu	0,1934	0,3344	1						
Ni	0,3439	0,7964	0,5583	1					
Sc	0,5914	0,8444	0,3378	0,6305	1				
Sr	-0,441	-0,71	-0,212	-0,637	-0,699	1			
V	0,502	0,3916	-0,025	-0,034	0,6929	-0,354	1		
Zn	0,4852	0,3458	-0,024	-0,066	0,6524	-0,307	0,9193	1	
MgO	0,1582	0,5685	0,4317	0,8384	0,3831	-0,476	-0,335	-0,292	1
	Strong correlation = 1								

Trace element concentration is largely controlled by the partition coefficients of the element into the minerals present in dominant lithologies. Ba (Fig 22A) displays a weak positive correlation with MgO (r = 0.1581), averaging 103 ppm in the LCZ and 75 ppm in the UCZ, with the highest value of 290 ppm found at depth 1710.30 m (quartz-feldspar patch) and the lowest value of 10 ppm found at a depth of 1749.50 m (anorthosite). Ba usually has a higher partition coefficient in plagioclase when compared to orthopyroxene (Table 11). However, evidence of this is not seen in the study interval as plagioclase-rich lithologies (i.e. gabbronorite and anorthosite) reveal lower Ba concentrations than plagioclase-poor rocks (plagioclase-bearing pyroxenite and melagabbronorite). A significant increase is seen in Ba concentration at the levels of chromitite layers in both zones, averaging 145 ppm in the LCZ and 146 ppm in the UCZ (Fig 22A), which is unexpected as Ba has a low partition coefficient for spinel (Table 11).

Co (Fig 22B) displays a moderate positive correlation with MgO (r = 0.5685), averaging 88 ppm in the LCZ and 57 ppm in the UCZ, with a high value of 110 ppm found at depths 1722.70 m and 1749.20 m (chromite-bearing norite). The lowest value of 3 ppm is found at 1749.50 m in anorthosite. This is reflective of Co partitioning preferentially into orthopyroxene as opposed to plagioclase, as seen in Table 11. An increase in Co concentration is also revealed at the chromitite layers throughout the study interval, which is explained by the high partition coefficient of Co into spinel (Table 11).

Cu (Fig 22C) displays a weak positive correlation with MgO (r = 0.4317), averaging 31 ppm in the LCZ and averaging 15 ppm in the UCZ. Both plagioclase and

orthopyroxene have the same partition coefficient of <0.1 for Cu (Table 11). It is uncertain why Cu appears to be preferentially concentrated within the plagioclase-bearing pyroxenites of the LCZ. There is no consistency in terms of distribution relative to the chromitite layers as it displays a decrease at MG4B and MG1, an increase at MG4A and MG3, with no change at MG2 in comparison to the adjacent lithologies (Fig 24F). Although not observed, lithologies displaying elevated Cu values may possibly contain disseminated sulphides.

Ni (Fig 22D) displays a strong positive correlation with MgO, averaging 544 ppm in the LCZ and 295 ppm in the UCZ, varying between 10 ppm and 660 ppm. This is reflective of preferential incorporation into pyroxene rather than plagioclase (Table 11). A decrease in Ni concentration is detected at the chromitite layers, apart from at MG3, which displays a slight increase (Fig 24E).

Sc displays two trends, revealing distribution differences between chromite-bearing and chromite-free lithologies when plotted against MgO (Fig 22E). Sc varies between 10 ppm and 60 ppm, displaying a weak positive correlation with MgO (r = 0.3831). It averages 44 ppm in the LCZ and 29 ppm in the UCZ. Partition coefficient values for Sc in orthopyroxene are not available as seen in Table 11. However, clinopyroxene has a higher value than plagioclase and Sc is therefore preferentially incorporated into clinopyroxene, explaining the high value in the LCZ. An increase in concentration is seen in all the chromitite layers throughout the UCZ-LCZ interval (Fig 24D), reflecting the high partition coefficient of Sc into spinel in comparison to the rest of the mineralogy.

Sr (Fig 22F) displays a weak negative correlation with MgO (r = -0.476). A decrease in the maximum Sr concentration with increasing MgO is observed, varying between 10 ppm and 450 ppm. It averages 86 ppm in the LCZ and 213 ppm in the UCZ. This is reflective of preferential incorporation into plagioclase rather than pyroxene. A decrease in Sr concentration is seen in all the chromitite layers (Fig 24G). This further reflects incorporation into plagioclase rather than spinel (Table 11).

V displays two contrasting trends, revealing differences in chromite-bearing and chromite-free lithologies. V concentrations are generally <500 ppm in the chromite-free lithologies, whereas in the chromitite-bearing lithologies, V is typically higher than 500 ppm. The element varies between 2 ppm and 2260 ppm, averaging 473 pm in the

UCZ and 446 ppm in the LCZ. Overall, V (Fig 22G) displays weak negative correlation with MgO (r = -0.335).

Zn varies between 20 ppm and 500 ppm, displaying a positive correlation with MgO in both chromite-bearing and chromite-free lithologies, respectively. It averages a value of 154 ppm in the UCZ and 148 ppm in the LCZ. All the chromitite layers display a significant increase in Zn concentration throughout the study interval, reflecting the high partition coefficient for spinel (Table 11).

Zr varies between 10 ppm and 80 ppm, with most of the measured points below the detection limit of 1 pm regardless of lithology. However, plagioclase-bearing pyroxenite is the exception, having an average value of 18.57 ppm in the UCZ and 19.5 ppm in the LCZ. Zr is largely incorporated into pyroxene rather than plagioclase (Table 11), which explains why Zr is detected in lithologies dominated by pyroxenes and it is below the detection limit in the other lithologies.

U and Th measured below the detection limit of 3 ppm, whereas Y is measured at 10 ppm throughout the study interval. Rb and Pb measured below 30 ppm, with Nb measuring at 10 ppm.

Table 11: Partition coefficients for selected trace elements into plagioclase, pyroxene and chromite in basaltic melts.

Elements	Plagioclase	Orthopyroxene	Clinopyroxene	Spinel (chromite)
Ba	0.68[b]	<1.11x10^{-5}[i]	0.00068[g]	0.0006[k]
Co	0.03[b]	2[a]	1.2[a]	4.7[l]
Cr	0.02[c]	3.7-17[j]	13[c]	3.43[k]
Cu	<0.1[b]	<0.1[b]	<0.1[b]	3.1[m]
Ni	0.06[c]	1.1[d]	2.6[d]	
Sc	0.008[b]		3.3[b]	0.36[l]
Sr	2[e]	0.007[c]	0.067[c]	0.0047[k]
V	0.1[c]	0.3[a]	1.5[a]	1.3[k]
Zn	0.13[b]		0.49[b]	3.6[l]
Zr	0.0127[f]	0.02[h]	0.123[g]	0.3[l]

References: A) Frey *et al*. (1978); b) Paster *et al*. (1974); c) Bougault and Hekinion (1974); d) Mysen (1978); e) Mckenzie and O'Nions (1991); f) Bindeman *et al*. (1998); g) Hart and Dunn (1993); h) Keleman and Dunn (1992); i) Beattie (1993); j) Ewart *et al*. (1973); k) Elkins *et al*. (2008); l) Horn *et al*. (1994); m) Klemme *et al*. (2006).

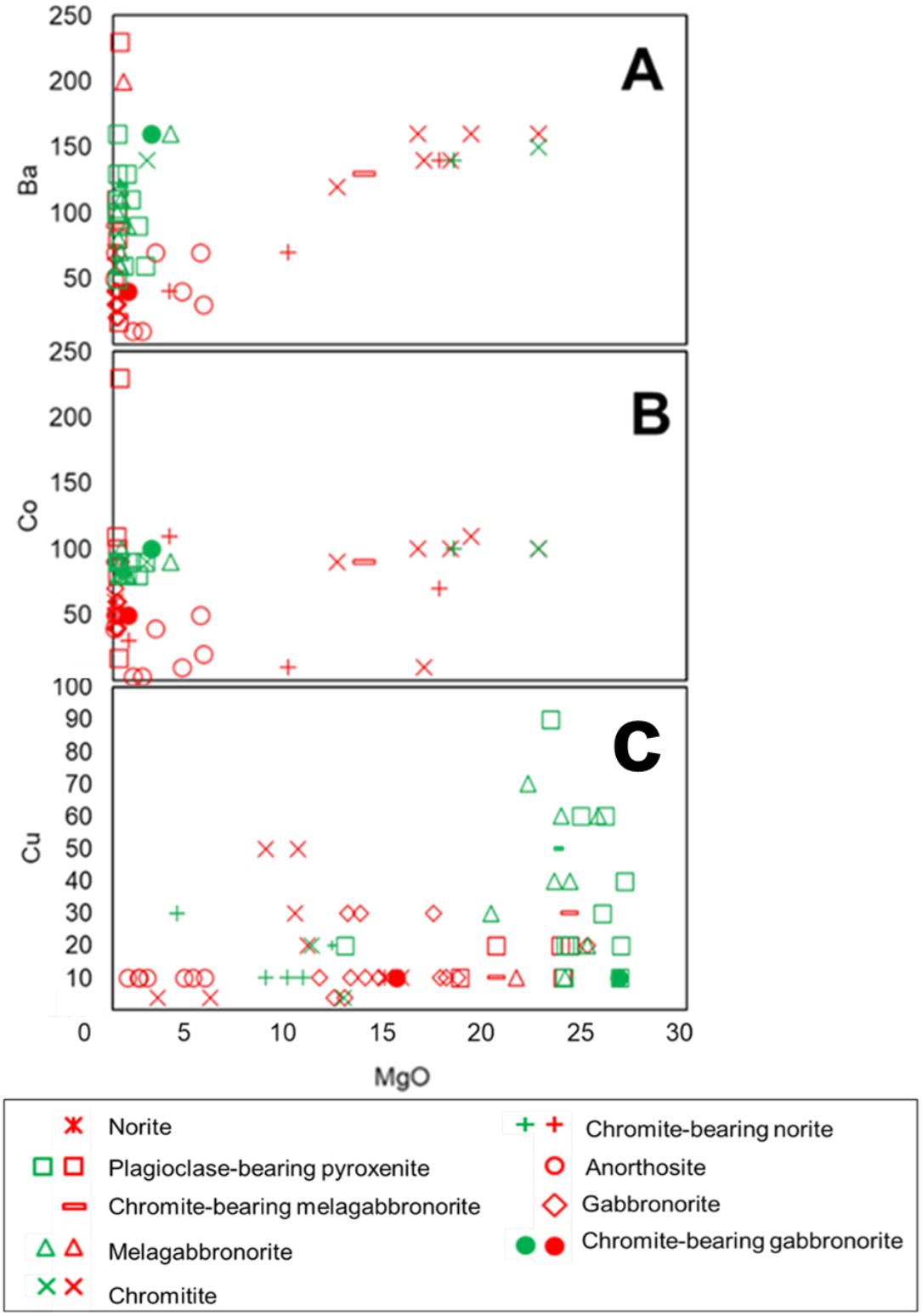

Figure 22: (A-I), binary variation diagrams for whole-rock trace elements vs MgO in the study interval (Red = UCZ, Green = LCZ).

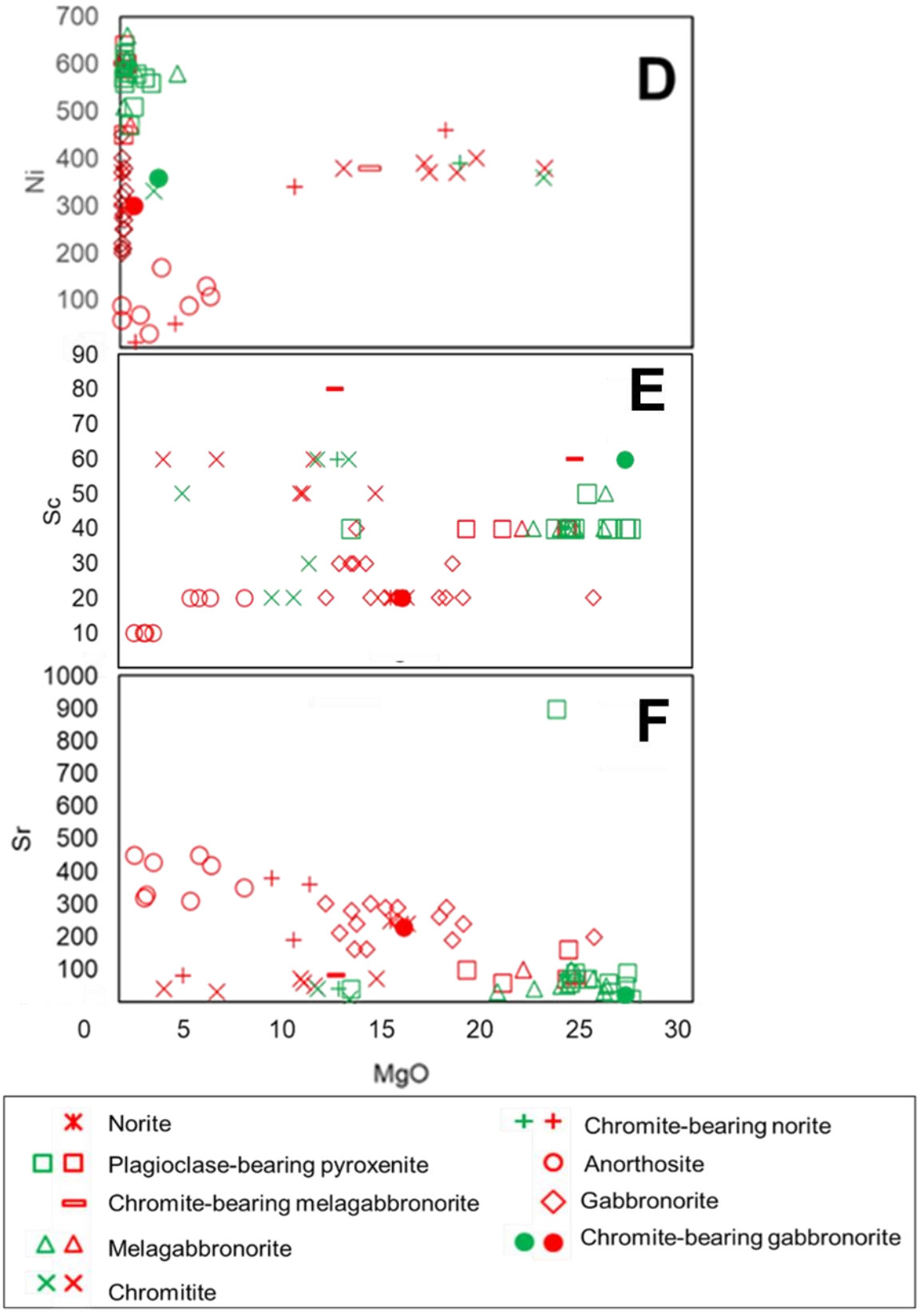

Figure 22: Continued

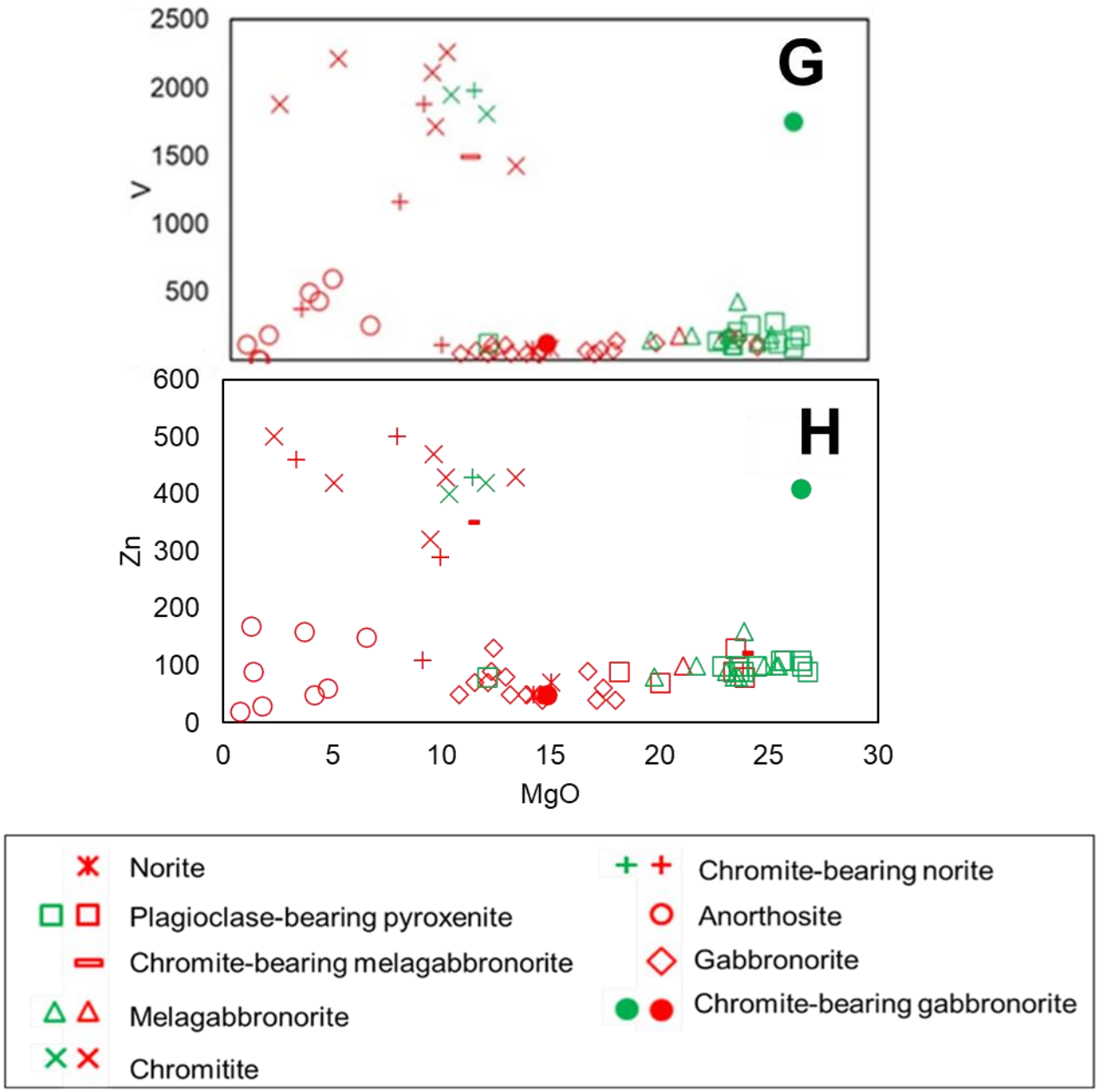

Figure 22: Continued

Upon discovery of the existence of 2 contrasting trends of some trace elements vs MgO (Fig 22), binary variation diagrams for Cr vs trace elements were prepared and are presented in Fig 23.

From the resulting plots in Figure 23, Ba, Co, Cu, Ni, Sc, V and Zn all display a positive correlation with Cr in chromite-bearing lithologies throughout the UCZ-LCZ study interval, whereas Sr displays a negative correlation. This attests to the fact that Ba, Co, Cu, Ni, Sc, V and Zn have an affinity towards chromite-bearing lithologies as well as plagioclase-bearing pyroxenite and melagabbronorite to some lesser extent. Table 11 also shows that most have higher partition coefficients in spinel in comparison to plagioclase and the pyroxenes.

Sr displays a negative correlation with Cr, reflecting low partition coefficient into chromite, rather preferring partitioning into plagioclase (Table 11). Hence, chromite-poor lithologies generally have higher Sr values in comparison to chromite-rich lithologies (Fig 24G).

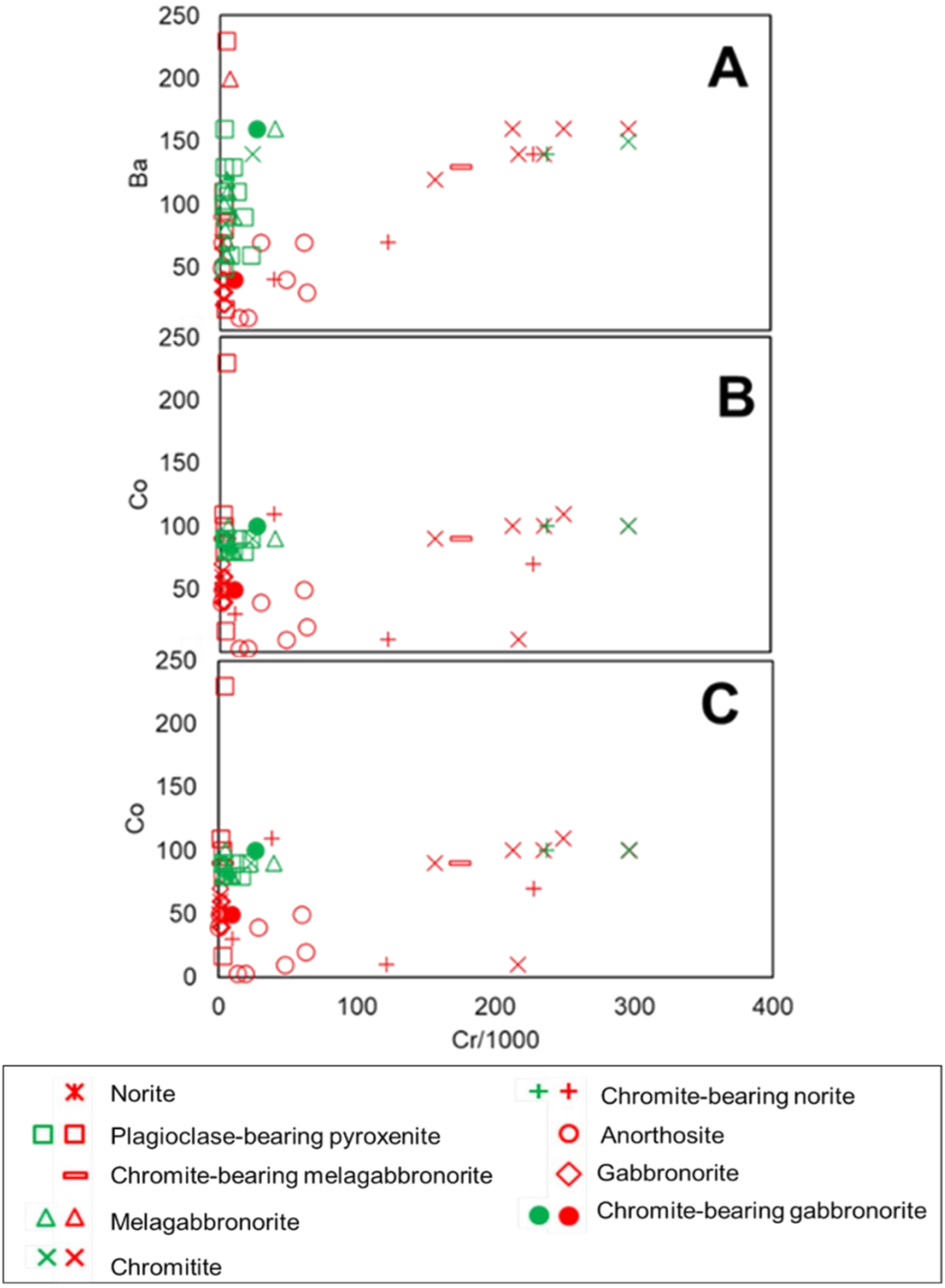

Figure 23: (A-I), binary variation diagrams for whole-rock trace elements vs Cr in the study interval (Red = UCZ, Green = LCZ).

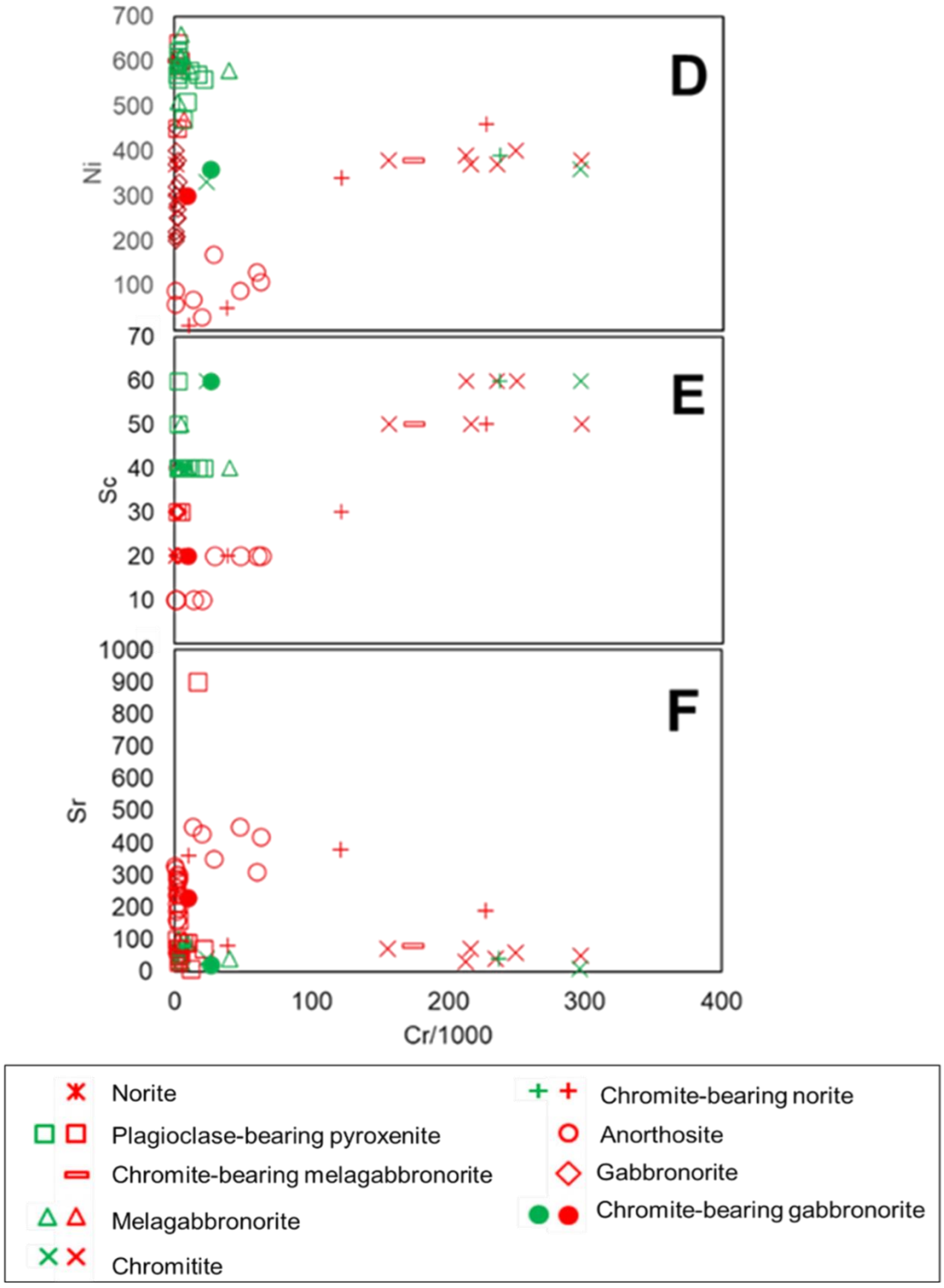

Figure 23: Continued

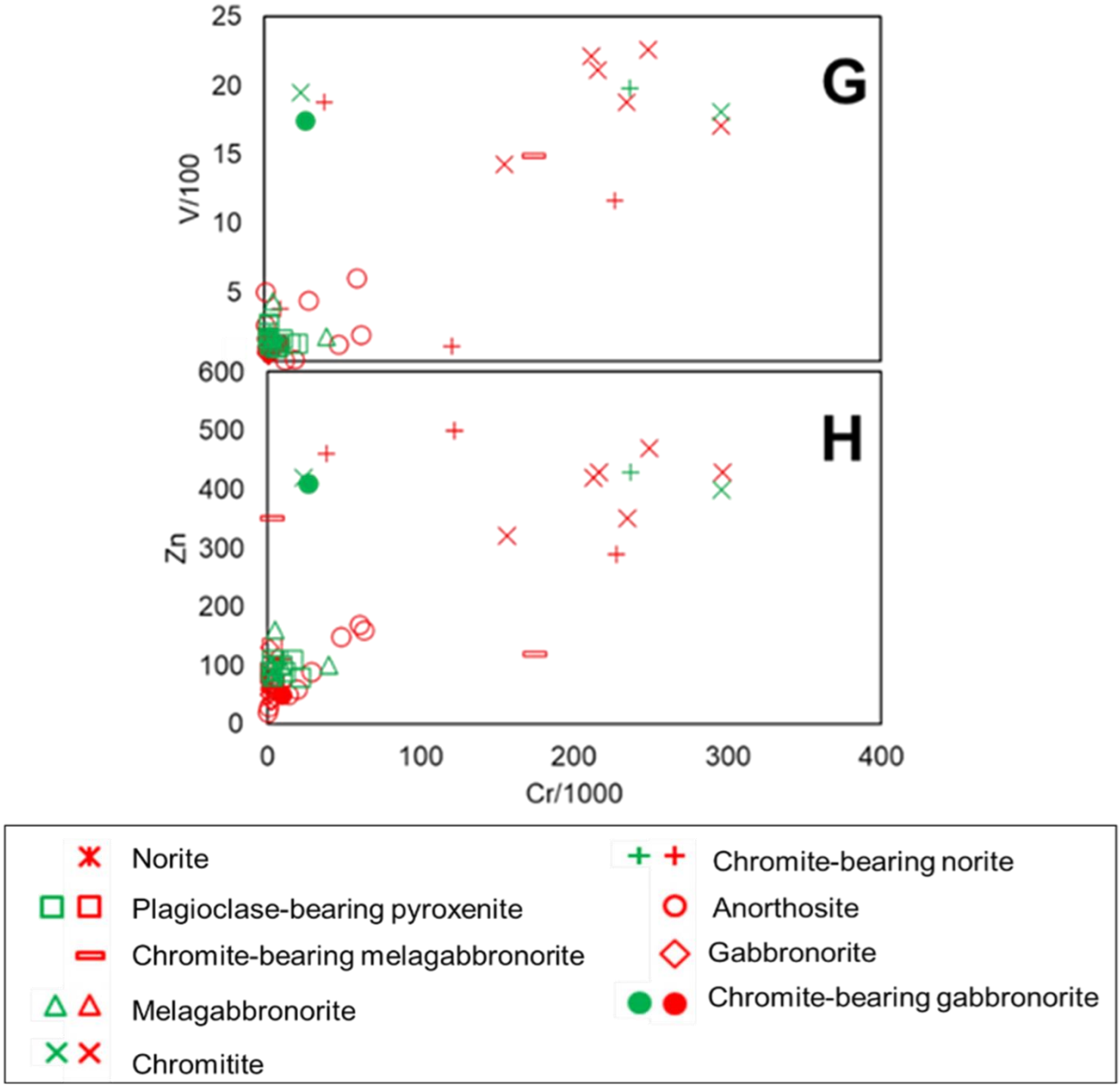

Figure 23: Continued

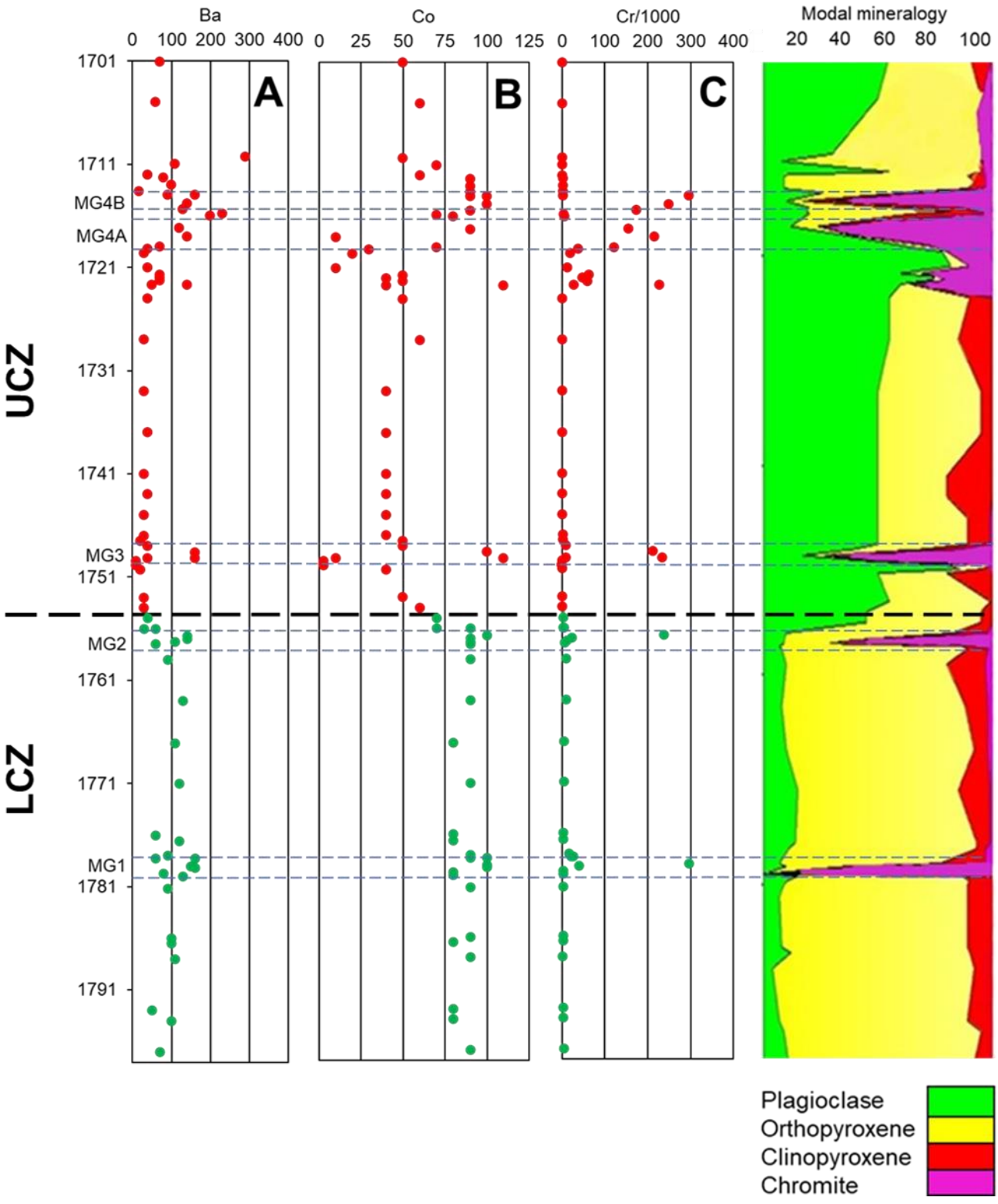

Figure 24: Whole-rock trace elements vs depth along with modal mineralogy for the study interval (Red = UCZ, Green = LCZ). Dashed blue lines indicate extent of chromitite layers.

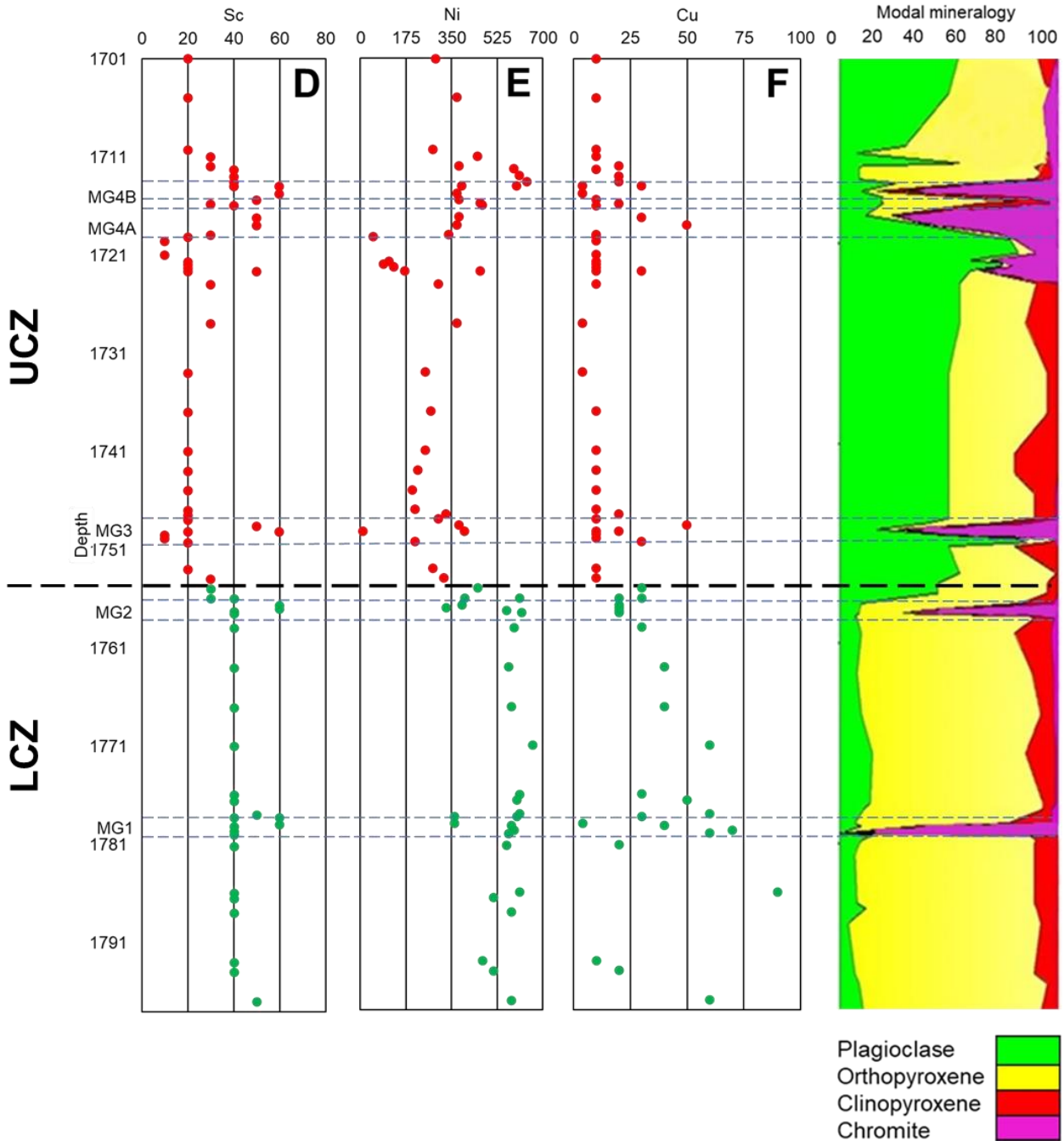

Figure 24: Continued

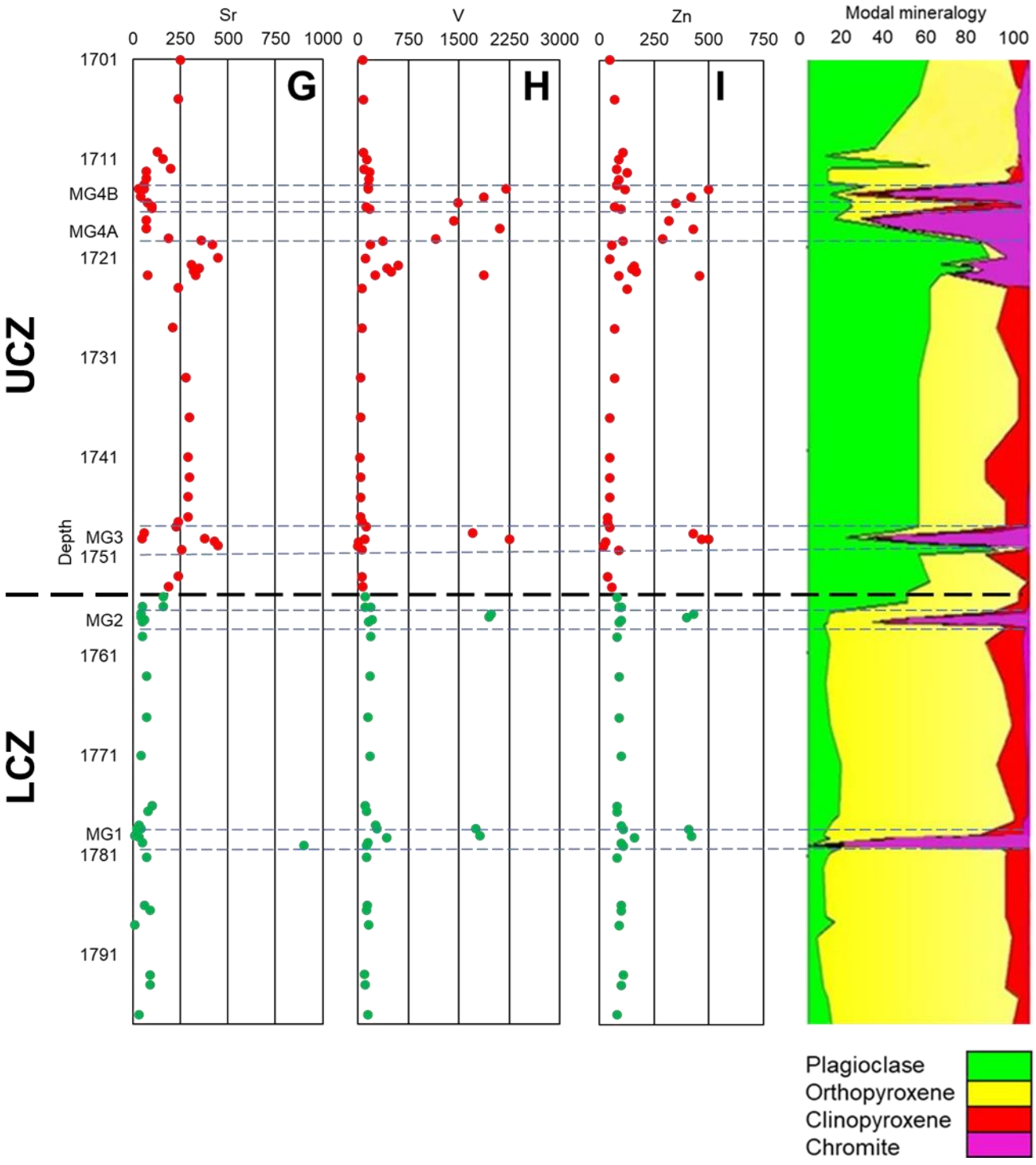

Figure 24: Continued

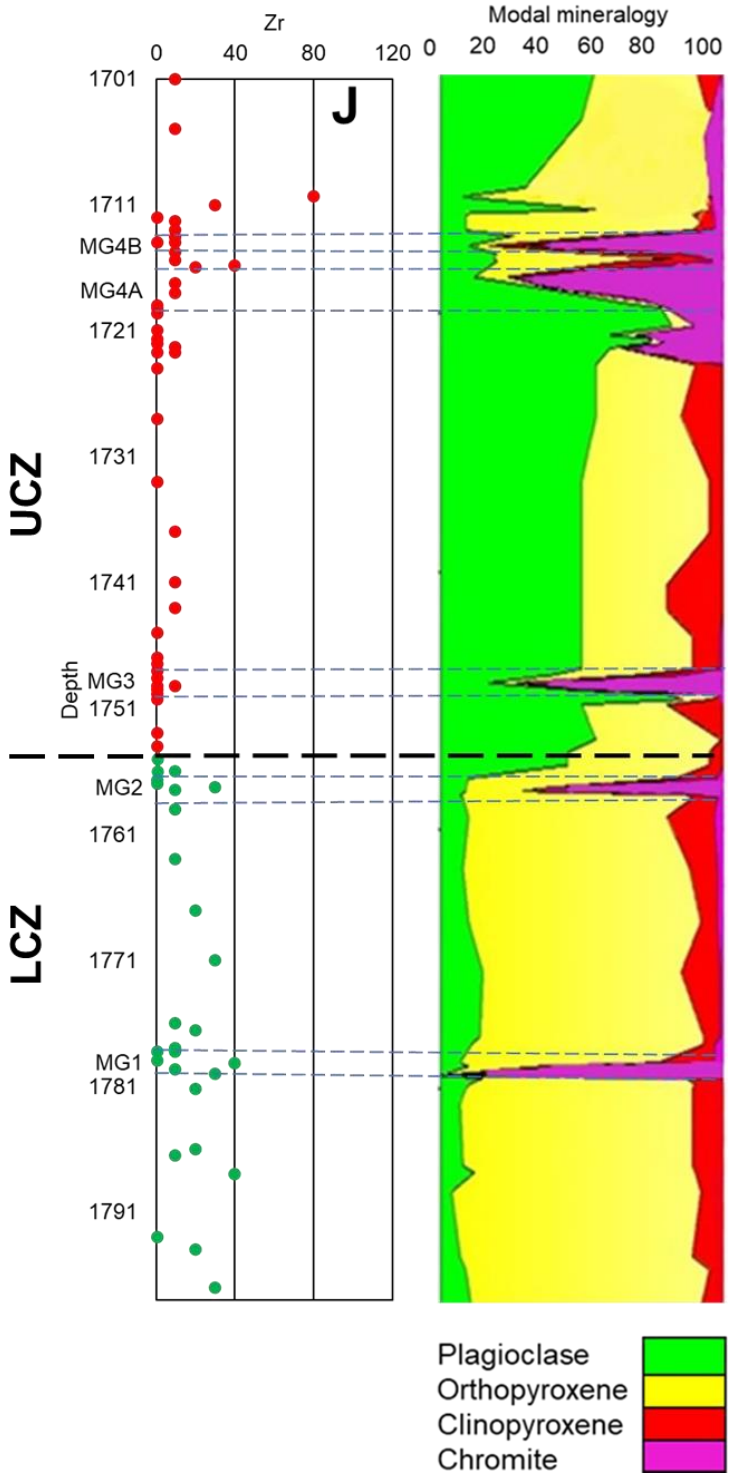

Figure 24: Continued

3.4. Whole-rock REE geochemistry

Lanthanide concentrations for the analysed rocks in the UCZ-LCZ interval are presented in Appendix C. Figures 25 and 27 show chondrite normalized REE abundances for the LCZ and UCZ, respectively. Figure 28 presents REE variation against whole-rock MgO and Figure 29 presents variations in the REE vs depth.

The analysed LCZ samples reveal La concentrations covering a range 2.94-60 times chondrites, whereas Lu concentrations cover a range 0.48-4.39 times chondrites (Fig 25). REE trends in this study are similar to those presented by Maier and Barnes (1998) for the entire LCZ interval (insert in Fig 25). Enrichment of LREE is revealed in all analysed samples, with Ce/Sm_N averaging a value of 2.33. Tb/Yb_N has an average value of 1, revealing a lack of HREE fractionation in the LCZ interval

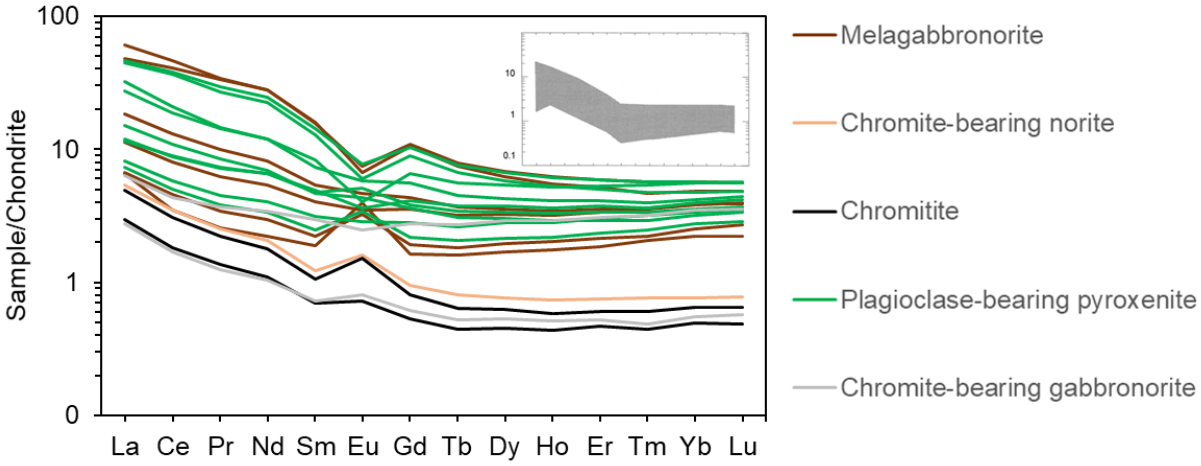

Figure 25: Chondrite normalized REE abundances of the LCZ samples in this study. Insert represents comparison by Maier and Barnes (1998) for the entire LCZ. Chondrite normalization factors were taken from Anders and Grevesse (1989).

Variations in the europium anomaly (hereafter Eu/Eu*) are displayed by analysed samples up the CZ stratigraphy (Fig 26). From the base of the LCZ to a depth of 1788 m, a positive Eu/Eu* value of 1.26 is displayed by plagioclase-bearing pyroxenite. This is followed by a decrease to a negative Eu/Eu* value of 0.54, also in plagioclase-bearing pyroxenite. The depth between 1788 m and 1779.20 m reveals a negative Eu/Eu* value, averaging 0.64. The chromitite layer (MG1) at 1779 m reveals a value of 1.18, decreasing to a value of 0.79 in plagioclase bearing pyroxenite at a depth of 1778 m. Another increase to a value of 1.58 is encountered at 1776 m in melagabbronorite, followed by a decrease to a value of 0.56 also in melagabbronorite

at 1771 m. The Eu/Eu* value remains varyingly negative until a depth of 1763 m, increasing to a value of 1.20 in plagioclase-bearing pyroxenite. A decrease to a value of 0.92 follows at depth 1759 m in melagabbronorite, remaining varyingly negative up until the chromitite layer (MG2) at 1756.70 m, displaying a value of 1.63. Eu/Eu* remains positive up until the top of the LCZ. Europium ideally prefers incorporation into plagioclase than pyroxene and in this case all the analysed samples were expected to have negative Eu/Eu* as pyroxene is the dominant phase. Positive Eu/Eu* displayed by samples in the LCZ is suggestive of some degree of plagioclase enrichment.

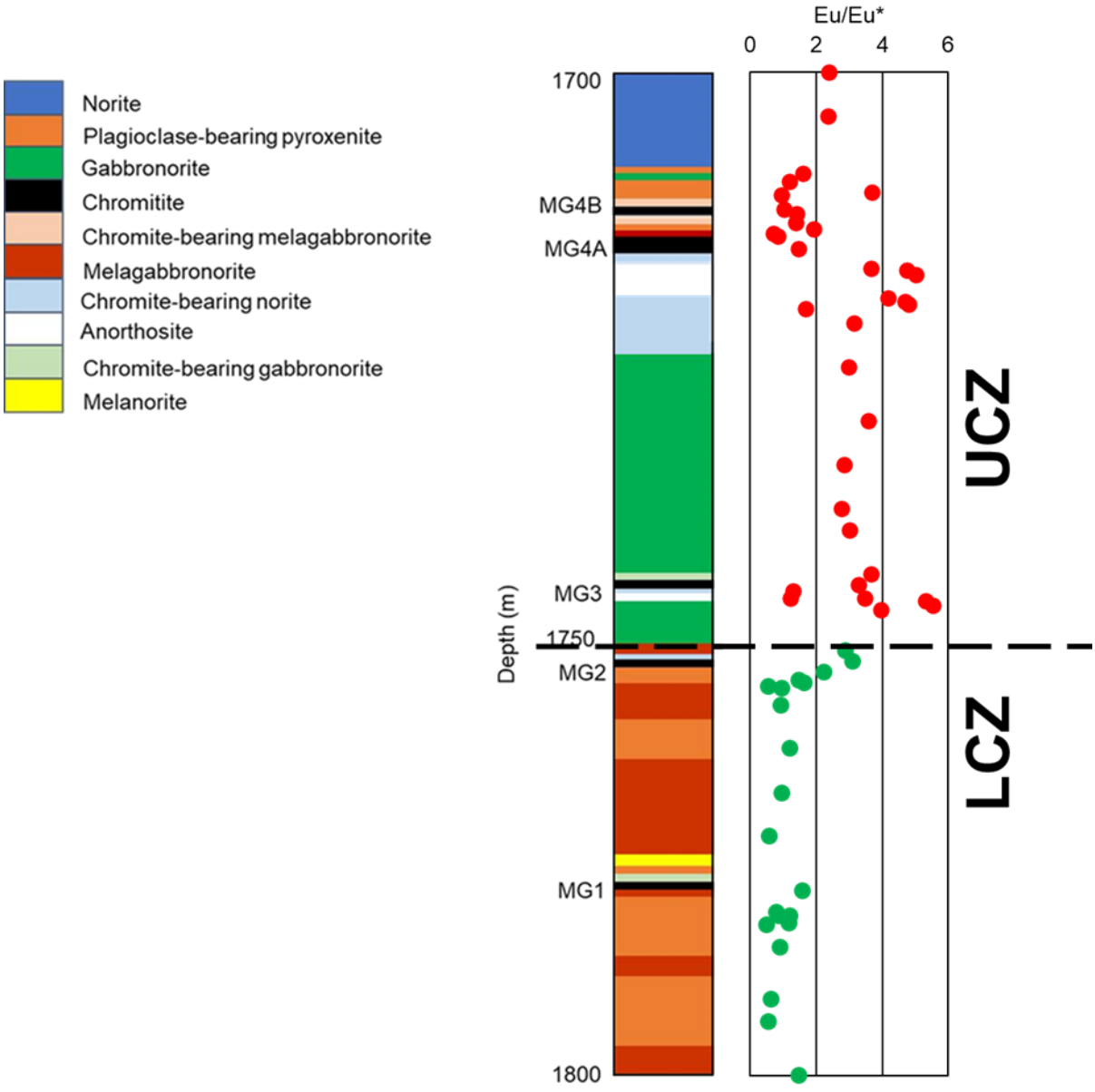

Figure 26: Europium anomaly up the LCZ-UCZ stratigraphy (Red = UCZ, Green = LCZ).

In the UCZ, La concentration of all the analysed samples has a range 5.26-47.88 times chondrites. Lu concentrations reveal a range 0.32-4.79 times chondrites (Fig 27). LREE enrichment is also detected in the UCZ interval, with Ce/Sm_N averaging 2.93. Tb/Yb_N averages a value of 1.06, indicating limited fractionation of the HREE in all analysed samples. A positive Eu/Eu* is also displayed by the UCZ samples, with only two samples between the depth of 1715.80 m and 1716 m (plagioclase-bearing pyroxenite and melagabbronorite) displaying negative Eu/Eu* (Fig 26).

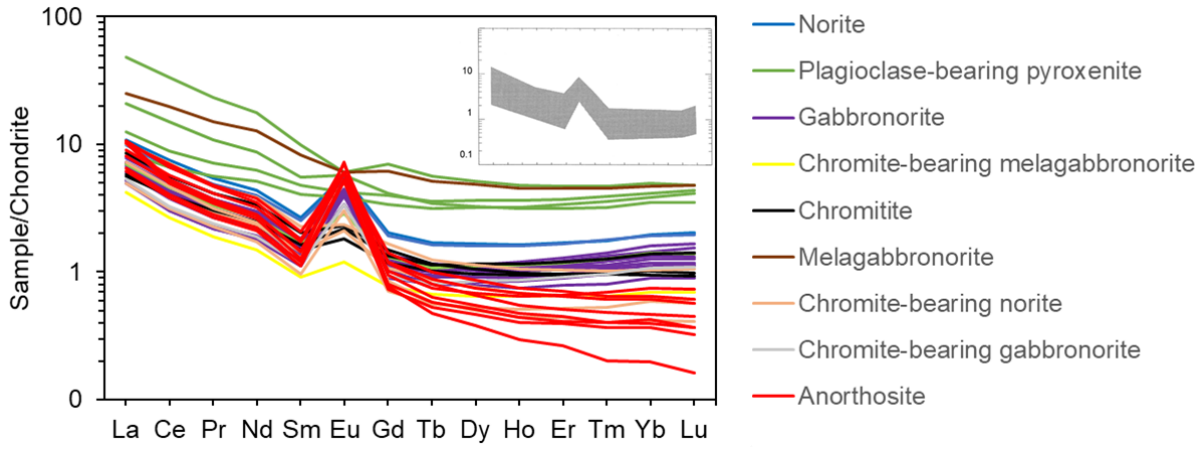

Figure 27: Chondrite normalised REE abundances of the UCZ samples. Insert represents comparison with Maier and Barnes (1998) for the entire UCZ interval. Chondrite normalization factors were taken from Anders and Grevesse (1989).

Low REE concentration is displayed by most of the lithologies in the UCZ-LCZ interval, except for plagioclase-bearing pyroxenite and melagabbronorite displaying high REE concentration (Fig 28). Moreover, melagabbronorite and plagioclase-bearing pyroxenite also display variations against depth (Fig 29), indicating that REE variation is more common in mafic lithologies than felsic lithologies. From the base to the top of the LCZ, REE data points are widely scattered, with no recognisable trend.

The UCZ varies in comparison to the LCZ, displaying very limited variation across the stratigraphy (Fig 29). A linear trend is seen from the base of the UCZ to the top, with a scattering of points encountered between depth 1711 m and 1716 m, coinciding with lithologies that are composed of mafic minerals.

LREE in the UCZ-LCZ interval display no correlation with whole-rock MgO for the majority of lithologies (Fig 29A-E). Melagabbronorite and plagioclase-bearing pyroxenite are the exception, displaying a positive correlation with whole-rock MgO. HREE (Fig 29G-N) display a weak positive correlation when plotted against whole-

rock MgO in the majority of lithologies. However, melagabbronorite and plagioclase bearing pyroxenite display a positive correlation with whole-rock MgO. Eu which is characterised by chaotic scattering when plotted against MgO, reveals no correlation whatsoever (Fig 28F). This indicates preferential incorporation into plagioclase rather than orthopyroxene.

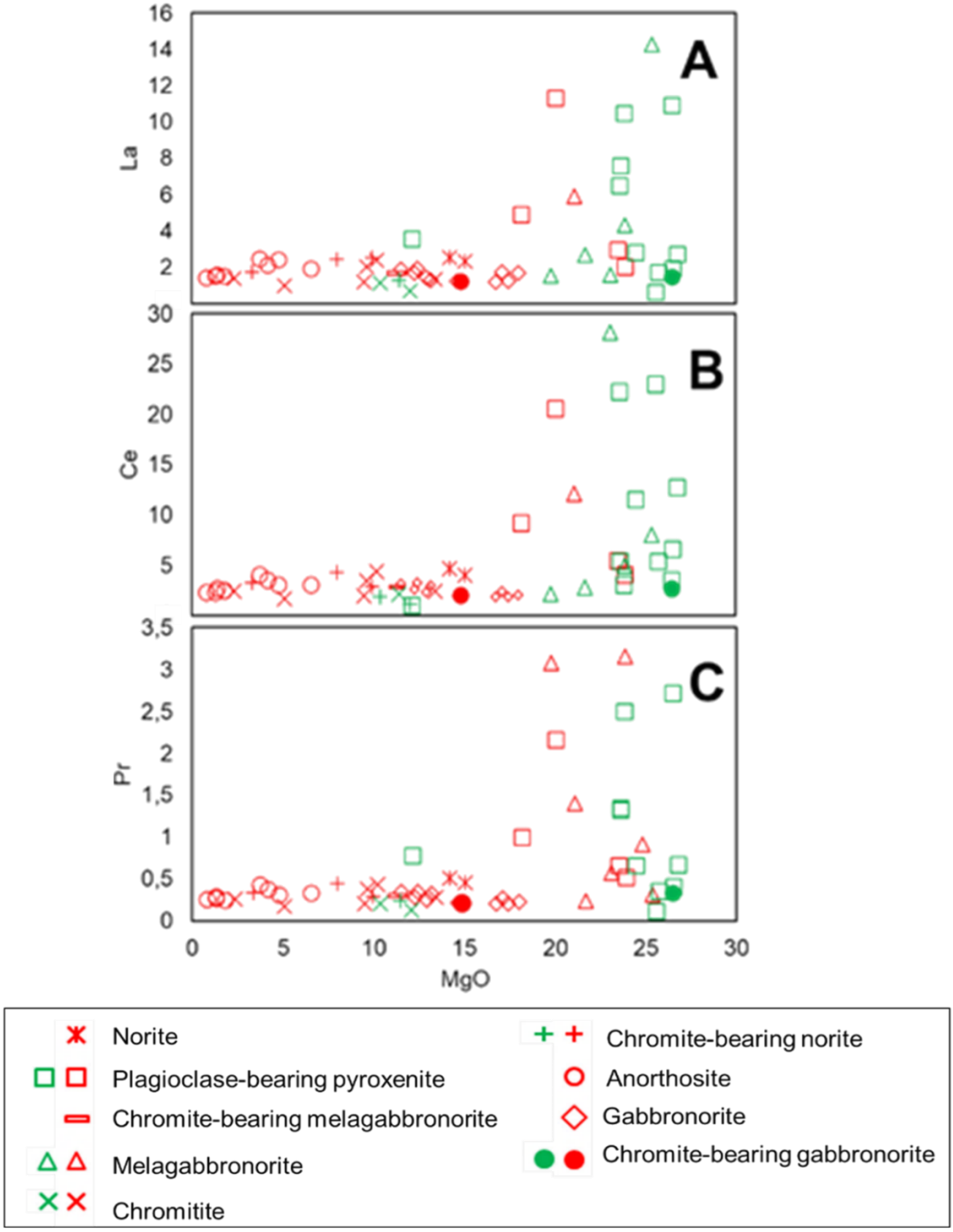

Figure 28: Binary variation diagrams for REE vs whole-rock MgO (Red = UCZ, Green = LCZ).

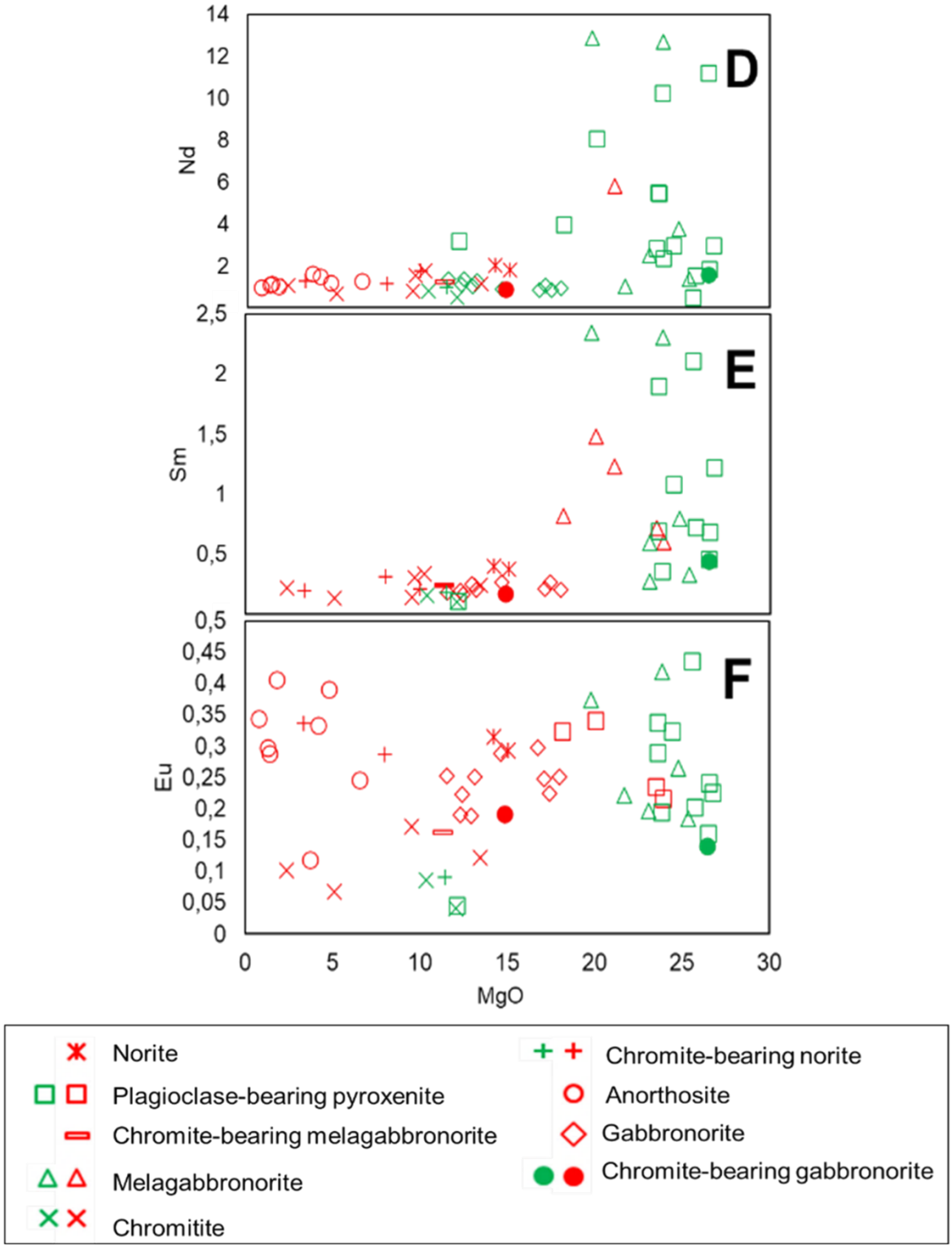

Figure 28: Continued

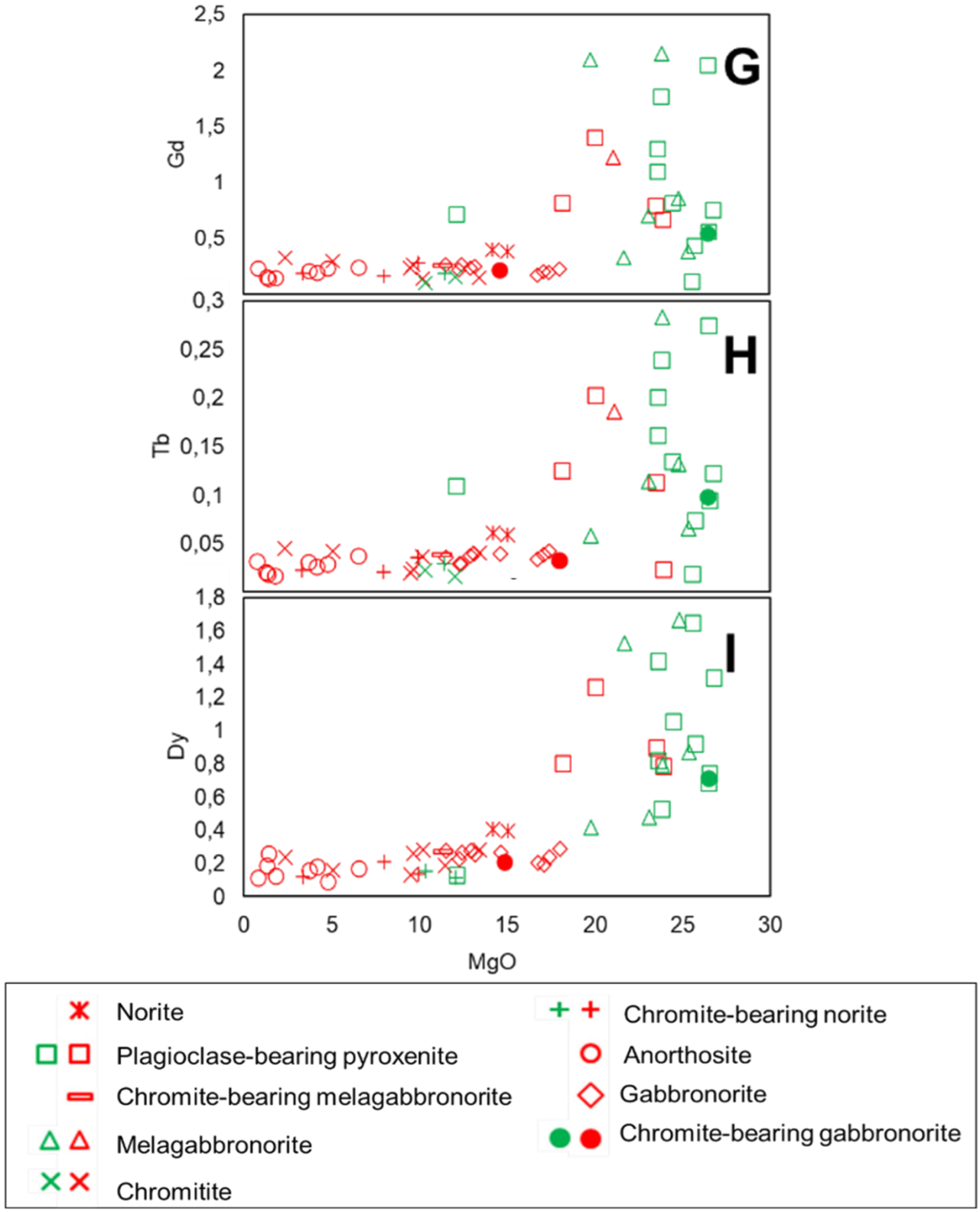

Figure 28: Continued

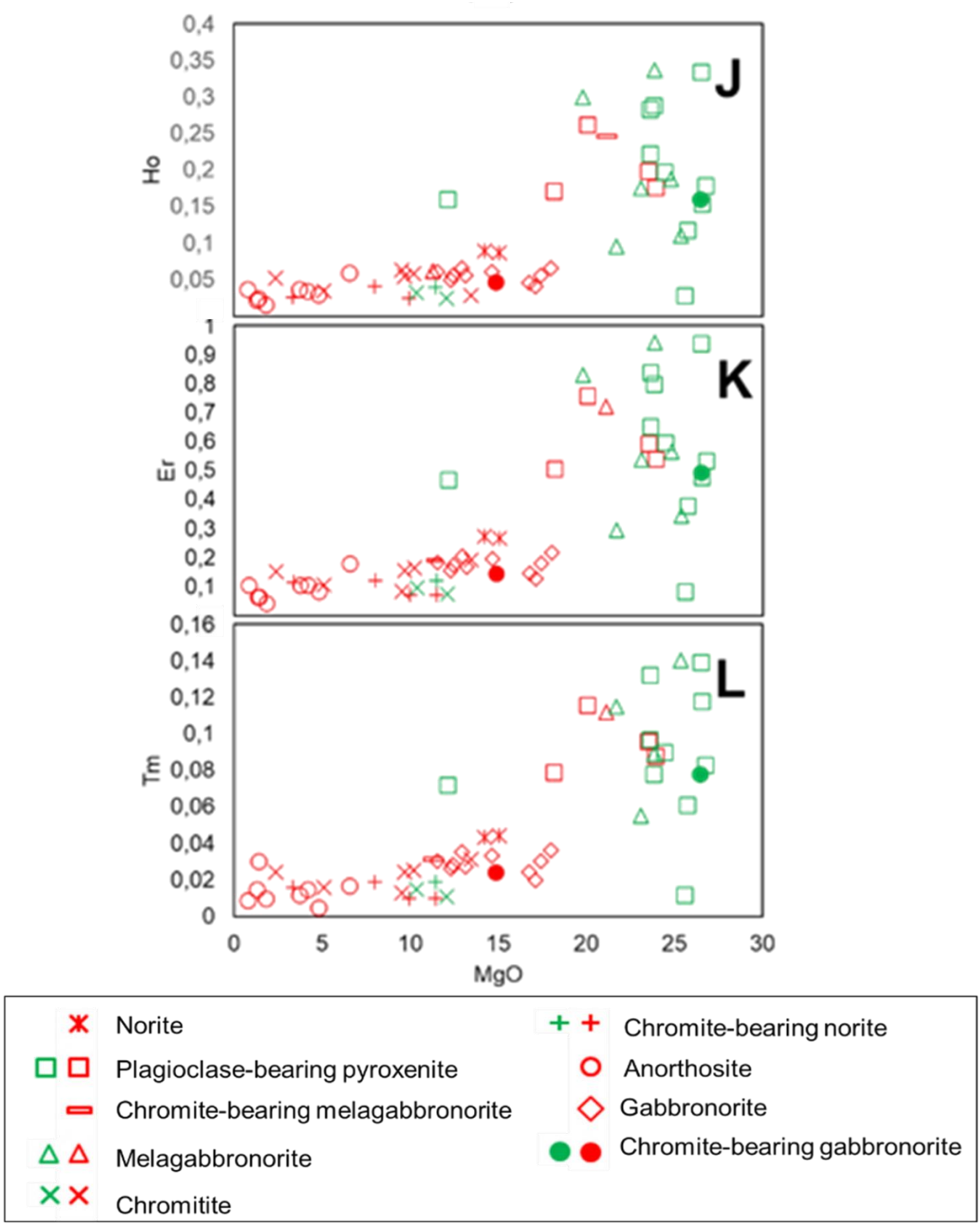

Figure 28: Continued

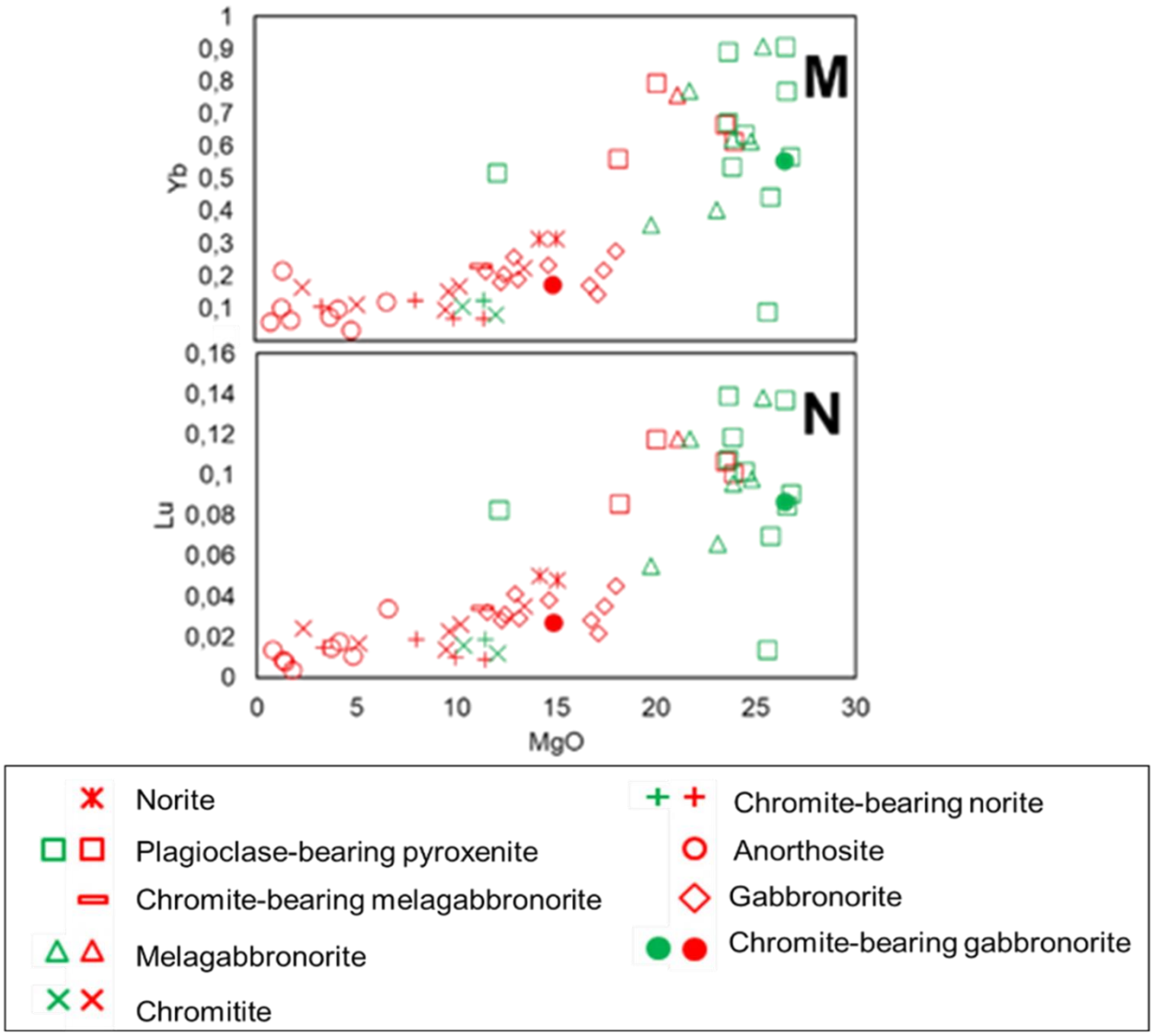

Figure 28: Continued

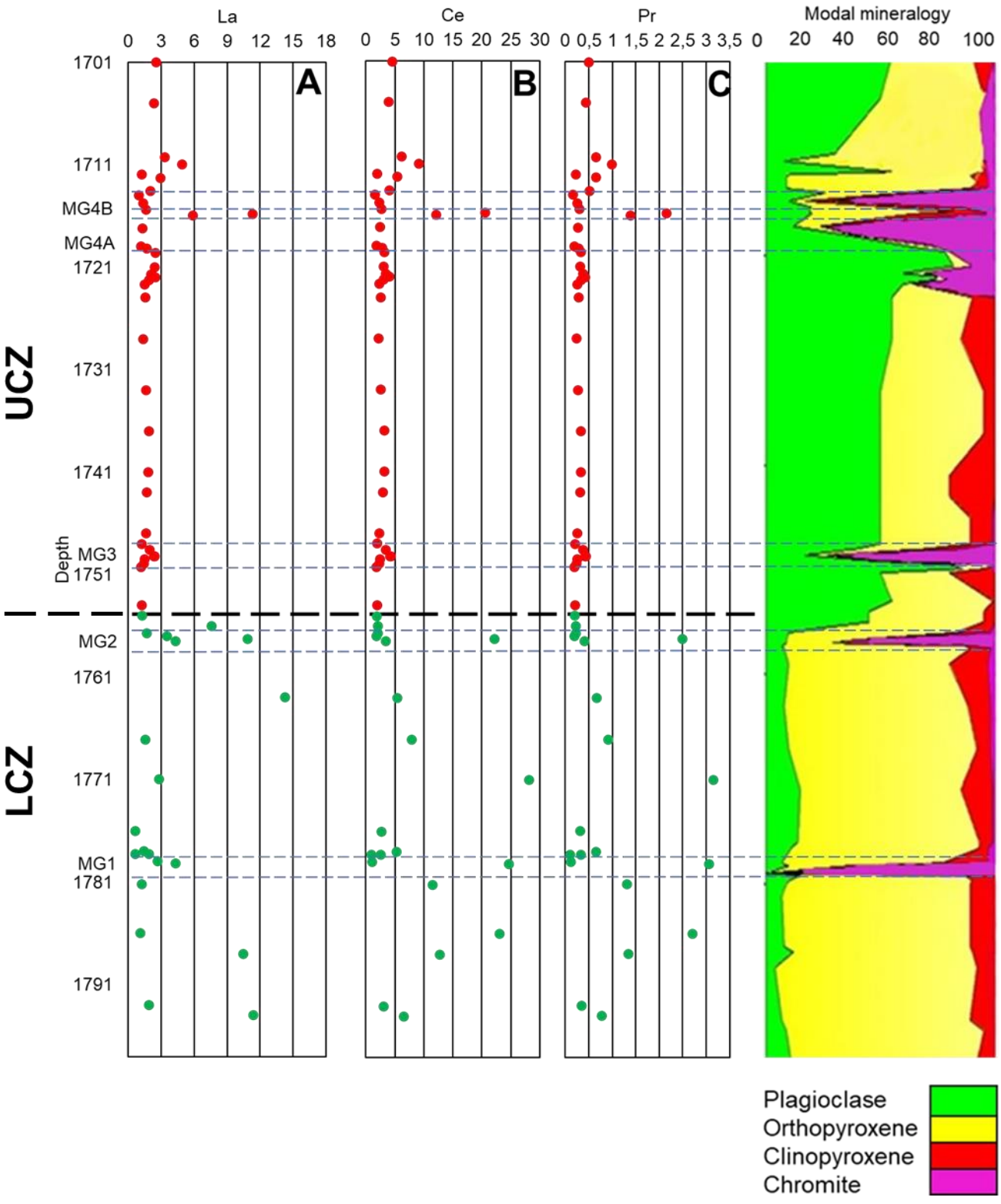

Figure 29: Whole-rock REE vs depth along with modal mineralogy (Red = UCZ, Green = LCZ). Dashed blue lines indicate extent of chromitite layers.

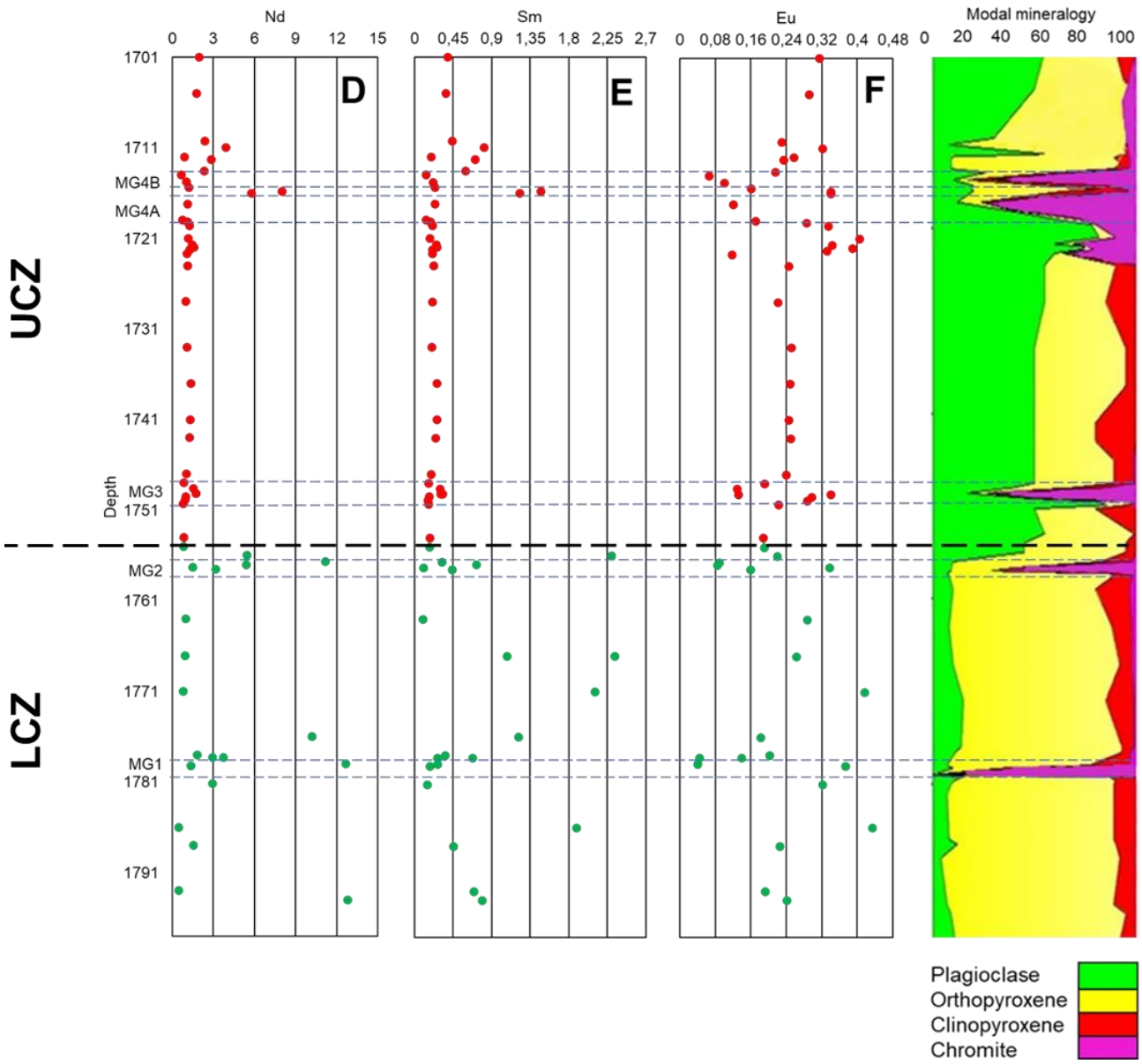

Figure 29: Continued

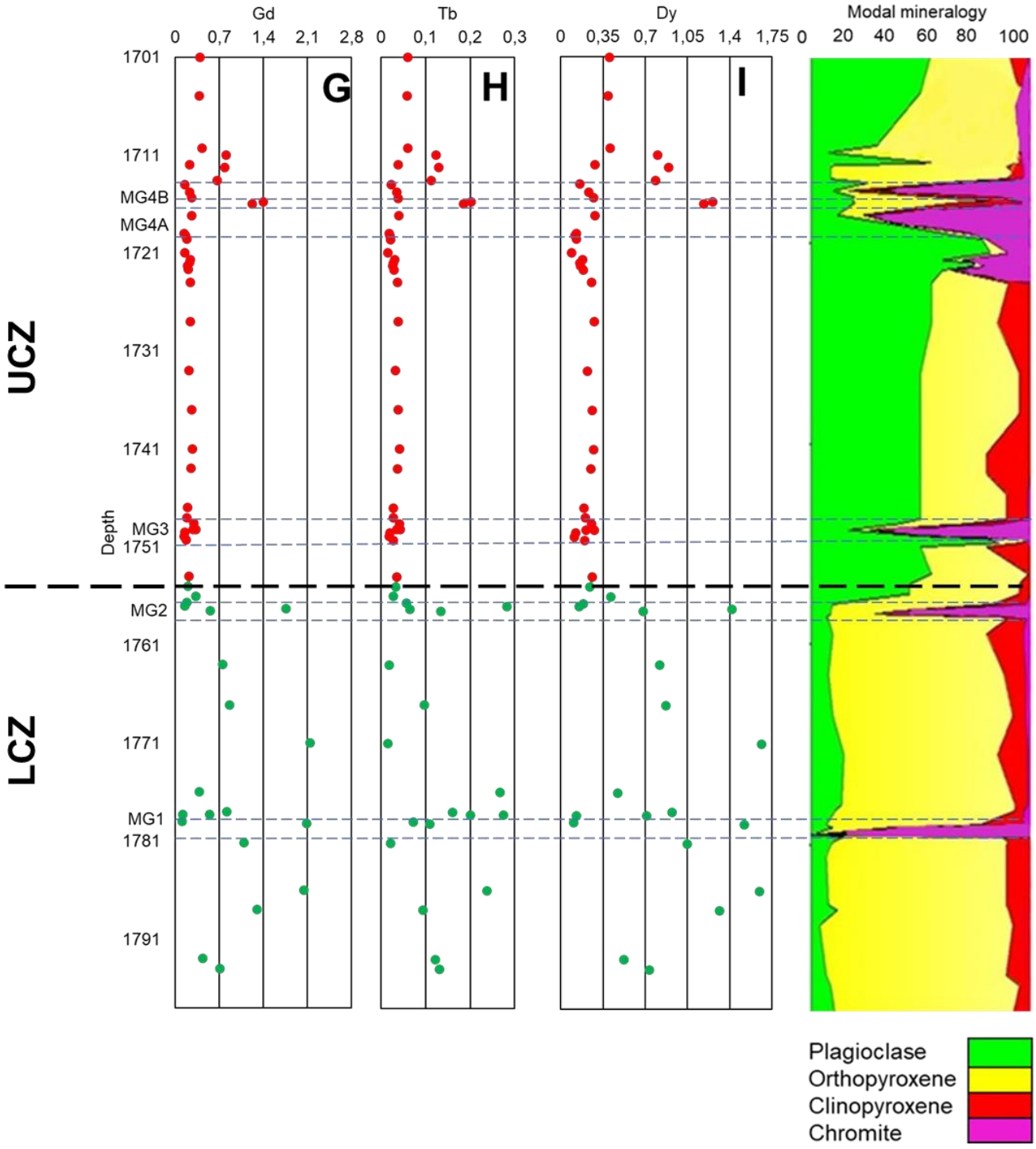

Figure 29: Continued

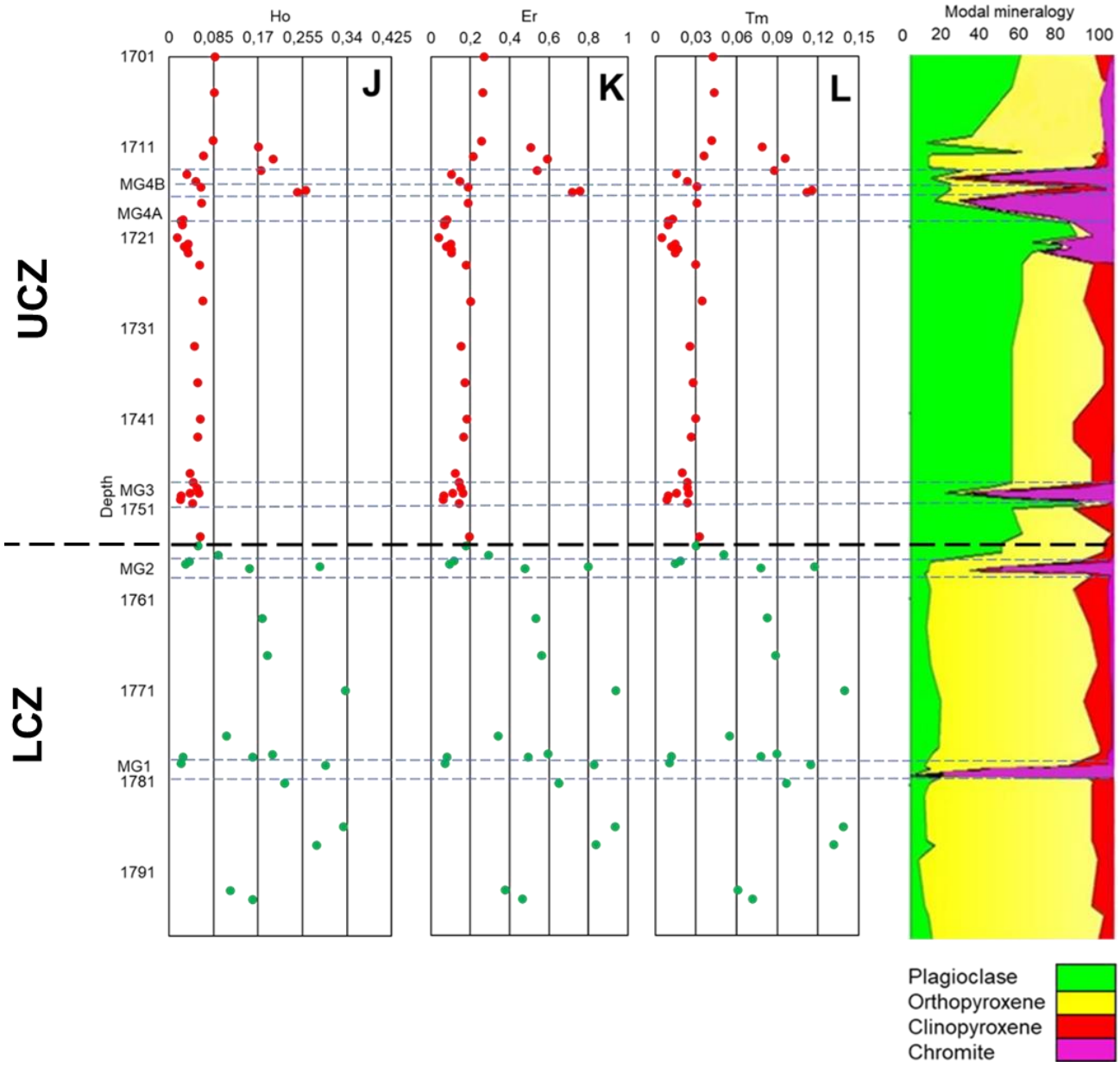

Figure 29: Continued

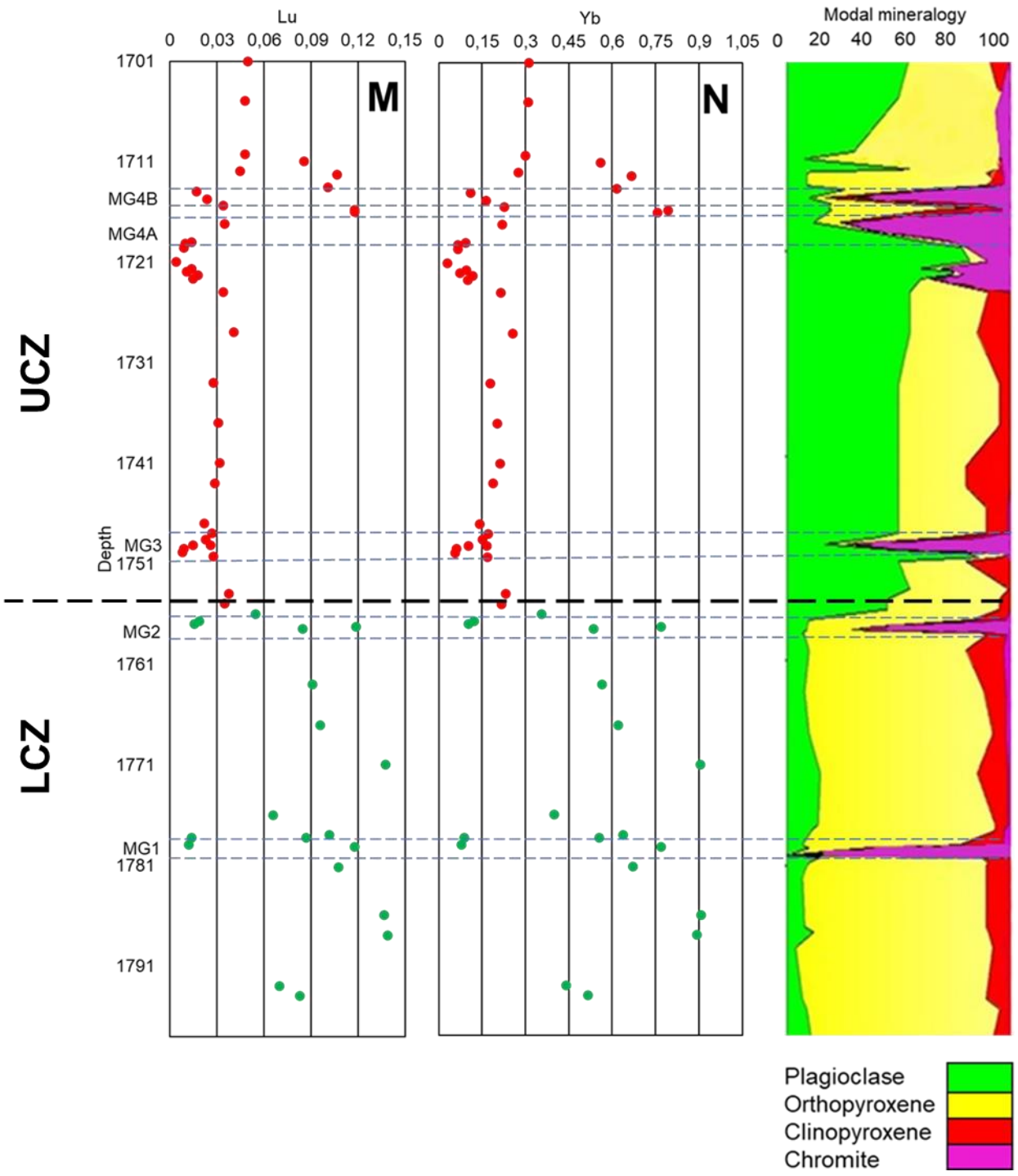

Figure 29: Continued

3.5. Plagioclase mineral chemistry

Plagioclase compositional data are presented in Appendix D and all the analysed spots are plotted against depth in Figure 31. Average An% = 100*Ca/(Ca+Na+K) is plotted against depth in Figure 32, with error bars representing 2σ-standard deviations.

The entire UCZ-LCZ study interval displays conspicuous An% variations. An% averages 72.21 ± 2.15%, varying between 50.92% and 87.44% throughout the entire study interval. Plagioclase An% in the UCZ averages 82.10 ± 1.90%, varying between 71.88% and 87.44%, whereas it averages 73.58 ± 2.60%, varying between 50.92% and 84.41%, in the LCZ. Plagioclase compositional data of the UCZ-LCZ study interval are illustrated by the molar proportion (Ca-Na-K) ternary plot (Fig 30), revealing a range of plagioclase compositions within the labradorite (An_{50-70}) and bytownite (An_{70-90}) fields. The insert in Figure 29 illustrates a comparison with Kottke-Levin (2011) for a corresponding stratigraphic level in the Eastern limb, revealing similar plagioclase compositions.

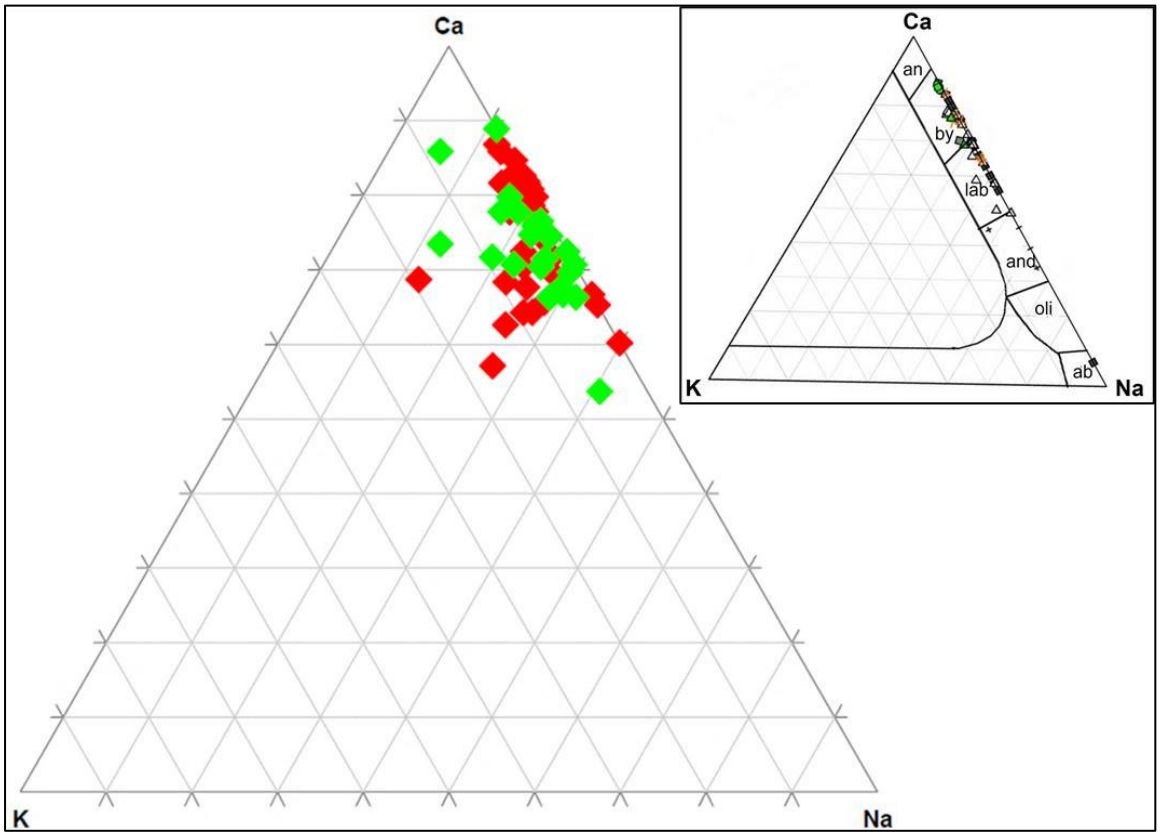

Figure 30: Molar proportion (Ca-Na-K) ternary plot displaying average plagioclase compositional range for all the analysis spots (Red = UCZ, Green = LCZ). Insert makes a comparison to Kottke-Levin (2011).

Substantial scattering of analysed points is observed in the LCZ, in comparison to the UCZ (Fig 30). Scattered points at the same depth indicate variation in An% within a sample in both the LCZ and UCZ (Fig 31). Points analysed on lithologies having mafic compositions are more scattered than points analysed on feldspathic lithologies, which is probably a reflection of the intercumulus nature of plagioclase in the mafic lithologies. For instance, there is a greater degree of An% variation within samples throughout the LCZ, which is entirely made up of plagioclase-bearing pyroxenite, melagabbronorite and to a lesser extent chromitite. The UCZ is diverse in terms of lithologies, with gabbronorite being the most abundant lithology. From the base of the UCZ up to a depth of 1719 m, lithologies containing felsic compositions are abundant, displaying an undeviating linear trend in intra-sample An% variation up the stratigraphy, indicated by restricted scattering of analysed points in Figure 30. From 1719 m to 1715 m plagioclase-bearing pyroxenite along with chromitite are encountered in the UCZ interval, which disturb the linear trend indicated by slight scattering of the analysed points (Fig 31).

An upward increase in the plagioclase An% in the LCZ, from the base of the study interval at depth 1797 m having a value of 64.7%, to the top at depth 1756.70 m, having a value of 84.41%. From the base at depth 1797 m, An% increases from 64.7% to 80% at depth 1794 m. This is followed by a decrease to 67.81% at 1793 m. A slight increase is encountered between depth 1793 m and 1780 m, with An% averaging 69.83%. This is succeeded by the largest decrease in the entire LCZ interval, with An% decreasing to 50.92% at depth 1779.20 m, coinciding with the MG1 chromitite layer (Fig 31). Another slight increase follows between 1778 m and 1757.50 m, with An% averaging 76.78%. Another reversal is encountered at 1756.70 m, with An% increasing to 84.41% followed by a decrease to 69.57% An%, at depth 1756 marking the top of the LCZ interval. This coincides with the MG2 chromitite layer (Fig 31). In summary, lithologies below the MG1 reveal a lower An% at 71.68% in comparison to lithologies above the MG1 at 78.83%, with the MG2 hanging wall revealing values that are >80%.

At the base of the UCZ from a depth of 1755 m to 1749 m, an initial increase in An% is observed from previously low values in the LCZ (Fig 31). The average An% is fairly constant at this depth range averaging 86.81%. This is followed by a slight decrease, with An% decreasing to an average 85.56% between depth 1749.50 m and 1747 m,

coinciding with the MG3 chromitite layer (Fig 31). Another reversal is observed between depth 1747 m and 1741 m, wherein a slight increase in An% is observed averaging 85.94%. This is followed by a decrease between 1741 m and 1722.70 m, with An% averaging 84.99%, denoting an undeviating trend over an interval of almost 20 m, which is the longest in the entire UCZ-LCZ study interval (Fig 31). A further decrease in An% is observed between depth 1722.70 m and 1721.70 m, with An% averaging 84.41%. This is followed by a slight increase between depth 1721 m and 1719 m, with An% averaging 85.60%. A significant decrease is encountered at depth 1719 m and 1712 m, with An% dropping to an average of 73.04%, coinciding with the appearance of the MG4A and MG4B chromitite layers which are found sandwiched between plagioclase-bearing pyroxenite, chromite-bearing melagabbronorite and melagabbronorite (Fig 31). Another reversal is observed at depth 1712 m to 1711 m, with An% averaging 83.42% followed by another drop to 71.88% at depth 1710.30 m. At the top of the UCZ interval another increase in An% (84.42%) is observed.

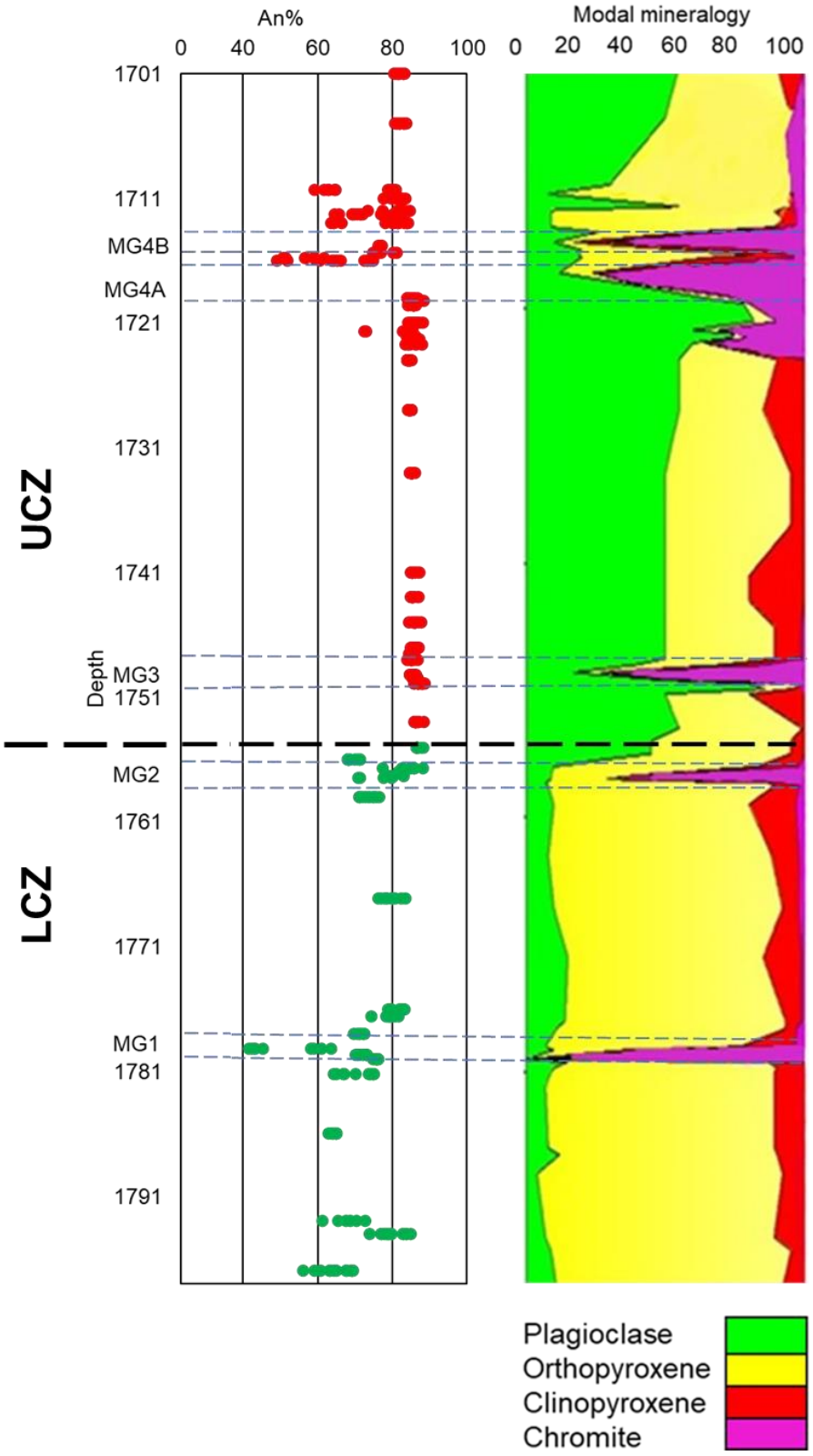

Figure 31: Plagioclase An% analysed spots against depth along with modal mineralogy. (Red = UCZ, Green = LCZ).

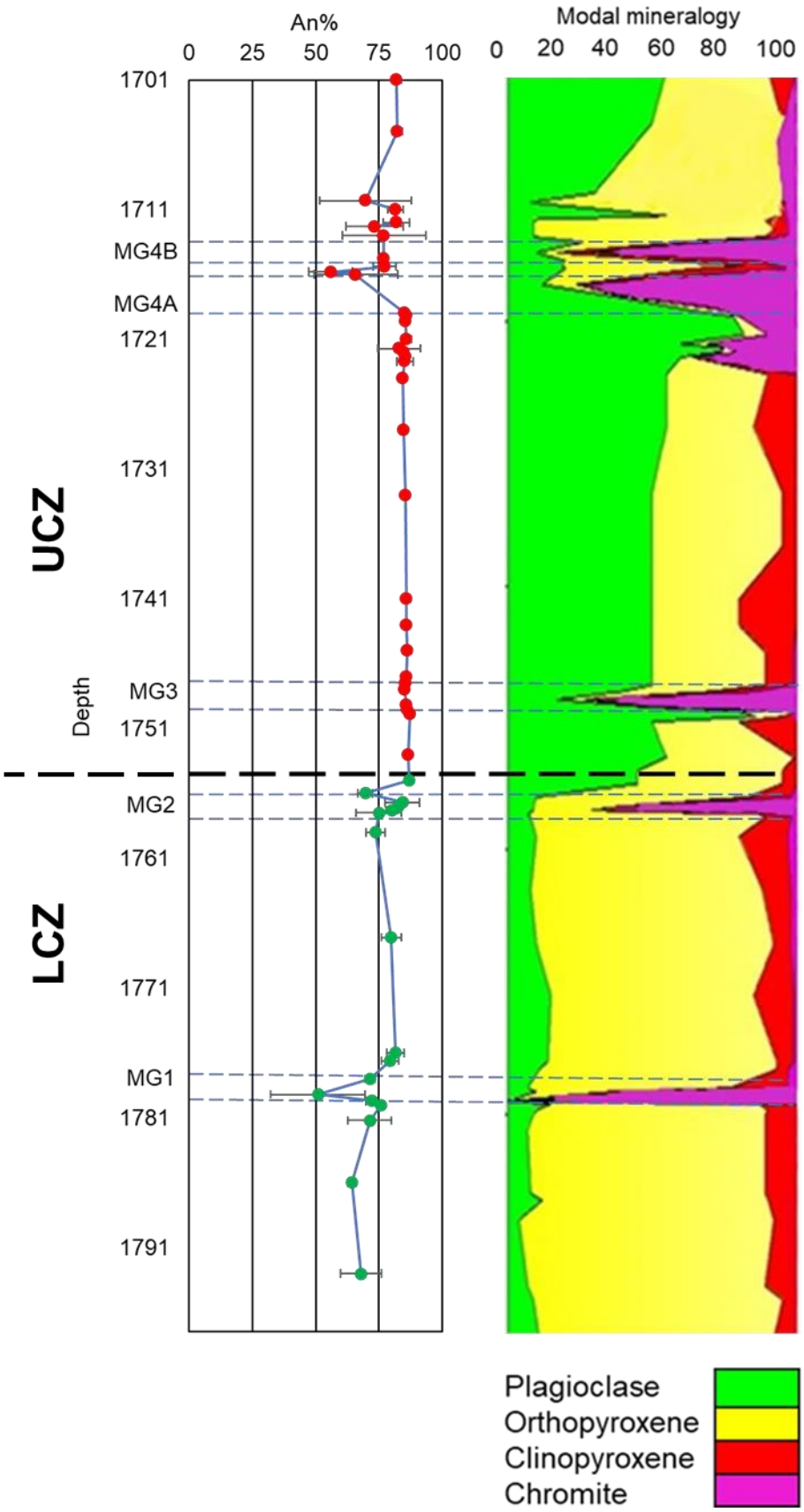

Figure 32: Average plagioclase An% against depth along with modal mineralogy. Error bars represent 2σ-standard deviation. Note that error bars are obscured by symbols in some silicate lithologies especially in the UCZ. (Red circles = UCZ, Green circles = LCZ).

3.6. Plagioclase strontium isotope geochemistry

Strontium isotopic data are presented in Appendix E and in Table 12. The in-situ initial $^{87}Sr/^{86}Sr$ ratio (hereafter Sr_i) of plagioclase crystals, recalculated to 2054.4 Ma (Scoates and Friedman, 2008) displays slight variability across the UCZ-LCZ study interval (Fig 33, 34 and 35).

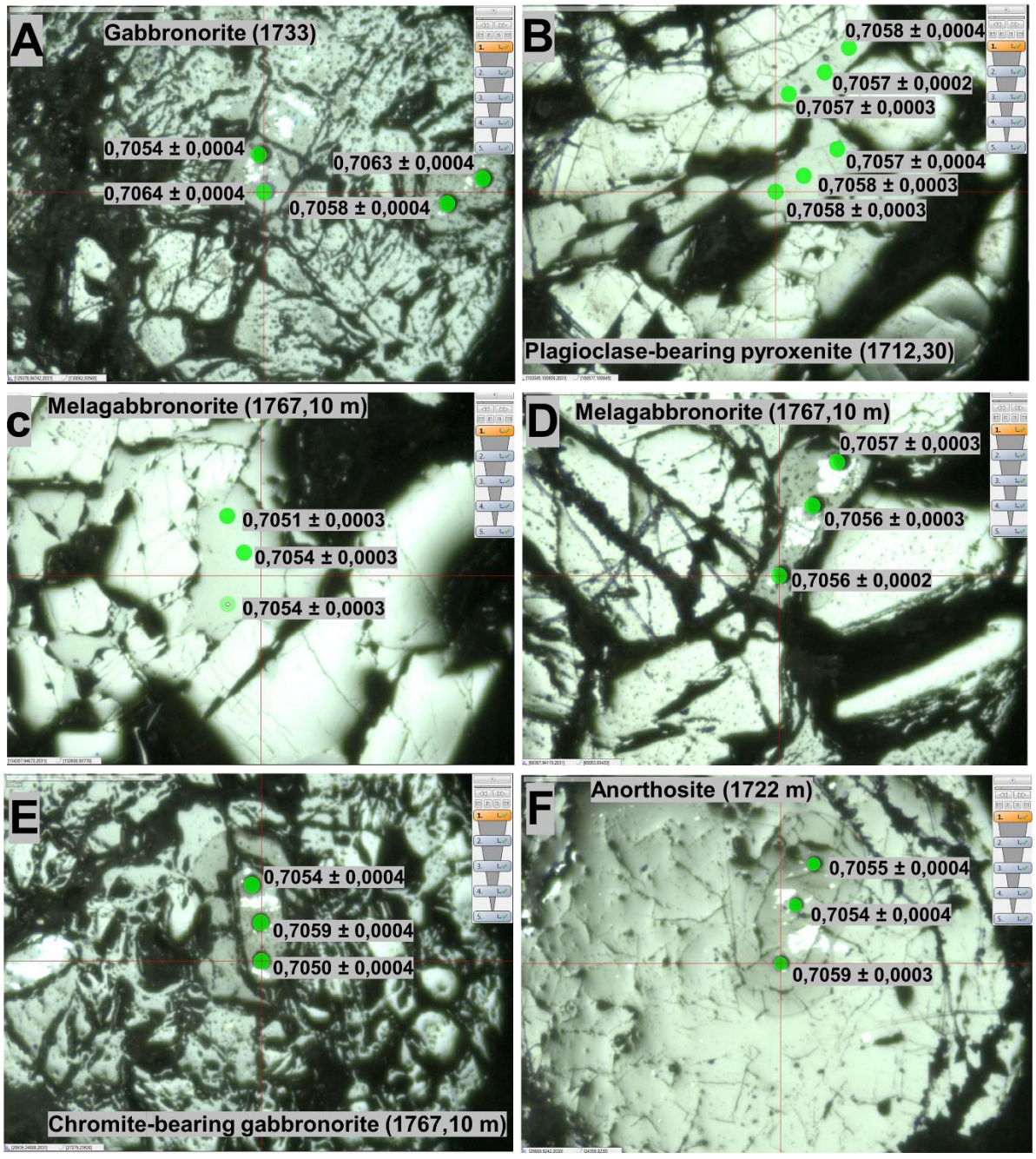

Figure 33: A to F. Selected reflected light images of plagioclase and corresponding Sri measurements, with 2σ-standard errors.

Sr_i measurements in the LCZ averages 0.7054 ± 0.0004, ranging between 0.7034 and 0.7066. Sr_i measurements in the UCZ averages 0.7059 ± 0.0003, ranging between a minimum of 0.7047 and a maximum of 0.7072. The UCZ is, on average, slightly more radiogenic than the LCZ. Errors for individual Sr_i measurements are expressed as 2σ-standard errors.

From the base of the LCZ interval at depth 1793 m, the Sr_i value averages 0.7056. An increase to an average value of 0.7058 at depth 1786 m follows, which is the highest value throughout the entire LCZ interval. A decrease to an average value of 0.7050 at depth 1779 m follows, coinciding with the MG1 chromitite layer. A significant increase to a value of 0.7057 is observed at depth 1776 m, succeeded by a decrease to a value of 0.7054 at depth 1767.10 m, further dropping to a value of 0.7053 at depth 1757.55 m. A slight increase to 0.7055 is encountered at depth 1757 m. MG2 attains an average value of 0.7047, decreasing to the lowest value in the entire LCZ interval. Marking the top of the LCZ interval, an increase to a value of 0.7055 is observed going into the UCZ. Average Sr_i values in the LCZ are plotted against depth in Figure 34 along with error bars representing 2σ-standard deviations. Samples at the level of the chromitite layers display the most variability as exemplified by the length of errors bars, and the spread in Sr_i of individual spots (Fig 34).

From the base of the UCZ at depth 1755 m, the Sr_i value averages 0.7056, which increases to the highest average value in the entire UCZ interval at depth 1750 m attaining an average value of 0.7066 just below MG3. This is followed by a decrease to the lowest Sr_i value in the UCZ interval, averaging 0.7055 at depth 1749 m. This coincides with the MG3 chromitite layer. A slight increase to an average value of 0.7059 at depth 1748.60 m follows. The Sr_i stays relatively stable between depth 1748 m and 1722.30 m, with an average value of 0.7059. Minor fluctuations are observed over this range of about 30 m, with an overall increase from 0.7059 at 1748 m to 0.7060 at 1722.30 m. Sr_i decreases to a value of 0.7056 at depth 1722 m followed by an increase to 0.7060 at 1721.70 m. This is followed by another decrease to a value of 0.7058 at 1719 m, coinciding with the MG4A chromitite layer. Another increase to a value of 0.7062 follows at depth 1715.40 m, followed by a decrease to a value of 0.7057 at depth 1712 m, coinciding with the MG4B chromitite layer. A slight increase follows, averaging 0.7059 at depth 1711 m, followed by a decrease to 0.7058 at 1705 m, increasing to 0.7062 at depth 1701 m, marking the top of the UCZ interval.

Table 12 reveals that there is no significant evidence for intercrystalline nor intracrystalline Sr_i variation in most of the measured samples throughout the study interval, with analysed spots displaying similar Sr_i values and overlapping errors (Table 10). However, variations are detected between chromitite layers and silicate lithologies of the LCZ, with Sr_i measurements in these chromitite layers revealing a lower Sr_i average value (also Fig 34) and large variations in the Sr-isotopic composition for individual measured spots (also Fig 33). For example, all the silicate lithologies in the LCZ have an average Sr_i value of 0.7055 ± 0.0003. This is dissimilar to the three measurements that were taken in two crystals of the MG1 layer (highlighted in yellow in Table 12). Two measurements in crystal 2 reveal the same value of 0.7067 ± 0.0016, whilst a single measurement in crystal 1 reveals a value of 0.7034 ± 0.0014 (see Table 10). MG2 has a value of 0.7041 ± 0.0013 (measured values are highlighted in Table 10), which is dissimilar to measured values in adjacent lithologies. Chromitites reveal larger uncertainties than silicates, proving isotopic variation between the silicates and the chromitites (Fig 34 and 35). This is not the case in the UCZ, with the Sr_i value remains consistent throughout this interval and having overlapping errors.

Table 12: Comparison between core and rim analysed values in the entire UCZ-LCZ interval

Depth	Sample	Crystal	Core	2σ-SE	Rim 1	2σ-SE	Rim 2	2σ-SE
1701	MM1	1	0,7073	0,0008	0,7073	0,0008	0,7063	0,0008
		2	0,7060	0,0003	0,7057	0,0005	0,7057	0,0003
1705	MM2	1	0,7059	0,0004	0,7064	0,0004		
		2	0,7055	0,0003	0,7052	0,0003		
1710	MM3	1	0,7057	0,0005	0,7066	0,0005	0,7057	0,0005
1711	MM4	1	0,7056	0,0003	0,7065	0,0004		
		2	0,7060	0,0004	0,7061	0,0003		
		3	0,7058	0,0004	0,7060	0,0004		
1712	MM5	1	0,7058	0,0002	0,7061	0,0002		
		2	0,7057	0,0002	0,7064	0,0002		
		3	0,7058	0,0002	0,7061	0,0002		
1712	MM6	1	0,7059	0,0002	0,7057	0,0004		
		2	0,7058	0,0002	0,7059	0,0004	0,7057	0,0004
		3	0,7059	0,0002	0,7059	0,0004		
1713	MM7	1	0,7056	0,0004	0,7060	0,0004	0,7059	0,0004
1714	MM8	1	0,7056	0,0004	0,7064	0,0004		
1715	MM10	1	0,7060	0,0004	0,7058	0,0004	0,7060	0,0004

Table 12: Continued

Depth	Sample	Crystal	Core	2σ-SE	Rim 1	2σ-SE	Rim 2	2σ-SE
1715	MM11	1	0,7057	0,0004	0,7058	0,0004	0,7061	0,0004
1716	MM12	1	0,7048	0,0004	0,7064	0,0004	0,7066	0,0004
		2	0,7065	0,0004	0,7071	0,0004		
1717	MM14	1	0,7063	0,0004	0,7056	0,0004	0,7063	0,0004
1718	MM15	1	0,7058	0,0004				
		2	0,7061	0,0004				
1719	MM16	1	0,7059	0,0004	0,7058	0,0004	0,7060	0,0004
		2	0,7056	0,0004	0,7057	0,0004	0,7058	0,0004
		3	0,7059	0,0004	0,7061	0,0004	0,7057	0,0004
1719	MM17	1	0,7058	0,0004	0,7056	0,0004	0,7059	0,0004
		2	0,7056	0,0004	0,7059	0,0004	0,7057	0,0004
1721	MM19	1	0,7057	0,0004	0,7058	0,0004	0,7063	0,0004
1722	MM20	1	0,7063	0,0004	0,7060	0,0004	0,7059	0,0004
		2	0,7060	0,0004	0,7061	0,0004	0,7061	0,0004
		3	0,7060	0,0004	0,7058	0,0004		
1722	MM21	1	0,7054	0,0004	0,7060	0,0004	0,7060	0,0004
		2	0,7054	0,0004	0,7054	0,0004	0,7058	0,0004
		3	0,7056	0,0004	0,7059	0,0004	0,7053	0,0004
1722	MM22	1	0,7059	0,0004				
1724	MM24	1	0,7061	0,0004	0,7062	0,0004		
		2	0,7058	0,0004	0,7064	0,0004		
1728	MM25	1	0,7059	0,0004	0,7060	0,0004	0,7061	0,0004
		2	0,7061	0,0004	0,7051	0,0004	0,7056	0,0004
		3	0,7055	0,0004	0,7061	0,0004		
		1	0,7064	0,0004	0,7055	0,0004	0,7058	0,0004
1733	MM26	2	0,7060	0,0004	0,7059	0,0004	0,7064	0,0004
1741	MM28	1	0,7055	0,0004	0,7059	0,0004		
		2	0,7053	0,0004	0,7059	0,0004	0,7062	0,0004
1743	MM29	1	0,7058	0,0004	0,7054	0,0004	0,7058	0,0004
		2	0,7063	0,0004	0,7060	0,0004	0,7055	0,0004
		3			0,7063	0,0004	0,7063	0,0004
1745	MM30	1	0,7059	0,0004	0,7056	0,0004	0,7058	0,0004
		2	0,7060	0,0004	0,7054	0,0004	0,7058	0,0004
		3	0,7065	0,0005	0,7055	0,0004	0,7060	0,0004
1747	MM31	1	0,7058	0,0005	0,7053	0,0004	0,7058	0,0004
		2	0,7064	0,0005	0,7056	0,0005	0,7060	0,0005
1748	MM32	1	0,7060	0,0005	0,7061	0,0005		
		2	0,7060	0,0005	0,7060	0,0005		
1748	M33	1	0,7059	0,0005	0,7066	0,0005	0,7106	0,0005
		2	0,7062	0,0005	0,7065	0,0005	0,7066	0,0005
1749	MM34	1	0,7056	0,0005	0,7062	0,0005		
1749	MM35	1	0,7056	0,0005		0,0005		
1750	MM36	1	0,7066	0,0005		0,0005		
1753	MM39	1	0,7052	0,0004	0,7056	0,0004	0,7068	0,0005

Table 10: Continued

Depth	Sample	Crystal	Core	2σ-SE	Rim 1	2σ-SE	Rim 2	2σ-SE
		2	0,7057	0,0004	0,7060	0,0004	0,7056	0,0004
		3			0,7057	0,0004	0,7059	0,0004
1755	MM41	1			0,7056	0,0004		
1756	MM42	1	0,7056	0,0005				
		2	0,7056	0,0005				
1757	MM43	1	0,7041	0,0005				
1757	MM44	1	0,7055	0,0004				
1758	MM46	1	0,7055	0,0004	0,7050	0,0004	0,7057	0,0004
1767	MM49	1	0,7058	0,0004	0,7057	0,0004		
		2	0,7053	0,0005	0,7054	0,0005	0,7053	0,0005
		3	0,7055	0,0005	0,7054	0,0005	0,7052	0,0005
1776	MM51	1	0,7056	0,0005	0,7059	0,0005		
		2	0,7057	0,0005	0,7056	0,0005	0,7057	0,0005
1778	MM54	1	0,7034	0,0006				
		2	0,7067	0,0003	0,7067	0,0003		
1780	MM57	1	0,7053	0,0002	0,7055	0,0002		
1781	MM59	1	0,7052	0,0002				
		2	0,7053	0,0002	0,7056	0,0002	0,7054	0,0002
		3	0,7054	0,0002	0,7055	0,0002	0,7058	0,0002
1786	MM60	1	0,7059	0,0003	0,7056	0,0002		
		2	0,7058	0,0003				
		3	0,7057	0,0003				
1793	MM63	1	0,7059	0,0004	0,7056	0,0003	0,7053	0,0004
		2	0,7061	0,0003	0,7052	0,0006		

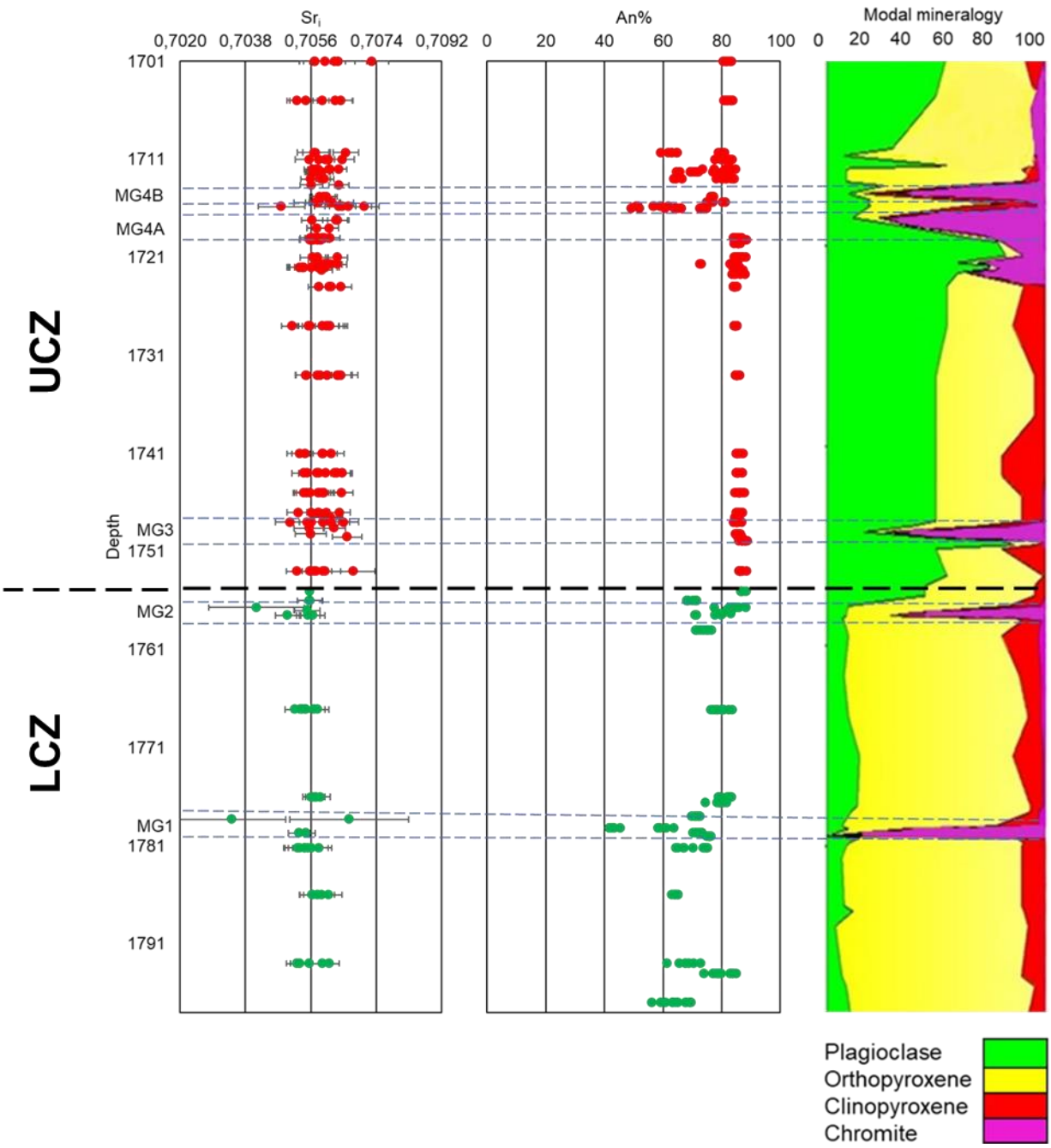

Figure 34: Sri and An% in plagioclase analysed spots against depth along with modal mineralogy. Note error bars representing 2σ-standard error for Sri (Red circles = UCZ, Green circles =LCZ).

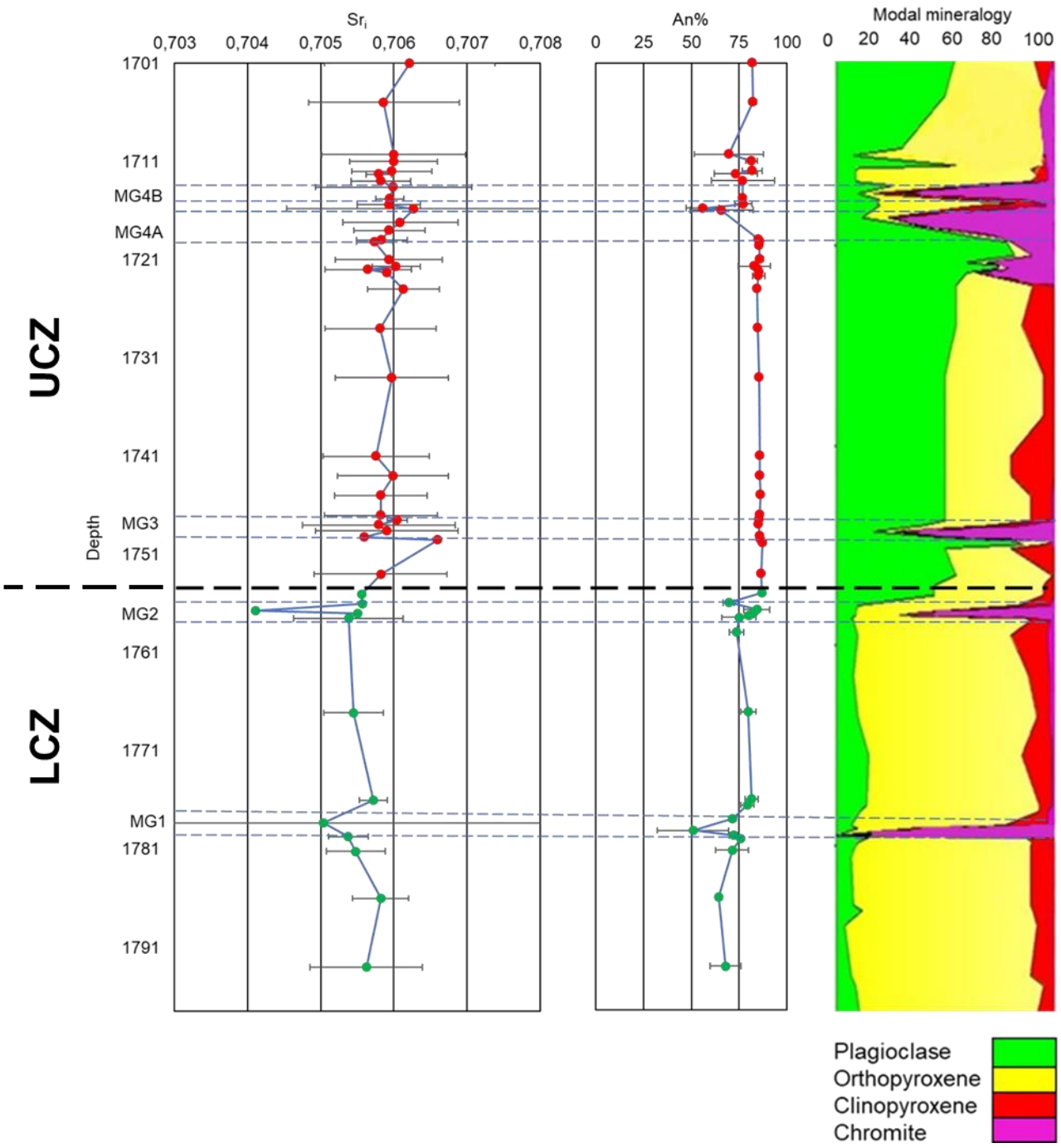

Figure 35: Average Sri and An% in plagioclase crystals against depth along with modal mineralogy. Error bars representing 2σ-standard deviations. Note that some error bars are obscured by symbols (Red circles = UCZ, Green circles = LCZ).

3.7. Chromite mineral chemistry

Chromite compositional data are presented in Appendix F. A total of 30 chromite crystals were analysed for MgO, Al_2O_3, TiO_2, Cr_2O_3 and Fe_2O_3, using energy dispersive X-ray spectrometry. Only 3 crystals were selected for analysis per chromitite layer (MG1-4), along with 3 chromite crystals from adjacent chromite-bearing lithologies (depending on the presence of chromite crystals) above (hanging wall) or below (footwall) the respective chromitite layers. Analysed spots in chromite crystals display slight compositional variations from rim to core in both the chromitite layers and the chromite-bearing lithologies (Fig 38). Compositional zoning (intracrystalline variation) is revealed by measured points across the surface of chromite crystals, with analysed points either increasing or decreasing in comparison to the previous analysed point. This is indicated by the molar Cr# = 100*Cr/(Cr+Al) vs Mg# = 100*Mg/(Mg+Fe) plots in Figure 38, with each colour representing a different crystal.

Chromite crystals in the chromitite layers (MG1-4) vary in composition when compared to the chromite-bearing lithologies footwalls and hanging walls (Fig 39). For instance, the chromium number (Cr#) and magnesium number (Mg#) value for crystals in the MG1 chromitite layer is 82.71 and 30.3 on average, respectively. The adjacent footwall averages 85.47 (Cr#) and 23.12 (Mg#). An increase in the Cr# is observed whereas, there is a decrease in Mg#. This relationship is common in all the chromitite layers and adjacent footwalls and hanging walls throughout the study interval, with varying values.

Intercrystalline variations were not detected in the analysed chromite crystals found in both the chromitite layers and their adjacent hanging wall or footwall lithologies. Analysed crystals have a similar pattern when Cr# is plotted against Mg# for all the 3 crystals within the same sample, Cr# vs Mg# almost overlap in Figure 38. Though some slight variations can be detected in some crystals, there is a lack of sufficient evidence to prove the existence of compositional variations amongst the analysed crystals. Cr# (Fig 36) and Mg# (Fig 37) vs depth profiles from this study are compared to Kottke-Levin (2011) for the same stratigraphical interval in the Eastern limb. Cr# values in this study overlap with those of Kottke-Levin (2011), whereas Mg# reveal lower values.

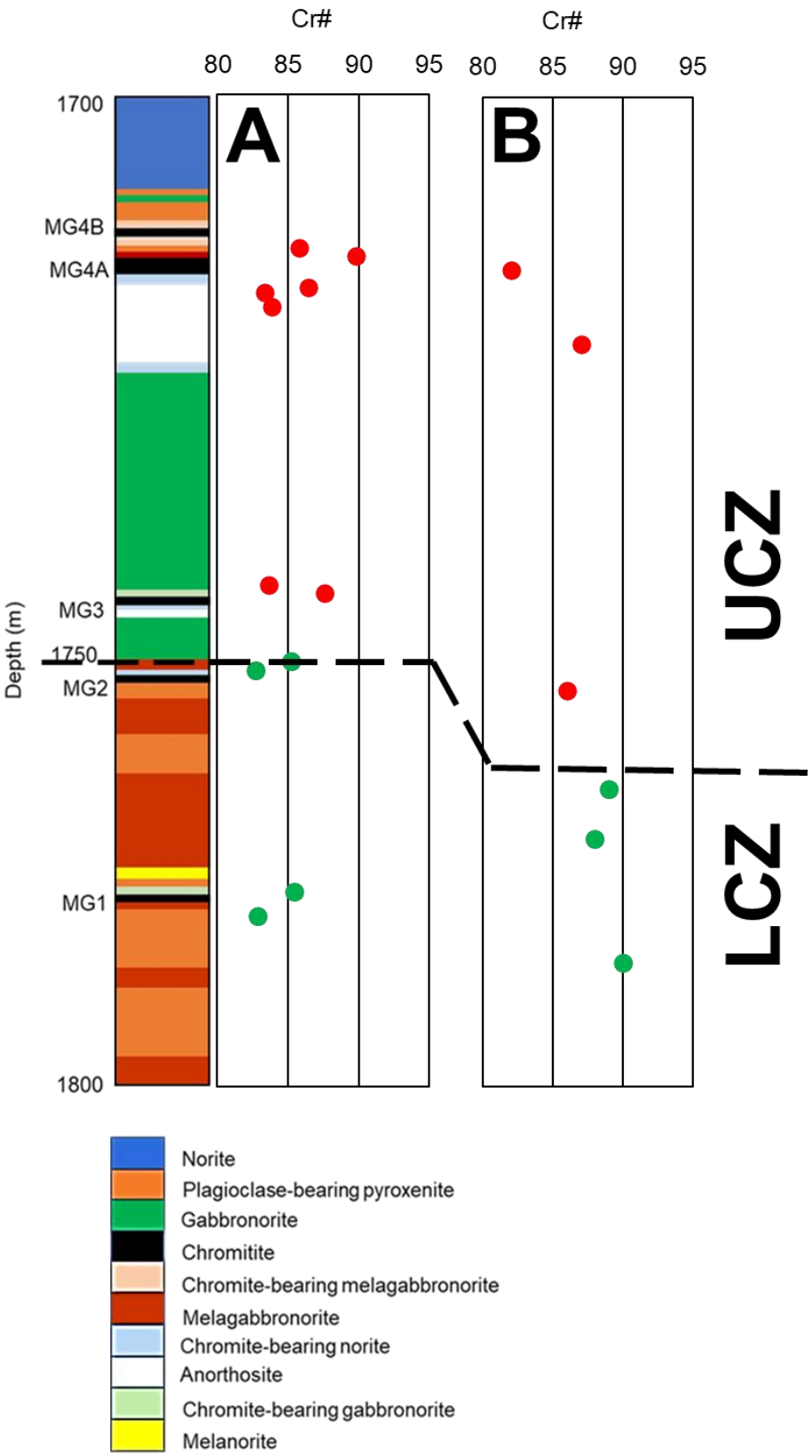

Figure 36: Cr# comparison in (A) this study and (B) Kottke-Levin (2011). (Red circles = UCZ, Green circles = LCZ).

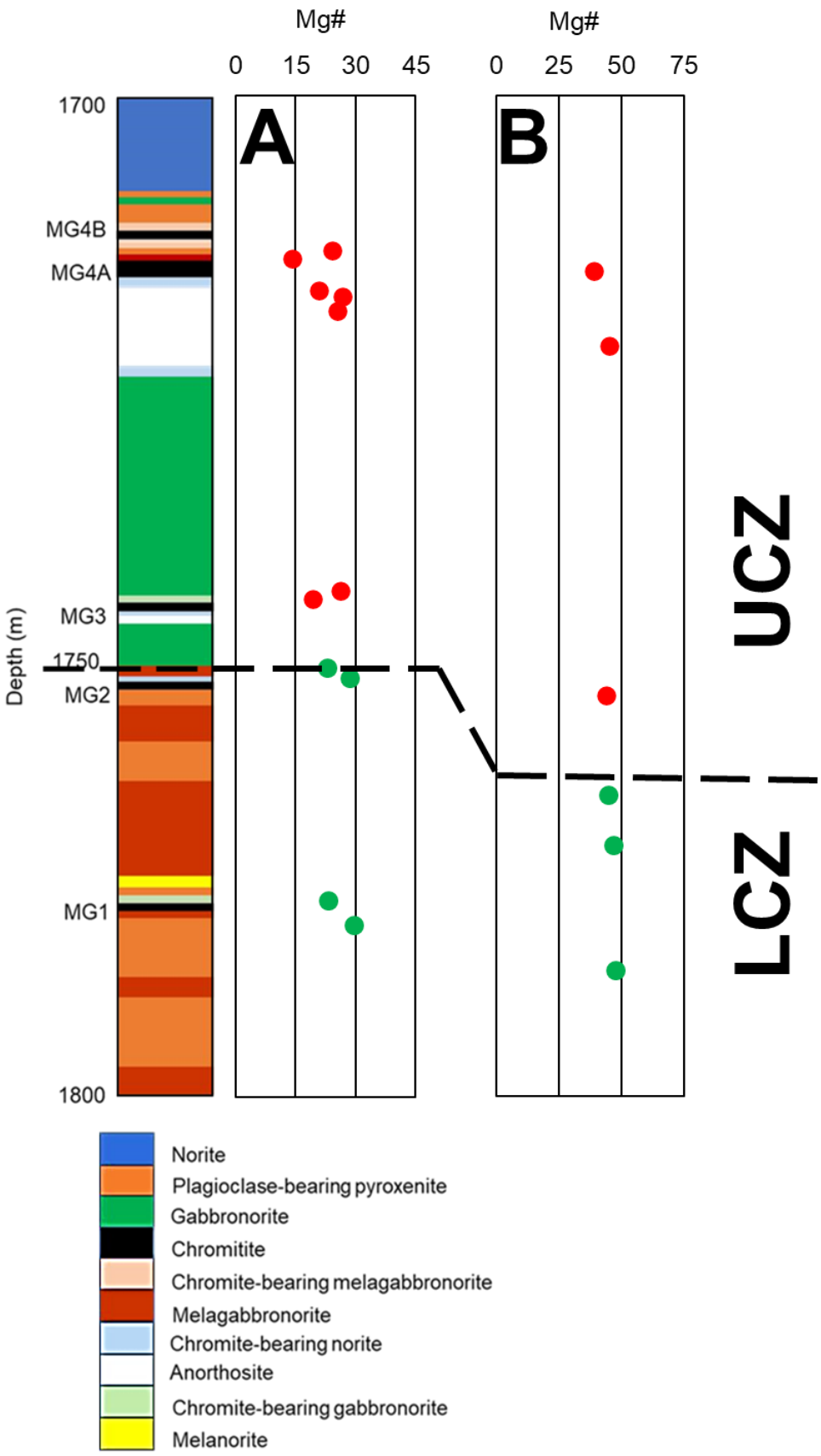

Figure 37: Mg# comparison in (A) this study and (B) Kottke-Levin (2011). (Red circles = UCZ, Green circles = LCZ).

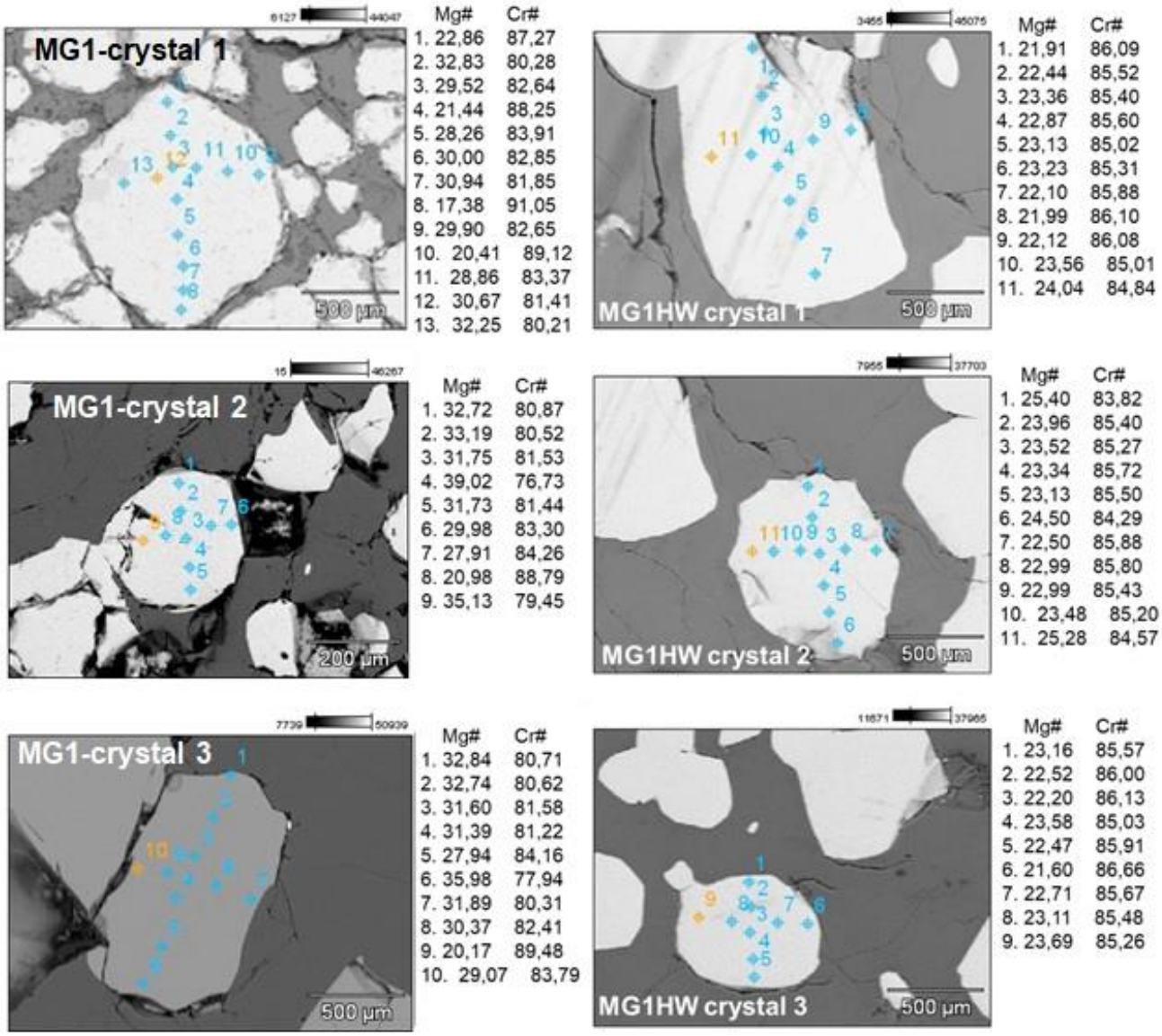

Figure 38: Comparison between MG1 crystals and adjacent hanging wall crystals.

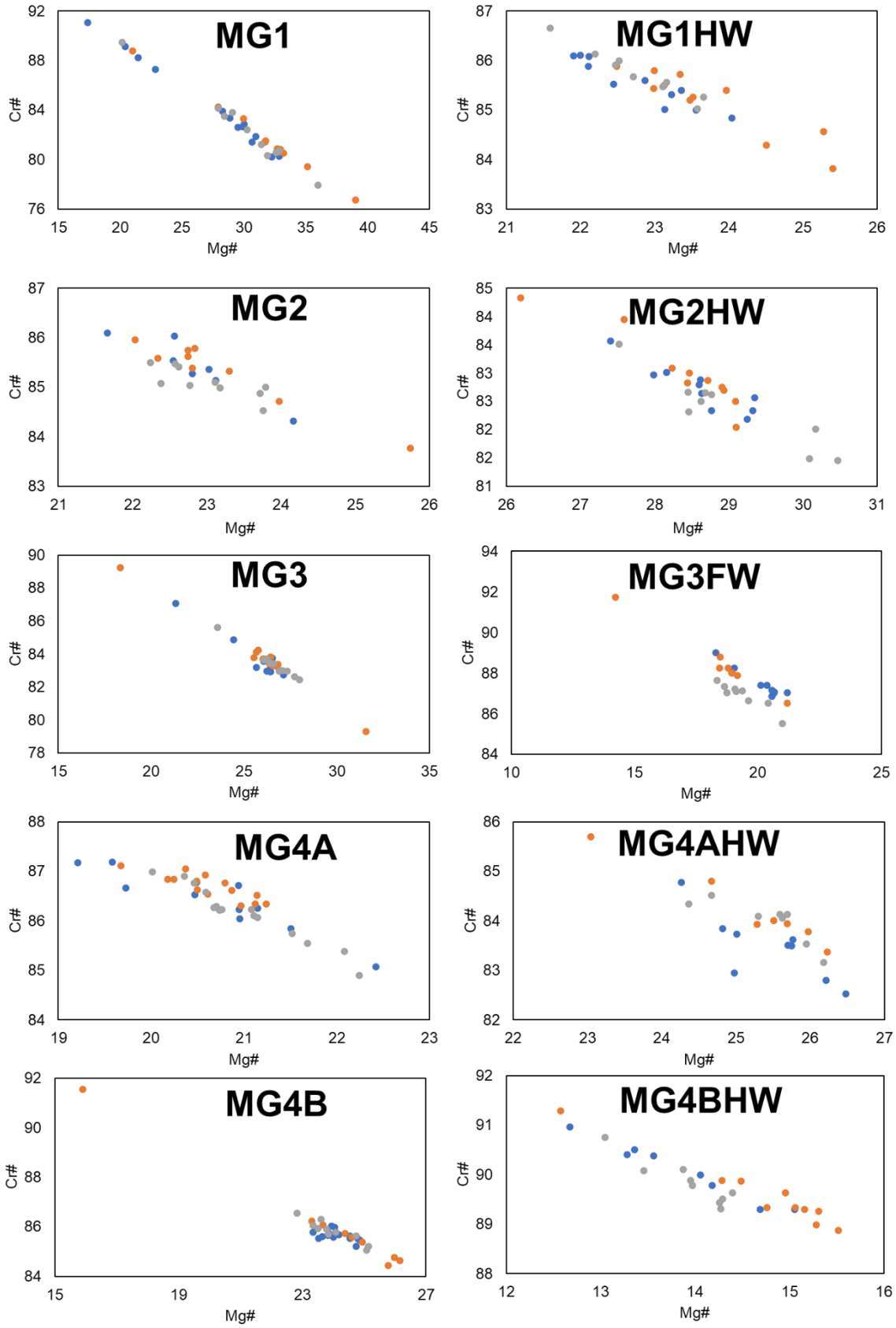

Figure 39: Binary variation diagrams displaying Cr# vs Mg# for the analysed chromite crystals. Note each colour represent a single crystal.

4. Discussion

Numerous Sr isotope studies have been conducted in the CZ of the RLS which focused on the economical parts of the CZ (e.g. Merensky and UG2 units), with the uneconomical parts not given sufficient attention. In this study, plagioclase mineral chemistry (Sr isotope and mineral compositions), chromite mineral chemistry as well as whole-rock geochemistry across the LCZ-UCZ transition are used to infer probable processes operational during emplacement of the CZ. The study aims to (1) investigate the presence or absence of intra- intracrystalline isotopic disequilibrium in plagioclase (2) to investigate differences between the LCZ and UCZ from a geochemical, petrological and Sr isotopic perspective and (3) to refine chromitite formation models using the data obtained over the course of the study. A review of varying chromitite formation models is given below.

Chromitite formation models

The origins of chromitite layers in the BC complex are still a subject of considerable debate, with numerous models having been proposed since the discovery of the intrusion. The classical crystal sorting model remains one of the oldest suggested models for chromitite formation, which entails gravitational sorting of chromite crystals due to density and size variations. Heavier and larger chromite crystals sink to the bottom of the magma chamber, whereas smaller and lighter crystals remain in suspension (Jackson, 1967). However, Campbell (1978) states settling of chromite crystals will be hindered if the settling velocity is surpassed by convection velocity. Irvine (1977) proposed that chromitites form as a result of mixing between resident magma and newly injected primitive magma, which over time drives the hybrid magma into the chromite stability field. Eales and Cawthorn (1996) refuted this stating that mass balance is the main problem with this model as huge volumes of magma are required to produce chromitites. Cameron (1977) credited chromite formation to total pressure changes in the magma chamber induced by tectonism. Furthermore, pressure changes within the magma chamber were initiated by magma addition, which increased the magma volume driving the crystallization path towards the chromite field. Linpin (1993) proposed that the nucleation and expansion of CO_2 bubbles rising to the top of the Stillwater Complex magma chamber caused pressure increase within the chamber. The magma was driven towards the chromite field (olivine-chromite-

quartz ternary), subsequently triggering chromitite formation. Eales (2000) proposed that deep seated staging chambers are responsible for chromitite in the overall BC chamber, with chromitite layers forming as a result of the intrusion of chromite-laden crystal mushes. Kinnaird *et al*. (2002) made Sr_i measurements from two drill cores located in Steelpoort (Eastern BC) and Brakspruit (Western BC). They found high Sr_i values in plagioclase within chromitite layers and low Sr_i values in plagioclase within adjacent silicate lithologies. They attributed the high Sr_i in chromitite layers to contamination by a radiogenic source, probably the roof lithologies. Concurrent mixing between resident and fresh magma as well as contamination via interaction with the roof lithologies led to entrainment of chromite to the chamber floor producing chromitite layers that have higher Sr_i. Schannor *et al*. (2018) disputed this model after finding plagioclase that had exceedingly radiogenic Sr_i in the UG2 footwall pyroxenites but less radiogenic Sr_i in the UG2 chromitite. They argued against chromite crystallization as a product of interaction between roof lithologies and fresh magma intrusion. They proposed that Sr_i differences in plagioclase within the UG2 chromitite layer and pyroxenite footwall is suggestive of fluid infiltration resulting from dehydrating country lithologies beneath the BC. Mondal and Mathez (2007) proposed that chromitites are a result of injection of fresh magma batches containing suspended chromite. This magma from a deeper staging chamber was injected into a resident magma chamber. They suggested that the BC may possibly represent the topmost chamber in a network of chambers connected to the mantle. Cawthorn (2011) opposed formation of chromitites via mixing of magmas, instead pressure increases in the resident magma triggered by the basal injection of a fresh primitive magma led to chromite formation in the resident magma. Mass balance compliance issue is encountered in this model, as a restricted amount of Cr is available in basaltic melts.

Using field evidence from potholes, Latypov *et al*. (2017) dismissed gravity dominated crystal settling models and crystal dominated slurries models for chromitite formation in the BC. Important findings made by these authors include wrapping of chromitite layers over uneven margins of potholes and the presence of thin silicate partings in chromitite layers that are compositionally and texturally different. They deemed this impossible if chromite was emplaced via the aforementioned models. They concluded that chromitite layers formed in response to dense and superheated magma along the base of the chamber, eventually melting chamber floor cumulates succeeded by in-

situ chromite crystallization on the uneven chamber floor. This model, however, discounts the presence of isotopic excursions coinciding with the presence of chromitite layers as found by Kinnaird *et al*. (2002), Kruger (2005), Seabrook *et al*. (2005) and this study.

Moreover, there are contrasting findings in measured Sr_i values between this study and that of Kinnaird *et al*. (2002), a major difference being that Kinnard *et al*. (2002) reported high Sr_i values in plagioclase at the level of the chromitite layers and low values in adjacent lithologies. The opposite is observed in this study, with low Sr_i values at the level of chromitite layers and high values in adjacent lithologies.

Lithological variations

In the study area, the LCZ is primarily comprised of orthopyroxene-dominated lithologies namely plagioclase-bearing pyroxenite and melagabbronorite that display cryptic layering, hosting 2 chromitite layers (MG1 and MG2). The UCZ is comprised of diverse lithologies also hosting 2 chromitite layers (MG3 and MG4), with the majority of UCZ lithologies dominated by plagioclase. Modal layering is observed throughout the UCZ. Variations in the modal mineralogy (Fig 40) in this study are similar to those of Kottke-Levin (2011) for the Eastern Limb.

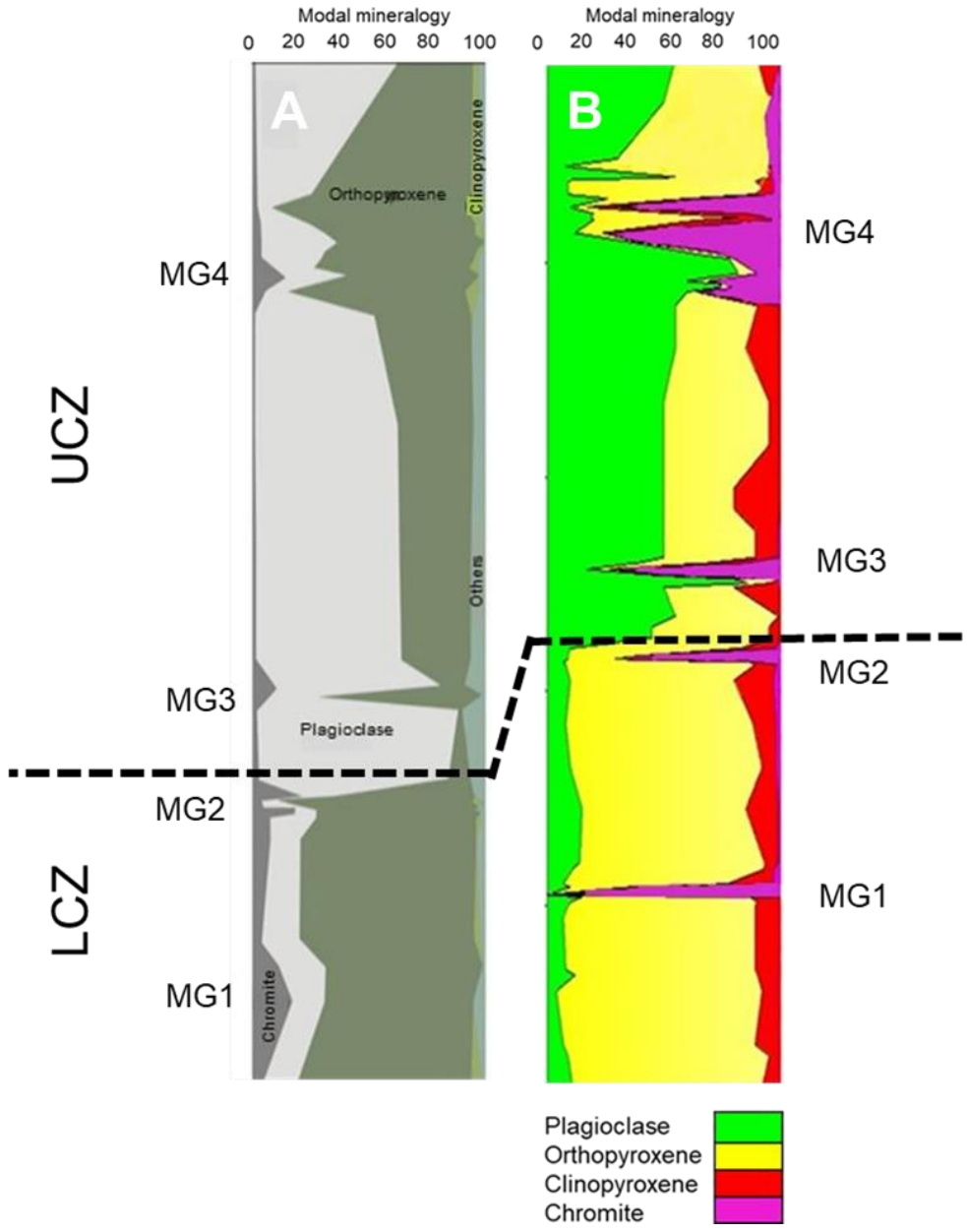

Figure 40: Modal mineralogy comparison in (A) Kottke-Levin (2011) and (B) this study.

Whole-rock major and trace elements

Whole-rock geochemistry reflects dominant mineral phases throughout the study interval, with the ratio between plagioclase and pyroxene controlling the chemical composition of lithologies. Chromite additionally controls whole-rock compositions at the level of chromitite layers in both the UCZ and LCZ, as both plagioclase and orthopyroxene are interstitial to chromite.

According to Giebel (2013), major elements can be used to explain changes in dominant minerals reflecting partitioning of major elements into cumulus phases. Whole-rock major element plots against depth (see Fig 21) reveal that Al_2O_3, CaO, Na_2O and K_2O concentrations are high above the UCZ-LCZ transition, reflecting the abundance of plagioclase in the UCZ. Fe_2O_3, MnO, MgO and TiO_2 concentrations are high below the UCZ-LCZ transition, reflecting the abundance of orthopyroxene in the LCZ. However, it must be noted that SiO_2 has no preference for either plagioclase or orthopyroxene throughout the study interval, revealing compositional breaks only at the level of chromitite layers, where SiO_2 decreases relative to that in the under- and overlying silicate-dominated lithologies. All analysed major elements reveal an almost uniform trend up the UCZ-LCZ stratigraphy, except at the level of the chromitite layers where either an increase or decrease transpires. Cr_2O_3, TiO_2 and Fe_2O_3 concentrations all reveal an increase at the level of chromitite layers, coinciding with decreasing whole-rock Mg#. MnO, MgO, CaO, Na_2O, K_2O and P_2O_5 concentrations decrease at the level of chromitite layers. Whole-rock Mg# averages 76.31 in the LCZ, whereas it averages 66.64 in the UCZ. Whole-rock Mg# exhibits an undeviating trend up the UCZ-LCZ stratigraphy, interpreted here to represent repetitive influxes of magma that balanced crystallization. An exception is observed at the level of chromitite layers where the Mg# decreases. This is attributed to chromite being the dominant phase. A saw-tooth trend is observed at the level of chromitite layers. However, this is short-lived as Mg# immediately reverts to an undeviating trend until an encounter with another chromitite layer. This is a recurring pattern throughout the UCZ-LCZ interval, with saw-tooth trends observed at the level of chromitite layers and linear trends revealed by intervening silicate lithologies (Fig 41).

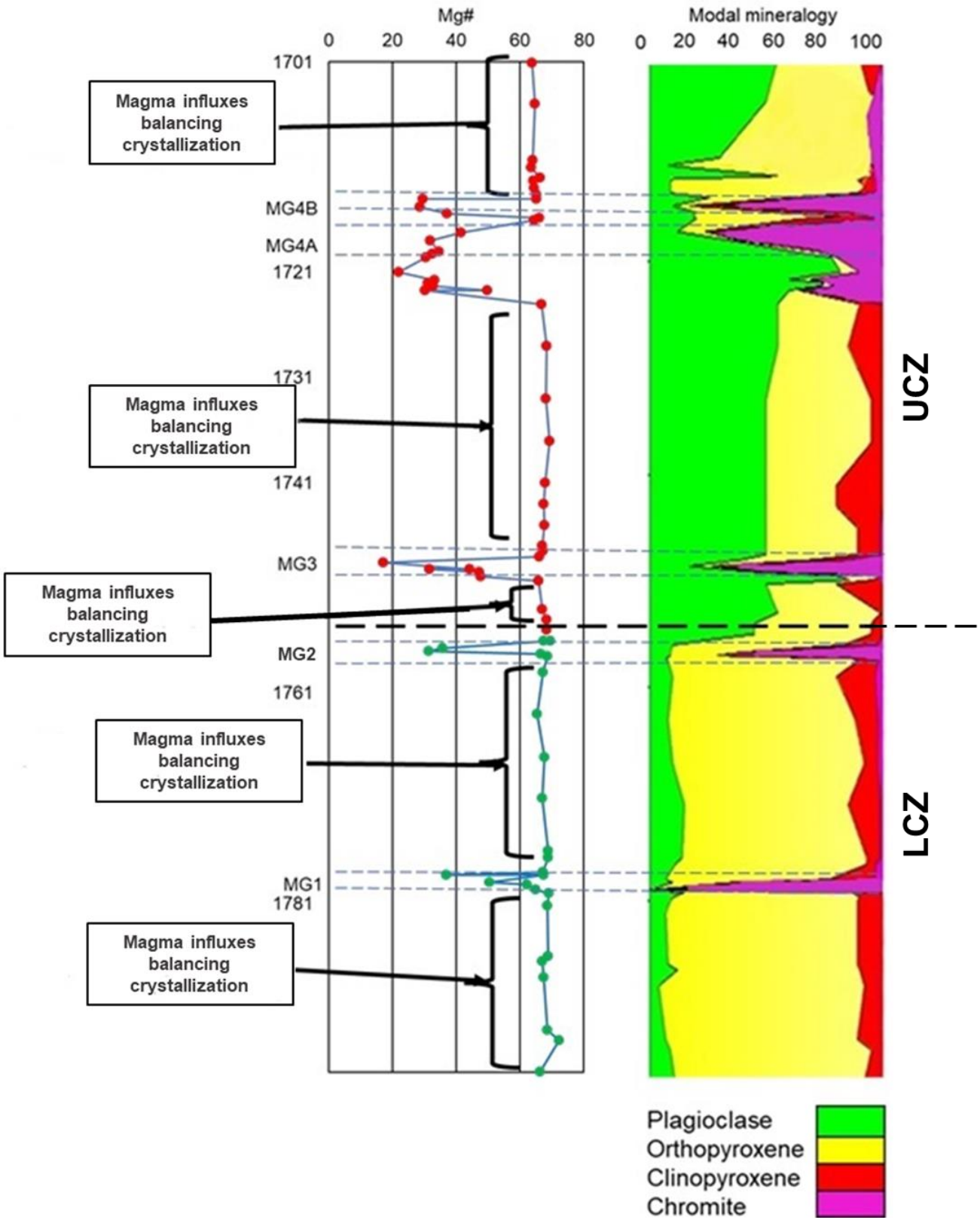

Figure 41: Whole-rock Mg# trends in the UCZ-LCZ interval (Red circles = UCZ, Green circles = LCZ).

Whole-rock trace elements reveal compositional breaks at the UCZ-LCZ transition and at the level of the chromitite layers (see Fig 24), with Ba and Sr partitioning into plagioclase (UCZ). Ni is partitioned into orthopyroxene (LCZ), whereas Zr, Co, Cr, Sc, V and Zn are partitioned into chromite (MG1-4). This is reflective of varying proportions of different minerals in the study interval. In chromite-free lithologies whole-rock Cr/V ratio provides a good differentiation index when plotted against depth (Maier *et al*. 2012). Figure 42 reveals an undeviating trend for the Cr/V ratio in most of the silicate lithologies up the UCZ-LCZ interval, with breaks observed at the level of the chromitite layers. Similar to the whole-rock Mg#, the Cr/V ratio reveals two trends up the UCZ-LCZ interval: 1) an undeviating trend observed in chromite free lithologies; and 2) an increase at the chromitite layers. This may be attributed to repetitive influxes of magma, with varying chromite composition.

The LCZ interval displays REE variations, with orthopyroxene bearing lithologies (melagabbronorite and plagioclase-bearing pyroxenite) dominating the stratigraphy. The UCZ reveals limited REE variability, which is dominated by plagioclase-dominated lithologies (norite and gabbronorite). A uniform trend is observed up the UCZ stratigraphy, with REE compositional breaks occurring at the level of the chromitite layers (see Fig 29). This is suggestive of nominal variation of trapped liquids in the UCZ, especially in chromite-free lithologies. REE variations at the level of the chromitite layers is suggestive of variations in trapped liquids. There is no recognisable REE trend within the LCZ in comparison to the UCZ, which reveals an almost chaotic distribution of REE, suggestive of significant variations in the amount of trapped liquid in the LCZ.

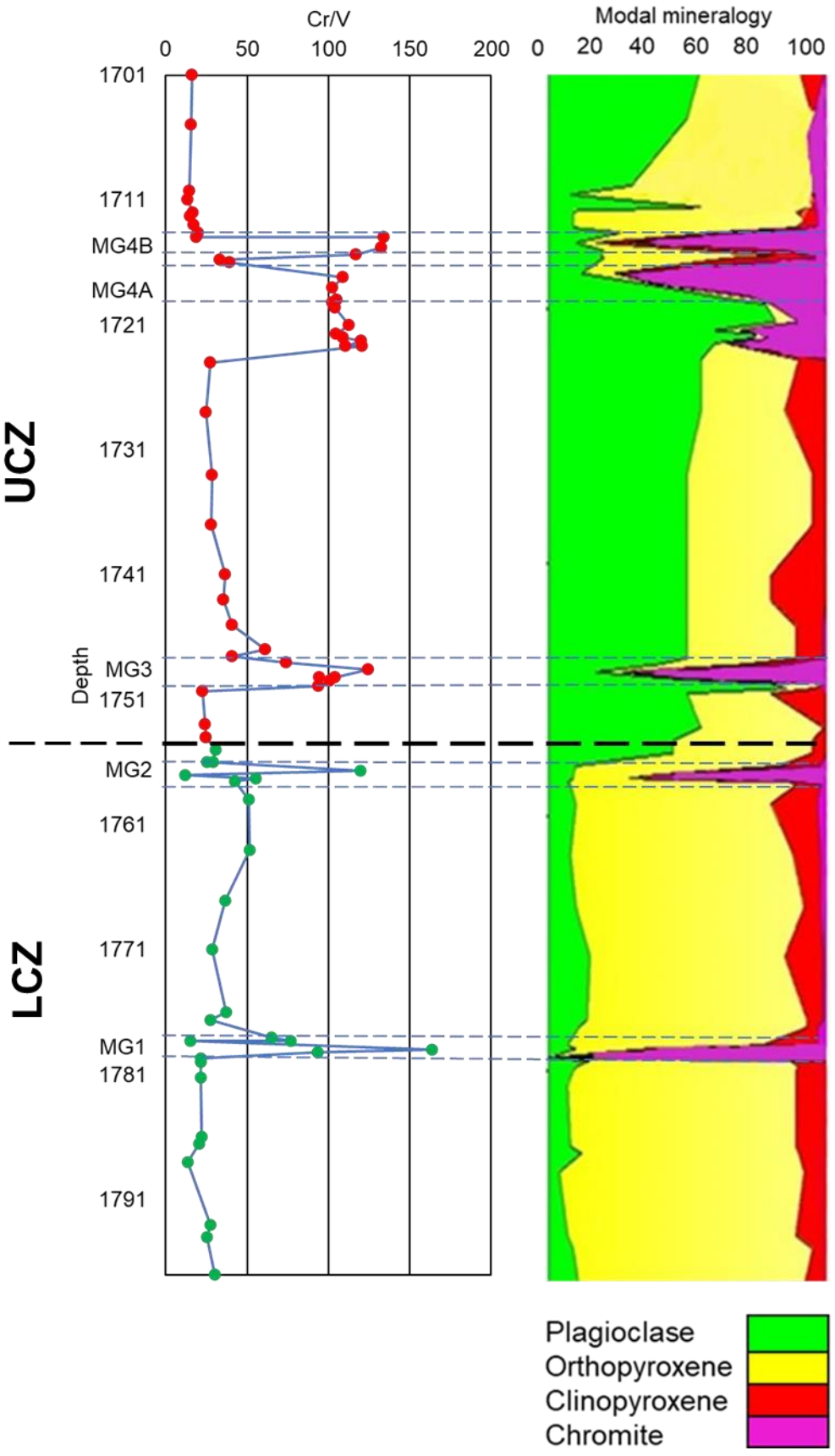

Figure 42: Whole-rock Cr/V ratio trends across the UCZ-LCZ interval (Red circles = UCZ, Green circles = LCZ).

Strontium isotopic variations across the LCZ-UCZ interval.

Upon compiling the Sr isotopic stratigraphy of the RLS in the Western limb, Kruger (1994; 2005) divided the RLS into 2 stages, which were responsible for the construction of the overall BC (see Fig 3). The 1st stage, termed the *Integration stage* entailed emplacement of various magma influxes characterised by isotopic heterogeneity. The LZ, CZ, and LMZ were emplaced during the 1st stage. The 2nd stage, termed the *Differentiation stage* is characterised by isotopic homogeneity, in conjunction with substantial amounts of fractionation and nominal addition of fresh magma. The UMZ and UZ were emplaced during this stage.

Data acquired across the LCZ-UCZ interval in this study are to some degree consistent with Kruger's (1994, 2005) *Integration stage*. However, it must be noted that Kruger's (1994, 2005) Sr_i data was collected on whole-rock samples, whereas Sr_i data in this study was collected of in-situ plagioclase mineral separates. Mineral scale Sr isotopic shifts are detected between chromitites and silicates of the LCZ, whereas there is little evidence of isotopic variations in lithologies of the UCZ. The inflections in Sr_i observed at the levels of both the MG1 and MG2 chromitite layers and the lack thereof across the MG4 chromitite layer may point to the notion that different processes are operational in the formation of chromitites in the LCZ as opposed to the UCZ. For instance, the Sr_i inflections at MG1 and MG2 suggest mixing of Sr_i heterogenous magmas, resulting in the formation of the chromitite layers. The lack of Sr_i inflections at MG4, suggest mixing of multiple Sr_i homogenous magmas.

The transition between the LCZ and UCZ is characterised by a consistent increase in average Sr_i values of plagioclase from 0.7056 immediately above the MG2 chromitite to 0.7066 immediately below the MG3 chromitite layer. This appears to be the single largest and sustained increase in Sr_i observed across the entire study interval and represents compelling evidence for the addition of isotopically distinct magma at the level of the UCZ-LCZ transition. On average, the UCZ (0.7059 ± 0.0003) is slightly more radiogenic than the LCZ (0.7054 ± 0.0004), which suggests that the magma introduced at the level of the transition between these zones was more radiogenic than the resident LCZ magma. As shown by Kruger (1994), this trend towards more radiogenic Sr isotopic compositions extends through the UCZ well into the MZ.

Plagioclase in plagioclase-bearing pyroxenite and melagabbronorite exhibits the same average Sr_i value of 0.7055 throughout the LCZ interval, which is within the 0.7045-0.7060 LCZ range proposed by Kruger (2005), with a few outliers. This value shifts significantly to a value of 0.7050 at MG1 (see Fig 34) deviating from both the adjacent footwall and hanging wall. This is suggestive of magma addition, which mixed with the resident magma, resulting in the formation of the MG1 chromitite layer. Another shift in Sr_i is encountered at MG2, with a value of 0.7041 exhibited by MG2, which is also dissimilar to adjacent lithologies. This also suggests another magma addition, which mixed with the resident magma resulting in the formation of MG2.

It must be noted that the UCZ has an average Sr_i value of 0.7059 ±0.0003, whereas the LCZ has a value of 0.7054 ± 0.0003, suggesting that the UCZ magma was more radiogenic than the LCZ magma, as explained above. This shift transpires between MG2 and MG3, coinciding with a shift in dominant mineral phase, which was previously orthopyroxene in the LCZ to plagioclase in the UCZ (see Fig 10). Eales *et al*. (1990) attributed cumulus plagioclase in the UCZ to intrusion of the B2 magma (~0.7065-0.7075 in Kruger, 1994, 2005), which mixed with the B1 resident magma (~0.7050 in Kruger, 1994, 2005). In this study Sr_i data of the UCZ reveals a mixed lineage between the B1 and B2 magma (see Table 10), confirming findings by Kruger (2005) as well as Eales *et al*. *(*1986). The B1 (LCZ) was residual in the overall BC chamber, which mixed with the newly injected B2 magma (UCZ).

Sr_i in the UCZ averages 0.7059 (max = 0.7072; min = 0.7047), with most analysed values agreeing with the 0.7055-0.7064 UCZ range provided by Kruger (2005). The Sr_i value reveals a major increase just below the MG3 chromitite layer at 0.7066, signifying magma addition going into the UCZ, as explained above. A decrease to a value of 0.7059 is encountered at the level of the MG3 layer. The MG3 chromitite may therefore also have formed in response to the mixing of compositionally dissimilar magmas. The hanging wall above the MG3 chromitite represents the longest interval in the entire UCZ-LCZ interval wherein there is a steady Sr_i value up the UCZ stratigraphy for about 30 m, averaging 0.7058. The near-constancy in Sr_i across this interval, coupled with limited differentiation as exemplified by plagioclase An% and whole-rock Mg# is suggestive of the repeated or prolonged influx of compositionally similar magma.

The depth range between 1719 m and 1701 m is quite complex in terms of the lithologies present. It is characterised by the occurrence of multiple intercalated lithologies over a short space that are isotopically similar. The order up the stratigraphy is as follows: MG4A marks the bottom of this depth range with Sr_i averaging 0.7060, overlain by plagioclase-bearing pyroxenite (0.7063), then chromitite (MG4B) sandwiched by chromite-bearing melagabbronorite all averaging 0.7059. Plagioclase bearing pyroxenite follows averaging 0.7058, overlain by gabbronorite and another plagioclase-bearing pyroxenite both averaging 0.7059. Norite with Sr_i averaging 0.7060 marks the top of the UCZ for the study interval.

Focusing on the chromitite layers, both MG4A and MG4B layers are isotopically similar averaging 0.7060 and 0.7059, respectively. They also exhibit Sr_i values that are within error of the under- and overlying silicate lithologies. For the MG4 package, there is, therefore, no compelling Sr isotopic evidence to support magma mixing as a process responsible for chromitite formation. As explained above, the MG4 chromitite may therefore have formed differently to chromitites within the LCZ. Alternatively, and this is the favoured model, the MG4 chromitite may also have formed in response to magma mixing, similar to the MG1 to MG3 chromitite layers, albeit through the mixing of magmas with indistinguishable Sr-isotopic compositions.

Proposed model

Isotopic dissimilarities are detected between chromitites and their host rocks in the LCZ, whereas there are not any major dissimilarities in the UCZ, particularly across the MG4 chromitite. The variations in Sr_i seen at the level of the MG1 and MG2 are consistent with the model proposed by Kinnaird *et al*. (2002). However, Kinnaird *et al*. (2002) reported higher Sr_i values within the chromitite layers than their adjacent footwall and hanging wall lithologies, which were attributed to magma interaction and then contamination by roof lithologies. Data presented in this study reveal that chromitite layers of the LCZ exhibit lower Sr_i values in comparison to adjacent lithologies. In consideration of this, it is proposed that fresh magma additions that eventually constructed the chromitite layers interacted with the roof lithologies as suggested by Kinnaird *et al*. (2002). However, the degree of interaction was probably nominal. The magmas that intruded over the study interval therefore represent “primitive” magma that has limited influence of contamination by roof lithologies.

Sr_i data in the LCZ interval provide evidence for the intrusion of isotopically dissimilar magma at the level of chromitite layers, as seen by decreasing of Sr_i within the MG1 and MG2 chromitite layers. Chromitite formation may therefore be attributed in part to mixing between the isotopically dissimilar new magma and LCZ resident magma (Fig 43).

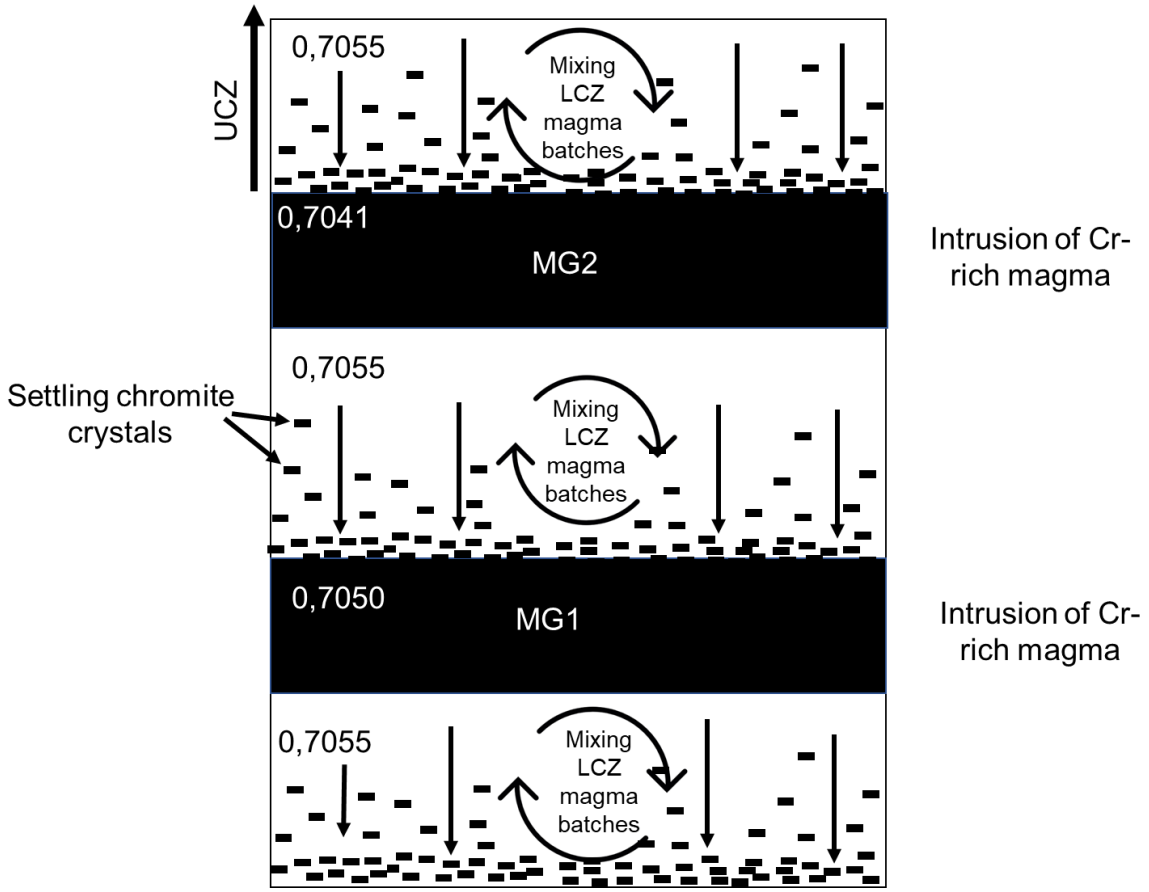

Figure 43: Illustration of model in the LCZ.

However, the chromitites of the UCZ reveal similar Sr_i values as adjacent lithologies, with only MG3 considered to be a product of mixing on Sr isotopic grounds, due to a sustained increase in Sr_i between the top of the MG2 and the base of the MG3. The MG3 chromitite layer probably formed in response to the intrusion and subsequent mixing of the (more radiogenic) UCZ magma with the resident (less radiogenic) LCZ magma. Although no isotopic evidence was found to support the intrusion of magma at the level of the MG4 chromitite, this does not disprove that magma mixing may also have been operational in its formation. If so, the magma that mixed with the resident magma at this level would need to have had the same Sr isotopic composition as the resident magma. Evidence in support of the repetitive influx of magma that had the

same Sr isotopic composition as the resident magma below the level of the MG4 comes from the lack of differentiation (as exemplified by plagioclase An% and whole-rock Mg#) over an interval of ~30 m. The same interval exhibits no variation in plagioclase Sr_i (Fig 44).

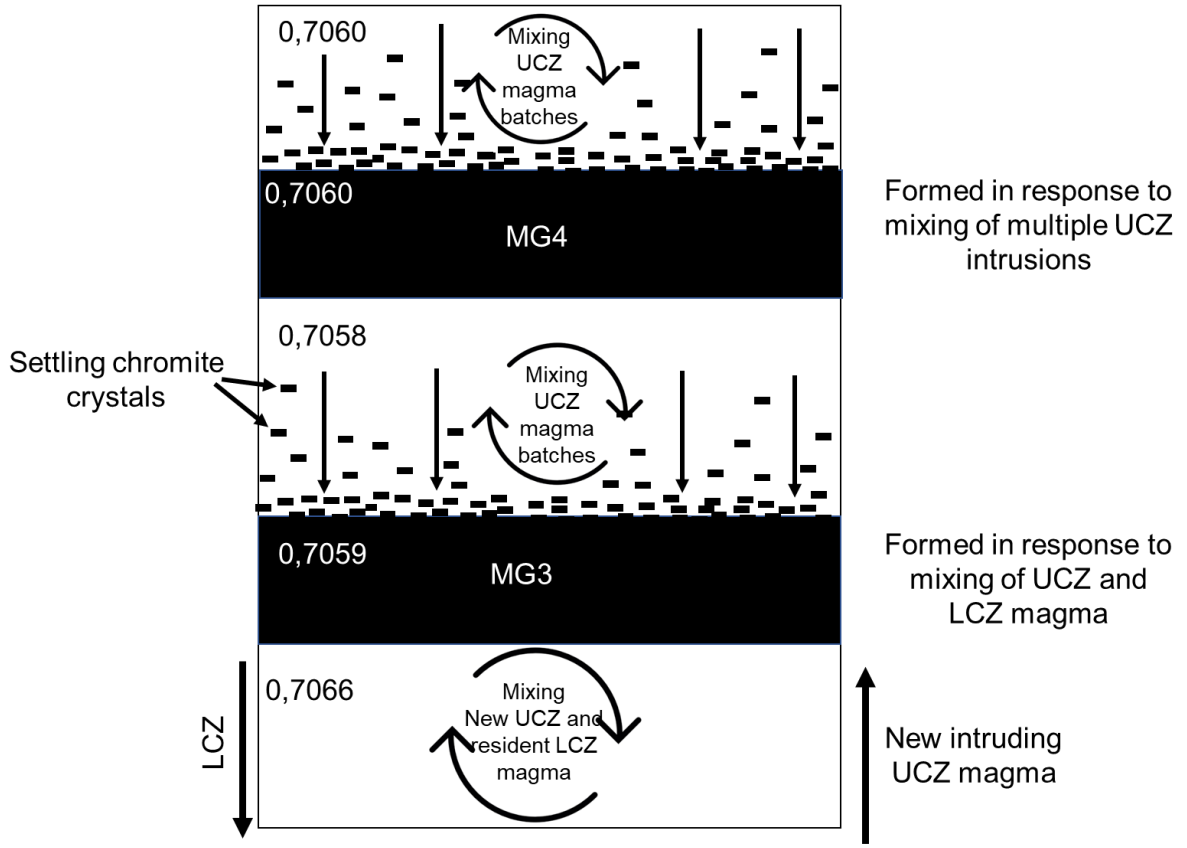

Figure 44: Illustration of model in the UCZ.

The distinct variations in plagioclase Sr_i that are coincident with the location of chromitite layers across the study interval excluding MG4 contradict the model proposed by Latypov *et al*. (2018), as in-situ formation of chromitites would not result in Sr isotopic discontinuities at or within chromitite layers. Similarly, models that suggest chromitite formation in response to changes in intensive parameters (e.g. Cameron, 1977; Cawthorn, 2011) cannot account for Sr isotopic excursions at the level of chromitite layers.

Even though repeated magma influxes and consequent mixing appears to be exceedingly common across the study interval and likely important in the formation of chromitite layers, the Cr mass balance paradox (Eales, 2002) remains. In order to account for this, it is suggested that many of the magma influxes were not aphyric but instead carried a suspended load of chromite that accumulated to form chromitite

layers. Additional chromite may have formed in response to the mixing of newly intruded and resident magma. Evidence in support of such an argument was presented in Table 12 above for the MG1 chromitite layer, which showed the presence of plagioclase exhibiting isotopic disequilibrium, with one plagioclase crystal having Sr_i of 0.7034 and another having Sr_i of 0.7067. Despite the large errors on both determinations, the errors do not overlap. It is interesting to note that the Sr_i values on both crystals are different to those in the immediately under- and overlying lithologies.

Therefore, the presence of plagioclase displaying isotopic disequilibrium within the MG1 chromitite is not a reflection of the mixing of two different populations of plagioclase, one representing plagioclase phenocrysts intruded along with chromite and the other plagioclase that crystallised from the resident magma. Instead, a chromite-laden magma hosting multiple, isotopically distinct populations of plagioclase phenocrysts could account for these observations.

5. Conclusions

This study of the LCZ-UCZ transition in the Western Limb of the Bushveld Complex showed the presence of distinct Sr isotopic excursions coincident with the MG1 and MG2 chromitite layers and a consistent increase in the Sr_i of plagioclase between the MG2 and MG3 chromitite layers, followed by a decrease in the Sr_i of plagioclase to a value that remains virtually unchanged throughout the MG3 and MG4 chromitite layers and intervening silicate lithologies. In addition, multiple isotopically distinct populations of plagioclase were identified in the MG1 chromitite layer. The results support the importance of magma mixing, most likely between chromite-laden magmas and resident magma, in the formation of the Middle Group chromitites, and argue against chromitite formation models that are attributed to variations in intensive parameters or to the in-situ crystallisation of chromite.

6. References

Anders, E., Grevesse, N. (1989). Abundances of the elements: Meteoritic and solar.

Geochimica et Cosmochimica Acta 53, 197-214.

Beattie, P. (1993). The effect of partial melting of spinel peridotite on uranium series disequilibria: constraints from partitioning studies. Earth and Planetary Science Letters 177, 379-391

Beukes, J.J., Roelofse, F., Gauert, C.D.K., Grobler, D.F., Ueckermann, H. (2021). Strontium isotope variations in the Flatreef on Macalacaskop, northern Bushveld Complex: implications of the source of platinum-group elements in the Merensky Reef. Mineral Deposita 56, 45-57.

Biesheuvel, K. (1970). An interpretation of a gravimetric survey in the area west of the Pilanesberg in the Western Transvaal *In.* Visser, D.J.L., Von Gruenewaldt, G., (Eds). Symposium on the Bushveld Igneous Complex and other layered Intrusions.

Geological Society of South Africa Special Publication 1, 266-282.

Bindeman, I.N., Davis, A.M., Drake, M.J. (1998). Ion microprobe study of plagioclase-basalt partition experiments at natural concentration levels of trace elements. Geochimica et Cosmochimica Acta 62, 1175-1193.

Bougault, H., Hekinian, R. (1974). Rift valley in the Atlantic Ocean near 36°50'N; petrology and geochemistry of basaltic rocks. Earth and Planetary Science Letters 24, 249-261.

Cameron, E.N. (1977). Chromite in the central sector of the eastern Bushveld complex, South Africa. American Mineralogist 62, 1082-1096.

Cameron, E.N. (1980). Evolution of the lower critical zone, central sector, eastern Bushveld Complex, and its chromite deposits. Economic Geology 75, 845-871.

Campbell, I.H. (1978). Some problems with the cumulus theory. Lithos 11, 311-323.

Cawthorn, R.G., Walraven, F. (1998). Emplacement and crystallization time for the Bushveld Complex. Journal of petrology 39, 1669-1687.

Cawthorn, R.G., Webb, S.J. (2001). Connectivity between the western and eastern limbs of the Bushveld Complex. Tectonophysics 330, 195-209.

Cawthorn, R.G., Eales, H.V., Walraven F., Uken, R., Watkeys, M.K. (2006). The Bushveld Complex. *In.* Johnson, M.R., Anhaeusser, C.R., Thomas, R.J. (Eds). The geology of South Africa. Geological Society of South Africa/Council for Geoscience. p261.

Cawthorn, R.G. (2011). Geological interpretations from the PGE distribution in the Bushveld Merensky and UG2 chromitite reefs. Journal of the Southern African Institute of Mining and Metallurgy 111, 67-79.

Cawthorn, R.G., (2015). The Bushveld Complex, South Africa. *In*: Charlier, B., Namur, O., Latypov, R., & Tegner, C. (eds) Layered Intrusions. Berlin: Springer, 517-587

Chutas, N.I., Bates, E., Prevec, S.A., Coleman, D.S., Boudreau, A.E. (2012). Sr and

Pb isotopic disequilibrium between coexisting plagioclase and orthopyroxene in the Bushveld Complex, South Africa: micro drilling and progressive leaching evidence for sub-liquidus contamination within a crystal mush. Contributions to Mineral Petrology 163, 653-668.

Davidson, J.P., Font, L., Charlier, B.L.A., Tepley III, F.J. (2007). Mineral-scale Sr isotope variation in plutonic rocks – a tool for unravelling the evolution of magma systems. Transactions of the Royal Society of Edinburgh: Earth Sciences, 97, 00-00.

De Waal, S.A., Maier, W.D., Armstrong, R.A. Gauert, C.D.K. (2001). Parental magma and emplacement of the stratiform Uitkomst Complex, South Africa. Canadian Mineralogist 39, 557-571.

Du Plessis, C.P., Walraven, F. (1990). The tectonic setting of the Bushveld Complex in Southern Africa, Part 1. Structural deformation and distribution. Tectonophysics 179, 305-319.

Eales, H.V., Marsh, J.S., Mitchell, A.A., De Klerk, W.J., Kruger, F.J., Field, M. (1986). Some geochemical constraints upon models for the crystallization of the upper critical-main zone interval northwestern Bushveld complex. Mineralogical magazine 50, 567-582.

Eales, H.V., De klerk, W.J., Butcher, A.R. (1990a). The cyclic unit beneath the UG1 chromitite (UGIFW unit) at RPM Union Section Platinum Mine Rosetta Stone of the Bushveld Upper Critical Zone?. Mineralogical Magazine, 54, 23-43.

Eales, H.V., De klerk, W.J., Teigler, B. (1990b). Evidence for magma mixing processes within the critical and lower zones of the north-western bushveld complex, South Africa. Chemical Geology 88, 261-278.

Eales, H.V., Botha, W.J., Hattingh, P.J., De Klerk, W.J., Maier, W.D., Odgers, A.T.R. (1993). The mafic rocks of the Bushveld Complex: a review of emplacement and crystallization history, and mineralization, in the light of recent data. Journal of African Earth Sciences 16, 21-142.

Eales, H.V., Cawthorn, R.G. (1996). The Bushveld Complex. *In*. Cawthorn, R.G. (Ed).

Layered intrusions: 15 developments in petrology. Elsevier, p.181-229.

Eales, H.V. (2002). Caveats in defining the magmas parental to the mafic rocks of the Bushveld Complex, and the manner of their emplacement: review and commentary.

Mineral Magazine 66, 815-832.

Eales, H.V. (2000). Implications of the chromium budget of the western limb of the Bushveld complex. South African Journal of Geology 103, 141-150.

Elburg, M.A., Vroon, P., van der Wagt, B., Tchalikian, A. (2005). Sr and Pb isotopic composition of five USGS glasses (BHVO-2G, BIR-1G, BCR-2G, TB-1G, NKT-1G). Chemical Geology 223, 196-207.

Elkins, L., Gaetani, G. and Sims, K. (2008). Partitioning of U and Th during garnet pyroxenite partial melting: Constraints on the source of alkaline ocean island basalts. Earth and Planetary Science Letters 265, 270-286.

Ewart, A., Bryan, W.B., Gill, J.B. (1973) Mineralogy and geochemistry of the younger volcanic islands of Tonga. Journal of Petrology 14, 429-465.

Frey, F.A., Green, D.H., Roy, S.D. (1978). Integrated models of basalt petrogenesis: a study of quartz tholeiites to olivine melilites from South-eastern Australia utilizing geochemical and experimental petrological data. Journal of Petrology 19, 463-513.

Faure, G. (2001). Origin of igneous rock: The isotopic evidence. Springer. p367.

Flanagan, F.J. (1984). Three USGS mafic rock reference samples, W-2, DNC-1, and BIR-1. U.S. Geological Survey Bulletin 1623, 54pp.

Giebel, R.J. (2013). Mineralogy, PGE, whole-rock geochemistry and mineral chemistry of the upper Critical Zone (Bastard Reef, Merensky Reef, Upper Group 2 intervals) in borehole TRP 272. Masters Dissertation. University of the Free State, Bloemfontein.

Hall, A.L. (1932). The Bushveld Igneous Complex of the central Transvaal. Geological Survey Memoir 28. Government Printer, Pretoria, 530p.

Hamilton, P.J. (1977). Sr isotope and trace element studies of the Great Dyke and Bushveld mafic phase and their relation to early Proterozoic magma genesis in southern Africa. Journal of petrology 18, 24-52.

Harmer, R.E., Armstrong, R.A. (2000). Duration of the Bushveld Complex (senolato) magmatism: constraints from new SHRIMP zircon chronology. Abstracts and program, Workshop on the Bushveld Complex, Gethane Lodge, Burgersfort, South Africa.

Hart, S.R., Dunn, T. (1993). Experimental cpx/melt partitioning of 24 trace elements.

Contributions to Mineralogy and Petrology 113, 1-8.

Horn, I., Foley, S.F., Jackson, S.E., Jenner, G.A. (1994). Experimentally determined partitioning of high field strength- and selected transition elements between spinel and basaltic melt. Chemical Geology 117, 193-218.

Irvine, T.N. (1975). Crystallization sequences in the Muskox intrusion and other layered intrusions - II. Origin of chromitite layers and similar deposits of other magmatic ores. Geochimica Cosmochimica Acta 39, 991-1020.

Irvine, T.N. (1977). Origin of chromitite layers in the Muskox Intrusion and other stratiform intrusion; a new interpretation. Geology 5, 273-277.

Jackson, E.D. (1967). Ultramafic cumulates in the Stillwater, Great Dyke and Bushveld intrusions. *In*. Wyllie, P.J. (Eds). Ultramafic and related rocks. John Wiley and Sons, N.Y., 20-38.

Karykowski, B.T., Yang, S.H., Maier, W.D., Lahaye, Y., Lissenberg, C.J., O'Brien, H. (2018). In situ Sr Isotope compositions of plagioclase from a complete stratigraphic

profile of the Bushveld Complex, South Africa: Evidence for extensive magma mixing and percolation. Journal of Petrology 58, 2285-2308.

Keleman, P.B., Dunn, J.T. (1992). Depletion of Nb relative to other highly incompatible elements by melt/rock reaction in the upper mantle. EOS, Transactions of the American Geophysical Union 73, 656-657.

Kennedy, B., Mcdonald, I., Tanner, D., Longridge, L. (2018). The Troctolite unit of the Northern Bushveld Complex: Genesis and mineralization potential. MDSG conference paper. Brighton, United Kingdom.

Kinnaird, J.A., Kruger, F.J., Nex, P.A.M., Cawthorn, R.G. (2002). Chromitites of the bushveld complex - process of formation PGE enrichment. University of the Witwatersrand, Economic geology research institute information circular 369.

Kinnaird, J.A. (2005). The Bushveld Large Igneous Province. School of Geosciences, University of Witwatersrand, P 3-39.

Klemme, S., Gunther, D., Hametner, K., Prowatke, S. and Zack, T. (2006). The partitioning of trace elements between ilmenite, spinel, armalcolite and silicate melts with implications for the early differentiation of the moon. Chemical Geology 234, 251263.

Kottke-Levin, (2011). A geochemical study of the Middle Group chromitites, Helena mine, Bushveld complex, South Africa. PhD thesis. University of the Free State, Bloemfontein.

Kruger, F.J. (2005). Filling the Bushveld Complex magma chamber: lateral expansion, roof and floor interaction, magmatic unconformities, and the formation of giant chromitite, PGE and Ti-V-magnetitite deposits. Mineralium Deposita 40, 451-472.

Kruger, F.J. (1994). The Sr-isotopic stratigraphy of the western Bushveld Complex. South African Journal of Geology 97, 393-398.

Kruger, F.J., Sharpe, J.S., (1982). Significance of $^{87}Sr/^{86}Sr$ ratios in the Merensky cyclic unit of the Bushveld Complex. Nature 298, 53-55.

Kruger, F.J. (1989). The geochronology and Sr-isotope geochemistry of the Molopo Farms Complex, Bushveld Magmatic Province: a preliminary report. Molopo Botswana

(Pty) Ltd. Final Report for Prospecting Licences 14/85 and 38/90. Open File Report, Geological Survey Botwsana.

Latypov, R., Costin, G., Chistyakova, S., Hunt, E.J., Mukherjee, R., Naldrett, T. (2018). Platinum-bearing chromite layers are caused by pressure reduction during magma ascent. Nature Communications 9, 462.

Latypov, R., Chistyakova, S., Mukherjee, R. (2017). A novel hypothesis for origin of massive chromitites in the Bushveld Igneous Complex. Journal of Petrology 58, 18991940.

Lee, C.A., Butcher, A.R. (1990). Cyclicity in the Sr isotope stratigraphy through the Merensky and Bastard reef units, Atok Section, eastern Bushveld Complex.

Economic geology 85, 877-883.

Lehloenya, P.B. (2017). Chemical and isotopic variations in plagioclase across the transition between the Main and Upper Zones, Western Bushveld Complex. Masters Dissertation. University of the Free State, Bloemfontein.

Le Maitre, R.W., Bateman, P., Dudek, A.,Keller, J. (1989). A Classification of Igneous rocks and Glossary of Term: Recommendations of the International Union of Geological Sciences Subcommission on the Systematics of Igneous Rocks. Blackwell Scientific Publications, Oxford.

Lipin, B.R. (1993). Pressure increases, the formation of chromite seams, and the development of the ultramafic series in the Stillwater Complex, Montana. Journal of Petrology 34, 955-976.

Maghdour-Mashhour, R. Hayes, B. Bolhar, R. Ueckermann, H. (2021). Sill intrusion into pyroxenitic mush and the development of the Lower-Upper Critical Zone boundary of the Bushveld Complex: Implications for the origin of stratiform anorthosites and chromitites in layered intrusions. Oxford University Press. Oxford.

Maier, W.D., Barnes, S.J. (1998). Concentrations of rare earth elements in silicate rocks of the Lower, Critical and Main Zones of the Bushveld Complex. Chemical geology 150, 85-103.

Maier, W.D., Barnes, S.J., Groves, D.I. (2012). The Bushveld Complex, South Africa: formation of platinum– palladium, chrome- and vanadium-rich layers via hydrodynamic

sorting of a mobilized cumulate slurry in a large, relatively slowly cooling, subsiding magma chamber. Mineralium Deposita 48, 1–56.

Mangwegape, M. Roelofse, F., Mock, T., Carlson, W.R. (2015). The Sr-isotopic stratigraphy of the Northern Limb of the Bushveld Complex, South Africa. Journal of African Earth Sciences 113, 95-100.

Mapeo, R.B.M., Kampuznu, A.B., Ramokate, L.V., Corfu, F., Key, R.M. (2004). Bushveld-age magamatism in south-eastern Botswana: evidence from U-Pb zircon and titanite geochronology of the Moshaneng Complex. South African Journal of Geology 107, 219-232.

Mckenzie, D., O'nions, R.K. (1991). Partial melt distributions from inversion of rare Earth element concentrations. Journal of Petrology 32, 1021-1091.

Mondal, S.K., Mathez, E.D. (2007). Origin of the UG2 chromitite layer, Bushveld Complex. Journal of Petrology 48, 495-510.

Molyneux, T.G. (1970). A geological investigation of the Bushveld Complex in Sekhukhuneland and part of the Steelpoort Valley. Transactions of the Geological Society of South Africa 77, 329-338.

Mysen, B. (1978). Experimental determination of nickel partition coefficients between liquid, pargasite and garnet peridotite minerals and concentration limits of behaviour according to Henry's Law at high pressure and temperature. American Journal of Science 278, 217-243.

Nex, P.A., Kinnaird, J.A., Ingle, L.J., van der Vyver, B.A., Cawthorn, R.G. (1998). A new stratigraphy for the Main Zone of the Bushveld Complex, in the Rustenburg area. South African Journal of Geology 101, 215-223.

Prevec, S.A., Ashwal, L.D., Mkaza, M.S. (2005). Mineral disequilibrium in the Merensky Reef, western Bushveld Complex, South Africa: new Sm–Nd isotopic evidence. Contributions to Mineral Petrology 149, 306-315.

Paster, T.P., Schauwecker, D.S., Haskin, L.A. (1974). The behaviour of some trace elements during solidification of the Skaergaard layered series. Geochimica et Cosmochimica Acta 38, 1549-1577.

Raczek, I., Stoll, B., Hofmann, A.W., Jochum, K.P. (2001). High precision trace element data for the USGS reference materials BCR-1, BCR-2, BHVO-2, AGV-1, AGV-2, DTS-1, DTS-2, GSP-1and GSP-2 by ID-TIMS and MIC-SSMS. The journal for geostandards and geoanalysis 25, 77-86.

Roelofse, F. (2010). Constraints on the magmatic evolution of the lower Main Zone and Platreef on the Northern Limb of the Bushveld Complex as inferred from the Moordkopje drill core. PhD Thesis. University of the Witwatersrand, Johannesburg.

Roelofse, F., Ashwal, L.D. (2012). The Lower Main Zone in the Northern Limb of the Bushveld Complex-a >1.3km Thick Sequence of Intruded and Variably Contaminated Crystal Mushes. Journal of petrology 53, 1449-1476.

Roelofse, F., Ashwal, L.D., Romer, R.L. (2015). Multiple, isotopically, heterogeneous plagioclase populations in the Bushveld Complex suggest mush intrusion. Chemierder Erde-Geochemistry 75, 465-471.

South African Commission on Stratigraphy. (1980). Stratigraphy of South Africa. Geological Survey of South Africa, Handbook 8. Pretoria: Geological Survey of South Africa, p. 690.

SARM. (2015). South African reference material. Mintek, Randburg, South Africa.

Seabrook, C.L., Cawthorn, R.G., Kruger, F.J. (2005). The Merensky Reef, Bushveld Complex: Mixing of Minerals Not Mixing of Magmas. Economic Geology, 100, 1911206.

Schannor, M., Veksler, I.V., Hecht, L., Harris, C., Romer, R.L., Manyeruke, T.D. (2018). Small-scale Sr and O isotope variations through the UG2 in the eastern Bushveld Complex: The role of crustal fluids. Chemical Geology 485, 100-112.

Schouwstra, R.P., Kinloch, E.D., Lee, C.A. (2000). A Short Geological Review of the Bushveld Complex. Platinum Metals Review 44, 33-39.

Scoates, J.S. Wall, C.J. Friedman, R.M. Weis, D. Mathez, E.A. VanTongeren, J.A. (2021). Dating the Bushveld Complex: Timing of crystallization, duration of magmatism, and cooling of the world’s largest layered intrusion and related rocks. Journal of petrology 2021, 1-39.

Scoates, J.S., Friedman, R.M. (2008). Precise age of the platiniferous Merensky reef, Bushveld Complex, South Africa, by the U-Pb zircon chemical abrasion ID-TIMS technique. Economic Geology103, 465-471.

Sharpe, M.R. (1985). Strontium isotope evidence for preserved density stratification in the main zone of the Bushveld Complex, South Africa. Nature 316, 119-126.

Steiger, R.H., Jäger, E. (1977). Subcommission on geochronology: convention on the use of decay constants in geo- and cosmochronology. Earth and Planetary Science Letters 36, 359-362.

Teigler, B., Eales, H.V. (1996). The Lower and Critical Zones of the western limb of the Bushveld Complex as intersected by the Nooitgedacht boreholes. Bulletin for the Geological Survey of South Africa 111, p.126

VanTongeren, J.A. (2018). Mixing and unmixing in the Bushveld Complex magma chamber. *In.* Mondal, S.K. Griffin, W.L. (eds). Processes and Ore Deposits of Ultramafic-Mafic Magmas through Space and Time. Elsevier, p.113-135.

Van Zyl, J.P. (1970). The petrology of the Merensky Reef and the associated rocks on Swartklip 988, Rustenburg District. Geological Society of South Africa, Special Publication1, 80-107.

Von Gruenewaldt, G. (1971). The Main and Upper Zones of the Bushveld Complex in the Roossenekal area, Eastern Transvaal. Transactions of the geological Society South Africa 76, 207- 227.

Webb, S.J., Cawthorn, R.G., Nguuri, T., James, D. (2004). Gravity modelling of Bushveld Complex connectivity supported by Southern African Seismic Experiment results. South African Journal of Geology 107, 207-218.

Willemse, J. (1969). The geology of the Bushveld Igneous Complex, the largest repository of magmatic ore deposits in the world. Economic Geology Monograph 4, 1-22.

Wilson, A.H., Zeh, A., Gerdes, A. (2017). In Situ Sr isotopes in Plagioclase and Trace Element Systematics in the Lowest Part of the Eastern Bushveld Complex: Dynamic Processes in an Evolving Magma Chamber. Journal of Petrology 58, 327–360.

Yang, S.H., Maier, W.D., Lahaye, Y., O'Brien, H. (2013). Strontium isotope disequilibrium of plagioclase in the Upper Critical Zone of the Bushveld Complex: evidence for mixing of crystal slurries. Contribution to Mineral Petrology166, 959-974.

Zeh, A., Ovtcharova, M., Wilson, A.H., Schaltegger, U. (2015). The Bushveld Complex was emplaced and cooled in less than one million years – results of zirconology, and geotectonic implications. Earth and Planetary Science Letters 418, 103-114.

7. Appendix

Appendix A

Table A-1: Whole-rock major element composition per analysed sample in w.t%, along with Mg# = 100*Mg/(Mg+Fe).

Sample	Depth (m)	SiO_2	TiO_2	Al_2O_3	Fe_2O_3	MnO	MgO	CaO	Na_2O	K_2O	P_2O_5	Cr_2O_3	LOI	Total	Mg#
MM1	1701	51,04	0,13	15,71	8,06	0,14	14,20	8,51	1,04	0,23	0,03	0,19	0,00	99,27	77,47
MM2	1705	52,13	0,13	14,73	8,21	0,14	15,05	8,17	1,42	0,20	0,03	0,21	0,00	100,42	78,14
MM3	1710,3	62,56	0,22	11,54	6,65	0,15	11,80	4,56	0,46	1,07	0,02	0,19	0,05	99,27	77,59
MM4	1711	53,48	0,21	10,24	10,43	0,18	18,14	6,39	1,27	0,29	0,04	0,27	0,00	100,96	77,24
MM5	1712	51,53	0,12	13,49	8,55	0,15	16,74	7,67	1,40	0,04	0,01	0,24	0,00	99,94	79,25
MM6	1712,3	54,21	0,24	4,82	13,06	0,23	23,48	3,66	0,75	0,32	0,02	0,40	0,01	101,17	77,82
MM7	1713	53,57	0,24	4,49	12,89	0,23	23,38	3,68	0,70	0,29	0,05	0,42	0,01	99,92	77,97
MM8	1713,6	53,27	0,21	4,49	12,78	0,22	23,89	3,73	0,40	0,16	0,02	0,47	0,01	99,63	78,49
MM9A	1714	53,66	0,21	4,43	12,77	0,23	23,80	3,72	0,66	0,26	0,06	0,44	0,00	100,25	78,43
MM9B	1714	9,32	0,95	14,08	23,02	0,25	9,66	1,19	0,30	0,14	0,02	43,35	0,04	102,24	45,01
MM10	1714,8	11,65	0,71	14,19	25,30	0,23	10,19	1,60	0,36	0,27	0,03	36,41	0,02	100,91	44,02
MM11	1715,4	21,32	0,65	15,40	19,13	0,21	11,29	3,91	0,69	0,14	0,02	25,48	0,02	98,22	53,51
MM12	1715,8	54,51	0,21	7,56	10,27	0,18	20,03	3,95	1,03	0,97	0,06	0,63	0,00	99,40	79,18
MM13	1716	53,04	0,20	7,21	11,60	0,20	21,10	4,45	1,03	0,59	0,07	1,03	0,01	100,51	78,02
MM14	1717,2	23,58	0,66	13,75	18,86	0,22	13,42	2,76	0,66	0,32	0,03	24,50	0,02	98,73	58,14
MM15	1718	16,40	0,85	16,50	20,38	0,21	9,50	2,52	0,60	0,21	0,03	32,50	0,04	99,66	47,64
MM16	1719	25,87	0,50	20,87	15,05	0,16	7,99	6,39	0,84	0,05	0,01	22,10	0,02	99,80	50,87
MM17	1719,2	40,09	0,21	28,04	6,92	0,07	3,34	12,25	1,61	0,09	0,01	5,68	0,01	98,31	48,51
MM18	1719,6	44,11	0,12	29,68	4,04	0,05	1,78	13,79	1,43	0,11	0,01	2,89	0,00	98,01	46,18

Sample	Depth (m)	SiO_2	TiO_2	Al_2O_3	Fe_2O_3	MnO	MgO	CaO	Na_2O	K_2O	P_2O_5	Cr_2O_3	LOI	Total	Mg#
MM19	1721	45,51	0,10	31,48	2,74	0,03	0,77	14,70	1,79	0,12	0,01	1,97	0,00	99,22	35,34
MM21	1722	37,85	0,28	27,09	9,13	0,10	4,15	11,23	1,63	0,12	0,01	7,00	0,01	98,59	46,99
MM22	1722,3	39,62	0,23	27,81	7,66	0,08	3,71	11,87	1,63	0,12	0,01	8,78	0,00	101,51	48,62
MM23A	1722,7	43,91	0,17	24,60	6,58	0,09	6,53	11,38	1,65	0,10	0,01	4,21	0,00	99,22	65,96
MM23B	1722,7	16,00	0,87	17,61	21,15	0,22	9,12	3,29	0,46	0,04	0,02	33,22	0,04	101,95	45,69
MM24	1724	51,26	0,11	15,75	7,28	0,13	14,63	8,69	0,99	0,16	0,01	0,28	0,02	99,30	79,68
MM25	1728	51,09	0,12	13,53	8,11	0,15	17,43	7,96	1,02	0,05	0,01	0,25	0,00	99,71	80,74
MM26	1733	49,75	0,09	17,79	6,05	0,10	12,94	9,82	1,41	0,06	0,01	0,21	0,00	98,23	80,68
MM27	1737	49,05	0,09	19,86	5,47	0,09	12,29	10,17	1,38	0,09	0,02	0,21	0,00	98,71	81,43
MM28	1741	50,52	0,10	18,94	5,89	0,10	12,41	10,29	1,51	0,08	0,02	0,21	0,00	100,06	80,44
MM29	1743	50,03	0,09	19,42	5,58	0,10	11,54	10,40	1,53	0,20	0,02	0,26	0,00	99,16	80,12
MM30	1745	50,26	0,09	19,07	5,78	0,11	12,12	10,21	1,11	0,19	0,02	0,30	0,00	99,23	80,38
MM31	1747	49,96	0,08	20,73	5,33	0,10	10,81	10,87	1,33	0,11	0,01	0,45	0,00	99,77	79,82
MM32	1747,5	49,65	0,09	18,56	7,09	0,12	14,53	9,89	1,31	0,04	0,01	0,42	0,00	101,70	79,99
MM33	1748	49,13	0,11	16,46	7,63	0,13	14,84	8,62	1,08	0,01	0,04	1,41	0,00	99,45	79,14
MM34	1748,6	14,96	0,67	17,06	24,61	0,20	5,08	2,29	0,48	0,06	0,02	33,82	0,03	99,21	28,73
MM35A	1749,2	47,43	0,09	30,43	2,95	0,04	2,34	14,56	1,57	0,13	0,01	1,52	1,00	100,06	60,73
MM35B	1749,2	14,46	0,69	17,48	21,44	0,23	9,94	2,40	0,43	0,05	0,02	34,35	0,04	101,44	47,48
MM36	1749,5	48,10	0,04	30,11	1,44	0,02	1,29	15,24	1,64	0,16	0,01	0,15	0,00	98,20	63,53
MM37	1749,9	48,11	0,04	30,48	1,51	0,02	1,38	15,40	1,55	0,12	0,01	0,07	0,00	98,69	64,02
MM38	1750,3	51,08	0,09	17,66	6,86	0,12	13,16	9,81	0,82	0,11	0,01	0,23	0,00	99,95	78,91

Sample	Depth (m)	SiO_2	TiO_2	Al_2O_3	Fe_2O_3	MnO	MgO	CaO	Na_2O	K_2O	P_2O_5	Cr_2O_3	LOI	Total	Mg#
MM39	1753	50,39	0,09	16,72	6,87	0,12	13,91	9,29	1,22	0,38	0,02	0,25	0,00	99,25	79,79
MM40	1754	51,62	0,11	13,44	7,94	0,15	17,11	7,74	0,67	0,13	0,01	0,29	0,00	99,19	80,79
MM41	1755	51,04	0,12	13,05	8,37	0,15	18,00	7,12	0,94	0,04	0,01	0,49	0,00	99,33	80,77
MM42A	1756	52,94	0,23	4,14	12,04	0,22	24,80	3,70	0,90	0,28	0,02	0,47	0,00	99,72	80,07
MM42B	1756	51,98	0,13	12,20	8,68	0,15	19,77	7,38	0,50	0,02	0,01	0,70	0,00	101,53	81,64
MM43	1756,7	13,50	0,69	15,92	20,56	0,22	11,45	1,78	0,41	0,02	0,01	35,50	0,04	100,01	52,07
MM44	1757	11,61	0,64	15,31	22,54	0,20	10,36	1,46	0,31	0,01	0,01	39,30	0,03	101,71	47,27
MM45	1757,3	51,78	0,20	5,50	11,84	0,20	23,60	3,82	0,77	0,23	0,17	1,69	0,01	99,80	79,55
MM46	1757,5	51,91	0,20	3,80	12,16	0,22	26,46	3,18	0,58	0,03	0,02	0,99	0,00	99,54	80,94
MM47	1759	52,13	0,23	4,46	12,10	0,22	24,78	3,49	0,57	0,07	0,02	1,42	0,00	99,48	79,99
MM48	1763	51,34	0,23	5,23	12,55	0,20	23,61	3,82	0,92	0,15	0,01	1,35	0,00	99,39	78,59
MM49	1767,1	53,27	0,24	5,23	11,47	0,20	23,87	3,93	0,65	0,16	0,04	0,80	0,06	99,91	80,24
MM50	1771	54,07	0,30	3,29	12,50	0,22	25,37	3,53	0,61	0,30	0,27	0,75	0,00	101,20	79,84
MM51	1776	52,67	0,15	6,93	10,43	0,19	23,08	4,48	0,73	0,11	0,02	0,59	0,00	99,37	81,20
MM52	1776,6	53,59	0,21	5,97	10,48	0,19	23,07	5,16	0,71	0,20	0,04	0,52	0,00	100,13	81,11
MM53	1778	51,09	0,29	5,22	12,52	0,22	25,72	3,20	0,39	0,11	0,03	2,46	0,00	101,24	80,04
MM54A	1778,3	11,19	0,71	13,55	20,66	0,24	12,10	0,94	0,49	0,07	0,01	41,26	0,04	101,18	53,33
MM54B	1778,3	50,54	0,27	4,23	12,84	0,22	26,45	3,14	0,13	0,01	0,01	3,86	0,01	101,69	80,08
MM55	1779	11,46	0,54	16,52	11,90	0,20	12,05	2,86	0,15	0,26	0,01	43,26	0,04	99,15	66,39
MM56	1779,2	45,89	0,42	7,53	13,20	0,20	21,68	3,63	0,55	0,20	0,25	5,85	0,01	99,38	76,22
MM57	1779,7	51,30	0,25	5,81	12,74	0,19	23,64	4,44	0,72	0,07	0,02	0,48	0,00	99,67	78,36

Sample	Depth (m)	SiO_2	TiO_2	Al_2O_3	Fe_2O_3	MnO	MgO	CaO	Na_2O	K_2O	P_2O_5	Cr_2O_3	LOI	Total	Mg#
MM58	1780	53,55	0,24	5,94	10,27	0,19	22,85	4,48	0,90	0,17	0,04	0,40	0,00	99,02	81,28
MM59	1781,2	53,74	0,24	4,91	11,23	0,20	24,45	3,71	0,86	0,07	0,09	0,41	0,00	99,91	80,95
MM60	1786	53,78	0,26	4,89	11,56	0,20	25,56	3,19	0,75	0,08	0,09	0,45	0,00	100,80	81,18
MM61	1786,5	53,75	0,25	4,95	11,61	0,21	23,43	3,87	1,03	0,11	0,13	0,39	0,00	99,72	79,75
MM62	1788	55,42	0,37	2,12	12,91	0,23	26,75	2,43	0,24	0,40	0,03	0,32	0,00	101,21	80,17
MM63	1793	53,62	0,16	6,35	10,89	0,19	23,81	4,34	0,81	0,08	0,01	0,40	0,00	100,66	81,01
MM64	1794	51,22	0,19	6,12	10,17	0,18	26,53	4,37	0,96	0,21	0,03	0,41	0,00	100,38	83,57
MM65	1797	54,82	0,29	2,96	13,00	0,22	25,44	2,89	0,43	0,32	0,05	0,66	0,50	101,57	79,25

Appendix B

Table B-1: Whole-rock trace element composition per analysed sample in ppm, along with Cr/V ratio.

Sample	Depth (m)	Ba	Co	Cr	Cu	Nb	Ni	Pb	Rb	Sc	Sr	Th	U	V	Y	Zn	Zr	Cr/V
MM1	1701	70	50	1280	10	b.d.l	290	b.d.l	b.d.l	20	250	b.d.l	b.d.l	80	b.d.l	50	10	16,00
MM2	1705	60	60	1420	10	b.d.l	370	b.d.l	b.d.l	20	240	b.d.l	b.d.l	90	b.d.l	70	10	15,78
MM3	1710,3	290	50	1330	10	10	280	20	30	20	130	b.d.l	b.d.l	90	b.d.l	110	80	14,78
MM4	1711	110	70	1880	10	b.d.l	450	b.d.l	10	30	160	b.d.l	b.d.l	140	b.d.l	90	30	13,43
MM5	1712	40	60	1650	20	b.d.l	380	b.d.l	b.d.l	30	200	b.d.l	b.d.l	100	b.d.l	80	b.d.l	16,50
MM6	1712,3	80	90	2720	10	b.d.l	590	b.d.l	b.d.l	40	70	b.d.l	b.d.l	180	b.d.l	130	10	15,11
MM7	1713	100	90	2890	20	b.d.l	610	b.d.l	10	40	70	b.d.l	b.d.l	170	b.d.l	90	10	17,00
MM8	1713,6	17	90	3200	20	b.d.l	640	b.d.l	b.d.l	40	60	b.d.l	b.d.l	160	b.d.l	80	10	20,00
MM9A	1714	90	90	3000	30	b.d.l	600	b.d.l	b.d.l	40	60	b.d.l	b.d.l	160	b.d.l	120	10	18,75
MM9B	1714	160	100	296600	4	b.d.l	390	b.d.l	b.d.l	60	30	b.d.l	b.d.l	2210	b.d.l	500	b.d.l	134,21
MM10	1714,8	140	100	249130	4	b.d.l	370	b.d.l	b.d.l	60	40	b.d.l	b.d.l	1880	b.d.l	420	10	132,52
MM11	1715,4	130	90	174340	10	b.d.l	380	b.d.l	b.d.l	50	80	b.d.l	b.d.l	1490	b.d.l	350	10	117,01
MM12	1715,8	230	70	4310	20	b.d.l	460	b.d.l	30	30	100	b.d.l	b.d.l	130	b.d.l	70	40	33,15
MM13	1716	200	80	7050	10	b.d.l	470	b.d.l	10	40	100	b.d.l	b.d.l	180	b.d.l	100	20	39,17
MM14	1717,2	120	90	155990	30	b.d.l	380	b.d.l	b.d.l	50	70	b.d.l	b.d.l	1430	b.d.l	320	10	109,08
MM15	1718	140	10	216390	50	b.d.l	370	b.d.l	b.d.l	50	70	b.d.l	b.d.l	2110	b.d.l	430	10	102,55
MM16	1719	70	70	121770	10	b.d.l	340	b.d.l	b.d.l	30	190	b.d.l	b.d.l	1160	b.d.l	290	b.d.l	104,97
MM17	1719,2	40	30	38880	10	b.d.l	50	b.d.l	b.d.l	20	360	b.d.l	b.d.l	380	b.d.l	110	b.d.l	102,32
MM18	1719,6	30	20	19780	10	b.d.l	30	b.d.l	b.d.l	10	420	b.d.l	b.d.l	190	b.d.l	60	b.d.l	104,11
MM19	1721	40	10	13510	10	b.d.l	70	b.d.l	b.d.l	10	450	b.d.l	b.d.l	120	b.d.l	50	b.d.l	112,58

Sample	Depth (m)	Ba	Co	Cr	Cu	Nb	Ni	Pb	Rb	Sc	Sr	Th	U	V	Y	Zn	Zr	Cr/V
MM20	1721,7	70	50	62870	10	b.d.l	110	b.d.l	b.d.l	20	310	b.d.l	b.d.l	600	b.d.l	160	b.d.l	104,78
MM21	1722	70	40	47890	10	b.d.l	90	b.d.l	b.d.l	20	350	b.d.l	b.d.l	440	b.d.l	150	b.d.l	108,84
MM22	1722,3	70	50	60050	10	b.d.l	130	b.d.l	b.d.l	20	320	b.d.l	b.d.l	500	b.d.l	170	10	120,10
MM23A	1722,7	50	40	28800	10	b.d.l	170	b.d.l	b.d.l	20	330	b.d.l	b.d.l	260	b.d.l	90	b.d.l	110,77
MM23B	1722,7	140	110	227310	30	b.d.l	460	b.d.l	b.d.l	50	80	b.d.l	b.d.l	1880	b.d.l	460	10	120,91
MM24	1724	40	50	1930	10	b.d.l	300	b.d.l	b.d.l	30	240	b.d.l	b.d.l	70	b.d.l	130	b.d.l	27,57
MM25	1728	30	60	1740	4	b.d.l	370	b.d.l	b.d.l	30	210	b.d.l	b.d.l	70	b.d.l	70	b.d.l	24,86
MM26	1733	30	40	1420	4	b.d.l	250	b.d.l	b.d.l	20	280	b.d.l	b.d.l	50	b.d.l	70	b.d.l	28,40
MM27	1737	40	40	1410	10	b.d.l	270	b.d.l	b.d.l	20	300	b.d.l	b.d.l	50	b.d.l	50	10	28,20
MM28	1741	30	40	1450	10	b.d.l	250	b.d.l	b.d.l	20	290	b.d.l	b.d.l	40	b.d.l	50	10	36,25
MM29	1743	40	40	1760	10	b.d.l	220	b.d.l	b.d.l	20	300	b.d.l	b.d.l	50	b.d.l	50	10	35,20
MM30	1745	30	40	2050	10	b.d.l	200	b.d.l	b.d.l	20	290	b.d.l	b.d.l	50	b.d.l	50	b.d.l	41,00
MM31	1747	30	40	3070	10	b.d.l	210	b.d.l	b.d.l	20	290	b.d.l	b.d.l	50	b.d.l	40	b.d.l	61,40
MM32	1747,5	20	50	2850	20	b.d.l	330	b.d.l	b.d.l	20	240	b.d.l	b.d.l	70	b.d.l	40	b.d.l	40,71
MM33	1748	40	50	9660	10	b.d.l	300	b.d.l	b.d.l	20	230	b.d.l	b.d.l	130	b.d.l	50	b.d.l	74,31
MM34	1748,6	160	100	212490	50	b.d.l	380	b.d.l	b.d.l	50	60	b.d.l	b.d.l	1710	b.d.l	430	b.d.l	124,26
MM35A	1749,2	160	110	235030	20	b.d.l	400	b.d.l	b.d.l	60	50	b.d.l	b.d.l	2260	b.d.l	470	b.d.l	104,00
MM35B	1749,2	40	10	10410	10	b.d.l	10	b.d.l	b.d.l	20	380	b.d.l	b.d.l	110	b.d.l	500	10	94,64
MM36	1749,5	10	3	1010	10	b.d.l	90	b.d.l	b.d.l	10	430	b.d.l	b.d.l	10	b.d.l	30	b.d.l	101,00
MM37	1749,9	10	3	470	10	b.d.l	60	b.d.l	b.d.l	10	450	b.d.l	b.d.l	5	b.d.l	20	b.d.l	94,00
MM38	1750,3	20	40	1570	30	b.d.l	210	b.d.l	b.d.l	20	260	b.d.l	b.d.l	70	b.d.l	90	b.d.l	22,43

Sample	Depth (m)	Ba	Co	Cr	Cu	Nb	Ni	Pb	Rb	Sc	Sr	Th	U	V	Y	Zn	Zr	Cr/V
MM39	1753	30	50	1680	10	b.d.l	280	b.d.l	b.d.l	20	240	b.d.l	b.d.l	70	b.d.l	40	b.d.l	24,00
MM40	1754	30	60	1970	10	b.d.l	320	b.d.l	b.d.l	30	190	b.d.l	b.d.l	80	b.d.l	60	b.d.l	24,63
MM41	1755	40	70	3340	30	b.d.l	450	b.d.l	b.d.l	30	160	b.d.l	b.d.l	110	b.d.l	80	b.d.l	30,36
MM42A	1756	30	70	3190	30	b.d.l	400	b.d.l	b.d.l	30	160	b.d.l	b.d.l	110	b.d.l	90	b.d.l	29,00
MM42B	1756	60	90	4780	20	b.d.l	610	b.d.l	b.d.l	40	50	b.d.l	b.d.l	190	b.d.l	100	10	25,16
MM43	1756,7	140	100	237130	20	b.d.l	390	b.d.l	b.d.l	60	40	b.d.l	b.d.l	1980	b.d.l	430	b.d.l	119,76
MM44	1757	140	90	23440	20	b.d.l	330	b.d.l	b.d.l	60	40	b.d.l	b.d.l	1950	b.d.l	400	b.d.l	12,02
MM45	1757,3	110	90	11570	20	b.d.l	560	b.d.l	10	40	60	b.d.l	b.d.l	210	b.d.l	100	30	55,10
MM46	1757,5	60	90	6750	20	b.d.l	620	b.d.l	b.d.l	40	50	b.d.l	b.d.l	160	b.d.l	90	10	42,19
MM47	1759	90	90	9730	30	b.d.l	590	b.d.l	b.d.l	40	50	b.d.l	b.d.l	190	b.d.l	80	10	51,21
MM48	1763	130	90	9270	40	b.d.l	570	b.d.l	b.d.l	40	70	b.d.l	b.d.l	180	b.d.l	90	10	51,50
MM49	1767,1	110	80	5480	40	b.d.l	580	b.d.l	10	40	70	b.d.l	b.d.l	150	b.d.l	90	20	36,53
MM50	1771	120	90	5140	60	b.d.l	660	b.d.l	10	40	40	b.d.l	b.d.l	180	b.d.l	100	30	28,56
MM51	1776	60	80	4070	30	b.d.l	610	b.d.l	b.d.l	40	100	b.d.l	b.d.l	110	b.d.l	80	10	37,00
MM52	1776,6	120	80	3530	50	b.d.l	600	b.d.l	10	40	80	b.d.l	b.d.l	130	b.d.l	80	20	27,15
MM53	1778	90	90	16840	60	b.d.l	610	b.d.l	b.d.l	50	30	b.d.l	b.d.l	260	b.d.l	100	10	64,77
MM54A	1778,3	60	90	21550	30	b.d.l	600	b.d.l	b.d.l	40	40	b.d.l	b.d.l	280	b.d.l	110	10	76,96
MM54B	1778,3	160	100	26430	10	b.d.l	360	b.d.l	b.d.l	60	20	b.d.l	b.d.l	1750	b.d.l	410	b.d.l	15,10
MM55	1779	150	100	296020	4	b.d.l	360	b.d.l	b.d.l	60	10	b.d.l	b.d.l	1810	b.d.l	420	b.d.l	163,55
MM56	1779,2	160	100	40050	40	b.d.l	580	b.d.l	10	40	30	b.d.l	b.d.l	430	b.d.l	160	40	93,14
MM57	1779,7	80	80	3250	70	b.d.l	590	b.d.l	b.d.l	40	50	b.d.l	b.d.l	150	b.d.l	100	10	21,67
MM58	1780	130	80	2770	60	b.d.l	570	b.d.l	10	40	900	b.d.l	b.d.l	130	b.d.l	110	30	21,31
MM59	1781,2	90	90	2820	20	b.d.l	560	b.d.l	b.d.l	40	70	b.d.l	b.d.l	130	b.d.l	80	20	21,69
MM60	1786	100	90	3080	90	b.d.l	610	b.d.l	b.d.l	40	60	b.d.l	b.d.l	140	b.d.l	100	20	22,00
MM61	1786,5	100	80	2670	10	b.d.l	510	b.d.l	b.d.l	40	90	b.d.l	b.d.l	130	b.d.l	100	10	20,54

Sample	Depth (m)	Ba	Co	Cr	Cu	Nb	Ni	Pb	Rb	Sc	Sr	Th	U	V	Y	Zn	Zr	Cr/V
MM62	1788	110	90	2170	10	b.d.l	580	b.d.l	20	40	10	b.d.l	b.d.l	160	b.d.l	90	40	13,56	14,5
MM63	1793	50	80	2730	10	b.d.l	470	b.d.l	b.d.l	40	90	b.d.l	b.d.l	100	b.d.l	110	b.d.l	27,30	
MM64	1794	100	80	2800	20	b.d.l	510	b.d.l	b.d.l	40	90	b.d.l	b.d.l	110	b.d.l	100	20	25,45	
MM65	1797	70	90	4490	60	b.d.l	580	b.d.l	b.d.l	50	30	b.d.l	b.d.l	150	b.d.l	80	30	29,93	

Appendix C

Table C-1: Whole-rock REE composition per analysed sample in ppm.

Sample	Depth (m)	La	Ce	Pr	Nd	Sm	Eu	Gd	Tb	Dy	Ho	Er	Tm	Yb	Lu
MM1	1701	2,555	4,636	0,508	1,99	0,396	0,315	0,401	0,061	0,406	0,089	0,272	0,043	0,313	0,05
MM2	1705	2,35	4,05	0,451	1,812	0,371	0,293	0,382	0,059	0,393	0,087	0,266	0,044	0,312	0,048
MM3	1710,3	3,337	6,24	0,657	2,394	0,446	0,231	0,426	0,062	0,411	0,085	0,258	0,042	0,301	0,048
MM4	1711	4,914	9,198	1,005	3,957	0,819	0,323	0,817	0,125	0,805	0,171	0,507	0,079	0,561	0,086
MM5	1712	1,276	2,059	0,226	0,912	0,2	0,258	0,227	0,04	0,287	0,066	0,216	0,036	0,276	0,045
MM6	1712,3	2,98	5,487	0,659	2,86	0,713	0,235	0,795	0,13	0,897	0,199	0,593	0,096	0,669	0,107
MM8	1713,6	2,028	4,064	0,52	2,359	0,604	0,217	0,675	0,113	0,786	0,176	0,54	0,088	0,616	0,101
MM9B	1714	1,004	1,628	0,175	0,681	0,136	0,067	0,155	0,024	0,16	0,035	0,105	0,016	0,111	0,017
MM10	1714,8	1,389	2,411	0,265	1,063	0,219	0,102	0,234	0,037	0,238	0,052	0,15	0,024	0,164	0,024
MM11	1715,4	1,667	2,805	0,307	1,228	0,246	0,162	0,262	0,039	0,274	0,062	0,19	0,031	0,228	0,034
MM12	1715,8	11,348	20,639	2,168	8,055	1,478	0,341	1,404	0,203	1,264	0,262	0,757	0,116	0,794	0,118
MM13	1716	5,932	12,146	1,403	5,817	1,231	0,342	1,228	0,186	1,189	0,246	0,721	0,112	0,758	0,118
MM14	1717,2	1,338	2,463	0,281	1,141	0,243	0,122	0,266	0,041	0,285	0,063	0,191	0,031	0,222	0,035
MM16	1719	1,171	1,911	0,209	0,786	0,143	0,172	0,141	0,02	0,13	0,028	0,083	0,013	0,095	0,014
MM17	1719,2	1,723	2,867	0,294	1,122	0,192	0,287	0,17	0,021	0,122	0,024	0,07	0,01	0,067	0,01
MM18	1719,6	2,517	3,277	0,341	1,29	0,213	0,336	0,188	0,023	0,135	0,026	0,072	0,01	0,068	0,009
MM19	1721	2,437	3,06	0,317	1,201	0,186	0,406	0,153	0,017	0,093	0,016	0,042	0,005	0,032	0,004
MM20	1721,7	2,133	3,542	0,383	1,468	0,256	0,344	0,239	0,032	0,183	0,037	0,104	0,015	0,098	0,014

Sample	Depth (m)	La	Ce	Pr	Nd	Sm	Eu	Gd	Tb	Dy	Ho	Er	Tm	Yb	Lu
MM21	1722	2,507	4,097	0,432	1,617	0,265	0,391	0,234	0,029	0,161	0,03	0,082	0,012	0,075	0,011
MM22	1722,3	1,916	3,109	0,333	1,268	0,215	0,333	0,201	0,027	0,169	0,035	0,105	0,017	0,12	0,018
MM23A	1722,7	1,519	2,354	0,267	1,078	0,212	0,119	0,213	0,031	0,188	0,037	0,105	0,015	0,101	0,015
MM24	1724	1,606	2,673	0,29	1,142	0,229	0,246	0,244	0,038	0,26	0,059	0,18	0,03	0,216	0,034
MM25	1728	1,427	2,297	0,248	1,004	0,215	0,222	0,239	0,039	0,279	0,065	0,205	0,035	0,258	0,041
MM26	1733	1,664	2,571	0,282	1,107	0,206	0,252	0,22	0,033	0,226	0,049	0,154	0,026	0,179	0,028
MM27	1737	1,919	3,249	0,345	1,355	0,263	0,25	0,266	0,04	0,263	0,056	0,174	0,028	0,203	0,031
MM28	1741	1,867	3,196	0,346	1,349	0,269	0,247	0,271	0,042	0,275	0,06	0,184	0,03	0,214	0,032
MM29	1743	1,717	2,964	0,329	1,288	0,25	0,251	0,255	0,038	0,255	0,056	0,168	0,027	0,19	0,029
MM31	1747	1,688	2,433	0,267	1,032	0,197	0,241	0,202	0,029	0,194	0,041	0,127	0,02	0,143	0,022
MM33	1748	1,261	2,009	0,221	0,866	0,17	0,192	0,186	0,029	0,207	0,047	0,146	0,024	0,173	0,027
MM34	1748,6	2,015	3,455	0,385	1,548	0,303	0,13	0,298	0,042	0,259	0,054	0,154	0,024	0,152	0,023
MM35A	1749,2	2,378	4,338	0,439	1,763	0,336	0,133	0,328	0,045	0,28	0,058	0,165	0,025	0,167	0,026
MM35B	1749,2	2,443	4,273	0,447	1,737	0,309	0,341	0,282	0,036	0,212	0,041	0,113	0,016	0,104	0,015
MM36	1749,5	1,543	2,5	0,264	1,017	0,176	0,298	0,16	0,021	0,125	0,024	0,066	0,01	0,063	0,009
MM37	1749,9	1,453	2,364	0,25	0,959	0,165	0,288	0,146	0,019	0,114	0,022	0,063	0,009	0,059	0,008
MM38	1750,3	1,184	1,864	0,204	0,817	0,166	0,224	0,177	0,029	0,203	0,046	0,144	0,024	0,171	0,028
MM40	1754	1,247	1,963	0,214	0,872	0,184	0,189	0,217	0,036	0,264	0,061	0,196	0,033	0,233	0,038
MM41	1755	1,239	1,87	0,202	0,825	0,173	0,19	0,201	0,034	0,24	0,056	0,178	0,03	0,218	0,035
MM42B	1756	1,559	2,15	0,237	1,011	0,277	0,221	0,327	0,058	0,417	0,095	0,295	0,051	0,356	0,055
MM43	1756,7	1,279	2,124	0,234	0,948	0,181	0,09	0,188	0,029	0,187	0,04	0,121	0,019	0,124	0,019

Sample	Depth (m)	La	Ce	Pr	Nd	Sm	Eu	Gd	Tb	Dy	Ho	Er	Tm	Yb	Lu
MM44	1757	1,154	1,884	0,207	0,812	0,157	0,086	0,16	0,023	0,154	0,032	0,097	0,015	0,104	0,016
MM45	1757,3	10,485	22,307	2,506	10,24	1,895	0,338	1,768	0,239	1,42	0,288	0,799	0,118	0,769	0,119
MM46	1757,5	1,921	3,519	0,418	1,824	0,46	0,16	0,561	0,095	0,686	0,154	0,479	0,078	0,538	0,085
MM47	1759	2,667	4,915	0,578	2,474	0,593	0,196	0,700	0,114	0,793	0,175	0,538	0,088	0,615	0,098
MM48	1763	2,734	5,447	0,679	2,976	0,697	0,289	0,756	0,123	0,821	0,179	0,533	0,083	0,567	0,091
MM49	1767,1	4,332	8,019	0,918	3,74	0,793	0,264	0,862	0,132	0,873	0,188	0,564	0,089	0,622	0,096
MM50	1771	14,297	28,213	3,155	12,7	2,3	0,418	2,147	0,283	1,664	0,337	0,941	0,14	0,906	0,138
MM51	1776	1,584	2,784	0,318	1,36	0,328	0,184	0,381	0,066	0,477	0,11	0,343	0,055	0,402	0,066
MM53	1778	2,824	5,399	0,666	2,974	0,726	0,203	0,819	0,135	0,923	0,198	0,596	0,09	0,638	0,102
MM54A	1778,3	0,656	1,043	0,116	0,473	0,107	0,045	0,123	0,019	0,131	0,028	0,084	0,012	0,089	0,014
MM54B	1778,3	1,497	2,655	0,34	1,569	0,441	0,14	0,55	0,098	0,716	0,16	0,494	0,078	0,557	0,087
MM55	1779	0,699	1,117	0,126	0,497	0,103	0,041	0,106	0,016	0,112	0,024	0,075	0,011	0,08	0,012
MM56	1779,2	11,445	24,739	3,077	12,846	2,343	0,374	2,092	0,268	1,523	0,299	0,83	0,115	0,77	0,118
MM59	1781,2	6,53	11,52	1,325	5,481	1,085	0,323	1,1	0,162	1,053	0,222	0,652	0,097	0,673	0,108
MM60	1786	10,922	23,074	2,724	11,208	2,107	0,435	2,051	0,275	1,651	0,334	0,937	0,139	0,908	0,137
MM62	1788	7,59	12,752	1,353	5,443	1,219	0,226	1,3	0,201	1,316	0,283	0,84	0,132	0,893	0,139
MM63	1793	1,744	3,09	0,354	1,526	0,363	0,194	0,436	0,074	0,527	0,118	0,378	0,061	0,443	0,07
MM64	1794	3,578	6,657	0,779	3,192	0,686	0,242	0,715	0,11	0,739	0,16	0,468	0,072	0,517	0,083

Appendix D

Table D-1: In-situ plagioclase major element composition for individual spots in wt.% along with anorthite content (An%).

Sample/Points	Depth (m)	SiO_2	TiO_2	Al_2O_3	Cr_2O_3	FeO	MnO	MgO	CaO	Na_2O	K_2O	Total	An%
MM1-1.2	1701	49,69	0,02	30,75	<0,01	0,26	<0,01	0,02	15,2	3,03	0,26	99,23	82,21
MM1-1.3	1701	50,44	0,04	30,8	<0,01	0,25	<0,01	0,01	14,8	3,23	0,25	99,81	80,96
MM1-1.4	1701	48,95	0,03	30,91	<0,01	0,27	0,01	0,01	15,54	2,91	0,22	98,86	83,24
MM1-1.5	1701	50,87	0,03	30,93	<0,01	0,24	<0,01	0,03	14,75	3,23	0,25	100,32	80,91
MM1-2.1	1701	49,65	0,03	31,32	0,01	0,3	0,01	0,03	15,31	2,86	0,18	99,69	83,43
MM1-2.2	1701	49,44	0,02	31,05	<0,01	0,25	<0,01	0,03	15,28	2,94	0,22	99,24	82,86
MM1-2.3	1701	50,68	0,03	30,81	<0,01	0,27	<0,01	0,03	14,58	3,27	0,23	99,88	80,64
MM1-2.4	1701	49,44	0,04	31,21	0,01	0,28	0,01	0,01	15,41	2,97	0,21	99,59	82,89
MM1-2.5	1701	49,8	0,02	31,04	<0,01	0,28	<0,01	0,03	15,06	3,06	0,22	99,5	82,12
MM1-3.1	1701	50,63	<0,01	31,09	0,02	0,37	<0,01	0,01	14,81	3,11	0,25	100,29	81,51
MM1-3.2	1701	49,95	0,02	30,63	<0,01	0,3	<0,01	0,02	14,94	3,1	0,24	99,2	81,73
MM1-3.3	1701	49,96	0,02	30,94	0,01	0,31	<0,01	0,02	14,82	3,09	0,22	99,4	81,74
MM1-3.4	1701	49,55	0,03	30,76	0,01	0,36	0,01	0,02	15,1	3,11	0,25	99,19	81,80
MM1-3.5	1701	50,88	0,05	31,37	<0,01	0,38	0,01	0,02	14,67	3,12	0,26	100,76	81,27
MM2-1.1	1705	50,6	0,01	30,85	<0,01	0,26	0,01	0,03	14,68	3,11	0,23	99,79	81,47
MM2-1.2	1705	49,69	<0,01	31,01	<0,01	0,24	0,01	0,02	15,23	2,88	0,19	99,28	83,22
MM2-1.3	1705	50,45	0,03	30,64	<0,01	0,26	<0,01	0,04	14,66	3,26	0,23	99,57	80,77
MM2-1.4	1705	49,33	0,02	31,33	<0,01	0,26	<0,01	0,02	15,36	2,79	0,15	99,26	83,93
MM2-1.5	1705	49,93	0,04	31,34	<0,01	0,26	<0,01	0,03	15,33	2,83	0,2	99,94	83,50

Sample/Points	Depth (m)	SiO_2	TiO_2	Al_2O_3	Cr_2O_3	FeO	MnO	MgO	CaO	Na_2O	K_2O	Total	An%
MM2-2.1	1705	49,61	0,03	31,41	<0,01	0,23	<0,01	0,01	15,40	2,83	0,18	99,69	83,65
MM2-2.2	1705	49,74	<0,01	31,39	0,01	0,20	<0,01	0,02	15,39	2,91	0,19	99,85	83,23
MM2-2.3	1705	50,31	0,02	31,08	<0,01	0,27	<0,01	<0,01	15,08	3,04	0,22	100,01	82,22
MM2-2.4	1705	50,25	0,02	31,33	<0,01	0,24	<0,01	0,02	15,17	2,95	0,16	100,14	82,99
MM2-2.5	1705	50,79	0,01	30,90	<0,01	0,25	<0,01	0,02	14,85	3,26	0,21	100,3	81,06
MM2-3.1	1705	50,66	0,01	31,30	<0,01	0,34	<0,01	0,02	14,86	2,99	0,20	100,39	82,33
MM2-3.2	1705	50,37	0,01	30,98	<0,01	0,34	<0,01	0,02	14,82	3,11	0,22	99,87	81,65
MM2-3.3	1705	50,19	0,01	30,81	0,02	0,35	<0,01	0,03	14,91	3,21	0,23	99,76	81,25
MM2-3.4	1705	50,05	0,01	31,26	<0,01	0,41	<0,01	0,01	15,02	3,03	0,21	100,01	82,26
MM2-3.5	1705	49,94	<0,01	30,91	0,01	0,36	<0,01	0,02	14,81	3,05	0,21	99,31	81,96
MM3-1.1	1710,3	55,20	0,01	27,27	0,01	0,20	0,01	<0,01	10,27	5,85	0,16	98,99	63,08
MM3-1.2	1710,3	55,61	0,01	27,31	<0,01	0,18	<0,01	<0,01	10,19	5,77	0,19	99,26	63,10
MM3-1.3	1710,3	56,02	0,02	26,67	<0,01	0,16	<0,01	<0,01	9,46	6,29	0,19	98,81	59,35
MM3-1.4	1710,3	55,10	0,03	27,76	0,01	0,19	<0,01	0,02	10,46	5,57	0,17	99,29	64,57
MM3-1.5	1710,3	55,06	<0,01	27,10	0,01	0,20	<0,01	0,01	10,09	6,06	0,17	98,71	61,83
MM3-2.1	1710,3	50,99	<0,01	31,04	<0,01	0,25	<0,01	0,01	14,64	3,36	0,05	100,34	81,11
MM3-2.2	1710,3	50,28	<0,01	30,74	<0,01	0,28	<0,01	<0,01	14,55	3,44	0,12	99,42	80,34
MM3-2.3	1710,3	51,06	0,02	30,94	0,01	0,15	<0,01	0,01	14,23	3,60	0,05	100,06	79,59
MM3-2.4	1710,3	56,28	<0,01	27,71	<0,01	0,22	<0,01	<0,01	10,43	5,54	0,10	100,29	64,90
MM3-3.1	1710,3	50,95	0,02	30,60	<0,01	0,16	<0,01	<0,01	14,10	3,70	0,08	99,62	78,86
MM4-1.1	1711	49,77	0,05	30,48	<0,01	0,24	<0,01	0,01	14,42	3,31	0,20	98,49	80,42
MM4-1.2	1711	49,63	0,04	30,81	<0,01	0,23	0,01	0,02	14,73	3,13	0,18	98,78	81,65

Sample/Points	Depth (m)	SiO_2	TiO_2	Al_2O_3	Cr_2O_3	FeO	MnO	MgO	CaO	Na_2O	K_2O	Total	An%
MM4-1.3	1711	49,58	0,03	30,97	<0,01	0,25	<0,01	0,02	14,80	3,04	0,17	98,85	82,18
MM4-2.1	1711	49,77	<0,01	31,35	0,01	0,21	0,02	0,01	15,03	3,08	0,17	99,65	82,22
MM4-2.2	1711	49,29	0,03	31,29	0,01	0,21	0,01	0,01	14,89	2,96	0,18	98,88	82,58
MM4-2.3	1711	49,37	0,02	31,54	<0,01	0,23	0,01	0,01	15,21	2,81	0,16	99,35	83,66
MM4-2.4	1711	50,08	0,02	30,95	0,02	0,22	<0,01	<0,01	14,61	3,29	0,12	99,32	81,08
MM4-2.5	1711	50,96	<0,01	30,15	<0,01	0,17	<0,01	0,03	13,66	3,69	0,22	98,89	77,75
MM4-3.1	1711	49,65	0,05	30,79	0,01	0,22	<0,01	0,01	14,75	3,21	0,19	98,87	81,27
MM4-3.2	1711	50,42	0,04	30,60	<0,01	0,23	<0,01	0,02	14,11	3,33	0,21	98,99	79,94
MM4-3.3	1711	49,57	0,03	31,03	0,01	0,22	<0,01	0,01	14,79	3,02	0,18	98,86	82,21
MM4-3.4	1711	49,81	0,02	31,17	0,01	0,24	<0,01	0,01	14,92	3	0,19	99,36	82,39
MM5-1.1	1712	49,70	0,02	31,09	0,01	0,24	<0,01	0,03	14,92	2,90	0,18	99,09	82,89
MM5-1.2	1712	49,99	0,04	30,86	<0,01	0,22	<0,01	0,02	14,54	3,16	0,19	99,02	81,27
MM5-1.3	1712	52,83	0,04	29,39	<0,01	0,12	0,01	0,01	12,49	4,31	0,19	99,39	73,51
MM5-1.4	1712	49,95	0,02	31,29	<0,01	0,24	0,01	0,03	14,83	2,92	0,18	99,47	82,71
MM5-1.5	1712	49,78	0,04	31,22	0,01	0,20	<0,01	0,02	14,76	3,10	0,18	99,32	81,82
MM5-1.6	1712	51,64	0,04	30,12	<0,01	0,19	<0,01	0,04	13,48	3,71	0,21	99,44	77,47
MM5-2.1	1712	49,99	0,03	31,48	<0,01	0,24	0,01	0,02	15,02	2,97	0,17	99,94	82,71
MM5-2.2	1712	49,88	0,02	31,41	<0,01	0,23	<0,01	0,01	15,01	2,93	0,15	99,65	82,97
MM5-2.3	1712	49,39	<0,01	31,44	0,01	0,25	<0,01	0,02	15,28	2,87	0,15	99,43	83,50
MM5-2.4	1712	49,55	0,01	30,96	0,01	0,21	<0,01	0,02	14,85	3,08	0,15	98,84	82,13

Sample/Points	Depth (m)	SiO_2	TiO_2	Al_2O_3	Cr_2O_3	FeO	MnO	MgO	CaO	Na_2O	K_2O	Total	An%
MM5-2.5	1712	50,06	0,02	31,32	0,01	0,24	0,01	0,03	14,96	2,94	0,17	99,75	82,79
MM5-2.6	1712	49,59	0,02	31,10	<0,01	0,23	<0,01	0,02	14,99	3,02	0,17	99,14	82,45
MM5-3.1	1712	49,40	0,05	31,01	<0,01	0,19	<0,01	0,03	14,79	3,01	0,16	98,63	82,35
MM5-3.2	1712	49,26	0,01	30,91	<0,01	0,18	<0,01	<0,01	14,72	2,99	0,16	98,23	82,37
MM5-3.3	1712	49,89	0,01	31,08	0,01	0,23	<0,01	0,03	14,56	2,95	0,17	98,93	82,35
MM5-3.4	1712	49,31	0,02	31,33	<0,01	0,24	<0,01	0,02	14,96	2,79	0,17	98,83	83,48
MM5-3.5	1712	48,27	0,03	31,60	0,02	0,23	<0,01	0,02	15,43	2,65	0,13	98,36	84,73
MM6-1.1	1712,3	53,78	<0,01	28,69	<0,01	0,15	<0,01	0,02	11,89	4,74	0,32	99,59	70,15
MM6-1.2	1712,3	53,93	0,03	28,67	<0,01	0,25	0,01	<0,01	11,71	4,78	0,33	99,7	69,62
MM6-1.3	1712,3	53,10	0,05	28,95	<0,01	0,23	<0,01	0,01	12,21	4,50	0,32	99,36	71,70
MM6-1.4	1712,3	52,79	0,05	29,05	<0,01	0,20	0,01	0,01	12,32	4,42	0,32	99,18	72,22
MM6-1.5	1712,3	53,06	0,02	28,84	<0,01	0,18	<0,01	0,02	11,93	4,63	0,31	98,99	70,72
MM6-2.1	1712,3	51,38	0,04	30,06	<0,01	0,23	<0,01	0,02	13,63	3,82	0,25	99,43	77,01
MM6-2.2	1712,3	50,97	0,03	30,26	<0,01	0,18	<0,01	0,02	13,82	3,75	0,21	99,24	77,73
MM6-2.3	1712,3	49,39	0,02	31,23	<0,01	0,22	<0,01	<0,01	15,05	3,01	0,19	99,1	82,47
MM6-2.4	1712,3	50,21	0,02	30,82	<0,01	0,23	0,02	0,02	14,31	3,28	0,21	99,12	80,39
MM6-2.5	1712,3	49,66	0,02	30,94	0,01	0,22	<0,01	0,01	14,69	3,19	0,19	98,92	81,29
MM6-3.1	1712,3	53,90	0,01	29,08	0,01	0,17	0,01	0,02	11,93	4,50	0,26	99,89	71,48
MM6-3.2	1712,3	54,45	0,05	27,53	0,01	0,22	0,01	0,02	10,71	5,50	0,35	98,86	64,67
MM6-3.3	1712,3	54,39	0,02	27,73	0,02	0,16	0,01	0,02	11	5,36	0,37	99,08	65,75
MM6-3.4	1712,3	54,34	0,03	28,47	<0,01	0,17	<0,01	<0,01	11,53	4,75	0,32	99,62	69,46

Sample/Points	Depth (m)	SiO_2	TiO_2	Al_2O_3	Cr_2O_3	FeO	MnO	MgO	CaO	Na_2O	K_2O	Total	An%
MM7-1.1	1713	49,52	0,02	31,02	0,01	0,21	0,01	0,01	14,86	3,16	0,19	99,02	81,60
MM7-1.2	1713	50,24	0,02	30,66	0,02	0,19	<0,01	0,02	14,35	3,39	0,19	99,07	80,03
MM7-1.3	1713	48,65	0,02	31,40	<0,01	0,20	<0,01	0,02	15,39	2,81	0,15	98,63	83,87
MM7-1.4	1713	48,56	0,04	31,21	<0,01	0,23	0,01	0,02	15,28	2,89	0,17	98,41	83,32
MM7-1.5	1713	48,74	0,04	31,42	0,01	0,24	<0,01	0,01	15,48	2,78	0,14	98,86	84,13
MM7-2.1	1713	48,54	0,02	31,44	0,01	0,26	<0,01	0,04	15,50	2,72	0,15	98,7	84,38
MM7-2.2	1713	49,66	0,02	31,13	0,01	0,25	<0,01	0,01	14,85	3,14	0,20	99,28	81,64
MM7-2.3	1713	49,35	0,02	30,72	<0,01	0,21	<0,01	0,02	14,72	3,13	0,20	98,37	81,55
MM7-2.4	1713	50,38	0,02	30,17	<0,01	0,19	<0,01	0,02	14,04	3,70	0,18	98,7	78,35
MM7-2.5	1713	49,59	0,03	30,50	<0,01	0,15	0,01	0,02	14,58	3,34	0,18	98,4	80,55
MM7-3.1	1713	54,55	0,04	28,03	<0,01	0,20	<0,01	<0,01	11,10	5,32	0,28	99,53	66,47
MM7-3.2	1713	54,93	0,02	27,36	0,01	0,16	<0,01	<0,01	10,38	5,53	0,36	98,75	63,80
MM7-3.3	1713	54,71	0,03	27,57	<0,01	0,18	<0,01	<0,01	10,50	5,42	0,35	98,77	64,54
MM7-3.4	1713	54,22	0,04	27,32	<0,01	0,17	<0,01	0,03	10,65	5,54	0,36	98,32	64,35
MM10-2.1	1714,8	52,29	0,01	30,58	0,05	0,09	0,01	<0,01	13,41	3,98	0,03	100,46	76,98
MM10-2.2	1714,8	52,54	0,02	30,30	0,10	0,13	<0,01	<0,01	13,24	4,09	0,01	100,43	76,36
MM10-2.3	1714,8	51,22	<0,01	30,25	0,08	0,09	<0,01	<0,01	13,55	3,97	0,02	99,19	77,25
MM11-1.1	1715,4	52,39	<0,01	31,36	<0,01	0,27	<0,01	<0,01	13,18	3,84	0,08	101,12	77,08
MM11-1.2	1715,4	51,84	<0,01	30,36	<0,01	0,19	<0,01	0,02	13,30	3,92	0,12	99,77	76,70
MM11-1.3	1715,4	49,41	0,01	30,83	<0,01	0,19	<0,01	0,01	14,84	3,36	0,06	98,72	81,27
MM11-1.4	1715,4	49,86	0,02	30,76	0,02	0,19	<0,01	0,01	14,50	3,53	0,04	98,92	80,24
MM11-2.1	1715,4	51	0,03	29,91	<0,01	0,21	<0,01	0,03	13,37	3,88	0,26	98,69	76,36

Sample/Points	Depth (m)	SiO_2	TiO_2	Al_2O_3	Cr_2O_3	FeO	MnO	MgO	CaO	Na_2O	K_2O	Total	An%
MM11-2.2	1715,4	51,74	0,01	29,91	<0,01	0,21	0,01	0,03	13,17	4,19	0,21	99,47	74,96
MM11-2.4	1715,4	51,35	0,03	30,13	<0,01	0,21	<0,01	0,01	13,56	3,88	0,25	99,43	76,65
MM12-1.2	1715,8	56,89	0,05	26,11	<0,01	0,15	<0,01	0,02	8,93	6,37	0,43	98,95	56,77
MM12-1.3	1715,8	55,59	0,05	26,70	<0,01	0,17	<0,01	0,01	9,96	5,80	0,37	98,65	61,75
MM12-1.4	1715,8	56,6	0,04	26,32	<0,01	0,15	0,01	<0,01	9,48	6,12	0,43	99,15	59,14
MM12-1.5	1715,8	56,32	0,03	26,54	<0,01	0,12	0,01	<0,01	9,62	6,21	0,40	99,24	59,27
MM12-2.1	1715,8	58,61	0,02	25,09	<0,01	0,19	0,01	0,02	7,79	7,11	0,44	99,28	50,78
MM12-2.3	1715,8	58,49	0,02	25,22	<0,01	0,15	<0,01	0,02	7,90	7,11	0,40	99,31	51,27
MM12-3.4	1715,8	58,29	<0,01	25,26	<0,01	0,13	0,01	<0,01	7,94	7,11	0,38	99,13	51,46
MM12-3.5	1715,8	57	0,05	26,03	<0,01	0,14	<0,01	<0,01	9,04	6,52	0,34	99,12	56,86
MM13-1.1	1716	53,06	0,03	29,27	<0,01	0,19	0,01	0,01	12,34	4,40	0,25	99,57	72,63
MM13-1.2	1716	51,91	0,02	29,50	<0,01	0,17	<0,01	0,02	12,70	4,14	0,24	98,71	74,36
MM13-1.3	1716	53,19	0,05	29,67	0,02	0,17	<0,01	0,02	12,65	3,98	0,25	99,99	74,94
MM13-1.4	1716	51,73	0,04	29,02	<0,01	0,18	0,01	<0,01	12,57	4,34	0,25	98,13	73,25
MM13-1.5	1716	52,40	0,04	29,46	0,02	0,16	<0,01	0,02	12,61	4,28	0,23	99,22	73,66
MM13-2.1	1716	54,40	0,04	27,35	<0,01	0,11	0,01	0,01	10,49	5,48	0,31	98,2	64,43
MM13-2.2	1716	55,98	0,04	27,88	0,01	0,16	0,02	0,01	10,22	5,08	0,33	99,73	65,39
MM13-2.3	1716	54,83	0,06	27,77	<0,01	0,13	<0,01	0,01	10,58	5,33	0,30	99,02	65,27
MM13-2.4	1716	55,56	0,04	27,58	<0,01	0,16	<0,01	<0,01	10,31	5,46	0,36	99,46	63,92
MM13-2.5	1716	55,56	0,04	28,06	<0,01	0,17	<0,01	0,01	10,61	5,04	0,35	99,84	66,31
MM13-3.1	1716	59,03	0,01	24,97	<0,01	0,14	<0,01	0,02	7,32	7,17	0,36	99,03	49,29

Sample/Points	Depth (m)	SiO_2	TiO_2	Al_2O_3	Cr_2O_3	FeO	MnO	MgO	CaO	Na_2O	K_2O	Total	An%
MM13-3.2	1716	57,96	<0,01	25,29	<0,01	0,20	<0,01	0,02	7,90	6,79	0,51	98,66	51,97
MM16-1.1	1719	48,55	<0,01	31,88	0,01	0,16	<0,01	0,03	15,90	2,55	0,15	99,23	85,48
MM16-1.2	1719	48,27	0,01	32,20	<0,01	0,14	<0,01	0,01	15,95	2,58	0,15	99,31	85,39
MM16-1.3	1719	48,38	<0,01	31,89	<0,01	0,16	<0,01	0,01	15,94	2,62	0,16	99,15	85,15
MM16-1.4	1719	48,75	0,01	31,89	<0,01	0,16	<0,01	0,01	15,70	2,63	0,18	99,32	84,82
MM16-1.5	1719	48,60	0,02	31,93	<0,01	0,16	<0,01	0,03	15,84	2,65	0,16	99,39	84,93
MM16-1.6	1719	48,55	0,01	31,80	<0,01	0,17	<0,01	0,02	15,81	2,63	0,16	99,15	85,00
MM16-2.1	1719	48,18	0,03	32,10	0,01	0,18	<0,01	0,03	16,09	2,47	0,15	99,23	86,00
MM16-2.2	1719	47,72	0,01	32,38	0,01	0,18	<0,01	0,02	16,51	2,35	0,14	99,32	86,89
MM16-2.3	1719	48,37	0,02	32,17	0,01	0,18	<0,01	0,02	16,17	2,47	0,15	99,55	86,06
MM16-2.4	1719	48,65	0,01	31,54	0,02	0,18	<0,01	0,02	15,45	2,74	0,19	98,79	84,06
MM16-2.5	1719	48,54	0,01	31,96	<0,01	0,16	<0,01	<0,01	15,73	2,67	0,17	99,24	84,71
MM16-2.6	1719	48,62	<0,01	31,91	<0,01	0,18	<0,01	0,02	15,73	2,68	0,18	99,31	84,62
MM16-3.1	1719	48,67	0,02	31,91	<0,01	0,16	<0,01	0,03	15,68	2,66	0,19	99,32	84,62
MM16-3.2	1719	48,90	<0,01	31,84	0,01	0,16	<0,01	0,01	15,55	2,66	0,17	99,3	84,60
MM16-3.3	1719	48,83	0,05	31,58	<0,01	0,16	0,01	0,02	15,51	2,73	0,19	99,08	84,16
MM16-3.4	1719	48,68	<0,01	31,71	<0,01	0,16	0,01	0,02	15,75	2,69	0,20	99,22	84,50
MM17-1.1	1719,2	48,55	<0,01	32,45	0,06	0,21	<0,01	0,02	16,30	2,33	0,13	100,05	86,89
MM17-1.2	1719,2	48,07	<0,01	31,94	0,05	0,18	<0,01	0,03	15,99	2,50	0,14	98,9	85,83
MM17-1.3	1719,2	48,04	0,02	32,04	0,07	0,19	<0,01	0,02	16	2,48	0,13	98,99	85,98
MM17-1.4	1719,2	48,50	0,01	31,86	<0,01	0,15	<0,01	0,02	15,81	2,58	0,14	99,08	85,32

Sample/Points	Depth (m)	SiO_2	TiO_2	Al_2O_3	Cr_2O_3	FeO	MnO	MgO	CaO	Na_2O	K_2O	Total	An%
MM17-1.5	1719,2	48,63	0,03	31,64	<0,01	0,14	0,01	0,02	15,69	2,65	0,14	98,94	84,90
MM17-1.7	1719,2	48,23	<0,01	32,09	0,04	0,18	<0,01	0,02	16,08	2,50	0,13	99,27	85,94
MM17-1.8	1719,2	48,08	0,02	32,02	<0,01	0,14	<0,01	0,03	16,06	2,44	0,14	98,95	86,16
MM17-1.9	1719,2	48,49	0,03	31,89	0,02	0,14	0,01	0,02	15,89	2,53	0,14	99,16	85,61
MM17-2.1	1719,2	49,26	0,02	32,17	0,01	0,11	<0,01	0,02	15,94	2,55	0,15	100,23	85,52
MM17-2.2	1719,2	49,06	0,01	32,16	<0,01	0,14	<0,01	0,02	15,87	2,55	0,13	99,94	85,55
MM17-2.3	1719,2	48,87	0,02	32	<0,01	0,17	<0,01	0,02	15,84	2,56	0,16	99,63	85,34
MM17-2.4	1719,2	48,43	0,02	31,97	<0,01	0,16	0,01	0,01	15,88	2,55	0,16	99,19	85,42
MM17-2.5	1719,2	47,96	0,01	32,19	<0,01	0,15	<0,01	0,02	16,17	2,36	0,13	98,98	86,66
MM17-2.6	1719,2	47,56	<0,01	32,59	<0,01	0,15	<0,01	0,01	16,80	2,09	0,10	99,31	88,47
MM17-2.7	1719,2	48,64	<0,01	31,92	<0,01	0,15	<0,01	<0,01	15,78	2,56	0,16	99,22	85,30
MM17-2.8	1719,2	49,04	0,03	32,33	0,02	0,14	<0,01	0,01	16,08	2,46	0,15	100,26	86,04
MM17-3.1	1719,2	48,49	<0,01	31,91	<0,01	0,14	<0,01	0,01	15,80	2,58	0,12	99,06	85,41
MM17-3.2	1719,2	48,21	0,01	31,96	0,01	0,14	0,01	0,02	15,87	2,62	0,13	98,98	85,23
MM17-3.3	1719,2	48,50	0,03	31,69	0,01	0,15	<0,01	0,01	15,69	2,61	0,15	98,85	85,04
MM18-1.1	1719,6	48,52	0,01	31,91	0,01	0,23	<0,01	0,05	15,88	2,47	0,17	99,25	85,75
MM18-1.2	1719,6	48,42	0,03	32,15	<0,01	0,23	0,01	0,03	15,97	2,47	0,13	99,42	86,00
MM18-1.3	1719,6	48,51	0,01	31,77	<0,01	0,20	<0,01	0,02	15,82	2,61	0,16	99,09	85,10
MM18-1.4	1719,6	48,47	<0,01	31,86	<0,01	0,22	<0,01	0,02	15,93	2,51	0,16	99,17	85,65
MM18-1.5	1719,6	48,97	0,02	31,84	<0,01	0,23	<0,01	0,04	15,93	2,51	0,16	99,7	85,65

Sample/Points	Depth (m)	SiO_2	TiO_2	Al_2O_3	Cr_2O_3	FeO	MnO	MgO	CaO	Na_2O	K_2O	Total	An%
MM18-2.1	1719,6	48,24	0,01	32,07	0,01	0,19	<0,01	0,03	16,04	2,47	0,13	99,19	86,05
MM18-2.3	1719,6	48,66	0,01	31,94	<0,01	0,19	<0,01	0,02	16,12	2,50	0,16	99,6	85,84
MM18-2.4	1719,6	48,92	0,02	31,91	<0,01	0,20	0,01	0,02	15,88	2,47	0,16	99,6	85,79
MM18-3.1	1719,6	48,38	<0,01	31,95	<0,01	0,22	<0,01	0,04	15,91	2,52	0,15	99,17	85,63
MM18-3.2	1719,6	48,74	0,03	31,59	0,01	0,21	0,01	0,02	15,73	2,74	0,18	99,25	84,34
MM18-3.3	1719,6	48,71	0,02	31,65	<0,01	0,22	<0,01	0,03	15,67	2,72	0,19	99,21	84,34
MM18-3.4	1719,6	48,41	<0,01	31,83	0,01	0,21	0,01	0,03	16,04	2,54	0,15	99,24	85,64
MM18-3.5	1719,6	48,03	0,03	32,04	0,01	0,21	<0,01	0,03	16,14	2,49	0,13	99,12	86,03
MM18-3.6	1719,6	48,50	0,02	31,84	<0,01	0,22	0,02	0,03	15,86	2,55	0,15	99,19	85,45
MM18-3.7	1719,6	48,05	<0,01	31,99	<0,01	0,19	<0,01	0,03	16,08	2,38	0,15	98,87	86,41
MM19-1.1	1721	49,20	0,01	31,65	<0,01	0,28	0,01	0,04	15,82	2,55	0,17	99,72	85,33
MM19-1.2	1721	48,36	0,02	31,26	<0,01	0,23	<0,01	0,03	15,85	2,61	0,14	98,51	85,22
MM19-1.3	1721	49,13	0,01	31,74	0,01	0,25	0,01	0,03	15,92	2,49	0,15	99,74	85,78
MM19-1.4	1721	49,01	0,01	32,36	<0,01	0,25	0,01	0,01	16,42	2,32	0,13	100,52	87,02
MM19-1.5	1721	48,38	<0,01	32,21	<0,01	0,24	0,01	0,03	16,65	2,30	0,13	99,96	87,26
MM19-2.1	1721	48,90	0,03	31,65	0,01	0,23	<0,01	0,04	15,95	2,66	0,16	99,64	84,98
MM19-2.2	1721	49,32	0,01	31,95	<0,01	0,23	<0,01	0,05	15,87	2,49	0,16	100,08	85,69
MM19-2.3	1721	48,81	0,01	31,65	<0,01	0,25	<0,01	0,02	15,82	2,5	0,17	99,22	85,56
MM19-2.4	1721	49,21	0,01	31,94	<0,01	0,27	<0,01	0,02	15,98	2,44	0,17	100,03	85,96
MM19-2.5	1721	49,30	0,01	31,83	0,01	0,27	0,01	0,04	16,04	2,53	0,16	100,21	85,64
MM19-2.6	1721	48,23	<0,01	31,96	<0,01	0,22	0,01	0,03	16,44	2,27	0,25	99,41	86,71
MM19-3.1	1721	47,85	<0,01	32,42	0,01	0,19	<0,01	0,03	16,83	2,10	0,11	99,54	88,39

Sample/Points	Depth (m)	SiO_2	TiO_2	Al_2O_3	Cr_2O_3	FeO	MnO	MgO	CaO	Na_2O	K_2O	Total	An%
MM19-3.2	1721	48,51	0,02	31,37	<0,01	0,20	<0,01	0,03	16,17	2,60	0,14	99,05	85,51
MM19-3.4	1721	49,23	0,01	31,74	<0,01	0,24	0,01	0,03	15,85	2,54	0,15	99,81	85,49
MM19-3.5	1721	49,62	0,01	31,44	<0,01	0,21	0,01	0,02	15,58	2,75	0,17	99,82	84,22
MM20-1.1	1721,7	53,07	0,07	28,91	<0,01	0,11	<0,01	0,03	12,59	4,39	0,33	99,51	72,73
MM20-1.2	1721,7	48,92	0,04	31,23	<0,01	0,16	0,01	0,02	15,65	2,83	0,16	99,02	83,96
MM20-1.3	1721,7	49,33	0,02	31,56	0,01	0,14	0,01	0,02	15,71	2,75	0,14	99,69	84,46
MM20-1.4	1721,7	48,96	0,01	31,35	<0,01	0,14	<0,01	0,02	15,62	2,78	0,16	99,05	84,16
MM20-1.5	1721,7	49,72	0,01	31,24	<0,01	0,13	<0,01	0,01	15,23	2,98	0,17	99,5	82,86
MM20-2.1	1721,7	49,07	0,01	31,68	0,01	0,15	0,01	0,02	15,92	2,57	0,12	99,56	85,55
MM20-2.2	1721,7	48,69	0,01	31,80	<0,01	0,13	0,01	0,01	16,07	2,59	0,14	99,45	85,48
MM20-2.3	1721,7	48,79	<0,01	31,34	<0,01	0,15	0,01	0,01	15,75	2,68	0,14	98,86	84,81
MM20-2.4	1721,7	48,68	0,02	31,73	0,02	0,15	<0,01	0,02	16,02	2,65	0,13	99,4	85,21
MM20-2.5	1721,7	49,13	0,02	31,56	<0,01	0,14	<0,01	0,03	15,61	2,71	0,16	99,38	84,47
MM20-3.1	1721,7	48,76	0,03	31,37	<0,01	0,14	0,01	0,03	15,74	2,66	0,14	98,89	84,90
MM20-3.2	1721,7	52,54	0,02	28,89	0,01	0,12	0,01	0,02	12,66	4,47	0,21	98,94	73,01
MM20-3.3	1721,7	48,95	<0,01	32,63	0,04	0,15	<0,01	0,02	15,13	2,44	0,12	99,48	85,53
MM20-3.4	1721,7	48,77	0,02	31,20	0,01	0,17	<0,01	0,02	15,57	2,77	0,16	98,69	84,16
MM20-3.5	1721,7	48,75	0,02	31,56	<0,01	0,14	<0,01	0,03	15,90	2,70	0,15	99,25	84,80
MM21-2.1	1722	47,96	0,02	31,59	<0,01	0,17	0,01	0,03	15,88	2,49	0,15	98,3	85,75
MM21-2.2	1722	48,20	0,03	31,30	<0,01	0,16	0,01	0,03	15,57	2,68	0,14	98,13	84,67
MM21-2.3	1722	48,21	0,02	31,40	<0,01	0,17	<0,01	0,03	15,77	2,59	0,17	98,36	85,11

Sample/Points	Depth (m)	SiO_2	TiO_2	Al_2O_3	Cr_2O_3	FeO	MnO	MgO	CaO	Na_2O	K_2O	Total	An%
MM21-2.4	1722	48,54	0,02	31,03	<0,01	0,18	<0,01	0,02	15,32	2,75	0,18	98,05	83,95
MM21-3.1	1722	48,14	0,03	31,59	<0,01	0,16	0,01	0,02	15,53	2,70	0,17	98,35	84,40
MM21-3.2	1722	48,04	0,01	31,57	0,01	0,18	<0,01	0,02	15,74	2,59	0,17	98,33	85,08
MM21-3.3	1722	47,88	0,01	31,62	0,01	0,15	0,01	0,02	15,65	2,67	0,17	98,18	84,64
MM21-3.4	1722	47,45	<0,01	31,95	0,02	0,17	0,02	0,04	16,09	2,43	0,14	98,3	86,23
MM21-3.5	1722	47,77	<0,01	31,54	0,01	0,19	0,01	0,04	15,65	2,65	0,16	98,02	84,78
MM21-3.6	1722	48,03	0,04	31,84	<0,01	0,14	0,01	0,03	15,65	2,60	0,14	98,48	85,10
MM22-1.1	1722,3	48,80	0,03	31,86	<0,01	0,20	<0,01	0,04	15,82	2,51	0,16	99,42	85,56
MM22-1.2	1722,3	48,49	0,01	32,03	<0,01	0,19	0,01	0,02	15,89	2,54	0,14	99,32	85,57
MM22-1.3	1722,3	48,78	0,01	31,70	<0,01	0,23	<0,01	0,03	15,71	2,63	0,16	99,25	84,92
MM22-1.4	1722,3	48,94	<0,01	31,63	0,01	0,20	<0,01	0,01	15,51	2,69	0,18	99,16	84,39
MM22-1.5	1722,3	48,83	0,01	32,11	<0,01	0,22	<0,01	0,04	15,73	2,59	0,16	99,69	85,12
MM22-1.6	1722,3	48,50	0,01	31,89	<0,01	0,21	<0,01	0,05	15,72	2,55	0,14	99,08	85,39
MM22-1.7	1722,3	48,63	<0,01	31,96	<0,01	0,19	<0,01	0,05	15,82	2,49	0,17	99,32	85,61
MM22-2.1	1722,3	50,19	0,04	33,19	<0,01	0,19	0,01	0,02	16,16	2,25	0,11	102,16	87,26
MM22-2.2	1722,3	48,74	0,02	32,14	0,01	0,20	0,01	0,04	15,79	2,54	0,16	99,66	85,40
MM22-2.3	1722,3	48,98	0,03	31,82	<0,01	0,19	0,01	0,02	15,74	2,59	0,15	99,54	85,17
MM22-2.4	1722,3	48,71	0,02	31,91	0,01	0,20	<0,01	0,04	15,83	2,59	0,15	99,46	85,25
MM22-2.5	1722,3	49,03	0,02	31,82	0,01	0,21	<0,01	0,04	15,71	2,63	0,18	99,64	84,83
MM22-2.6	1722,3	48,88	0,01	31,78	0,01	0,20	0,01	0,03	15,79	2,64	0,14	99,47	85,03
MM23-1.1	1722,7	49,28	0,02	31,38	<0,01	0,16	<0,01	0,01	15,43	2,84	0,17	99,29	83,68

Sample/Points	Depth (m)	SiO_2	TiO_2	Al_2O_3	Cr_2O_3	FeO	MnO	MgO	CaO	Na_2O	K_2O	Total	An%
MM23-1.2	1722,7	49,11	0,02	31,66	<0,01	0,20	0,02	0,02	15,43	2,74	0,15	99,32	84,22
MM23-1.4	1722,7	49,15	<0,01	33,06	<0,01	0,19	<0,01	0,01	16,57	2,15	0,11	101,25	88,00
MM23-1.5	1722,7	49,38	0,01	32,58	0,01	0,20	<0,01	0,03	15,99	2,37	0,13	100,69	86,48
MM23-1.6	1722,7	49,15	<0,01	31,96	0,01	0,16	0,02	0,01	15,60	2,63	0,16	99,7	84,83
MM24-1.1	1724	48,26	0,02	31,58	<0,01	0,28	<0,01	0,03	15,03	2,66	0,16	98,01	84,20
MM24-1.2	1724	48,54	0,04	31,33	<0,01	0,26	<0,01	0,02	15,32	2,70	0,15	98,36	84,31
MM24-1.3	1724	48,45	0,01	31,64	<0,01	0,26	0,01	0,02	15,29	2,56	0,16	98,42	84,90
MM24-1.4	1724	48,80	<0,01	31,53	<0,01	0,28	0,01	0,03	15,40	2,53	0,17	98,74	85,08
MM24-1.5	1724	48,91	0,02	31,69	<0,01	0,30	<0,01	0,02	15,24	2,59	0,15	98,92	84,76
MM24-1.6	1724	48,68	0,01	31,52	<0,01	0,28	<0,01	0,03	15,47	2,66	0,13	98,8	84,72
MM24-2.1	1724	48,72	0,03	31,43	<0,01	0,29	0,01	0,02	15,39	2,71	0,14	98,73	84,38
MM24-2.2	1724	48,10	<0,01	31,31	<0,01	0,33	<0,01	0,02	15,57	2,66	0,13	98,12	84,80
MM24-2.3	1724	48,78	0,02	31,42	0,01	0,25	<0,01	0,04	15,31	2,70	0,16	98,69	84,26
MM24-2.4	1724	48,81	0,01	31,83	0,02	0,27	0,01	0,02	15,41	2,50	0,14	99,03	85,37
MM24-2.5	1724	48,76	0,02	31,67	<0,01	0,29	<0,01	0,06	15,30	2,58	0,14	98,82	84,91
MM24-2.6	1724	49,01	0,02	31,77	<0,01	0,26	<0,01	0,01	15,33	2,60	0,14	99,16	84,84
MM24-3.1	1724	48,83	0,01	31,44	0,01	0,26	<0,01	0,05	15,19	2,65	0,16	98,58	84,39
MM24-3.2	1724	48,58	0,03	31,40	<0,01	0,29	0,01	0,02	15,14	2,70	0,16	98,32	84,11
MM24-3.3	1724	48,84	0,02	31,32	<0,01	0,30	<0,01	0,01	15,15	2,69	0,17	98,5	84,12
MM24-3.4	1724	48,63	<0,01	31,34	0,01	0,30	<0,01	0,03	15,13	2,70	0,14	98,28	84,20
MM24-3.5	1724	48,52	0,02	31,38	<0,01	0,26	0,01	0,01	15,22	2,68	0,14	98,24	84,37

Sample/Points	Depth (m)	SiO_2	TiO_2	Al_2O_3	Cr_2O_3	FeO	MnO	MgO	CaO	Na_2O	K_2O	Total	An%
MM24-3.6	1724	48,64	0,04	31,75	<0,01	0,25	0,01	0,02	15,31	2,65	0,15	98,83	84,54
MM25-1.2	1728	49,56	0,01	31,57	<0,01	0,25	0,01	0,04	15,72	2,65	0,16	99,96	84,84
MM25-1.3	1728	49,15	0,02	31,30	<0,01	0,26	<0,01	0,03	15,48	2,65	0,17	99,07	84,59
MM25-1.4	1728	49,17	0,03	31,38	<0,01	0,20	0,01	0,03	15,72	2,65	0,19	99,38	84,70
MM25-2.1	1728	49,21	0,02	31,3	0,02	0,27	0,01	0,01	15,81	2,64	0,17	99,47	84,91
MM25-2.3	1728	49,13	0,02	31,55	0,01	0,26	<0,01	0,03	15,80	2,57	0,17	99,54	85,22
MM25-2.4	1728	48,96	0,03	31,17	<0,01	0,26	0,01	0,01	15,59	2,68	0,18	98,89	84,50
MM25-2.5	1728	48,67	0,02	31,53	<0,01	0,23	0,01	0,02	15,79	2,58	0,14	99	85,31
MM25-2.6	1728	49,12	0,02	31,62	<0,01	0,25	<0,01	0,03	15,70	2,59	0,16	99,49	85,09
MM25-3.1	1728	49,30	0,03	31,27	<0,01	0,27	<0,01	0,05	15,50	2,68	0,19	99,28	84,38
MM25-3.2	1728	49,30	0,03	31,34	<0,01	0,28	<0,01	0,02	15,74	2,74	0,18	99,63	84,35
MM25-3.3	1728	49,18	0,01	31,79	<0,01	0,29	<0,01	0,01	15,87	2,61	0,16	99,92	85,14
MM25-3.4	1728	49,13	0,01	31,24	<0,01	0,31	<0,01	0,03	15,70	2,69	0,19	99,29	84,50
MM25-3.5	1728	49,56	0,03	31,56	0,01	0,28	<0,01	0,02	15,64	2,70	0,17	99,98	84,49
MM26-1.1	1733	48,89	0,02	31,85	<0,01	0,34	<0,01	0,02	15,68	2,62	0,13	99,54	85,08
MM26-1.2	1733	48,71	0,01	31,86	<0,01	0,33	0,02	0,03	15,75	2,54	0,12	99,38	85,55
MM26-1.3	1733	48,69	0,01	31,90	<0,01	0,27	0,01	0,02	15,50	2,67	0,12	99,18	84,75
MM26-1.4	1733	48,47	0,01	31,71	<0,01	0,27	<0,01	0,01	15,83	2,53	0,18	99,02	85,38
MM26-1.5	1733	48,76	<0,01	31,94	0,01	0,28	<0,01	0,03	15,56	2,59	0,13	99,29	85,12
MM26-1.6	1733	49,55	<0,01	32,34	<0,01	0,34	<0,01	0,01	15,57	2,50	0,11	100,42	85,64
MM26-2.1	1733	48,22	<0,01	31,98	0,01	0,29	0,01	0,03	15,97	2,43	0,12	99,06	86,23

Sample/Points	Depth (m)	SiO_2	TiO_2	Al_2O_3	Cr_2O_3	FeO	MnO	MgO	CaO	Na_2O	K_2O	Total	An%
MM26-2.2	1733	48,75	0,03	31,91	<0,01	0,31	<0,01	0,02	15,73	2,54	0,14	99,43	85,44
MM26-2.4	1733	48,38	0,04	31,79	<0,01	0,38	0,01	0,02	15,51	2,5	0,12	98,75	85,55
MM26-2.5	1733	48,72	<0,01	31,77	<0,01	0,40	0,02	0,02	15,75	2,62	0,14	99,43	85,09
MM26-2.6	1733	48,72	<0,01	31,92	<0,01	0,39	0,01	0,02	15,62	2,55	0,14	99,37	85,31
MM26-2.7	1733	48,19	<0,01	31,82	<0,01	0,35	<0,01	0,02	15,73	2,59	0,12	98,82	85,30
MM26-3.1	1733	47,96	0,01	31,56	<0,01	0,25	<0,01	0,02	15,87	2,61	0,13	98,41	85,28
MM26-3.2	1733	48,15	0,01	31,55	<0,01	0,25	<0,01	0,03	15,57	2,64	0,13	98,32	84,90
MM26-3.3	1733	48,33	0,03	31,61	0,01	0,22	<0,01	0,02	15,86	2,58	0,11	98,77	85,50
MM26-3.4	1733	48,53	<0,01	31,85	<0,01	0,26	<0,01	0,02	15,81	2,55	0,12	99,14	85,55
MM26-3.5	1733	48,43	0,03	31,91	<0,01	0,28	<0,01	0,01	15,68	2,53	0,12	99,01	85,54
MM28-1.1	1741	49,22	0,02	33,17	0,02	0,23	<0,01	<0,01	16,27	2,24	0,09	101,25	87,47
MM28-1.2	1741	49	<0,01	31,77	<0,01	0,22	0,01	0,01	15,74	2,55	0,12	99,43	85,50
MM28-1.3	1741	47,52	<0,01	32,12	<0,01	0,19	<0,01	0,01	16,35	2,38	0,10	98,66	86,83
MM28-2.1	1741	48,41	0,02	31,59	0,01	0,25	<0,01	0,01	15,73	2,63	0,12	98,77	85,12
MM28-2.2	1741	48,77	<0,01	31,78	<0,01	0,25	<0,01	0,02	15,90	2,63	0,12	99,46	85,25
MM28-2.3	1741	48,63	<0,01	31,83	<0,01	0,26	0,01	0,02	15,90	2,61	0,11	99,36	85,39
MM28-3.1	1741	49,02	0,03	32,02	<0,01	0,23	0,02	0,02	15,85	2,54	0,14	99,86	85,54
MM28-3.2	1741	48,82	<0,01	31,86	0,01	0,29	<0,01	0,04	15,87	2,54	0,14	99,58	85,55
MM28-3.3	1741	48,99	0,01	32,12	<0,01	0,26	<0,01	0,03	16	2,44	0,13	99,98	86,16
MM28-3.4	1741	49,12	0,01	32,06	<0,01	0,27	<0,01	0,03	15,79	2,41	0,13	99,81	86,14
MM29-1.4	1743	48,96	0,01	31,84	0,01	0,28	0,01	0,04	15,90	2,52	0,13	99,7	85,71

Sample/Points	Depth (m)	SiO_2	TiO_2	Al_2O_3	Cr_2O_3	FeO	MnO	MgO	CaO	Na_2O	K_2O	Total	An%
MM29-1.5	1743	48,93	0,02	31,74	<0,01	0,26	<0,01	0,02	15,77	2,54	0,13	99,39	85,52
MM29-2.2	1743	48,74	0,01	31,89	<0,01	0,26	<0,01	0,02	15,89	2,57	0,11	99,49	85,57
MM29-2.3	1743	48,68	0,01	31,99	<0,01	0,25	0,01	0,01	16	2,58	0,09	99,57	85,70
MM29-2.4	1743	48,80	0,01	31,68	0,01	0,25	0,01	0,02	15,91	2,62	0,11	99,41	85,35
MM29-2.5	1743	48,65	0,02	31,88	<0,01	0,24	0,01	<0,01	16,14	2,58	0,10	99,63	85,76
MM29-3.1	1743	48,39	0,02	31,59	0,03	0,25	<0,01	0,01	15,74	2,57	0,13	98,73	85,36
MM29-3.2	1743	48,44	<0,01	31,57	<0,01	0,21	<0,01	0,02	15,79	2,58	0,11	98,74	85,44
MM29-3.3	1743	48,51	0,02	31,80	<0,01	0,24	0,01	0,02	16,02	2,60	0,12	99,33	85,49
MM29-3.4	1743	47,84	0,03	32,04	0,01	0,26	<0,01	0,02	16,27	2,31	0,11	98,9	87,05
MM29-3.5	1743	48,24	0,01	32,21	<0,01	0,28	<0,01	0,03	16,37	2,37	0,11	99,62	86,84
MM30-1.1	1745	48,57	0,02	32,13	<0,01	0,27	<0,01	0,02	15,95	2,39	0,13	99,48	86,36
MM30-1.2	1745	48,28	0,02	32,01	<0,01	0,25	<0,01	0,01	15,89	2,45	0,14	99,06	85,98
MM30-1.3	1745	48,47	0,01	31,89	<0,01	0,23	<0,01	0,01	15,93	2,48	0,12	99,16	85,97
MM30-1.4	1745	47,66	<0,01	32,56	<0,01	0,26	0,01	0,02	16,42	2,17	0,08	99,19	87,95
MM30-1.5	1745	48,29	<0,01	32,12	<0,01	0,25	0,01	0,04	15,93	2,42	0,11	99,17	86,29
MM30-2.1	1745	48,66	0,01	31,87	<0,01	0,27	<0,01	0,02	15,65	2,74	0,11	99,33	84,59
MM30-2.2	1745	48,30	0,02	32,05	<0,01	0,27	0,02	0,03	15,87	2,46	0,12	99,13	86,02
MM30-2.3	1745	48,16	0,03	31,75	0,02	0,22	<0,01	0,02	15,85	2,55	0,12	98,71	85,58
MM30-2.4	1745	48,14	0,03	32,01	<0,01	0,27	0,01	0,02	16,01	2,43	0,14	99,06	86,17
MM30-2.5	1745	48,22	0,02	31,94	<0,01	0,24	0,01	0,02	16,09	2,53	0,13	99,2	85,81
MM30-3.1	1745	48,44	0,01	32,30	<0,01	0,23	<0,01	0,03	15,96	2,40	0,11	99,48	86,41

Sample/Points	Depth (m)	SiO_2	TiO_2	Al_2O_3	Cr_2O_3	FeO	MnO	MgO	CaO	Na_2O	K_2O	Total	An%
MM30-3.2	1745	48,30	<0,01	32,24	0,01	0,22	0,02	0,01	16,11	2,47	0,10	99,47	86,24
MM30-3.4	1745	48,25	<0,01	32,42	0,01	0,17	<0,01	<0,01	16,30	2,32	0,07	99,54	87,21
MM31-1.1	1747	48,65	<0,01	31,64	<0,01	0,23	<0,01	0,01	16,08	2,52	0,13	99,26	85,85
MM31-1.2	1747	48,73	0,01	31,51	<0,01	0,29	<0,01	0,03	15,78	2,67	0,12	99,15	84,98
MM31-1.3	1747	48,74	0,03	31,86	<0,01	0,28	0,01	0,03	16,10	2,52	0,15	99,72	85,78
MM31-1.4	1747	48,81	0,02	31,38	<0,01	0,28	<0,01	0,01	15,73	2,59	0,13	98,95	85,26
MM31-1.5	1747	48,96	0,04	31,76	<0,01	0,26	0,01	0,03	15,98	2,56	0,13	99,72	85,59
MM31-2.1	1747	48,90	0,01	31,72	<0,01	0,25	<0,01	0,01	16,12	2,53	0,15	99,7	85,74
MM31-2.2	1747	48,50	0,03	31,78	<0,01	0,25	0,01	0,03	16,19	2,39	0,13	99,3	86,53
MM31-2.3	1747	48,89	0,01	31,77	0,01	0,27	0,02	0,02	16,01	2,50	0,15	99,65	85,80
MM31-2.4	1747	48,39	0,03	31,67	<0,01	0,28	0,01	0,01	16	2,56	0,14	99,09	85,56
MM31-3.1	1747	48,20	0,01	32,07	<0,01	0,26	0,01	0,04	16,22	2,28	0,12	99,22	87,11
MM31-3.2	1747	48,37	<0,01	31,58	<0,01	0,23	<0,01	0,01	16,12	2,51	0,13	98,95	85,93
MM31-3.3	1747	48,27	0,01	31,83	<0,01	0,27	<0,01	0,03	16,21	2,45	0,11	99,18	86,36
MM31-3.4	1747	48,14	0,02	31,93	<0,01	0,24	0,01	0,03	16,37	2,28	0,12	99,16	87,21
MM31-3.5	1747	48,90	0,01	31,75	<0,01	0,27	<0,01	0,02	16,11	2,50	0,13	99,71	85,97
MM32-1.1	1747,5	48,80	0,02	31,85	<0,01	0,26	<0,01	0,03	15,92	2,53	0,13	99,54	85,68
MM32-1.2	1747,5	49,11	0,01	31,52	<0,01	0,28	<0,01	0,04	15,73	2,66	0,15	99,5	84,84
MM32-1.3	1747,5	48,81	0,05	31,67	<0,01	0,29	<0,01	0,03	15,97	2,54	0,13	99,49	85,68
MM32-1.4	1747,5	48,19	0,02	31,61	<0,01	0,25	<0,01	0,03	16,10	2,50	0,14	98,84	85,91
MM32-1.5	1747,5	48,22	<0,01	31,47	<0,01	0,30	<0,01	0,04	16,12	2,57	0,14	98,87	85,61

Sample/Points	Depth (m)	SiO_2	TiO_2	Al_2O_3	Cr_2O_3	FeO	MnO	MgO	CaO	Na_2O	K_2O	Total	An%
MM32-1.6	1747,5	49,90	0,03	32,04	<0,01	0,26	0,01	0,02	15,88	2,57	0,17	100,88	85,28
MM32-2.2	1747,5	48,50	0,01	31,39	<0,01	0,28	0,01	0,03	15,91	2,56	0,15	98,83	85,45
MM32-2.3	1747,5	48,60	0,02	31,53	<0,01	0,24	<0,01	0,04	15,84	2,56	0,15	98,97	85,39
MM32-2.4	1747,5	48,54	<0,01	31,54	<0,01	0,26	0,01	0,02	16,08	2,50	0,15	99,09	85,85
MM32-2.5	1747,5	48,59	0,03	31,37	<0,01	0,25	0,01	0,03	15,91	2,63	0,16	98,98	85,08
MM32-2.6	1747,5	48,17	0,04	31,30	<0,01	0,25	<0,01	0,03	15,59	2,56	0,13	98,07	85,28
MM32-2.7	1747,5	48,41	0,02	31,26	0,01	0,26	0,02	0,02	15,34	2,63	0,17	98,14	84,56
MM33-1.1	1748	48,40	0,01	31,46	<0,01	0,24	<0,01	0,03	16,05	2,67	0,18	99,03	84,92
MM33-1.2	1748	49,08	0,01	31,84	<0,01	0,25	<0,01	0,03	15,93	2,58	0,18	99,9	85,23
MM33-1.3	1748	48,82	0,03	31,97	<0,01	0,23	<0,01	0,01	16,14	2,58	0,19	99,98	85,35
MM33-1.4	1748	48,19	0,01	31,89	<0,01	0,24	<0,01	0,02	16,44	2,35	0,15	99,29	86,80
MM33-1.5	1748	48,48	0,01	31,55	<0,01	0,25	0,01	0,02	16,05	2,52	0,17	99,06	85,65
MM33-2.1	1748	50,41	0,02	32,62	<0,01	0,23	0,01	0,03	15,32	2,58	0,14	101,37	84,92
MM33-2.2	1748	48,72	0,02	31,33	0,01	0,23	0,01	0,02	15,31	2,70	0,14	98,49	84,35
MM33-2.3	1748	48,73	0,02	31,37	<0,01	0,20	0,01	0,01	15,24	2,72	0,16	98,47	84,11
MM33-2.4	1748	48,74	0,01	31,39	<0,01	0,23	<0,01	0,03	15,43	2,62	0,12	98,57	84,92
MM33-3.1	1748	48,64	0,01	32,07	<0,01	0,23	0,01	0,03	16,04	2,56	0,15	99,74	85,55
MM33-3.2	1748	48,56	0,02	31,76	<0,01	0,22	<0,01	0,02	16,13	2,53	0,16	99,41	85,71
MM33-3.3	1748	48,71	0,02	31,76	0,01	0,25	0,02	0,03	15,85	2,54	0,18	99,36	85,35
MM33-3.4	1748	48,48	0,02	31,67	<0,01	0,25	<0,01	0,01	15,94	2,57	0,18	99,11	85,29
MM33-3.5	1748	48,90	0,01	31,58	<0,01	0,24	0,01	0,03	15,73	2,64	0,17	99,31	84,84

Sample/Points	Depth (m)	SiO_2	TiO_2	Al_2O_3	Cr_2O_3	FeO	MnO	MgO	CaO	Na_2O	K_2O	Total	An%
MM35-1.1	1749,2	48,27	0,01	31,92	0,01	0,21	<0,01	0,02	16,10	2,44	0,11	99,07	86,33
MM35-1.3	1749,2	48,66	0,02	31,82	<0,01	0,20	<0,01	0,01	15,82	2,52	0,11	99,16	85,75
MM35-1.4	1749,2	48,82	0,02	31,57	<0,01	0,20	<0,01	0,02	15,6	2,65	0,15	99,03	84,78
MM35-1.5	1749,2	48,13	0,01	31,80	<0,01	0,21	<0,01	0,03	16,02	2,48	0,13	98,81	85,99
MM35-1.6	1749,2	48,19	0,03	31,54	<0,01	0,18	<0,01	0,02	15,84	2,59	0,15	98,54	85,25
MM35-1.7	1749,2	48,46	0,02	31,9	<0,01	0,22	<0,01	0,03	15,83	2,44	0,12	99,03	86,08
MM35-1.8	1749,2	48,05	0,01	31,34	<0,01	0,19	0,01	0,01	15,65	2,67	0,16	98,09	84,69
MM36-1.1	1749,5	48,28	0,04	31,95	<0,01	0,40	0,02	0,02	16,06	2,36	0,13	99,25	86,58
MM36-1.2	1749,5	48,59	0,01	31,77	<0,01	0,44	0,02	0,02	15,84	2,57	0,13	99,39	85,44
MM36-1.3	1749,5	48,78	0,03	31,87	<0,01	0,36	0,01	0,03	15,91	2,57	0,10	99,67	85,63
MM36-2.1	1749,5	48,77	0,04	31,64	0,01	0,32	<0,01	0,01	15,92	2,54	0,12	99,37	85,68
MM36-2.2	1749,5	48,35	0,03	31,98	<0,01	0,40	<0,01	0,04	16,12	2,32	0,12	99,38	86,85
MM36-2.3	1749,5	48,39	0,02	31,95	<0,01	0,36	<0,01	0,01	16,11	2,39	0,14	99,38	86,43
MM37-1.1	1749,9	48,09	0,02	32,20	<0,01	0,36	<0,01	0,01	16,21	2,37	0,09	99,35	86,82
MM37-1.2	1749,9	48,21	0,01	32,16	<0,01	0,36	<0,01	0,02	16,34	2,33	0,10	99,53	87,05
MM37-1.3	1749,9	48,11	0,02	32,31	<0,01	0,40	0,01	0,03	16,39	2,35	0,12	99,73	86,90
MM37-1.4	1749,9	48,24	0,03	32,28	<0,01	0,39	<0,01	0,02	16,25	2,31	0,11	99,63	87,04
MM37-1.5	1749,9	47,58	0,03	32,66	<0,01	0,39	<0,01	0,02	16,67	2,10	0,09	99,55	88,39
MM37-1.6	1749,9	48,12	0,01	32,49	<0,01	0,42	0,01	0,01	16,60	2,20	0,10	99,96	87,83
MM37-2.1	1749,9	48,27	<0,01	32,46	0,01	0,35	0,01	0,01	16,41	2,30	0,11	99,93	87,19
MM37-2.2	1749,9	48,58	0,02	32,10	0,01	0,36	0,01	0,01	15,97	2,47	0,12	99,68	86,05

Sample/Points	Depth (m)	SiO_2	TiO_2	Al_2O_3	Cr_2O_3	FeO	MnO	MgO	CaO	Na_2O	K_2O	Total	An%
MM37-2.3	1749,9	48,50	<0,01	32,02	0,01	0,31	<0,01	<0,01	16,01	2,47	0,13	99,46	86,03
MM37-2.5	1749,9	47,98	<0,01	32,47	0,02	0,29	<0,01	0,01	16,51	2,23	0,11	99,62	87,59
MM37-3.1	1749,9	47,69	0,03	32,44	0,01	0,36	<0,01	<0,01	16,59	2,13	0,09	99,34	88,20
MM37-3.2	1749,9	47,86	0,01	32,41	<0,01	0,34	<0,01	0,03	16,68	2,18	0,11	99,63	87,93
MM37-3.3	1749,9	47,67	<0,01	32,53	<0,01	0,36	<0,01	0,02	16,47	2,14	0,10	99,3	88,03
MM37-3.4	1749,9	48,09	0,01	32,54	<0,01	0,39	<0,01	0,01	16,71	2,11	0,09	99,96	88,37
MM37-3.5	1749,9	47,44	0,01	32,72	<0,01	0,36	0,01	0,02	16,89	2,05	0,09	99,59	88,75
MM39-1.1	1753	48,43	0,02	31,93	<0,01	0,27	0,02	0,03	16,10	2,46	0,14	99,4	86,10
MM39-1.2	1753	48,34	0,02	31,97	<0,01	0,28	0,01	0,04	16,13	2,44	0,13	99,35	86,26
MM39-1.3	1753	49,10	0,04	32,07	<0,01	0,30	0,02	0,04	15,97	2,40	0,15	100,08	86,23
MM39-1.4	1753	48,59	0,02	31,98	<0,01	0,28	<0,01	0,02	16,26	2,50	0,14	99,79	86,03
MM39-2.1	1753	48,25	0,02	31,92	<0,01	0,25	<0,01	0,03	16,06	2,39	0,12	99,04	86,48
MM39-2.2	1753	48,19	0,02	32,11	0,01	0,30	<0,01	0,01	16,23	2,33	0,14	99,33	86,79
MM39-2.3	1753	48,24	0,03	32,17	<0,01	0,27	0,01	0,03	16,24	2,32	0,10	99,39	87,03
MM39-2.4	1753	48,23	0,02	31,82	<0,01	0,27	<0,01	0,02	16,10	2,42	0,12	99	86,37
MM39-2.5	1753	48,50	<0,01	32,23	<0,01	0,26	<0,01	0,02	16,12	2,27	0,13	99,55	87,04
MM39-3.1	1753	48,02	0,01	31,75	<0,01	0,27	<0,01	0,02	16,31	2,42	0,12	98,92	86,53
MM39-3.2	1753	48,73	0,02	31,98	<0,01	0,23	<0,01	0,01	16,01	2,36	0,12	99,47	86,59
MM39-3.3	1753	48,24	0,02	32,09	0,01	0,24	<0,01	0,02	16,17	2,43	0,10	99,3	86,47
MM39-3.4	1753	47,70	0,03	32,75	<0,01	0,25	<0,01	0,03	16,68	2,07	0,10	99,59	88,49
MM41-1.1	1755	47,78	0,01	32,23	<0,01	0,30	<0,01	0,01	16,11	2,30	0,16	98,89	86,75

Sample/Points	Depth (m)	SiO_2	TiO_2	Al_2O_3	Cr_2O_3	FeO	MnO	MgO	CaO	Na_2O	K_2O	Total	An%
MM41-1.2	1755	47,94	<0,01	32,02	<0,01	0,23	<0,01	0,02	16,11	2,30	0,19	98,81	86,61
MM41-1.4	1755	47,42	0,01	32,61	0,01	0,42	<0,01	0,02	16,59	2,08	0,11	99,28	88,34
MM41-1.5	1755	47,75	0,01	32,21	<0,01	0,41	<0,01	0,03	15,92	2,35	0,12	98,8	86,57
MM41-1.6	1755	47,97	<0,01	32,54	0,01	0,39	0,01	0,02	16,32	2,18	0,12	99,56	87,65
MM42-1.1	1756	54,10	0,03	28,20	<0,01	0,16	<0,01	<0,01	11,23	4,97	0,29	98,98	68,10
MM42-1.2	1756	53,94	0,06	28,31	<0,01	0,19	<0,01	0,02	11,35	4,96	0,32	99,14	68,25
MM42-1.3	1756	53,88	0,04	28,18	<0,01	0,18	0,01	0,02	11,35	4,86	0,36	98,87	68,50
MM42-1.4	1756	54,66	0,05	28,42	0,02	0,19	<0,01	0,03	11,39	4,88	0,35	100	68,53
MM42-1.5	1756	53,98	0,03	28,69	<0,01	0,20	<0,01	0,03	11,67	4,63	0,34	99,55	70,13
MM42-1.6	1756	53,21	0,03	28,89	0,01	0,21	0,01	0,03	11,98	4,51	0,27	99,14	71,48
MM42-1.7	1756	53,08	0,04	28,88	<0,01	0,19	<0,01	0,02	12,05	4,54	0,30	99,1	71,34
MM42-1.8	1756	53,11	0,06	28,84	<0,01	0,19	<0,01	0,04	11,98	4,57	0,29	99,09	71,14
MM42-2.1	1756	55,55	0,06	28,55	0,01	0,17	0,01	0,02	10,81	4,72	0,24	100,13	68,55
MM42-2.2	1756	56,47	0,02	28,83	<0,01	0,12	0,03	0,01	10,81	4,81	0,19	101,31	68,37
MM42-2.3	1756	54,48	0,03	29,04	0,02	0,23	<0,01	0,03	11,40	4,45	0,24	99,92	70,85
MM43-1.1	1756,7	48,12	0,02	31,94	0,10	0,20	<0,01	0,01	15,74	2,66	0,05	98,85	85,31
MM43-1.2	1756,7	50,15	<0,01	31,50	0,13	0,22	0,01	0,01	14,81	3,02	0,08	99,93	82,69
MM43-2.1	1756,7	50,30	0,01	30,18	0,14	0,21	0,01	0,02	13,78	3,85	0,12	98,62	77,63
MM43-2.2	1756,7	48,20	0,04	32,10	0,10	0,19	<0,01	0,03	16,04	2,56	0,06	99,32	85,96
MM43-2.3	1756,7	48,23	0,02	32,09	0,11	0,18	<0,01	0,02	16,02	2,57	0,07	99,32	85,85
MM43-2.4	1756,7	48,18	<0,01	33,61	0,22	0,26	0,02	0,03	16,09	2,07	0,06	100,54	88,31

Sample/Points	Depth (m)	SiO_2	TiO_2	Al_2O_3	Cr_2O_3	FeO	MnO	MgO	CaO	Na_2O	K_2O	Total	An%
MM43-2.5	1756,7	48,23	0,01	31,75	0,04	0,19	<0,01	0,02	15,88	2,72	0,06	98,92	85,10
MM44-1.2	1757	48,37	<0,01	31,60	0,19	0,22	<0,01	0,03	15,16	2,95	0,05	98,56	83,48
MM44-1.3	1757	49,75	<0,01	31,48	0,14	0,17	<0,01	0,02	14,97	3,12	0,06	99,71	82,48
MM44-1.4	1757	49,11	0,02	31,29	0,20	0,24	0,01	0,03	14,77	3,06	0,06	98,78	82,56
MM44-1.5	1757	50	0,04	31,32	0,15	0,18	<0,01	0,02	14,83	3,26	0,06	99,88	81,71
MM44-2.1	1757	48,77	0,02	31,46	0,09	0,17	0,01	0,02	15,03	3,03	0,04	98,66	83,04
MM44-2.2	1757	49,37	0,02	31,46	0,11	0,17	<0,01	0,02	15,08	3,04	0,05	99,32	82,99
MM44-2.3	1757	48,93	0,01	31,30	0,10	0,18	0,02	0,03	15,05	2,99	0,05	98,66	83,20
MM45-1.1	1757,3	49,56	0,01	31,40	0,01	0,25	<0,01	0,02	14,94	2,83	0,19	99,2	83,18
MM45-1.2	1757,3	50,14	0,01	30,39	<0,01	0,17	0,01	0,03	14,09	3,40	0,23	98,46	79,51
MM45-2.1	1757,3	50,92	<0,01	30,75	<0,01	0,21	0,01	0,02	14,09	3,40	0,26	99,66	79,38
MM45-2.2	1757,3	50,85	0,02	30,55	0,01	0,24	0,01	0,03	14,07	3,40	0,28	99,45	79,27
MM45-2.3	1757,3	50,48	0,02	30,45	<0,01	0,26	<0,01	0,03	14,07	3,35	0,26	98,93	79,58
MM45-2.4	1757,3	50,63	<0,01	30,61	0,01	0,22	<0,01	0,03	14,29	3,22	0,28	99,3	80,33
MM45-2.5	1757,3	50,84	<0,01	30,45	<0,01	0,25	<0,01	0,05	14,20	3,35	0,29	99,42	79,60
MM45-3.1	1757,3	50,65	0,02	30,54	<0,01	0,19	<0,01	0,04	14,32	3,27	0,23	99,27	80,36
MM45-3.2	1757,3	50,53	0,01	30,62	<0,01	0,20	<0,01	0,03	14,24	3,29	0,25	99,18	80,09
MM45-3.3	1757,3	50,34	0,02	30,33	0,01	0,19	<0,01	0,03	14,09	3,45	0,23	98,69	79,29
MM46-1.1	1757,5	52,96	0,02	28,64	<0,01	0,19	<0,01	<0,01	12,01	4,67	0,24	98,74	70,98
MM46-1.2	1757,5	52,04	0,03	28,50	0,02	0,23	<0,01	0,01	12,26	4,62	0,30	98	71,36
MM46-1.3	1757,5	50,71	0,03	30,07	0,02	0,15	<0,01	<0,01	13,88	3,70	0,27	98,83	77,76

Sample/Points	Depth (m)	SiO_2	TiO_2	Al_2O_3	Cr_2O_3	FeO	MnO	MgO	CaO	Na_2O	K_2O	Total	An%
MM46-1.4	1757,5	50,61	0,02	30,55	<0,01	0,23	0,01	0,01	14,37	3,40	0,21	99,41	79,92
MM47-1.2	1759	51,55	0,02	29,77	<0,01	0,15	0,01	0,02	13,26	4,07	0,17	99,03	75,77
MM47-1.3	1759	52,13	0,04	29,74	0,03	0,17	<0,01	0,02	13,05	4,08	0,23	99,48	75,17
MM47-1.4	1759	51,59	0,02	29,45	<0,01	0,18	0,01	0,01	13	4,17	0,19	98,63	74,88
MM47-3.1	1759	52,80	0,01	28,76	<0,01	0,16	<0,01	0,01	12,13	4,67	0,23	98,78	71,23
MM47-3.2	1759	53,15	0,04	28,66	<0,01	0,16	<0,01	0,01	12,22	4,61	0,27	99,11	71,46
MM47-3.3	1759	52,77	0,02	28,78	0,01	0,17	<0,01	<0,01	12,36	4,51	0,27	98,89	72,11
MM47-3.4	1759	52,92	0,03	28,67	<0,01	0,16	0,01	<0,01	12,17	4,62	0,25	98,83	71,42
MM47-4.1	1759	52,68	0,02	29,15	<0,01	0,21	<0,01	0,03	12,45	4,46	0,20	99,21	72,76
MM47-4.2	1759	52,59	0,03	29,17	<0,01	0,17	<0,01	0,02	12,48	4,29	0,19	98,93	73,58
MM47-4.3	1759	52,91	0,02	29,40	0,01	0,18	0,01	0,02	12,64	4,23	0,22	99,65	73,96
MM49-1.1	1767,1	50,27	0,02	31,37	<0,01	0,24	<0,01	0,02	15,06	2,99	0,19	100,14	82,57
MM49-1.2	1767,1	50,35	<0,01	31,91	0,01	0,14	<0,01	0,01	15,18	2,79	0,18	100,58	83,64
MM49-1.3	1767,1	51,81	0,01	31,39	<0,01	0,24	<0,01	0,02	14,38	3,18	0,22	101,24	80,88
MM49-1.4	1767,1	51,53	0,03	30,52	0,01	0,22	<0,01	0,02	14,15	3,27	0,22	99,98	80,22
MM49-2.1	1767,1	50,90	0,03	30	<0,01	0,28	0,01	0,02	13,78	3,55	0,25	98,82	78,38
MM49-2.2	1767,1	51,21	0,03	30,33	0,01	0,21	<0,01	0,02	13,80	3,64	0,26	99,53	77,97
MM49-2.3	1767,1	50,75	0,04	30,59	<0,01	0,22	<0,01	0,05	14,01	3,56	0,22	99,43	78,75
MM49-2.4	1767,1	51,47	0,02	29,92	<0,01	0,19	<0,01	0,01	13,51	3,91	0,28	99,3	76,33
MM49-2.5	1767,1	51,36	0,02	30,06	<0,01	0,16	0,01	0,01	13,53	3,77	0,24	99,15	77,14
MM49-2.6	1767,1	50,51	0,03	30,66	<0,01	0,19	<0,01	0,02	14,29	3,33	0,22	99,26	80,10

Sample/Points	Depth (m)	SiO_2	TiO_2	Al_2O_3	Cr_2O_3	FeO	MnO	MgO	CaO	Na_2O	K_2O	Total	An%
MM49-3.1	1767,1	49,42	0,02	30,58	<0,01	0,21	<0,01	0,04	14,45	3,31	0,21	98,22	80,41
MM49-3.3	1767,1	50,01	0,03	30,55	<0,01	0,23	<0,01	<0,01	14,44	3,27	0,19	98,72	80,67
MM49-3.4	1767,1	50,06	0,01	30,52	<0,01	0,19	0,01	0,04	14,38	3,34	0,21	98,76	80,20
MM51-1.1	1776	49,42	<0,01	31,04	0,01	0,25	<0,01	<0,01	15,12	3,01	0,11	98,96	82,89
MM51-1.2	1776	49,65	0,02	30,96	<0,01	0,20	0,01	0,03	14,77	3,10	0,13	98,88	82,06
MM51-1.3	1776	49,43	0,05	31,14	<0,01	0,19	0,01	0,02	15,05	2,99	0,13	99	82,83
MM51-1.4	1776	50,35	<0,01	30,54	<0,01	0,20	<0,01	0,01	14,31	3,46	0,14	99,01	79,90
MM51-1.5	1776	49,59	<0,01	31,08	<0,01	0,22	0,01	<0,01	14,95	3,03	0,13	99,02	82,55
MM51-1.6	1776	49,92	0,04	31,49	<0,01	0,24	<0,01	0,02	15,08	2,89	0,12	99,8	83,36
MM51-2.1	1776	50,46	0,03	30,38	<0,01	0,21	<0,01	0,02	13,73	3,34	0,18	98,34	79,59
MM51-2.2	1776	51,18	<0,01	30,59	0,02	0,24	<0,01	0,01	13,43	3,39	0,17	99,03	79,05
MM52-1.1	1776,6	50,75	0,04	30,73	<0,01	0,21	<0,01	0,02	14,02	3,42	0,20	99,4	79,48
MM52-1.2	1776,6	50,76	0,04	30,59	0,01	0,21	<0,01	0,02	13,88	3,54	0,22	99,28	78,68
MM52-1.3	1776,6	50,89	0,05	30,52	<0,01	0,20	<0,01	0,01	13,97	3,42	0,19	99,26	79,47
MM52-1.4	1776,6	50,57	0,02	30,87	0,01	0,20	<0,01	0,01	14,45	3,28	0,18	99,61	80,68
MM52-1.5	1776,6	50,42	0,02	31,07	<0,01	0,27	0,01	0,03	14,76	3,14	0,13	99,84	81,86
MM52-1.6	1776,6	50,40	0,03	30,56	0,01	0,19	<0,01	0,02	14,27	3,40	0,17	99,05	79,99
MM52-2.1	1776,6	50,56	0,03	30,38	<0,01	0,19	0,01	0,01	13,98	3,43	0,20	98,81	79,39
MM52-2.2	1776,6	50,76	0,01	30,24	0,01	0,20	<0,01	0,01	13,82	3,47	0,20	98,72	79,02
MM52-2.3	1776,6	50,69	0,03	30,40	0,01	0,22	0,01	0,03	14,14	3,52	0,19	99,24	79,22
MM52-2.4	1776,6	50,86	0,03	30,43	<0,01	0,21	<0,01	0,04	13,8	3,56	0,21	99,15	78,54

Sample/Points	Depth (m)	SiO_2	TiO_2	Al_2O_3	Cr_2O_3	FeO	MnO	MgO	CaO	Na_2O	K_2O	Total	An%
MM52-2.5	1776,6	50,77	0,03	30,61	<0,01	0,18	0,01	<0,01	14,14	3,36	0,18	99,28	79,98
MM52-3.2	1776,6	51,92	0,05	29,62	0,01	0,13	<0,01	0,01	12,86	4,17	0,21	98,97	74,59
MM53-1.1	1778	53,03	0,04	28,71	<0,01	0,20	<0,01	<0,01	12,05	4,69	0,2	98,92	71,13
MM53-1.2	1778	52,80	0,03	28,34	<0,01	0,20	<0,01	0,02	11,82	4,92	0,18	98,3	69,86
MM53-1.3	1778	53,52	0,06	28,51	<0,01	0,20	0,02	0,01	11,86	4,69	0,20	99,07	70,81
MM53-2.1	1778	53,78	0,05	29,19	<0,01	0,17	<0,01	0,02	12,21	4,38	0,20	100	72,72
MM53-2.2	1778	53,02	0,05	29,02	<0,01	0,19	0,01	0,01	12,32	4,58	0,20	99,4	72,05
MM53-2.3	1778	53,17	0,02	29,15	<0,01	0,18	0,01	0,04	12,30	4,50	0,21	99,59	72,31
MM53-2.4	1778	53,31	0,03	28,69	<0,01	0,27	0,01	0,02	12,15	4,66	0,20	99,33	71,43
MM56-1.1	1779,2	61,01	0,02	24,02	0,01	0,20	<0,01	0,02	6,19	8,04	0,40	99,9	42,31
MM56-1.2	1779,2	60,76	<0,01	24,36	<0,01	0,20	<0,01	0,01	6,39	8	0,38	100,09	43,26
MM56-1.3	1779,2	60,66	0,02	24,25	<0,01	0,19	<0,01	0,01	6,37	8,01	0,40	99,9	43,10
MM56-1.4	1779,2	60,92	<0,01	23,90	<0,01	0,15	<0,01	0,02	6,17	8,19	0,39	99,75	41,83
MM56-2.1	1779,2	54,85	0,04	27,27	<0,01	0,14	<0,01	0,01	10,52	5,69	0,28	98,8	63,80
MM56-2.2	1779,2	56,19	0,03	26,14	<0,01	0,17	<0,01	0,01	9,30	6,37	0,30	98,51	58,23
MM56-2.3	1779,2	56,51	0,03	26,53	<0,01	0,13	<0,01	0,02	9,47	6,31	0,27	99,27	59,00
MM56-2.4	1779,2	59,44	0,01	24,33	<0,01	0,15	<0,01	<0,01	6,79	7,62	0,49	98,84	45,57
MM56-2.5	1779,2	55,72	0,03	26,77	0,01	0,15	0,01	0,02	9,87	6	0,26	98,82	61,19
MM57-1.1	1779,7	52,10	0,04	28,97	<0,01	0,17	0,01	0,01	12,46	4,28	0,24	98,28	73,38
MM57-1.2	1779,7	52,91	0,04	29	0,02	0,15	<0,01	0,01	12,19	4,59	0,26	99,17	71,54
MM57-1.3	1779,7	52,36	0,08	28,76	<0,01	0,19	<0,01	<0,01	12,26	4,45	0,26	98,37	72,25

Sample/Points	Depth (m)	SiO_2	TiO_2	Al_2O_3	Cr_2O_3	FeO	MnO	MgO	CaO	Na_2O	K_2O	Total	An%
MM57-2.1	1779,7	53,63	0,04	29,13	<0,01	0,17	<0,01	0,02	12,09	4,39	0,23	99,71	72,35
MM57-3.1	1779,7	53,32	0,03	28,75	<0,01	0,20	<0,01	0,02	12,01	4,67	0,25	99,26	70,94
MM57-3.2	1779,7	53,48	0,03	28,83	<0,01	0,21	<0,01	0,02	11,81	4,71	0,30	99,4	70,21
MM57-3.3	1779,7	53,47	0,02	28,61	<0,01	0,20	0,01	0,02	11,81	4,65	0,26	99,05	70,63
MM57-4.1	1779,7	51,95	0,04	29,13	0,01	0,19	0,01	0,02	12,17	4,22	0,25	98	73,14
MM57-4.2	1779,7	52,65	0,05	29,02	<0,01	0,16	0,01	0,02	12,34	4,24	0,29	98,78	73,15
MM58-1.1	1780	52,01	0,05	30,03	<0,01	0,18	<0,01	0,02	13,13	3,92	0,24	99,57	75,94
MM58-1.2	1780	51,55	0,06	29,97	0,01	0,17	0,01	0,01	13,20	3,84	0,23	99,04	76,43
MM58-1.3	1780	51,79	0,03	29,63	<0,01	0,16	<0,01	<0,01	13	3,96	0,23	98,81	75,63
MM58-1.4	1780	52,23	0,02	30,04	<0,01	0,2	<0,01	0,01	12,98	3,82	0,23	99,55	76,22
MM58-1.5	1780	51,82	0,05	29,86	0,01	0,20	<0,01	0,02	13,13	3,91	0,22	99,22	76,07
MM58-2.1	1780	51,99	0,04	29,92	<0,01	0,20	0,01	0,02	13,08	3,96	0,23	99,43	75,74
MM58-2.2	1780	51,74	0,01	29,67	0,01	0,18	<0,01	<0,01	12,89	4,04	0,24	98,78	75,07
MM58-2.3	1780	51,82	0,02	29,67	0,01	0,17	0,01	0,02	12,84	4,03	0,23	98,83	75,09
MM58-2.4	1780	52	0,05	29,98	<0,01	0,14	<0,01	0,01	12,92	3,87	0,23	99,2	75,91
MM58-2.5	1780	51,74	0,01	29,83	<0,01	0,15	<0,01	0,01	13,20	3,96	0,23	99,14	75,91
MM59-1.1	1781,2	53,95	0,02	28,16	<0,01	0,09	<0,01	0,01	11,16	5,26	0,18	98,82	67,23
MM59-1.2	1781,2	54,56	0,07	27,64	<0,01	0,11	<0,01	<0,01	10,61	5,56	0,27	98,81	64,54
MM59-1.3	1781,2	53,73	0,06	27,86	<0,01	0,13	0,01	0,01	11,12	5,23	0,25	98,39	66,99
MM59-1.4	1781,2	54,94	0,03	28	<0,01	0,11	<0,01	<0,01	10,65	5,51	0,22	99,46	65,02
MM59-2.1	1781,2	51,78	0,04	29,41	<0,01	0,18	<0,01	0,01	12,96	4,10	0,24	98,72	74,91

Sample/Points	Depth (m)	SiO_2	TiO_2	Al_2O_3	Cr_2O_3	FeO	MnO	MgO	CaO	Na_2O	K_2O	Total	An%
MM59-2.2	1781,2	52,04	0,03	29,23	0,01	0,19	<0,01	0,02	12,79	4,28	0,27	98,86	73,76
MM59-3.1	1781,2	51,55	0,05	29,63	<0,01	0,20	<0,01	0,02	13,09	4,12	0,23	98,9	75,06
MM59-3.2	1781,2	51,75	0,05	29,42	<0,01	0,18	<0,01	0,01	13,03	4,23	0,22	98,89	74,54
MM59-3.3	1781,2	51,92	0,03	29,44	<0,01	0,11	0,01	<0,01	12,82	4,23	0,22	98,78	74,23
MM59-3.4	1781,2	51,05	0,03	29,64	0,01	0,17	<0,01	0,03	13,13	4,11	0,20	98,37	75,29
MM59-3.5	1781,2	53,30	0,01	28,90	<0,01	0,14	0,01	0,01	11,85	4,68	0,31	99,21	70,37
MM60-1.1	1786	55,31	0,03	27,87	0,01	0,13	0,01	0,01	10,56	5,49	0,19	99,6	65,02
MM60-1.2	1786	55,58	0,03	27,76	<0,01	0,10	<0,01	0,02	10,33	5,68	0,18	99,68	63,80
MM60-1.3	1786	55,28	0,01	28,04	0,01	0,14	<0,01	0,01	10,66	5,53	0,18	99,86	65,12
MM60-1.4	1786	55,10	0,03	27,79	<0,01	0,14	<0,01	0,01	10,59	5,66	0,14	99,47	64,61
MM60-1.5	1786	54,73	0,02	27,90	<0,01	0,15	<0,01	0,02	10,87	5,65	0,15	99,5	65,21
MM60-2.1	1786	55,63	0,02	27,56	<0,01	0,13	<0,01	<0,01	10,44	5,66	0,19	99,63	64,09
MM60-2.2	1786	55,01	0,05	27,72	0,01	0,16	<0,01	<0,01	10,61	5,71	0,18	99,44	64,30
MM60-2.3	1786	55,45	<0,01	27,45	0,01	0,11	0,01	0,01	10,24	5,79	0,22	99,28	63,02
MM63-1.1	1793	51,72	0,02	29,05	<0,01	0,17	0,02	0,04	12,46	4,37	0,25	98,09	72,95
MM63-1.2	1793	52,76	0,05	28,39	<0,01	0,17	<0,01	0,03	11,51	4,87	0,32	98,09	68,92
MM63-1.3	1793	52,83	0,02	28,68	<0,01	0,19	0,01	0,03	11,77	4,66	0,27	98,44	70,48
MM63-1.4	1793	53,72	0,04	27,97	<0,01	0,17	0,01	0,01	11,22	5,05	0,32	98,51	67,63
MM63-1.5	1793	54,78	0,04	27,65	0,02	0,17	0,01	0,01	10,75	5,33	0,33	99,08	65,51
MM63-2.1	1793	55,91	0,03	26,81	0,02	0,20	0,01	0,02	9,71	5,68	0,44	98,83	61,34
MM64-1.1	1794	48,57	0,02	31,50	<0,01	0,22	<0,01	<0,01	15,38	2,83	0,15	98,65	83,77

Sample/Points	Depth (m)	SiO_2	TiO_2	Al_2O_3	Cr_2O_3	FeO	MnO	MgO	CaO	Na_2O	K_2O	Total	An%
MM64-1.2	1794	48,27	0,03	31,70	<0,01	0,17	<0,01	0,02	15,76	2,63	0,13	98,71	85,10
MM64-1.4	1794	48,87	0,02	31,18	<0,01	0,19	<0,01	0,01	15,05	2,92	0,16	98,39	83,01
MM64-1.5	1794	48,53	0,03	31,40	0,01	0,18	<0,01	0,02	15,43	2,85	0,12	98,58	83,86
MM64-2.1	1794	50,14	0,01	30,66	<0,01	0,17	0,01	0,01	14,36	3,44	0,17	98,96	79,91
MM64-2.2	1794	50,68	0,02	30,57	0,01	0,13	<0,01	0,01	14,09	3,46	0,19	99,18	79,43
MM64-2.3	1794	52,50	0,01	30,22	<0,01	0,13	<0,01	0,01	13,25	3,75	0,20	100,05	77,03
MM64-2.4	1794	51,11	0,02	29,96	<0,01	0,15	0,01	0,05	13,04	4,37	0,19	98,91	74,09
MM64-3.1	1794	50,17	0,02	30,28	0,02	0,22	<0,01	0,01	14,05	3,53	0,18	98,48	79,11
MM64-3.2	1794	51,01	0,01	30,02	<0,01	0,20	<0,01	0,01	13,61	3,77	0,24	98,88	77,24
MM64-3.3	1794	50,40	0,03	30,24	<0,01	0,21	0,01	0,02	13,87	3,70	0,20	98,67	78,05
MM64-3.4	1794	50,26	0,02	30,04	<0,01	0,20	<0,01	0,03	13,97	3,55	0,19	98,26	78,88
MM64-3.5	1794	50,50	0,04	30,31	0,02	0,20	<0,01	0,02	13,88	3,60	0,21	98,78	78,46
MM64-3.6	1794	50,38	0,04	30,19	<0,01	0,19	<0,01	0,02	14,06	3,60	0,20	98,67	78,72
MM65-1.1	1797	53,97	0,01	28,37	<0,01	0,18	<0,01	<0,01	11,12	5,07	0,20	98,94	67,85
MM65-1.2	1797	53,36	0,03	28,51	<0,01	0,13	<0,01	0,02	11,53	4,82	0,21	98,62	69,63
MM65-1.3	1797	53,15	0,04	28,25	<0,01	0,14	<0,01	0,01	11,48	4,93	0,18	98,18	69,20
MM65-1.4	1797	53,60	0,05	28,32	<0,01	0,15	<0,01	0,01	11,43	4,83	0,20	98,58	69,44
MM65-2.1	1797	56,76	0,05	26,74	0,01	0,09	<0,01	<0,01	9,46	6,27	0,23	99,6	59,27
MM65-2.2	1797	56,01	0,04	27	0,01	0,12	<0,01	0,01	9,75	6,02	0,22	99,18	60,98
MM65-2.3	1797	55,67	0,06	27,40	<0,01	0,11	<0,01	0,04	10,29	5,72	0,21	99,5	63,44
MM65-2.4	1797	55,11	0,03	27,71	0,01	0,11	<0,01	0,01	10,57	5,65	0,18	99,39	64,45

Sample/Points	Depth (m)	SiO_2	TiO_2	Al_2O_3	Cr_2O_3	FeO	MnO	MgO	CaO	Na_2O	K_2O	Total	An%
MM65-3.1	1797	55,35	0,06	27,29	<0,01	0,14	<0,01	0,01	10,22	5,71	0,25	99,04	63,16
MM65-3.2	1797	54,32	0,04	28,30	<0,01	0,17	<0,01	0,01	11,19	5,13	0,22	99,38	67,65
MM65-3.3	1797	55,18	0,07	27,81	<0,01	0,17	0,01	<0,01	10,55	5,47	0,20	99,46	65,04

Appendix E

Table E-1: In-situ plagioclase Sr-isotopic composition for individual spots calculated at 2054.4 Ma.

Depth (m)	Points	Zone	$^{87}Sr/^{86}Sr_i$	2σ-SE	$^{87}Sr/^{86}Sr$	2σ-SE	$^{87}Rb/^{86}Sr$	2σ-SE	Rim/Core
1701	MM1-1-1	UCZ	0,7063	0,00083	0,7064	0,00083	0,0020	0,00011	Rim
1701	MM1-1-2	UCZ	0,7062	0,00073	0,7063	0,00073	0,0021	0,00011	Rim
1701	MM1-1-3	UCZ	0,7072	0,00078	0,7073	0,000778	0,0023	0,00011	Core
1701	MM1-2-1	UCZ	0,7057	0,00031	0,7058	0,000306	0,0030	0,00005	Rim
1701	MM1-2-3	UCZ	0,7057	0,00046	0,7080	0,000368	0,0767	0,00463	Rim
1701	MM1-2-2	UCZ	0,7060	0,00031	0,7061	0,000312	0,0044	0,00018	Core
1705	MM2-1-1	UCZ	0,7064	0,00043	0,7065	0,000428	0,0036	0,00006	Rim
1705	MM2-1-2	UCZ	0,7059	0,00035	0,7060	0,000354	0,0026	0,00005	Core
1705	MM2-2-1	UCZ	0,7052	0,00032	0,7077	0,000274	0,0847	0,00290	Rim
1705	MM2-2-2	UCZ	0,7054	0,00026	0,7058	0,000256	0,0100	0,00036	Core
1705	MM2-3-1	UCZ	0,7062	0,00027	0,7065	0,000268	0,0072	0,00039	Core
1710,3	MM3-1-1	UCZ	0,7056	0,00045	0,7059	0,000452	0,0064	0,00012	Core
1710,3	MM3-1-2	UCZ	0,7065	0,00050	0,7067	0,000498	0,0035	0,00008	Rim
1710,3	MM3-1-3	UCZ	0,7057	0,00046	0,7060	0,000456	0,0102	0,00033	Rim
1711	MM4-3-1	UCZ	0,7055	0,00034	0,7062	0,00034	0,0199	0,00073	Core
1711	MM4-3-2	UCZ	0,7064	0,00036	0,7065	0,00036	0,0006	0,00005	Rim
1711	MM4-2-1	UCZ	0,7060	0,00040	0,7060	0,0004	0,0012	0,00009	Rim
1711	MM4-2-2	UCZ	0,7060	0,00034	0,7061	0,000336	0,0006	0,00005	Core
1711	MM4-1-1	UCZ	0,7058	0,00038	0,7058	0,000376	0,0006	0,00005	Core
1711	MM4-1-2	UCZ	0,7060	0,00036	0,7060	0,000364	0,0008	0,00004	Rim

Depth (m)	Points	Zone	$^{87}Sr/^{86}Sr_i$	2σ-SE	$^{87}Sr/^{86}Sr$	2σ-SE	$^{87}Rb/^{86}Sr$	2σ-SE	Rim/Core
1712	MM5-2-1	UCZ	0,7063	0,00024	0,7065	0,000244	0,0036	0,00003	Rim
1712	MM5-3-1	UCZ	0,7061	0,00023	0,7063	0,000228	0,0039	0,00003	Rim
1712	MM5-3-2	UCZ	0,7056	0,00025	0,7057	0,000248	0,0027	0,00003	Core
1712	MM5-1-1	UCZ	0,7061	0,00025	0,7062	0,000246	0,0039	0,00003	Rim
1712	MM5-1-2	UCZ	0,7058	0,00024	0,7059	0,00024	0,0039	0,00003	Core
1712,3	MM6-1-1	UCZ	0,7059	0,000278	0,7059	0,000278	0,0008	0,00003	Core
1712,3	MM6-1-2	UCZ	0,7057	0,00026	0,7057	0,00026	0,0005	0,00003	Core
1712,3	MM6-2-1	UCZ	0,7058	0,000222	0,7059	0,000222	0,0008	0,00003	Rim
1712,3	MM6-2-1	UCZ	0,7057	0,000218	0,7058	0,000218	0,0009	0,00003	Core
1712,3	MM6-2-3	UCZ	0,7057	0,000244	0,7058	0,000244	0,0011	0,00004	Rim
1712,3	MM6-3-1	UCZ	0,7056	0,000236	0,7057	0,000236	0,0010	0,00004	Rim
1712,3	MM6-3-2	UCZ	0,7058	0,00024	0,7059	0,00024	0,0007	0,00003	Core
1712,3	MM6-3-3	UCZ	0,7058	0,00025	0,7059	0,00025	0,0006	0,00003	Rim
1713	MM7-3-1	UCZ	0,7059	0,00034	0,7060	0,000338	0,0003	0,00005	Rim
1713	MM7-3-3	UCZ	0,7058	0,00029	0,7059	0,00029	0,0002	0,00004	Rim
1713	MM7-3-2	UCZ	0,7055	0,00024	0,7056	0,000244	0,0003	0,00004	Core
1713,6	MM8-1-1	UCZ	0,7056	0,00026	0,7057	0,000256	0,0014	0,00004	Core
1713,6	MM8-1-2	UCZ	0,7063	0,00028	0,7064	0,000276	0,0010	0,00003	Rim
1714,8	MM10-2-1	UCZ	0,7058	0,00031	0,7059	0,000312	0,0021	0,00004	Rim
1714,8	MM10-2-2	UCZ	0,7059	0,00028	0,7060	0,000278	0,0025	0,00003	Core
1714,8	MM10-2-3	UCZ	0,7060	0,00027	0,7061	0,000268	0,0015	0,00003	Rim
1715,4	MM11-1-1	UCZ	0,7058	0,00031	0,7058	0,000308	0,0005	0,00004	Rim

Depth (m)	Points	Zone	$^{87}Sr/^{86}Sr_i$	2σ-SE	$^{87}Sr/^{86}Sr$	2σ-SE	$^{87}Rb/^{86}Sr$	2σ-SE	Rim/Core
1715,4	MM11-1-2	UCZ	0,7057	0,00029	0,7058	0,000292	0,0006	0,00004	Core
1715,4	MM11-2-1	UCZ	0,7057	0,00029	0,7058	0,000294	0,0004	0,00004	Core
1715,4	MM11-2-2	UCZ	0,7061	0,00029	0,7062	0,000288	0,0004	0,00004	Rim
1715,8	MM12-1-1	UCZ	0,7047	0,00063	0,7050	0,000632	0,0068	0,00011	Core
1715,8	MM12-1-2	UCZ	0,7063	0,00060	0,7067	0,000598	0,0105	0,00022	Rim
1715,8	MM12-1-3	UCZ	0,7066	0,00064	0,7069	0,000642	0,0075	0,00010	Rim
1715,8	MM12-2-1	UCZ	0,7070	0,00067	0,7072	0,00067	0,0057	0,00010	Rim
1715,8	MM12-2-2	UCZ	0,7064	0,00064	0,7067	0,00064	0,0091	0,00013	Core
1717,2	MM14-1-1	UCZ	0,7063	0,00041	0,7063	0,00036	0,0003	0,00005	Core
1717,2	MM14-1-3	UCZ	0,7056	0,00036	0,7056	0,000356	0,0003	0,00005	Rim
1717,2	MM14-1-2	UCZ	0,7063	0,00036	0,7063	0,000338	0,0002	0,00005	Rim
1718	MM15-1-1	UCZ	0,7057	0,00028	0,7058	0,000284	0,0002	0,00004	Core
1718	MM15-2-1	UCZ	0,7061	0,00027	0,7061	0,000274	0,0006	0,00004	Core
1719	MM16-1-1	UCZ	0,7058	0,00026	0,7059	0,000262	0,0043	0,00004	Rim
1719	MM16-1-2	UCZ	0,7059	0,00026	0,7060	0,000258	0,0038	0,00004	Core
1719	MM16-1-3	UCZ	0,7059	0,00024	0,7061	0,00024	0,0054	0,00003	Rim
1719	MM16-2-1	UCZ	0,7057	0,00029	0,7059	0,000286	0,0062	0,00004	Rim
1719	MM16-2-2	UCZ	0,7055	0,00024	0,7058	0,000236	0,0065	0,00003	Core
1719	MM16-2-3	UCZ	0,7057	0,00023	0,7059	0,000234	0,0050	0,00003	Rim
1719	MM16-3-1	UCZ	0,7061	0,00029	0,7063	0,000288	0,0056	0,00004	Rim
1719	MM16-3-2	UCZ	0,7059	0,00024	0,7062	0,000242	0,0080	0,00003	Core
1719	MM16-3-3	UCZ	0,7056	0,00027	0,7059	0,000266	0,0084	0,00003	Rim

Depth (m)	Points	Zone	$^{87}Sr/^{86}Sr_i$	2σ-SE	$^{87}Sr/^{86}Sr$	2σ-SE	$^{87}Rb/^{86}Sr$	2σ-SE	Rim/Core
1719,2	MM17-1-1	UCZ	0,7055	0,00026	0,7057	0,000262	0,0045	0,00003	Rim
1719,2	MM17-1-3	UCZ	0,7058	0,00028	0,7060	0,000278	0,0059	0,00003	Rim
1719,2	MM17-2-1	UCZ	0,7058	0,00028	0,7059	0,000278	0,0009	0,00004	Rim
1719,2	MM17-2-2	UCZ	0,7056	0,00024	0,7058	0,000242	0,0042	0,00010	Core
1719,2	MM17-2-3	UCZ	0,7056	0,00024	0,7058	0,000236	0,0027	0,00003	Rim
1721	MM19-1-1	UCZ	0,7056	0,00035	0,7057	0,00038	0,0018	0,00006	Core
1721	MM19-1-2	UCZ	0,7058	0,00039	0,7059	0,00039	0,0028	0,00004	Rim
1721	MM19-1-3	UCZ	0,7063	0,00035	0,7065	0,000352	0,0038	0,00004	Rim
1721,7	MM20-2-1	UCZ	0,7060	0,00026	0,7060	0,000264	0,0010	0,00003	Core
1721,7	MM20-2-3	UCZ	0,7057	0,00026	0,7058	0,000234	0,0007	0,00003	Rim
1721,7	MM20-1-2	UCZ	0,7063	0,00023	0,7064	0,000242	0,0010	0,00003	Core
1721,7	MM20-1-1	UCZ	0,7059	0,00024	0,7060	0,000256	0,0010	0,00003	Rim
1721,7	MM20-1-3	UCZ	0,7059	0,00026	0,7060	0,000222	0,0010	0,00004	Rim
1721,7	MM20-3-1	UCZ	0,7061	0,00022	0,7063	0,000266	0,0060	0,00049	Rim
1721,7	MM20-3-2	UCZ	0,7060	0,00027	0,7061	0,00025	0,0022	0,00003	Core
1721,7	MM20-3-3	UCZ	0,7060	0,00025	0,7061	0,00025	0,0028	0,00003	Rim
1722	MM21-1-1	UCZ	0,7060	0,00025	0,7061	0,00042	0,0048	0,00007	Rim
1722	MM21-1-2	UCZ	0,7054	0,00040	0,7060	0,000396	0,0200	0,00058	Core
1722	MM21-1-3	UCZ	0,7060	0,00039	0,7062	0,000388	0,0070	0,00013	Rim
1722	MM21-2-1	UCZ	0,7053	0,00038	0,7055	0,000382	0,0041	0,00007	Rim
1722	MM21-2-2	UCZ	0,7053	0,00038	0,7055	0,00038	0,0041	0,00005	Core
1722	MM21-2-3	UCZ	0,7058	0,00040	0,7059	0,0004	0,0029	0,00006	Rim

Depth (m)	Points	Zone	$^{87}Sr/^{86}Sr_i$	2σ-SE	$^{87}Sr/^{86}Sr$	2σ-SE	$^{87}Rb/^{86}Sr$	2σ-SE	Rim/Core
1722	MM21-3-1	UCZ	0,7059	0,00042	0,7060	0,000424	0,0018	0,00006	Rim
1722	MM21-3-3	UCZ	0,7052	0,00037	0,7054	0,000372	0,0031	0,00005	Rim
1722,3	MM22-1-1	UCZ	0,7059	0,00047	0,7059	0,00047	0,0003	0,00006	Core
1724	MM24-2-1	UCZ	0,7061	0,00033	0,7062	0,000326	0,0040	0,00004	Core
1724	MM24-2-2	UCZ	0,7061	0,00029	0,7062	0,000288	0,0024	0,00004	Rim
1724	MM24-3-2	UCZ	0,7064	0,00038	0,7083	0,000356	0,0627	0,00208	Rim
1724	MM24-3-1	UCZ	0,7058	0,00028	0,7059	0,00028	0,0023	0,00004	Core
1728	MM25-3-1	UCZ	0,7060	0,00030	0,7062	0,000302	0,0041	0,00004	Rim
1728	MM25-3-2	UCZ	0,7059	0,00029	0,7060	0,000286	0,0043	0,00004	Core
1728	MM25-3-3	UCZ	0,7061	0,00032	0,7067	0,000318	0,0191	0,00055	Rim
1728	MM25-2-1	UCZ	0,7050	0,00069	0,7140	0,000516	0,3009	0,00787	Rim
1728	MM25-2-3	UCZ	0,7055	0,00039	0,7080	0,000334	0,0816	0,00327	Rim
1728	MM25-2-2	UCZ	0,7061	0,00029	0,7065	0,000284	0,0131	0,00050	Core
1728	MM25-1-1	UCZ	0,7061	0,00031	0,7062	0,000314	0,0034	0,00004	Rim
1728	MM25-1-2	UCZ	0,7055	0,00027	0,7056	0,000266	0,0025	0,00004	Core
1733	MM26-2-1	UCZ	0,7054	0,00044	0,7064	0,00038	0,0326	0,00381	Rim
1733	MM26-2-2	UCZ	0,7064	0,00032	0,7066	0,000318	0,0060	0,00004	Core
1733	MM26-2-3	UCZ	0,7057	0,00029	0,7060	0,000286	0,0059	0,00003	Rim
1733	MM26-3-1	UCZ	0,7058	0,00032	0,7062	0,000314	0,0102	0,00059	Rim
1733	MM26-3-2	UCZ	0,7063	0,00032	0,7066	0,000324	0,0062	0,00004	Rim
1733	MM26-1-1	UCZ	0,7054	0,00031	0,7056	0,000312	0,0042	0,00004	Rim
1733	MM26-1-2	UCZ	0,7060	0,00032	0,7062	0,00032	0,0055	0,00004	Core

Depth (m)	Points	Zone	$^{87}Sr/^{86}Sr_i$	2σ-SE	$^{87}Sr/^{86}Sr$	2σ-SE	$^{87}Rb/^{86}Sr$	2σ-SE	Rim/Core
1733	MM26-1-3	UCZ	0,7063	0,00028	0,7065	0,000284	0,0040	0,00004	Rim
1741	MM28-1-2	UCZ	0,7054	0,00056	0,7087	0,000442	0,1085	0,00577	Core
1741	MM28-2-1	UCZ	0,7059	0,00039	0,7060	0,000392	0,0028	0,00007	Rim
1741	MM28-2-2	UCZ	0,7053	0,00038	0,7054	0,000384	0,0030	0,00011	Core
1741	MM28-2-3	UCZ	0,7061	0,00034	0,7062	0,00034	0,0016	0,00005	Rim
1743	MM29-2-1	UCZ	0,7054	0,00036	0,7055	0,000358	0,0020	0,00008	Rim
1743	MM29-2-2	UCZ	0,7057	0,00035	0,7064	0,000342	0,0202	0,00097	Core
1743	MM29-2-3	UCZ	0,7058	0,00034	0,7061	0,000344	0,0097	0,00030	Rim
1743	MM29-3-1	UCZ	0,7060	0,00039	0,7061	0,000388	0,0027	0,00005	Core
1743	MM29-3-2	UCZ	0,7064	0,00035	0,7066	0,00035	0,0027	0,00005	Rim
1743	MM29-3-3	UCZ	0,7055	0,00031	0,7056	0,00031	0,0026	0,00004	Rim
1743	MM29-1-1	UCZ	0,7062	0,00027	0,7063	0,000268	0,0028	0,00003	Rim
1743	MM29-1-2	UCZ	0,7063	0,00024	0,7064	0,000238	0,0024	0,00003	Core
1743	MM29-1-3	UCZ	0,7063	0,00024	0,7064	0,000242	0,0017	0,00003	Rim
1745	MM30-1-1	UCZ	0,7055	0,00041	0,7056	0,000412	0,0021	0,00005	Rim
1745	MM30-1-2	UCZ	0,7059	0,00037	0,7060	0,000368	0,0024	0,00006	Core
1745	MM30-1-3	UCZ	0,7058	0,00036	0,7059	0,000362	0,0025	0,00005	Rim
1745	MM30-2-1	UCZ	0,7054	0,00044	0,7064	0,000424	0,0326	0,00220	Rim
1745	MM30-2-2	UCZ	0,7059	0,00031	0,7068	0,000288	0,0291	0,00174	Core
1745	MM30-2-3	UCZ	0,7058	0,00026	0,7064	0,000256	0,0196	0,00082	Rim
1745	MM30-3-1	UCZ	0,7054	0,00042	0,7055	0,000422	0,0011	0,00006	Rim
1745	MM30-3-2	UCZ	0,7064	0,00038	0,7065	0,000376	0,0021	0,00006	Core

Depth (m)	Points	Zone	$^{87}Sr/^{86}Sr_i$	2σ-SE	$^{87}Sr/^{86}Sr$	2σ-SE	$^{87}Rb/^{86}Sr$	2σ-SE	Rim/Core
1745	MM30-3-3	UCZ	0,7059	0,00037	0,7060	0,000372	0,0016	0,00005	Rim
1747	MM31-1-2	UCZ	0,7058	0,00029	0,7063	0,000294	0,0154	0,00032	Core
1747	MM31-1-3	UCZ	0,7058	0,00031	0,7060	0,00031	0,0040	0,00004	Rim
1747	MM31-2-1	UCZ	0,7056	0,00031	0,7057	0,000312	0,0033	0,00005	Rim
1747	MM31-2-2	UCZ	0,7064	0,00028	0,7065	0,000284	0,0039	0,00004	Core
1747	MM31-2-3	UCZ	0,7060	0,00029	0,7061	0,000294	0,0026	0,00004	Rim
1747,5	MM32-1-1	UCZ	0,7061	0,00029	0,7062	0,000292	0,0029	0,00004	Rim
1747,5	MM32-1-2	UCZ	0,7060	0,00029	0,7064	0,000284	0,0145	0,00125	Core
1747,5	MM32-2-1	UCZ	0,7060	0,00032	0,7061	0,000316	0,0035	0,00004	Rim
1747,5	MM32-2-2	UCZ	0,7060	0,00030	0,7061	0,0003	0,0023	0,00004	Core
1748	MM33-2-1	UCZ	0,7055	0,00042	0,7066	0,000418	0,0371	0,00112	Rim
1748	MM33-2-2	UCZ	0,7059	0,00044	0,7075	0,00042	0,0519	0,00229	Core
1748	MM33-2-3	UCZ	0,7050	0,00054	0,7106	0,000444	0,1887	0,00526	Rim
1748	MM33-3-1	UCZ	0,7065	0,00042	0,7065	0,000422	0,0013	0,00007	Rim
1748	MM33-3-2	UCZ	0,7061	0,00042	0,7070	0,000416	0,0280	0,00087	Core
1748	MM33-3-3	UCZ	0,7056	0,00040	0,7066	0,0004	0,0330	0,00086	Rim
1748,6	MM34-1-1	UCZ	0,7062	0,00049	0,7063	0,00049	0,0002	0,00007	Rim
1748,6	MM34-2-1	UCZ	0,7055	0,00033	0,7070	0,000316	0,0474	0,00130	Core
1749,2	MM35-1-1	UCZ	0,7056	0,00030	0,7056	0,000302	0,0000	0,00004	Core
1749,5	MM36-1-1	UCZ	0,7066	0,00041	0,7067	0,000414	0,0020	0,00006	Core
1753	MM39-1-1	UCZ	0,7056	0,00043	0,7059	0,00043	0,0096	0,00030	Rim
1753	MM39-1-2	UCZ	0,7067	0,00041	0,7068	0,000408	0,0025	0,00005	Rim

Depth (m)	Points	Zone	$^{87}Sr/^{86}Sr_i$	2σ-SE	$^{87}Sr/^{86}Sr$	2σ-SE	$^{87}Rb/^{86}Sr$	2σ-SE	Rim/Core
1753	MM39-2-1	UCZ	0,7060	0,00045	0,7060	0,000452	0,0012	0,00006	Rim
1753	MM39-2-3	UCZ	0,7055	0,00042	0,7059	0,00042	0,0096	0,00035	Rim
1753	MM39-3-1	UCZ	0,7057	0,00029	0,7085	0,000288	0,0945	0,00092	Rim
1753	MM39-3-3	UCZ	0,7056	0,00028	0,7072	0,000276	0,0519	0,00116	Core
1753	MM39-3-3	UCZ	0,7059	0,00027	0,7060	0,000274	0,0032	0,00009	Rim
1755	MM41-1-2	UCZ	0,7055	0,00033	0,7059	0,000306	0,0106	0,00022	Rim
1756	MM42-1-1	LCZ	0,7055	0,00033	0,7056	0,000334	0,0023	0,00005	Core
1756	MM42-2-1	LCZ	0,7055	0,00035	0,7056	0,000354	0,0010	0,00005	Core
1756,7	MM43-2-1	LCZ	0,7041	0,00131	0,7041	0,000332	0,0007	0,00019	Core
1757	MM44-1-1	LCZ	0,7055	0,00035	0,7055	0,000352	0,0001	0,00005	Core
1757	MM44-2-1	LCZ	0,7055	0,00035	0,7055	0,000352	-0,0001	0,00005	Core
1757,5	MM46-1-1	LCZ	0,7049	0,00033	0,7050	0,000332	0,0001	0,00004	Core
1757,5	MM46-1-2	LCZ	0,7055	0,00032	0,7055	0,00032	0,0001	0,00004	Core
1757,5	MM46-1-3	LCZ	0,7056	0,00032	0,7057	0,000322	0,0003	0,00004	Rim
1767,1	MM49-1-1	LCZ	0,7057	0,00032	0,7058	0,000318	0,0021	0,00006	Core
1767,1	MM49-1-2	LCZ	0,7056	0,00029	0,7057	0,000294	0,0018	0,00004	Rim
1767,1	MM49-2-1	LCZ	0,7053	0,00026	0,7054	0,000264	0,0015	0,00003	Rim
1767,1	MM49-2-2	LCZ	0,7053	0,00024	0,7054	0,00024	0,0017	0,00003	Core
1767,1	MM49-2-3	LCZ	0,7053	0,00025	0,7054	0,000248	0,0018	0,00004	Rim
1767,1	MM49-3-1	LCZ	0,7054	0,00029	0,7055	0,000292	0,0015	0,00004	Rim
1767,1	MM49-3-2	LCZ	0,7054	0,00026	0,7055	0,000258	0,0030	0,00004	Core
1767,1	MM49-3-3	LCZ	0,7051	0,00027	0,7052	0,000274	0,0013	0,00003	Rim

Depth (m)	Points	Zone	$^{87}Sr/^{86}Sr_i$	2σ-SE	$^{87}Sr/^{86}Sr$	2σ-SE	$^{87}Rb/^{86}Sr$	2σ-SE	Rim/Core
1776	MM51-1-1	LCZ	0,7057	0,00027	0,7057	0,000266	0,0003	0,00003	Core
1776	MM51-2-1	LCZ	0,7056	0,00026	0,7057	0,00026	0,0002	0,00004	Rim
1776	MM51-2-2	LCZ	0,7056	0,00024	0,7056	0,000244	0,0004	0,00003	Core
1776	MM51-2-3	LCZ	0,7057	0,00024	0,7058	0,000242	0,0002	0,00003	Rim
1778,3	MM54-1-1	LCZ	0,7034	0,00148	0,7056	0,001478	0,0725	0,00095	Core
1778,3	MM54-2-1	LCZ	0,7066	0,00164	0,7067	0,001636	0,0018	0,00024	Core
1779,7	MM57-1-1	LCZ	0,7052	0,00029	0,7053	0,00029	0,0007	0,00004	Core
1779,7	MM57-1-2	LCZ	0,7054	0,00024	0,7055	0,00024	0,0007	0,00004	Rim
1781,2	MM59-1-1	LCZ	0,7052	0,00034	0,7052	0,00034	0,0003	0,00005	Core
1781,2	MM59-2-1	LCZ	0,7056	0,00045	0,7056	0,000452	0,0009	0,00006	Rim
1781,2	MM59-2-2	LCZ	0,7052	0,00043	0,7053	0,000426	0,0009	0,00006	Core
1781,2	MM59-2-3	LCZ	0,7054	0,00044	0,7054	0,00044	0,0004	0,00006	Rim
1781,2	MM59-3-1	LCZ	0,7055	0,00039	0,7056	0,000386	0,0011	0,00005	Rim
1781,2	MM59-3-2	LCZ	0,7054	0,00034	0,7055	0,000342	0,0013	0,00005	Core
1781,2	MM59-3-3	LCZ	0,7058	0,00035	0,7059	0,000352	0,0010	0,00004	Rim
1786	MM60-1-1	LCZ	0,7058	0,00039	0,7058	0,000386	0,0009	0,00005	Rim
1786	MM60-1-2	LCZ	0,7056	0,00034	0,7057	0,000344	0,0012	0,00005	Rim
1786	MM60-2-1	LCZ	0,7056	0,00035	0,7057	0,000346	0,0018	0,00005	Rim
1786	MM60-2-3	LCZ	0,7061	0,00036	0,7061	0,00036	0,0017	0,00006	Rim
1786	MM60-2-2	LCZ	0,7059	0,00035	0,7060	0,000352	0,0017	0,00005	Core
1793	MM63-1-1	LCZ	0,7055	0,00030	0,7056	0,000298	0,0015	0,00004	Rim
1793	MM63-1-2	LCZ	0,7059	0,00026	0,7059	0,000262	0,0011	0,00003	Core

Depth (m)	Points	Zone	$^{87}Sr/^{86}Sr_i$	2σ-SE	$^{87}Sr/^{86}Sr$	2σ-SE	$^{87}Rb/^{86}Sr$	2σ-SE	Rim/Core
1793	MM63-1-3	LCZ	0,7053	0,00026	0,7053	0,000258	0,0015	0,00003	Rim
1793	MM63-2-1	LCZ	0,7052	0,00029	0,7052	0,000294	0,0009	0,00004	Rim
1793	MM63-2-2	LCZ	0,7061	0,00028	0,7061	0,00028	0,0005	0,00003	Core

Appendix F

Table F-1: In-situ chromite major element compositions.

Depth (m)	Spots/sample	Lithology	Zone	MgO	Al_2O_3	TiO_2	Cr_2O_3	Fe_2O_3	Total
1714,8	MM10-1.1	Chromitite	UCZ	5,30	12,21	0,94	47,61	33,95	100,01
1714,8	MM10-1.2	Chromitite	UCZ	5,46	11,52	1,04	48,25	33,73	100
1714,8	MM10-1.3	Chromitite	UCZ	5,52	11,32	1,03	49,01	33,12	100
1714,8	MM10-1.4	Chromitite	UCZ	5,35	11,40	1,06	49,04	33,15	100
1714,8	MM10-1.5	Chromitite	UCZ	5,38	11,36	0,94	49,15	33,17	100
1714,8	MM10-1.6	Chromitite	UCZ	5,42	11,76	0,79	48,22	33,81	100
1714,8	MM10-1.7	Chromitite	UCZ	5,41	11,50	1,12	47,90	34,07	100
1714,8	MM10-1.8	Chromitite	UCZ	5,40	11,55	1,22	47,61	34,23	100,01
1714,8	MM10-1.9	Chromitite	UCZ	5,39	11,89	1,03	48,19	33,50	100
1714,8	MM10-1.10	Chromitite	UCZ	5,54	11,67	0,72	48,82	33,25	100
1714,8	MM10-1.11	Chromitite	UCZ	5,64	11,59	0,88	48,41	33,48	100
1714,8	MM10-1.12	Chromitite	UCZ	5,45	11,81	0,81	48,59	33,34	100
1714,8	MM10-1.13	Chromitite	UCZ	5,57	11,62	0,90	48,96	32,96	100,01
1714,8	MM10-1.14	Chromitite	UCZ	5,59	11,61	0,88	48,95	32,97	100
1714,8	MM10-2.1	Chromitite	UCZ	5,89	12,51	0,91	47,58	33,11	100
1714,8	MM10-2.2	Chromitite	UCZ	5,86	11,81	1,21	48,53	32,59	100
1714,8	MM10-2.3	Chromitite	UCZ	5,48	11,43	0,89	49,05	33,15	100
1714,8	MM10-2.4	Chromitite	UCZ	5,54	11,47	0,82	49,03	33,14	100
1714,8	MM10-2.5	Chromitite	UCZ	5,32	11,16	1,04	49,01	33,47	100
1714,8	MM10-2.6	Chromitite	UCZ	3,34	6,98	1,23	53,99	34,46	100
1714,8	MM10-2.7	Chromitite	UCZ	5,23	11,22	1,20	48,78	33,57	100
1714,8	MM10-2.8	Chromitite	UCZ	5,61	11,74	0,87	48,85	32,93	100
1714,8	MM10-2.9	Chromitite	UCZ	5,90	12,05	1,14	48,40	32,51	100
1714,8	MM10-3.1	Chromitite	UCZ	5,64	12,31	0,87	48,41	32,77	100
1714,8	MM10-3.2	Chromitite	UCZ	5,42	11,53	0,83	48,43	33,79	100
1714,8	MM10-3.3	Chromitite	UCZ	5,26	10,99	1,12	49,43	33,20	100

Depth (m)	Spots/sample	Lithology	Zone	MgO	Al_2O_3	TiO_2	Cr_2O_3	Fe_2O_3	Total
1714,8	MM10-3.5	Chromitite	UCZ	5,31	11,25	1,37	48,36	33,72	100,01
1714,8	MM10-3.6	Chromitite	UCZ	5,11	11,22	0,93	49,04	33,70	100
1714,8	MM10-3.7	Chromitite	UCZ	5,43	11,17	1,18	48,85	33,38	100,01
1714,8	MM10-3.8	Chromitite	UCZ	5,36	11,25	1,24	48,64	33,51	100
1714,8	MM10-3.9	Chromitite	UCZ	5,55	11,12	1,13	49,25	32,95	100
1714,8	MM10-3.10	Chromitite	UCZ	5,69	11,66	1,16	48,30	33,19	100
1715,4	MM11-1.1	Chr-melagabbronorite	UCZ	3,69	7,35	1,25	45,90	41,81	100
1715,4	MM11-1.2	Chr-melagabbronorite	UCZ	3,52	7,48	1,37	46,06	41,57	100
1715,4	MM11-1.3	Chr-melagabbronorite	UCZ	3,27	7,30	1,63	46,42	41,38	100
1715,4	MM11-1.4	Chr-melagabbronorite	UCZ	3,32	7,37	1,58	46,44	41,29	100
1715,4	MM11-1.5	Chr-melagabbronorite	UCZ	3,30	7,25	1,07	46,33	42,05	100
1715,4	MM11-1.6	Chr-melagabbronorite	UCZ	3,47	7,16	1,49	46,48	41,40	100
1715,4	MM11-1.7	Chr-melagabbronorite	UCZ	3,11	6,87	1,60	46,63	41,80	100,01
1715,4	MM11-1.8	Chr-melagabbronorite	UCZ	3,71	7,85	1,46	46,13	40,85	100
1715,4	MM11-2.1	Chr-melagabbronorite	UCZ	3,79	8,57	1,02	45,64	40,98	100
1715,4	MM11-2.2	Chr-melagabbronorite	UCZ	3,70	8,02	1,41	46,15	40,72	100
1715,4	MM11-2.3	Chr-melagabbronorite	UCZ	3,73	8,03	1,17	46,35	40,72	100
1715,4	MM11-2.4	Chr-melagabbronorite	UCZ	3,51	8,09	1,56	46,42	40,42	100
1715,4	MM11-2.5	Chr-melagabbronorite	UCZ	3,50	7,71	1,51	46,30	40,98	100
1715,4	MM11-2.6	Chr-melagabbronorite	UCZ	3,04	6,98	1,29	47,45	41,24	100
1715,4	MM11-2.7	Chr-melagabbronorite	UCZ	3,75	7,91	1,45	46,41	40,48	100
1715,4	MM11-2.8	Chr-melagabbronorite	UCZ	3,66	8,00	1,45	45,66	41,23	100
1715,4	MM11-2.9	Chr-melagabbronorite	UCZ	3,63	7,85	1,47	46,78	40,27	100
1715,4	MM11-2.10	Chr-melagabbronorite	UCZ	3,84	8,44	1,24	45,69	40,79	100
1715,4	MM11-3.1	Chr-melagabbronorite	UCZ	3,46	7,65	1,45	45,80	41,64	100
1715,4	MM11-3.2	Chr-melagabbronorite	UCZ	3,48	7,78	1,39	45,55	41,80	100
1715,4	MM11-3.3	Chr-melagabbronorite	UCZ	3,40	7,82	1,50	46,11	41,17	100
1715,4	MM11-3.4	Chr-melagabbronorite	UCZ	3,56	7,68	1,58	45,87	41,31	100
1715,4	MM11-3.5	Chr-melagabbronorite	UCZ	3,58	7,77	1,52	45,14	41,99	100

Depth (m)	Spots/sample	Lithology	Zone	MgO	Al_2O_3	TiO_2	Cr_2O_3	Fe_2O_3	Total
1715,4	MM11-3.7	Chr-melagabbronorite	UCZ	3,35	7,71	1,55	45,36	42,04	100,01
1715,4	MM11-3.8	Chr-melagabbronorite	UCZ	3,59	7,32	1,47	45,63	42,00	100,01
1715,4	MM11-3.9	Chr-melagabbronorite	UCZ	3,61	7,77	1,39	44,94	42,30	100,01
1717,2	MM14-1.1	Chromitite	UCZ	5,37	11,59	1,15	45,62	36,27	100
1717,2	MM14-1.2	Chromitite	UCZ	4,98	11,39	1,25	45,73	36,65	100
1717,2	MM14-1.3	Chromitite	UCZ	4,99	10,93	1,14	46,64	36,30	100
1717,2	MM14-1.4	Chromitite	UCZ	4,79	10,82	1,30	46,82	36,27	100
1717,2	MM14-1.5	Chromitite	UCZ	4,61	10,74	0,97	46,74	36,94	100
1717,2	MM14-1.6	Chromitite	UCZ	4,57	10,40	1,20	46,31	37,52	100
1717,2	MM14-1.7	Chromitite	UCZ	4,88	10,70	0,99	47,49	35,94	100
1717,2	MM14-1.8	Chromitite	UCZ	4,73	10,90	0,99	45,83	37,55	100
1717,2	MM14-1.9	Chromitite	UCZ	4,85	10,93	1,04	46,41	36,77	100
1717,2	MM14-1.10	Chromitite	UCZ	4,97	11,08	0,97	46,39	36,59	100
1717,2	MM14-1.11	Chromitite	UCZ	5,12	10,98	1,15	46,28	36,47	100
1717,2	MM14-2.1	Chromitite	UCZ	4,96	10,92	1,26	46,71	36,15	100
1717,2	MM14-2.2	Chromitite	UCZ	4,94	10,64	1,22	47,25	35,95	100
1717,2	MM14-2.3	Chromitite	UCZ	4,91	10,43	1,00	47,34	36,33	100,01
1717,2	MM14-2.4	Chromitite	UCZ	4,74	10,55	1,05	47,51	36,15	100
1717,2	MM14-2.5	Chromitite	UCZ	4,87	10,72	1,15	46,66	36,60	100
1717,2	MM14-2.6	Chromitite	UCZ	4,75	10,58	1,29	46,72	36,67	100,01
1717,2	MM14-2.7	Chromitite	UCZ	4,77	10,43	1,21	46,92	36,67	100
1717,2	MM14-2.8	Chromitite	UCZ	4,63	10,40	1,44	46,64	36,89	100
1717,2	MM14-2.9	Chromitite	UCZ	4,78	10,58	1,30	47,35	35,99	100
1717,2	MM14-2.10	Chromitite	UCZ	4,82	10,52	0,94	47,23	36,49	100
1717,2	MM14-2.11	Chromitite	UCZ	4,85	10,65	1,10	47,36	36,04	100
1717,2	MM14-2.12	Chromitite	UCZ	4,95	11,04	1,13	46,48	36,40	100
1717,2	MM14-2.13	Chromitite	UCZ	4,83	10,82	1,19	46,62	36,55	100,01
1717,2	MM14-2.14	Chromitite	UCZ	4,97	11,19	1,05	46,83	35,96	100
1717,2	MM14-3.1	Chromitite	UCZ	5,41	11,33	1,02	45,33	36,91	100

Depth (m)	Spots/sample	Lithology	Zone	MgO	Al_2O_3	TiO_2	Cr_2O_3	Fe_2O_3	Total
1717,2	MM14-3.3	Chromitite	UCZ	5,14	11,09	1,12	46,08	36,57	100
1717,2	MM14-3.4	Chromitite	UCZ	4,91	11,31	1,09	45,94	36,76	100,01
1717,2	MM14-3.5	Chromitite	UCZ	4,93	10,95	0,99	46,28	36,85	100
1717,2	MM14-3.6	Chromitite	UCZ	5,02	10,79	1,49	46,19	36,52	100,01
1717,2	MM14-3.7	Chromitite	UCZ	4,95	11,00	1,00	46,20	36,86	100,01
1717,2	MM14-3.8	Chromitite	UCZ	4,69	10,79	1,20	46,75	36,57	100
1717,2	MM14-3.9	Chromitite	UCZ	4,76	10,39	1,45	47,06	36,34	100
1717,2	MM14-3.10	Chromitite	UCZ	4,86	10,63	1,24	46,70	36,57	100
1717,2	MM14-3.11	Chromitite	UCZ	4,94	10,96	1,23	46,03	36,84	100
1717,2	MM14-3.12	Chromitite	UCZ	4,98	11,00	1,20	46,45	36,38	100,01
1717,2	MM14-3.13	Chromitite	UCZ	4,77	11,05	1,41	46,59	36,18	100
1717,2	MM14-3.14	Chromitite	UCZ	5,19	11,23	1,22	45,79	36,57	100
1717,2	MM14-3.15	Chromitite	UCZ	5,25	11,63	1,25	45,72	36,15	100
1718	MM15-1.1	Chromitite	UCZ	6,51	13,77	1,19	44,96	33,57	100
1718	MM15-1.2	Chromitite	UCZ	6,26	12,90	1,34	46,70	32,80	100
1718	MM15-1.3	Chromitite	UCZ	6,26	12,81	1,13	46,76	33,04	100
1718	MM15-1.4	Chromitite	UCZ	6,02	12,44	1,49	47,46	32,59	100
1718	MM15-1.5	Chromitite	UCZ	6,72	13,51	0,99	46,94	31,84	100
1718	MM15-1.6	Chromitite	UCZ	6,38	13,08	1,59	46,65	32,30	100
1718	MM15-1.7	Chromitite	UCZ	6,34	12,92	1,26	46,84	32,64	100
1718	MM15-2.1	Chromitite	UCZ	6,40	13,52	1,44	45,72	32,92	100
1718	MM15-2.2	Chromitite	UCZ	6,16	12,93	1,21	46,50	33,21	100,01
1718	MM15-2.3	Chromitite	UCZ	6,06	13,25	1,23	46,26	33,20	100
1718	MM15-2.4	Chromitite	UCZ	6,17	13,17	1,28	46,29	33,09	100
1718	MM15-2.5	Chromitite	UCZ	6,14	13,49	1,34	45,97	33,06	100
1718	MM15-2.6	Chromitite	UCZ	6,53	13,46	1,25	45,86	32,90	100
1718	MM15-2.7	Chromitite	UCZ	6,27	12,75	1,42	47,00	32,56	100
1718	MM15-2.8	Chromitite	UCZ	6,31	13,15	1,46	46,24	32,84	100
1718	MM15-2.9	Chromitite	UCZ	6,23	13,51	1,45	46,06	32,75	100

Depth (m)	Spots/sample	Lithology	Zone	MgO	Al_2O_3	TiO_2	Cr_2O_3	Fe_2O_3	Total
1718	MM15-3.2	Chromitite	UCZ	6,17	13,02	1,32	46,45	33,04	100
1718	MM15-3.3	Chromitite	UCZ	6,22	13,21	1,17	46,31	33,09	100
1718	MM15-3.4	Chromitite	UCZ	6,07	12,86	1,09	46,46	33,52	100
1718	MM15-3.5	Chromitite	UCZ	5,73	12,28	1,16	47,15	33,68	100
1718	MM15-3.6	Chromitite	UCZ	6,07	13,38	1,29	45,88	33,38	100
1718	MM15-3.7	Chromitite	UCZ	6,20	13,61	1,52	46,04	32,63	100
1718	MM15-3.8	Chromitite	UCZ	6,18	13,53	1,30	45,43	33,56	100
1718	MM15-3.9	Chromitite	UCZ	5,62	12,17	1,33	48,30	32,59	100,01
1718	MM15-3.10	Chromitite	UCZ	6,19	13,12	1,51	46,50	32,68	100
1718	MM15-3.11	Chromitite	UCZ	6,28	13,54	1,21	46,15	32,82	100
1718	MM15-3.12	Chromitite	UCZ	6,07	13,01	1,37	46,38	33,17	100
1718	MM15-3.13	Chromitite	UCZ	6,37	13,30	1,35	46,03	32,95	100
1719	MM16-1.1	Chr-norite	UCZ	6,23	13,59	1,28	44,69	34,21	100
1719	MM16-1.2	Chr-norite	UCZ	5,91	13,19	1,02	45,31	34,57	100
1719	MM16-1.3	Chr-norite	UCZ	6,01	13,38	1,11	45,73	33,78	100,01
1719	MM16-1.4	Chr-norite	UCZ	6,34	13,71	0,99	44,61	34,35	100
1719	MM16-1.5	Chr-norite	UCZ	6,06	13,53	0,98	43,92	35,51	100
1719	MM16-1.6	Chr-norite	UCZ	5,63	12,39	0,95	46,75	34,28	100
1719	MM16-1.7	Chr-norite	UCZ	6,05	12,96	1,22	45,64	34,13	100
1719	MM16-1.8	Chr-norite	UCZ	5,87	12,98	1,06	45,40	34,69	100
1719	MM16-1.9	Chr-norite	UCZ	6,04	13,23	1,18	45,56	33,99	100
1719	MM16-2.1	Chr-norite	UCZ	6,15	13,01	1,16	45,93	33,75	100
1719	MM16-2.2	Chr-norite	UCZ	5,94	12,74	0,98	46,50	33,84	100
1719	MM16-2.3	Chr-norite	UCZ	6,04	12,85	1,04	46,48	33,59	100
1719	MM16-2.4	Chr-norite	UCZ	5,68	12,23	1,00	47,25	33,84	100
1719	MM16-2.5	Chr-norite	UCZ	5,29	11,78	1,24	47,23	34,46	100
1719	MM16-2.6	Chr-norite	UCZ	5,95	12,41	1,01	46,32	34,31	100
1719	MM16-2.7	Chr-norite	UCZ	5,97	12,73	1,08	46,53	33,69	100
1719	MM16.3.1	Chr-norite	UCZ	6,09	13,04	0,94	46,02	33,91	100

Depth (m)	Spots/sample	Lithology	Zone	MgO	Al_2O_3	TiO_2	Cr_2O_3	Fe_2O_3	Total
1719	MM16.3.3	Chr-norite	UCZ	5,95	12,46	1,16	46,74	33,69	100
1719	MM16.3.4	Chr-norite	UCZ	5,73	12,49	1,02	46,62	34,14	100
1719	MM16.3.5	Chr-norite	UCZ	5,73	12,30	1,26	46,00	34,71	100
1719	MM16.3.6	Chr-norite	UCZ	6,21	12,84	1,09	45,69	34,17	100
1719	MM16.3.7	Chr-norite	UCZ	5,91	12,68	1,19	46,69	33,53	100
1719	MM16.3.8	Chr-norite	UCZ	5,90	12,50	1,12	46,50	33,99	100,01
1748,6	MM34-1.1	Chromitite	UCZ	6,07	13,31	1,08	45,96	33,58	100
1748,6	MM34-1.2	Chromitite	UCZ	5,61	12,80	0,87	46,91	33,81	100
1748,6	MM34-1.3	Chromitite	UCZ	6,25	13,74	0,84	45,23	33,94	100
1748,6	MM34-1.4	Chromitite	UCZ	6,22	13,31	1,12	45,52	33,83	100
1748,6	MM34-1.5	Chromitite	UCZ	6,39	13,58	0,86	45,66	33,51	100
1748,6	MM34-1.6	Chromitite	UCZ	6,10	13,57	0,87	45,01	34,45	100
1748,6	MM34-1.7	Chromitite	UCZ	6,11	12,88	1,11	46,90	33,01	100,01
1748,6	MM34-1.8	Chromitite	UCZ	6,13	13,35	0,97	46,23	33,32	100
1748,6	MM34-1.9	Chromitite	UCZ	6,05	13,50	1,11	45,96	33,38	100
1748,6	MM34-1.10	Chromitite	UCZ	6,24	13,38	0,93	45,24	34,22	100,01
1748,6	MM34-1.11	Chromitite	UCZ	4,82	11,15	0,98	48,32	34,73	100
1748,6	MM34-1.12	Chromitite	UCZ	6,20	13,58	1,18	45,92	33,12	100
1748,6	MM34-2.1	Chromitite	UCZ	7,54	16,73	0,82	43,02	31,89	100
1748,6	MM34-2.2	Chromitite	UCZ	6,22	13,59	0,96	46,06	33,17	100
1748,6	MM34-2.3	Chromitite	UCZ	6,05	13,36	1,01	46,22	33,37	100,01
1748,6	MM34-2.4	Chromitite	UCZ	6,16	13,11	0,95	46,22	33,57	100,01
1748,6	MM34-2.5	Chromitite	UCZ	6,08	13,13	0,87	46,91	33,01	100
1748,6	MM34-2.6	Chromitite	UCZ	6,23	13,21	0,91	46,51	33,14	100
1748,6	MM34-2.7	Chromitite	UCZ	6,06	12,99	1,10	46,28	33,57	100
1748,6	MM34-2.8	Chromitite	UCZ	5,92	12,68	1,04	47,10	33,26	100
1748,6	MM34-2.9	Chromitite	UCZ	6,04	13,24	1,00	46,22	33,50	100
1748,6	MM34-2.10	Chromitite	UCZ	5,92	13,11	0,79	46,74	33,45	100,01
1748,6	MM34-2.11	Chromitite	UCZ	5,96	13,30	0,91	45,94	33,89	100

Depth (m)	Spots/sample	Lithology	Zone	MgO	Al_2O_3	TiO_2	Cr_2O_3	Fe_2O_3	Total
1748,6	MM34-2.13	Chromitite	UCZ	4,06	9,25	1,16	50,23	35,30	100
1748,6	MM34-3.1	Chromitite	UCZ	6,55	13,85	0,87	45,87	32,87	100,01
1748,6	MM34-3.2	Chromitite	UCZ	6,14	13,18	1,09	46,19	33,40	100
1748,6	MM34-3.3	Chromitite	UCZ	6,32	13,48	1,00	45,97	33,24	100,01
1748,6	MM34-3.4	Chromitite	UCZ	6,29	13,38	1,34	45,61	33,38	100
1748,6	MM34-3.5	Chromitite	UCZ	6,06	13,37	0,94	46,14	33,49	100
1748,6	MM34-3.6	Chromitite	UCZ	5,39	11,80	0,88	47,86	34,08	100,01
1748,6	MM34-3.7	Chromitite	UCZ	6,05	13,23	1,15	46,38	33,19	100
1748,6	MM34-3.8	Chromitite	UCZ	6,13	13,76	1,16	45,95	33,00	100
1748,6	MM34-3.9	Chromitite	UCZ	6,35	13,41	1,20	46,07	32,97	100
1748,6	MM34-3.10	Chromitite	UCZ	6,47	13,78	1,01	45,86	32,88	100
1749,2	MM35-1.1	Chr-norite	UCZ	4,37	9,70	0,77	48,90	36,26	100
1749,22	MM35-1.2	Chr-norite	UCZ	4,80	10,23	0,85	48,00	36,12	100
1749,2	MM35-1.3	Chr-norite	UCZ	4,80	10,28	0,82	48,16	35,94	100
1749,2	MM35-1.4	Chr-norite	UCZ	4,83	10,34	0,84	47,61	36,38	100
1749,2	MM35-1.5	Chr-norite	UCZ	4,85	10,63	0,77	48,53	35,22	100
1749,2	MM35-1.6	Chr-norite	UCZ	4,10	9,91	0,74	49,51	35,75	100,01
1749,2	MM35-1.7	Chr-norite	UCZ	4,72	10,45		48,81	36,02	100
1749,2	MM35-1.8	Chr-norite	UCZ	4,64	10,57	0,85	48,00	35,94	100
1749,2	MM35-1.9	Chr-norite	UCZ	4,72	11,00	1,00	47,71	35,57	100
1749,2	MM35-2.1	Chr-norite	UCZ	2,66	21,38	0,64	44,02	31,31	100,01
1749,2	MM35-2.2	Chr-norite	UCZ	4,42	9,33	0,97	48,40	36,88	100
1749,2	MM35-2.3	Chr-norite	UCZ	4,31	9,21	1,07	48,23	37,18	100
1749,2	MM35-2.4	Chr-norite	UCZ	4,33	9,35	1,27	48,52	36,53	100
1749,2	MM35-2.5	Chr-norite	UCZ	4,42	9,30	1,06	48,31	36,92	100,01
1749,2	MM35-2.6	Chr-norite	UCZ	4,21	8,69	1,07	49,75	36,28	100
1749,2	MM35-2.7	Chr-norite	UCZ	4,47	9,33	1,10	48,31	36,79	100
1749,2	MM35-2.8	Chr-norite	UCZ	5,00	9,85	0,99	47,87	36,29	100
1749,2	MM35-3.1	Chr-norite	UCZ	4,92	9,49	1,13	47,07	37,39	100

Depth (m)	Spots/sample	Lithology	Zone	MgO	Al_2O_3	TiO_2	Cr_2O_3	Fe_2O_3	Total
1749,2	MM35-3.3	Chr-norite	UCZ	4,58	9,50	1,37	46,60	37,95	100
1749,2	MM35-3.4	Chr-norite	UCZ	4,52	9,35	1,16	46,52	38,46	100,01
1749,2	MM35-3.5	Chr-norite	UCZ	4,62	9,44	1,36	46,45	38,14	100,01
1749,2	MM35-3.6	Chr-norite	UCZ	4,43	9,10	1,16	46,81	38,50	100
1749,2	MM35-3.7	Chr-norite	UCZ	4,66	9,27	1,23	47,02	37,83	100,01
1749,2	MM35-3.8	Chr-norite	UCZ	4,60	9,67	0,80	46,03	38,90	100
1749,2	MM35-3.9	Chr-norite	UCZ	5,16	10,38	1,16	45,39	37,91	100
1756,7	MM43-1.1	Chr-norite	LCZ	5,34	10,55	1,26	47,06	35,79	100
1756,7	MM43-1.2	Chr-norite	LCZ	5,43	10,86	1,11	47,19	35,41	100
1756,7	MM43-1.3	Chr-norite	LCZ	5,77	11,53	1,15	46,22	35,33	100
1756,7	MM43-1.4	Chr-norite	LCZ	5,41	11,01	1,16	46,69	35,73	100
1756,7	MM43-1.5	Chr-norite	LCZ	5,10	10,60	1,27	47,04	35,99	100
1756,7	MM43-1.6	Chr-norite	LCZ	5,24	10,48	1,12	48,09	35,08	100,01
1756,7	MM43-1.7	Chr-norite	LCZ	5,48	11,03	1,12	46,80	35,57	100
1756,7	MM43-2.1	Chr-norite	LCZ	5,68	11,08	1,19	46,90	35,15	100
1756,7	MM43-2.2	Chr-norite	LCZ	5,48	10,72	1,14	47,47	35,19	100
1756,7	MM43-2.3	Chr-norite	LCZ	5,34	10,81	1,07	47,39	35,39	100
1756,7	MM43-2.4	Chr-norite	LCZ	5,31	10,61	1,09	46,98	36,01	100
1756,7	MM43-2.5	Chr-norite	LCZ	5,19	10,39	1,25	47,34	35,83	100
1756,7	MM43-2.6	Chr-norite	LCZ	5,32	10,81	0,92	47,69	35,26	100
1756,7	MM43-2.7	Chr-norite	LCZ	5,33	10,70	0,91	47,93	35,13	100
1756,7	MM43-2.8	Chr-norite	LCZ	5,38	11,29	0,95	46,85	35,54	100,01
1756,7	MM43-2.9	Chr-norite	LCZ	6,10	11,62	1,02	46,93	34,33	100
1756,7	MM43-3.1	Chr-norite	LCZ	5,32	11,39	1,04	46,64	35,61	100
1756,7	MM43-3.2	Chr-norite	LCZ	5,63	10,73	1,20	47,10	35,34	100
1756,7	MM43-3.3	Chr-norite	LCZ	5,48	11,06	1,25	46,64	35,58	100,01
1756,7	MM43-3.4	Chr-norite	LCZ	5,41	10,92	1,11	45,96	36,61	100,01
1756,7	MM43-3.5	Chr-norite	LCZ	5,59	11,35	0,93	47,21	34,93	100,01
1756,7	MM43-3.6	Chr-norite	LCZ	5,33	11,47	1,11	46,52	35,57	100

Depth (m)	Spots/sample	Lithology	Zone	MgO	Al_2O_3	TiO_2	Cr_2O_3	Fe_2O_3	Total
1756,7	MM43-3.8	Chr-norite	LCZ	5,52	11,11	1,11	46,56	35,70	100
1756,7	MM43-3.9	Chr-norite	LCZ	5,48	10,64	1,18	46,44	36,26	100
1756,7	MM43-3.10	Chr-norite	LCZ	5,30	10,87	1,11	46,57	36,15	100
1757	MM44-1.1	Chromitite	LCZ	6,79	13,17	0,95	47,16	31,93	100
1757	MM44-1.2	Chromitite	LCZ	6,50	12,75	0,94	47,18	32,64	100,01
1757	MM44-1.3	Chromitite	LCZ	6,60	12,94	0,97	47,34	32,15	100
1757	MM44-1.4	Chromitite	LCZ	6,76	12,87	0,89	47,72	31,76	100
1757	MM44-1.5	Chromitite	LCZ	6,19	12,47	2,45	46,90	31,99	100
1757	MM44-1.6	Chromitite	LCZ	6,48	13,12	0,97	47,18	32,26	100,01
1757	MM44-1.7	Chromitite	LCZ	6,66	12,78	0,91	47,26	32,39	100
1757	MM44-1.8	Chromitite	LCZ	6,62	12,66	0,72	47,78	32,22	100
1757	MM44-1.9	Chromitite	LCZ	6,74	12,85	1,04	46,81	32,57	100,01
1757	MM44-1.10	Chromitite	LCZ	6,80	13,45	0,90	46,75	32,10	100
1757	MM44-2.1	Chromitite	LCZ	6,75	12,80	0,90	47,44	32,11	100
1757	MM44-2.2	Chromitite	LCZ	6,68	12,83	0,69	47,75	32,05	100
1757	MM44-2.3	Chromitite	LCZ	6,60	12,96	0,88	47,60	31,97	100,01
1757	MM44-2.4	Chromitite	LCZ	6,66	13,01	0,98	47,43	31,92	100
1757	MM44-2.5	Chromitite	LCZ	6,50	12,82	0,85	47,61	32,23	100,01
1757	MM44-2.6	Chromitite	LCZ	6,82	13,19	1,12	46,45	32,42	100
1757	MM44-2.7	Chromitite	LCZ	6,21	12,42	1,17	48,40	31,80	100
1757	MM44-2.8	Chromitite	LCZ	6,59	12,83	0,86	47,37	32,35	100
1757	MM44-2.9	Chromitite	LCZ	6,56	12,63	0,92	47,73	32,16	100
1757	MM44-2.10	Chromitite	LCZ	5,98	12,28	0,89	47,97	32,88	100
1757	MM44-3.1	Chromitite	LCZ	6,91	14,13	0,80	46,95	31,21	100
1757	MM44-3.2	Chromitite	LCZ	6,59	13,14	1,11	46,82	32,34	100
1757	MM44-3.3	Chromitite	LCZ	6,64	13,32	1,10	46,64	32,30	100
1757	MM44-3.4	Chromitite	LCZ	7,02	13,71	1,39	46,06	31,83	100,01
1757	MM44-3.5	Chromitite	LCZ	6,69	13,11	0,98	46,42	32,81	100,01
1757	MM44-3.6	Chromitite	LCZ	6,29	12,93	0,97	47,49	32,32	100

Depth (m)	Spots/sample	Lithology	Zone	MgO	Al_2O_3	TiO_2	Cr_2O_3	Fe_2O_3	Total
1757	MM44-3.8	Chromitite	LCZ	6,63	13,12	1,01	47,06	32,18	100
1757	MM44-3.9	Chromitite	LCZ	7,07	14,24	0,93	46,28	31,48	100
1778,3	MM54-1.1	Chr-gabbronorite	LCZ	5,13	10,44	1,42	47,33	35,68	100
1778,3	MM54-1.2	Chr-gabbronorite	LCZ	5,32	10,35	1,63	46,83	35,87	100
1778,3	MM54-1.3	Chr-gabbronorite	LCZ	5,49	10,22	1,29	47,86	35,15	100,01
1778,3	MM54-1.4	Chr-gabbronorite	LCZ	5,35	10,59	1,45	47,40	35,21	100
1778,3	MM54-1.5	Chr-gabbronorite	LCZ	5,54	10,32	1,37	46,85	35,92	100
1778,3	MM54-1.6	Chr-gabbronorite	LCZ	5,47	10,59	1,32	47,34	35,28	100
1778,3	MM54-1.7	Chr-gabbronorite	LCZ	5,23	10,13	1,26	47,42	35,96	100
1778,3	MM54-1.8	Chr-gabbronorite	LCZ	5,17	10,20	1,12	47,74	35,77	100
1778,4	MM54-1.9	Chr-gabbronorite	LCZ	5,19	10,16	1,17	47,82	35,66	100
1778,3	MM54-1.10	Chr-gabbronorite	LCZ	5,61	10,34	1,13	47,40	35,52	100
1778,3	MM54-1.11	Chr-gabbronorite	LCZ	5,68	10,53	1,40	47,37	35,02	100
1778,3	MM54-2.1	Chr-gabbronorite	LCZ	6,04	11,54	1,17	46,63	34,62	100
1778,3	MM54-2.2	Chr-gabbronorite	LCZ	5,21	9,64	7,50	45,40	32,26	100,01
1778,3	MM54-2.3	Chr-gabbronorite	LCZ	5,53	10,54	1,14	47,70	35,09	100
1778,3	MM54-2.4	Chr-gabbronorite	LCZ	5,40	10,50	1,19	48,31	34,60	100
1778,3	MM54-2.5	Chr-gabbronorite	LCZ	5,46	10,14	1,03	47,97	35,41	100,01
1778,3	MM54-2.6	Chr-gabbronorite	LCZ	5,85	11,19	1,02	46,78	35,17	100,01
1778,3	MM54-2.7	Chr-gabbronorite	LCZ	5,26	10,60	1,08	47,69	35,37	100
1778,3	MM54-2.8	Chr-gabbronorite	LCZ	5,36	10,39	0,97	48,25	35,03	100
1778,3	MM54-2.9	Chr-gabbronorite	LCZ	5,45	10,33	0,95	47,64	35,63	100
1778,3	MM54-2.10	Chr-gabbronorite	LCZ	5,55	10,49	1,04	47,62	35,30	100
1778,3	MM54-2.11	Chr-gabbronorite	LCZ	5,91	10,83	0,91	48,26	34,09	100
1778,3	MM54-3.1	Chr-gabbronorite	LCZ	5,42	10,51	1,11	47,88	35,08	100
1778,3	MM54-3.2	Chr-gabbronorite	LCZ	5,23	10,28	1,52	47,87	35,10	100
1778,3	MM54-3.3	Chr-gabbronorite	LCZ	5,19	10,12	1,17	48,03	35,49	100
1778,3	MM54-3.4	Chr-gabbronorite	LCZ	5,61	10,13	1,30	47,48	35,48	100
1778,3	MM54-3.5	Chr-gabbronorite	LCZ	5,30	10,02	0,87	48,14	35,68	100,01

Depth (m)	Spots/sample	Lithology	Zone	MgO	Al_2O_3	TiO_2	Cr_2O_3	Fe_2O_3	Total
1778,3	MM54-3.7	Chr-gabbronorite	LCZ	5,35	9,94	1,52	47,67	35,53	100,01
1778,3	MM54-3.8	Chr-gabbronorite	LCZ	5,44	10,32	1,21	47,71	35,32	100
1779	MM54-3.9	Chr-gabbronorite	LCZ	5,57	10,26	1,10	48,00	35,07	100
1779	MM55-1.1	Chromitite	LCZ	4,98	10,29	1,07	50,87	32,79	100
1779	MM55-1.2	Chromitite	LCZ	7,68	14,30	0,76	46,60	30,66	100
1779	MM55-1.3	Chromitite	LCZ	6,75	12,99	0,93	47,88	31,45	100
1779	MM55-1.4	Chromitite	LCZ	4,64	9,42	0,84	51,93	33,17	100
1779	MM55-1.5	Chromitite	LCZ	6,34	11,89	1,10	49,27	31,40	100
1779	MM55-1.6	Chromitite	LCZ	6,79	12,46	0,98	48,88	30,90	100,01
1779	MM55-1.7	Chromitite	LCZ	7,10	13,37	0,88	47,73	30,92	100
1779	MM55-1.8	Chromitite	LCZ	3,59	7,70	0,99	54,42	33,31	100,01
1779	MM55-1.9	Chromitite	LCZ	6,82	12,72	0,85	48,41	31,20	100
1779	MM55-1.10	Chromitite	LCZ	4,35	8,71	0,78	53,07	33,09	100
1779	MM55-1.11	Chromitite	LCZ	6,51	12,56	0,98	48,64	31,31	100
1779	MM55-1.12	Chromitite	LCZ	7,21	13,04	0,90	47,04	31,81	100
1779	MM55-1.13	Chromitite	LCZ	7,67	13,65	0,93	46,32	31,44	100,01
1779	MM55-2.1	Chromitite	LCZ	7,58	13,34	0,87	47,80	30,41	100
1779	MM55-2.2	Chromitite	LCZ	7,70	13,80	0,83	47,42	30,25	100
1779	MM55-2.3	Chromitite	LCZ	7,29	13,32	0,84	47,97	30,58	100
1779	MM55-2.4	Chromitite	LCZ	10,27	6,42	1,54	50,45	31,32	100
1779	MM55-2.5	Chromitite	LCZ	7,29	13,47	0,97	47,67	30,61	100,01
1779	MM55-2.6	Chromitite	LCZ	6,70	12,12	0,86	49,79	30,53	100
1779	MM55-2.7	Chromitite	LCZ	6,23	11,80	0,87	49,71	31,39	100
1779	MM55-2.8	Chromitite	LCZ	4,43	9,55	1,18	52,29	32,55	100
1779	MM55-2.9	Chromitite	LCZ	8,17	14,48	0,86	47,07	29,43	100,01
1779	MM55-2.10	Chromitite	LCZ	7,55	14,15	0,83	47,49	29,98	100
1779	MM55-3.1	Chromitite	LCZ	7,63	13,40	0,96	47,57	30,44	100
1779	MM55-3.2	Chromitite	LCZ	7,62	13,83	0,76	47,25	30,54	100
1779	MM55-3.3	Chromitite	LCZ	7,61	13,86	0,77	47,06	30,70	100

Depth (m)	Spots/sample	Lithology	Zone	MgO	Al_2O_3	TiO_2	Cr_2O_3	Fe_2O_3	Total
1779	MM55-3.5	Chromitite	LCZ	6,25	11,95	0,88	49,47	31,45	100
1779	MM55-3.6	Chromitite	LCZ	8,60	15,48	0,79	45,27	29,86	100
1779	MM55-3.7	Chromitite	LCZ	7,66	13,09	0,78	46,55	31,92	100
1779	MM55-3.8	Chromitite	LCZ	6,91	12,77	0,98	48,23	31,11	100
1779	MM55-3.9	Chromitite	LCZ	4,24	8,36	0,94	53,72	32,74	100
1779	MM55-3.10	Chromitite	LCZ	6,46	11,90	1,10	49,78	30,76	100
1779	MM55-3.11	Chromitite	LCZ	6,48	11,65	1,13	48,93	31,81	100